Partial Wave Analysis of Neutral b_1 Meson at GLUEX

A THESIS
SUBMITTED TO THE FACULTY OF GRADUATE STUDIES AND RESEARCH
IN PARTIAL FULFILLMENT OF THE REQUIREMENTS
FOR THE DEGREE OF
DOCTOR OF PHILOSOPHY
IN
PHYSICS
UNIVERSITY OF REGINA

By
Karthik Suresh
Regina, Saskatchewan
September 2023

Abstract

A long-standing goal of hadron physics has been to understand how the quark and gluon degrees of freedom that are present in the fundamental QCD Lagrangian manifest themselves in the spectrum of hadrons. The GlueX experiment at JLab contributes to the global spectroscopy program through studies of the mesons produced using a beam of 8-9 GeV linearly polarized photons. This experiment focuses on the exploration of the light-quark domain, potentially accessing hybrid mesons with exotic J^{PC} quantum numbers in photoproduction reactions.

Recent Lattice QCD calculations predict that the lightest exotic $\pi_1(1600)$ decays primarily to a b_1 system and can be experimentally accessed through the dominant decay $b_1 \to \omega\pi^0$. In this dissertation, direct production of the b_1 meson $\gamma p \to b_1 p$ where the axial-vector meson $b_1(1235)$ decays to $\omega\pi^0$, is studied in detail. Results of Partial Wave Analysis (PWA) on the photoproduction of the $b_1(1235)$ meson system are shown, with emphasis on the extraction of D-wave to S-wave ratio (termed `dsratio`), which is a characteristic property of this meson and this coupling has been predicted by Lattice QCD calculations. The `dsratio` does not depend on the production mechanism nor on features such as the momentum transfer ($|t|$) or the polarization of the photon beam. PWA in the mass range between $1.0 - 2.0$ GeV was carried out in bins of 80 MeV, and three momentum transfer, $|-t|$, ranges. The analysis procedure was validated using Monte Carlo simulated data to be free of any potential biases.

Fits describe the five characteristic angles in the two-plane $b_1 \to \omega\pi^0 \to \pi^+\pi^-\pi^0\pi^0$ decay. An advanced model selection strategy used the metrics of Likelihood Ratio Test and information criteria Akaike Information Criterion and Bayesian Information Criterion, and demonstrated that the $[J^P]^{(\epsilon)}$ state of $[1^+]^{(+)}$ is the most dominant wave

which concludes that the photoproduction of b_1 is found to proceed through unnatural parity π^0 exchange. Additionally, the $[1^-]^{(+)}$ wave without resonant structure was found to be the second strongest wave. This is consistent with results in the literature from a complimentary experiment that was run more than two decades ago, with the current work exceeding the statistical precision by at least an order of magnitude and systematic uncertainty being competitive with previous measurements. Evidence of the need for higher waves in the higher mass region was found and is in agreement with past results. Contributions from individual m projections for the photoproduction of $\omega\pi^0$ corresponding to the $[1^+]$ as a function of $|t|$ are extracted and presented for the first time in this dissertation.

The `dsratio` was extracted under the condition of a fixed $D - S$ phase (termed `dphase`) and was shown to be constant as a function of variables. This was expected, although with a lower value than theoretical calculations for the highest $|t|$ bin, which will be investigated in future by others. A thorough set of systematic variations were performed to evaluate the systematic uncertainties. The study concluded that the largest error comes from the choice of the waveset used to describe the data. Future studies should include the variation of `dphase`.

Finally, service contributions were made towards the gain calibration of the Barrel Calorimeter detector built by the Regina group. Additionally, for a period of eight months, a pioneering study was carried out using Artificial Intelligence towards the dimensional and positional optimization of a detector, for the Electron-Ion Collider (EIC) facility under the proto-collaboration named ECCE. The results of this study are summarized in this dissertation.

Acknowledgements

I am deeply grateful to my PhD advisor, Dr. Zisis Papandreou, for your unwavering support and guidance since the day I joined your group. Your expertise in physics, particularly in building detectors, has captivated me. I am grateful for your availability and willingness to discuss both subject matter and broader topics. I am especially thankful for allowing me to explore various research areas during my PhD journey. I immensely appreciate your patience with me and continual encouragement.

I extend my heartfelt thanks to my co-supervisor, Dr. Cristiano Fanelli, who introduced me to the world of Artificial Intelligence and Machine Learning. Working closely with you has been invaluable and has ignited my passion for data science. Your constant motivation and encouragement have pushed me to surpass my limits. You have always been there for discussions, both academic and personal. Your dedication to work has been truly inspiring.

I also want to express my gratitude to our collaborators at GlueX and Thomas Jefferson National Accelerator Facility as this dissertation would not have been possible without them. Specifically, I want to thank Dr. Justin Stevens, whose mentorship has guided me towards achieving the physics objectives of this dissertation. Your expertise in physics and data analysis has greatly enhanced my understanding and made my PhD journey smoother. I am grateful for your accessibility and willingness to address any questions I ask you. I would like to acknowledge Dr. Elton Smith and Dr. Mark Dalton for their valuable mentoring and discussions, which deepened my understanding of the workings of the BCAL.

This work was supported by the Natural Science and Engineering Research Council of Canada Grant No.SAPPJ-2018-00021. I thank FGSR for providing additional aid through Teaching Assistantships and Thesis awards during the course of PhD.

Dedication

I owe my deepest gratitude to my family and extended family members, who have been instrumental in shaping my journey this far. My parents, Mr. Suresh Ramamoorthy and Ms. Parvatha Varthini, have played an integral role in my upbringing and without their unwavering support, I would not have reached this point. I am especially grateful to my sister, Ms. Ramya Suresh, whose support enabled me to pursue my Ph.D. Thank you for being there for me and supporting me throughout these years.

I want to express my heartfelt appreciation to the love of my life, Pavithra Anantharaman Sudhakari. You have not only inspired me to embark on this research journey but have been my pillar of emotional support through all the challenges. Your presence has brought stability to my life, and you continue to be my greatest inspiration. Our discussions have made me realize that science extends beyond boundaries and can ignite even the most romantic conversations. Thank you for helping me broaden my perspective on science.

Lastly, I would like to extend my thanks to all my friends, with a special mention to Dr. Dilli Raj Paudyal and his family, who made Regina feel like a home away from home. Your friendship has been invaluable, and your support has made this journey more fulfilling.

To my family, my partner, and my friends, I am forever grateful for your unwavering support, love, and encouragement. Your presence in my life has been the driving force behind my accomplishments, and I am deeply thankful for each and every one of you. This dissertation is a dedication to all of you.

Contents

List of Figures

List of Tables

Glossary

LH_2 Liquid Hydrogen. 2, 45, 50, 65

AIC Akaike Information Criterion. ii, x, 89–91, 97–99, 105–107, 116, 121, 175

BCAL Barrel Calorimeter. v, ix, xv, xvi, xviii, xxi, 2, 48–62, 67, 68, 174, 179, 200, 201

BIC Bayesian Information Criterion. ii, x, 91, 97–99, 105–107, 116, 121, 175

BNL Brookhaven National Laboratory. 34, 111, 139

CDC Central Drift Chamber. xxi, 45, 46, 68

CEBAF Continuous Electron Beam Accelerator Facility. ix, xv, 38, 39, 41, 65

FCAL Forward Calorimeter. xxi, 48, 50–52, 67, 68, 179

FDC Forward Drift Chamber. 45–47

GlueX GlueX Experiment. ii, v, ix–xi, xiii–xix, xxi–xxiii, 2, 3, 18, 20, 26, 33, 36, 37, 39–41, 45, 47, 48, 52, 54, 57, 62–67, 70–83, 92, 101–108, 111, 112, 114, 115, 118–122, 124–128, 132–136, 174–176, 179, 200, 201, 209, 213–218, 220, 222–227

JPAC Joint Physics Analysis Center. xxi, 16, 26, 27, 133, 134

LQCD Lattice Quantum ChromoDynamics. viii, xv, 13–16, 26

LRT Likelihood Ratio Test. ii, x, 88, 89, 97, 98, 105–107, 116, 117, 121, 175

PID Particle Identification Detector. ix, 47

PMT Photo Multiplier Tubes. 48, 51

PWA Partial Wave Analysis. ii, ix, x, xii, xxii, 3, 24, 32, 34, 71, 74, 77–80, 84, 87, 92, 93, 95, 101, 102, 108, 109, 113, 116, 119, 123, 174, 175, 178, 179

QCD Quantum ChromoDynamics. ii, viii, 2, 4, 10–15, 140, 141

QM Quark Model. viii, xxi, 5–7, 10

SC Start Counter. xxi, 46–48, 67, 68

SM Standard Model. viii, 3–5

TJNAF Thomas Jefferson National Accelerator Facility. v, 37–39, 139, 180

TOF Time Of Flight. xxi, 48, 67, 68, 162

TTL Tracking and Timing layer. 166, 169

`AmpTools` AmpTools. xxi, 78, 83–85, 174

EA Evolutionary Algorithm. 151

ECCE EIC Comprehensive Chromodynamics Experiment. iii, xii, xiv, xviii, xix, 3, 139, 146, 147, 150, 155, 156, 161, 170, 176, 177, 228, 229, 231, 232, 236–238

EIC Electron-Ion Collider. iii, xi, xii, xvii, 2, 3, 138–146, 156, 157, 163, 170, 172

FADC Flash - Analog to Digital Converter. 49, 52, 54, 55, 59, 60

MOBO Multi Objective Bayesian Optimization. xii, 154, 155, 159, 172, 176, 230, 235, 236

MOEA Multi Objective Evolutionary Algorithm. xii, xviii, 151, 153, 154, 159, 162, 165, 172, 176, 230

MOO Multi Objective Optimization. xii, xiv, xviii, 139, 148–151, 153, 159, 229, 230

SiPM Silicon PhotoMultipliers. 49, 54–56, 59, 60, 62

TDC Time to Digital Converter. 56

Nomenclature followed in this dissertation

- **Mass** - GeV ; $c = 1$
- **Momentum** - GeV/c
- **Mandelstam t** ($|t|$) - GeV^2 ; $c = 1$

Chapter 1

Introduction

Mid-high energy physics experiments like GlueX and Electron-Ion Collider (EIC) are designed to understand the interactions of quarks and gluons inside hadrons. Quarks are the building blocks of protons and neutrons (quark triplets). These form the bulk of our universe's matter, along with a large number of other strongly interacting particles, like hadrons, ranging from light mesons ($q\bar{q}$ system) to heavy pentaquarks systems. The experiments aim to understand the "glue" that binds us all. In GlueX, the spectrum of hadrons is studied using collisions between a linearly polarized beam of photons and Liquid Hydrogen (LH_2) target. Quantum ChromoDynamics (QCD) prediction of these exotic and hybrid states have been validated with relatively scarce experimental evidence. GlueX aims to study the properties of the exotics and hybrid mesons at a relatively high rate and with unprecedented precision.

The Electron-Ion Collider (EIC) aims to understand the hadronic structure and map out the 3D structure of nuclei. It also seeks to solve the long-standing proton spin puzzle to extract the exact contributions of gluonic and quark spins to the total spin of the hadron. EIC is envisioned to be built in the next decade and will be using an electron beam colliding with proton/nuclei with a wide range of center of mass energies.

Both experiments will expand our current understanding of strong interactions and quark-gluon interactions. A brief overview of the current state of understanding in particle physics is presented in Chapter 1 along with experimental evidence for hybrid and exotic mesons. A special focus has been given to explain in detail the b_1 ($J^{PC} = 1^{+-}$) mesonic state and its history. Chapter 2 describes the experimental setup for GlueX and explains its data management and processing pipelines. Chapter 3 describes various Barrel Calorimeter (BCAL) performance studies including the gain calibration efforts from fall 2018 until fall 2021. Chapter 4 discusses the analysis level cuts performed to extract $\omega\pi^0$ from GlueX-I data. Chapter 5 and Chapter 6 describe in detail the Partial Wave Analysis (PWA) efforts made on the $\omega\pi^0$ channel at GlueX to extract the properties of neutral b_1 at GlueX. Chapter 7 describes the work carried out with the EIC Comprehensive Chromodynamics Experiment (ECCE) proto collaboration to design the tracker using AI-based techniques. Finally, Chapter 8 draws significant conclusions on the PWA on the $\omega\pi^0$ channel at GlueX and discusses future possible studies to improve the PWA performed in this dissertation. Chapter 8 also summarizes the significant outcomes of the AI-assisted design studies made for EIC and outlines the future possible optimization pipeline that can be deployed to optimize the ePIC detector for EIC and also outlines the conceptual workflow for a generic large-scale experimental design optimization.

1.1 The Standard Model (SM)

The Standard Model (SM) of particle physics is a theoretical framework that describes fundamental particles and their interactions. It is one of the successful theories that has been able to explain a wide range of phenomena in particle physics and has been extensively tested through a variety of experiments. There are four types of forces in nature: (i) the Strong Nuclear force (ii) the Electromagnetic force (iii) the Weak Nuclear force, and (iv) the Gravitational force (listed in decreasing order of strength). The SM is successful in explaining the first three types of forces listed above while it fails to describe the theory of gravity.

The SM categorizes particles having intrinsic half-integer spin as fermions which are the building blocks of matter and particles with integer spin as bosons which are force carriers (mediators) between different particles. Fermions are further classified into two categories, namely quarks and leptons. Quarks have a color charge which is affected by the strong force and hence binds quarks and gluons into composite particles, while leptons are not affected by the strong force. Each particle in the SM can be identified using a unique set of quantum numbers.

The SM consists of three main components that explain the three types of forces, namely the electroweak theory, the strong nuclear force theory Quantum ChromoDynamics (QCD), and the Higgs mechanism.

The electroweak theory describes the weak and electromagnetic interactions, which are responsible for phenomena such as beta decay and the decay of neutral particles. It is based on the unification of the weak and electromagnetic interactions and is described by the electroweak gauge theory ($SU(2) \times U(1)$). The $W^{\pm}$ and the Z bosons are the mediators of the weak force.

QCD describes the strong nuclear force using the group $SU(3)$, which is responsible for the confinement of quarks inside protons and neutrons and the interaction between them. In QCD, the strong nuclear force is mediated by the exchange of particles called gluons. Gluons carry the "color charge" which is the property that causes the confinement of quarks inside protons and neutrons, and the interaction between them.

QCD can accurately predict the properties of subatomic particles and their interactions, and it has been successful in explaining a wide range of phenomena in particle physics. More information about QCD will be presented in the next section.

The Higgs mechanism is responsible for giving particles mass. It describes the Higgs field, a scalar field that permeates all of space, and the Higgs boson, a particle that is associated with the Higgs field. When other particles interact with the Higgs field, they acquire mass.

A schematic summary of the SM is shown in Figure 1.1.

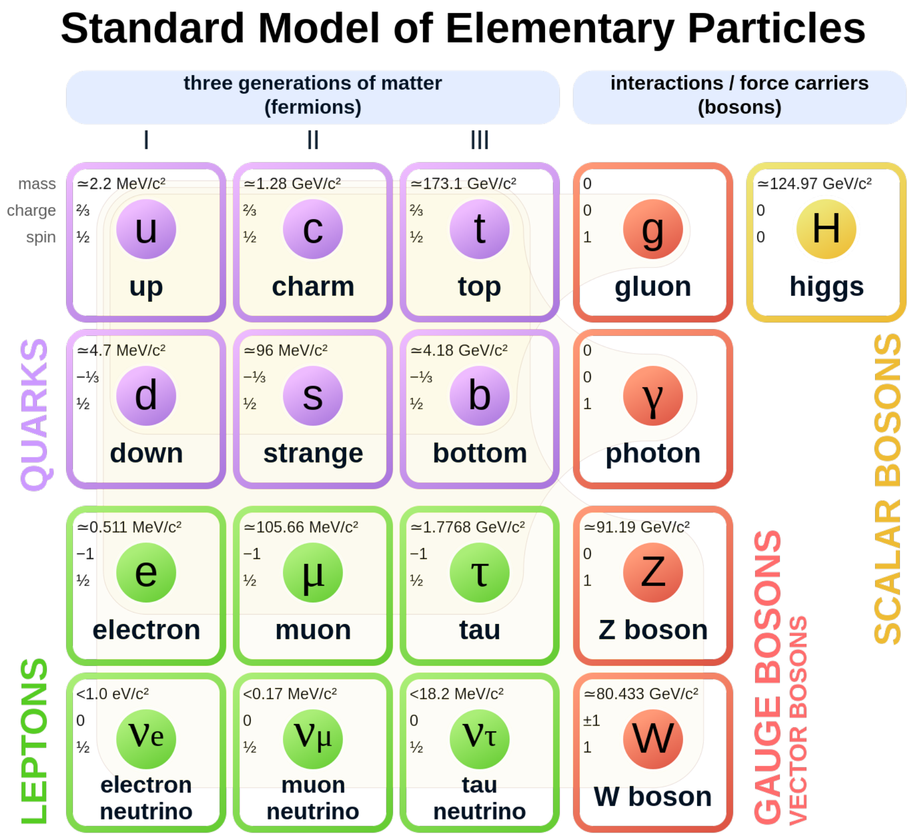

Figure 1.1: Fundamental particles according to the Standard Model. All known fundamental particles are classified into quarks, leptons, gauge bosons, and the Higgs boson. Figure from [1].

1.1.1 The Quark Model (QM)

The Quark Model (QM) is a theoretical framework that describes the properties and behaviour of quarks. Quarks are the fundamental building blocks of protons and neutrons, which make up the nucleus of an atom. The QM was first proposed by Murray Gell-Mann [2] in 1964 and later independently by George Zweig [3] in the same year. Over the next decade since the proposal of the QM, various contributions resulted in a variety of QM descriptions of hadrons. Generically, the description of hadronic properties using only the role of the quark-content part of the wave function of the hadron is called the QM.

According to the QM, the protons and neutrons are made up of quarks with specific quantum numbers. The QM describes quarks as having two types of properties: flavor and spin. The flavor property describes the different types of quarks, such as up, down, charm, strange, top and bottom[1]. Quarks are strongly interacting fermions with spin $\frac{1}{2}$ and positive parity. Quarks have an additive baryon number of $\frac{1}{3}$. The charge of a given flavor of quark is defined through the generalized Gell-Mann-Nishijima formula as shown in Equation. 1.1. A summary of the quantum numbers of the quarks is shown in Table 1.1.

$$\mathcal{Q} = I_z + \frac{\mathcal{B} + S + C + B + T}{2} \tag{1.1}$$

where, $\mathcal{Q}$ is the charge of the quark, I_z is the z component of the isospin quantum number, $\mathcal{B}$ is the baryon number, S, C, B, T are strangeness, charmness, bottomness, and topness quantum numbers.

---

[1] The QM [2, 3] only included light favoured quarks namely, up, down and strange quarks.

	u	**d**	**c**	**s**	**t**	**b**
$\mathcal{Q}$ - electric charge [e]	$\frac{2}{3}$	$-\frac{1}{3}$	$\frac{2}{3}$	$-\frac{1}{3}$	$\frac{2}{3}$	$-\frac{1}{3}$
I - isospin	$\frac{1}{2}$	$\frac{1}{2}$	0	0	0	0
I_z - isospin z component	$\frac{1}{2}$	$-\frac{1}{2}$	0	0	0	0
B - Baryon number	$\frac{1}{3}$	$\frac{1}{3}$	$\frac{1}{3}$	$\frac{1}{3}$	$\frac{1}{3}$	$\frac{1}{3}$
S- Strangeness	0	0	0	-1	0	0
C - Charm	0	0	$+1$	0	0	0
B - Bottomness	0	0	0	0	0	-1
T - Topness	0	0	0	0	0	$+1$

Table 1.1: Quantum numbers of quarks. Antiquarks have the opposite signs for each of the corresponding quantum numbers. only u and d have non zero isospin of $\frac{1}{2}$.

The QM predicts four states of quark-antiquark bound systems. (i) Mesons (quark doublets $q\bar{q}$), (ii) Baryons (quark triplets) and has $\mathcal{B} = 1$, (iii) Tetraquarks, and (iv) Pentaquarks [4]. The mesons and baryons are minimal particle content states, which can be color singlets in an $SU(3)$ gauge theory. In spite of describing the hadron structure by considering only the $q\bar{q}$ interactions is incomplete, it successfully explains a wide range of phenomena in particle physics. It predicts the properties of subatomic particles like their masses and some of their interactions. The QM is not part of the QM of particle physics it forms the foundation of the Standard Model (SM) of particle physics, which describes the fundamental particles and their interactions as seen in previous Section 1.1.

1.1.2 Mesons

Mesons have baryon number $\mathbf{B} = 0$ and are $q\bar{q}$ bound states of the quarks (q) and antiquarks $(\bar{q})$. Meson states $(q\bar{q})$ can be constructed by respecting the following quantum rules:

Total Spin (J): quarks (q) and anti-quarks ($\bar{q}$) have an intrinsic spin $\frac{1}{2}$. In a $q\bar{q}$ system, the constituents can combine resulting in a total spin (S), 0 (anti-aligned) or 1 (aligned). In addition to the total intrinsic spin, the $q\bar{q}$ can have a relative orbital angular momentum (L) between them. This gives rise to a total spin (J) of the meson which could be from $J = |L - S|$ to $|L + S|$. A schematic illustration of the total spin of a meson is shown in Figure 1.2a. The meson states are expressed in spectroscopic notation as ${}^{2s+1}L_J$.

Isospin (I): Analogous to the intrinsic spin of elementary particles, Isospin is used to describe the properties of hadrons. Isospin is non-zero only for u and d quarks. The Isospin (I) of the quarks add up like any other quantum numbers resulting in spin-triplet or singlet states ($I_z = -I$ to I) for a $q\bar{q}$ system.

Parity (P): Parity is a reflection operator when applied on a wavefunction ψ inverts the system through origin. The eigen value equation for a Parity operator on a $q\bar{q}$ is $\hat{\mathcal{P}}\,|q\bar{q}\rangle = k_P\,|q\bar{q}\rangle$. k_P is the eigen value of the operator taking $+1$ (even parity) or -1 (odd parity). Parity for a given meson can be defined as $P(q\bar{q}) = (-1)^{L+1}$.

Charge Conjugation (C) and G Parity (G): represents the transformation of the particle into its antiparticle. This reverses several properties of the particle such as charge and magnetic moment. The charge conjugation operator inverts the electric charge, isospin and its hypercharge. Charge conjugation eigen value equation for a $q\bar{q}$ state is $C\,|q\bar{q}\rangle = k_C\,|q\bar{q}\rangle$. k_C can be $+1$ or -1. Charge conjugation for a given meson is defined as $C(q\bar{q}) = (-1)^{L+S}$. It can be noted that charge conjugation can only be applied to electrically neutral states. Therefore, an extension that can be applied to electrically charged states is G-Parity, which involves a rotation in the isospin and the electrical charge. The G-parity for a given meson is $G(q\bar{q}) = (-1)^{L+S+I}$.

Respecting the quantum rules mesons can now be constructed using a pair of $q\bar{q}$ states. Mesons with light flavours of quarks (u, d, s) such that $C = B = T = 0$ are called light flavour mesons. Figure 1.2 (bottom row) shows two nonets of mesons constructed in ground state $L = 0$ with $S = [0, 1]$. The mesons are arranged based on their overall charge $\mathcal{Q}$, Strangeness (S) and its z component of its isospin (I).

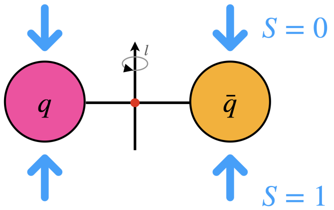

(a) Total spin angular momentum of $q\bar{q}$ system

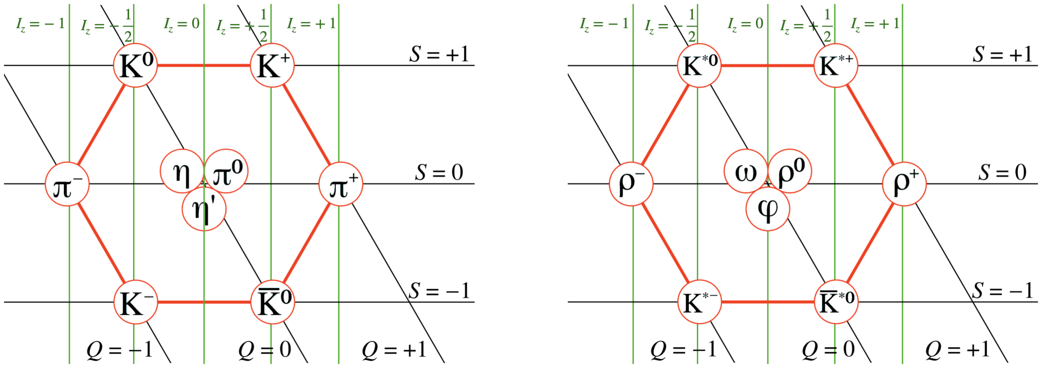

(b) Pseudo-scalar meson $(S = 0)$ nonet **(c)** Vector meson $(S = 1)$ nonet

Figure 1.2: Top row figure (a) is a schematic showing the $q\bar{q}$'s intrinsic spin and relative orbital angular momentum combining to yield the total spin J of the system. The bottom row shows the two-state mesons corresponding to $L = 0$ between the $q\bar{q}$ system. The nonet on the bottom left (b) is the meson octet corresponding to $S = 0$. The nonet on the bottom right corresponds to $S = 1$. The S in the bottom row figures refers to the Strangeness of the quarks. Figures are adapted from [5, 6].

The nomenclature of mesons in literature is based on its J^{PC} quantum numbers. Detailed nomenclature of mesons up to $J^{PC} = 2^{++}$ are summarized in the Table 1.2.

State $^{2s+1}l_J$	Name	S	L	Total Spin J^{PC}	$I = 0$	$I = 1$	$I = \frac{1}{2}$
$^1S_0$	Pseudo Scalar	0	0	0^{-+}	$\eta, \eta^{'}$	π	K
$^3S_1$	Vector	1	0	1^{--}	ω, ϕ	ρ	K^*
$^1P_1$	Axial Vector	0	1	1^{+-}	$h_1, h_1^{'}$	b_1	K_1
$^3P_0$	Scalar	1	1	0^{++}	$f_0, f_0^{'}$	a_0	K_1^*
$^3P_1$	Axial Vector	1	1	1^{++}	$f_1, f_1^{'}$	a_1	K_1
$^3P_2$	Tensor	1	1	2^{++}	$f_2, f_2^{'}$	a_2	K_2^*

Table 1.2: Table summarizing the mesons as predicted by QM up to $L = 1$ and $S = 1$.

By applying these quantum rules, a set of J^{PC} states (0^{--}, 0^{+-}, 1^{-+}, 2^{+-}, 3^{-+}, etc.) are forbidden by the QM. Observations of these states will be a solid indication that the mesons are not only composed of contributions from quark-antiquark ($q\bar{q}$) pair but gluonic excitation may also play a role in its state composition.

1.1.3 Quantum ChromoDynamics (QCD)

Quantum ChromoDynamics (QCD) describes the strong nuclear force, which is responsible for the confinement of quarks inside protons and neutrons, and the interaction between them. It is based on the $SU(3)$ color, $SU(3)_c$ gauge symmetry group with the colored quarks and anti-quarks as its fundamental triplet, and the eight vector gauge fields (gluons) as its fundamental octet representations. The theory of QCD is analogous to the theory of electromagnetism on smaller scales, Quantum ElectroDynamics (QED). QED represents the interaction between charged particles through the exchange of photons. The electric charge interacts with the exchange of photons. Since photons do not have an electric charge they do not interact with other photons. Analogous to the electric charge, in QCD, gluons are the mediators of the strong force, and each of the constituents carries a charge, called the color charge. There are three types of color charges, namely Red (R), Blue (B), and Green (G). An important property of QCD is 'color-confinement', Since in QCD, gluons as well as quarks are considered as dynamical degrees of freedom, physical color-neutral states outside the quark model are allowed in the spectrum of hadrons as summarized below.

1. Glueballs are states that do not contain any valence quarks in their composition. Glueballs are predicted to be in doublets (gg) and triplets (ggg).
2. Hybrid mesons ($q\bar{q}g$) are quark doublet states with gluonic degrees of freedom.
3. Hybrid baryons ($qqqg$) are quark triplet states with contributions from gluonic degrees of freedom.

The coupling of the three color combinations of quarks ($a = 1, 2, 3$), with its eight colors of gluons ($C = 1, 2, ..., 8$) is described by the QCD Lagrangian,

$$\mathcal{L}_{\text{QCD}} = \sum_{q} \bar{\psi}_{q,a}(i\gamma^{\mu}\partial_{\mu}\delta_{ab} - g_s\gamma^{\mu}\frac{\lambda_{ab}^{C}}{2}\mathcal{A}_{\mu}^{C} - m_q\delta_{ab})\psi_{q,b} - \frac{1}{4}F_{\mu\nu}^{A}F^{A\mu\nu} \tag{1.2}$$

where, γ^{μ} are the dirac γ-matrices. The $\psi_{q,b}$ are quark field spinors for a quark flavor q and mass m_q. with a color index that runs from $a = 1 - 3$ corresponding to the three quark flavors. The $\mathcal{A}_{\mu}^{C}$ corresponds to the vector potentials of the eight gluonic fields. The strength of interactions in QCD is known as coupling constant (α_s) which is related to the quantity g_s as $\alpha_s = \frac{g_s^2}{4\pi}$. Finally the field tensor $F_{\mu\nu}^{A}$ is given as

$$\begin{aligned} F^A_{\mu\nu} &= \partial_\mu \mathcal{A}^A_\nu - \partial_\nu \mathcal{A}^A_\mu - g_s f_{ABC} \mathcal{A}^B_\mu \mathcal{A}^C_\nu \\ [t^A, t^B] &= i f_{ABC} t^C \end{aligned} \tag{1.3}$$

where f_{ABC} are the structure constants of the $SU(3)$ group.

The QCD coupling constant α_s is a function of the distance between the quarks. The coupling constant α_s is observed to be stronger at the lower end of the energy scale, i.e. long distances. This property leads to two inherent properties of QCD, namely the (i) “confinement”, where the system becomes more bound at lower energies resulting in no freely observable/measurable quarks and (ii) “asymptotic” freedom, where some gauge theories that strong coupling becomes weak involving large momentum transfers (“hard processes”) leading to perturbative theories to explain the processes. Figure 1.3 shows the coupling strength of strong interactions (α_s) as a function of energy scale Q.

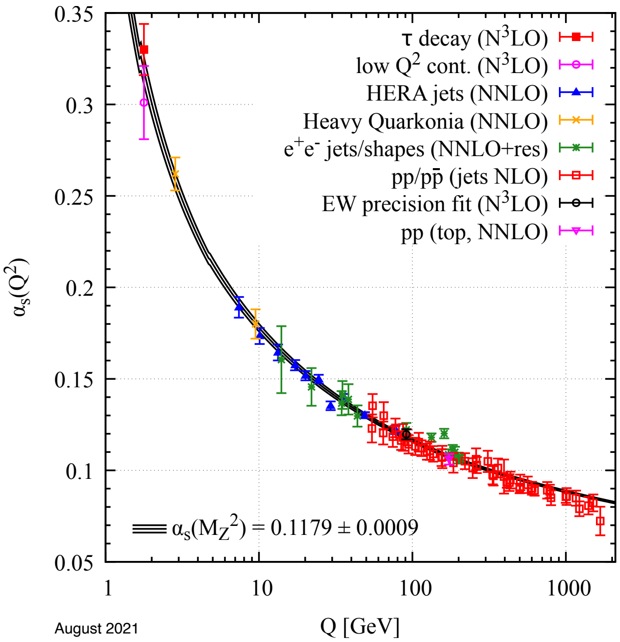

Figure 1.3: Summary of measurement of α_s as a function of energy scale Q. The coupling constant for strong interaction increases at the lower end of the energy scale (i.e. at a long distance), resulting in tight bound states as the color charges are pulled away from each other. Figure taken from [7].

One of the most important characteristics of QCD is that it is a non-perturbative theory at lower energy ($Q < 0.1$ TeV), which means that it cannot be solved analytically but has to be solved using numerical methods such as Lattice QCD. This makes the calculations of some important phenomena, such as the behaviour of quarks inside protons and neutrons, extremely difficult.

1.1.4 Lattice Quantum ChromoDynamics (LQCD)

The growth of the coupling constant α_s in the infrared (low energy scales as in Figure 1.3) requires the use of non-perturbative methods to determine the low energy properties of QCD. LQCD [4] is a numerical method used to solve the equations of

QCD on a discrete Euclidean space-time lattice.

LQCD is based on the idea of approximating the continuous space-time of QCD by a finite, discrete lattice. The lattice is a four-dimensional grid of points, where each point corresponds to a quark field and is linked by its gauge fields. The lattice spacing a, or distance between the points, is a key parameter of the method and it determines the precision of the calculations. The continuum theory is recovered by taking the limit of vanishing the lattice spacing, which can be reached by tuning the bare coupling constant to zero according to the renormalization group.

The equations of QCD are then discretized on the lattice, allowing the use of numerical techniques, such as Monte Carlo methods, to generate approximate solutions. These solutions can then be used to calculate various physical observables, such as the masses of subatomic particles, the structure of protons and neutrons, and the properties of hadrons.

LQCD has been successful in explaining a wide range of phenomena in particle physics, such as the confinement of quarks and the properties of hadrons. It has also been used to study the properties of the quark-gluon plasma, a state of matter that existed in the early universe, and to make predictions for experiments at particle colliders. LQCD predicts several states which do not follow the simple quark model rules for J^{PC}. This means that the quark and gluon degrees of freedom are as well accounted which gives rise to “exotic states”.

One of the main challenges of LQCD is the high computational cost of the calculations. It requires large amounts of memory and computational power, and the calculations can take weeks or months to complete. Additionally, the precision of the calculations is limited by the lattice spacing a, which must be small enough to accurately represent the continuous space-time of QCD, but not so small that the calculations become infeasible.

Figure 1.4 shows the LQCD prediction of the light meson spectrum. The results shown in the figure are performed with a pion mass of $m_\pi = 391$ MeVin a hyperlattice of dimensions $24^3 \times 128$. The prediction includes the light exotic meson state $J^{PC} = 1^{-+}$ and its predicted errors. The predicted 1^{-+} has very little light-strange mixing in most of the spectrum and is dominated by u, d quark states.

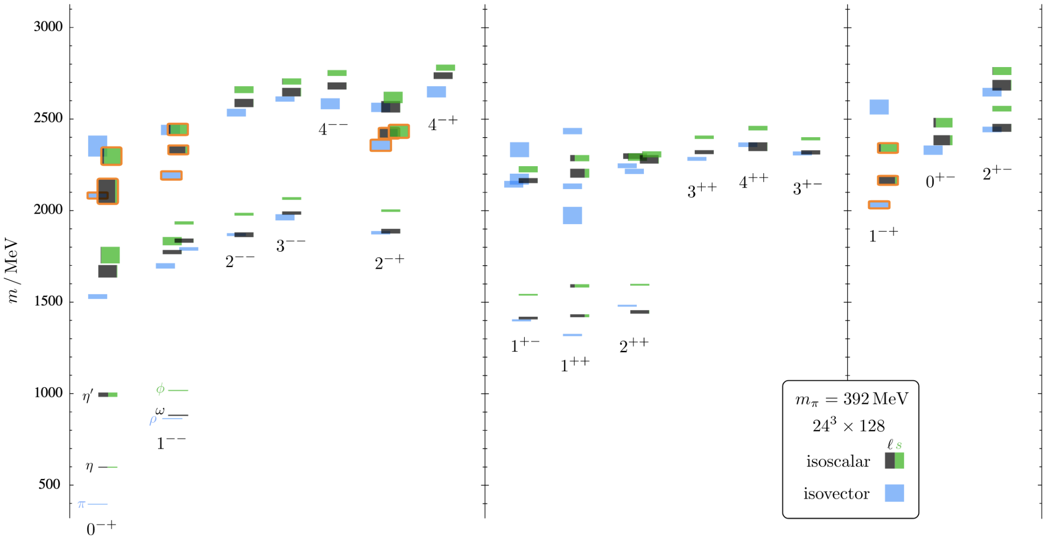

Figure 1.4: Isoscalar (green and black) and isovector (blue) as a function of mass in its y-axis. States are labelled as J^{PC}. The black and green color indicates relatively non-strange and strange components. Orange outlines are the hybrid states. The exotic states are shown in the rightmost column. Figure from [8].

A few predicted exotic states along with their predicted allowed decay modes can be found in [9, 10].

1.1.5 Prediction of Exotic π_1 meson

The lightest exotic that is proposed by the Hadspec Collaboration [8] is π_1 in $J^{PC} = 1^{-+}$. The state is postulated as the lightest hybrid meson supermultiplet, which corresponds to a chromomagnetic excitation coupled to a color octet $q\bar{q}$ through an S-wave. Previous experiments [11–18] have searched for this exotic state in the decay channel of $\eta\pi$ and $\eta^{'}\pi$ system. This is because, any state in either of these systems with odd angular momentum L will have exotic quantum numbers $J^{PC} = 1^{-+}, 3^{-+}, ...$ additionally observing a P or a $F-$wave in $\eta^{'}\pi$ system, is clear evidence of an exotic wave. However, experiments found two resonant peaks $\pi_1(1400)$ [11–15, 18] and $\pi_1(1600)$ [16–19]. These observations of two nearby 1^{-+} hybrids below 2 GeV are surprising. Hence, the existence of $\pi_1(1400)$ and $\pi_1(1600)$ was controversial until 2019, when Joint Physics Analysis Center (JPAC) [20] published a fit of the intensities extracted by the COMPASS [18]. This fit was done with a coupled-channel amplitude enforcing unitarity and analyticity of the S-matrix. This resulted in a exotic π_1 resonant pole, with a mass of $1564 \pm 24 \pm 86$ MeVand width $492 \pm 54 \pm 102$ MeVthat couples to both $\eta\pi$ and $\eta^{'}\pi$. This finally resolved tension and eliminated $\pi_1(1400)$ as an exotic as the observed peak was concluded to be the $\eta\pi$ coupling peak on the real energy axis.

The Had-Spec Collaboration published their LQCD results [21] of the branching fractions of this exotic state $\pi_1(1600)$, predicting that π_1 decays predominantly into $b_1\pi$ system by at least an order of magnitude greater than the other decay modes. Therefore, understanding the b_1 mesons is crucial in understanding the exotic π_1. The axial-vector b_1 is a non-exotic $q\bar{q}$ state and can be well explained using a simple constituent quark model. b_1 decays predominantly into a $\omega\pi$ system. Hence, this dissertation focuses on understanding the reaction $b_1 \to \omega\pi^0$.

1.2 Photoproduction of $b_1 \to \omega\pi^0$

The axial-vector $b_1(1235)$ is a isovector triplet state $(b_1^0, b_1^\mp)$. The b_1 predominantly decays into the $\omega\pi$ system. The radiative decays of the $b_1(1235 \to \pi^\pm\gamma)$ meson was also observed with estimated width of $\Gamma(b_1) = 0.230 \pm 0.060$ keV [22]. However, in this dissertation, the neutral $b_1 \to \omega\pi^0$ is analyzed in detail. The $\omega\pi^0$ decay channel for $b_1(1235)$ has been observed in several experiments using pion (π) or anti-proton ($\bar{p}$) beams on a proton (p) target. Properties of b_1 meson can be found in Table 1.3

$b_1(1235)$	$I^G(J^{PC}) = 1^+(1^{+-})$
Mass	$1229.5 \pm 3.2 MeV$
Width	$142 \pm 9 MeV$
D/S Amplitude Ratio ($b_1(1235) \to \omega\pi$)	0.277 ± 0.027
D/S Amplitude Phase Difference	$10 \pm 5^\circ$
Dominant Decay Mode	$\omega\pi$
Other Decay Modes	$\pi^\pm\gamma$, $\eta\rho$, $K^{*\pm}K^\mp$, $KK\pi^0$, $\phi\pi$

Table 1.3: Summary of b_1 axial-vector meson. Detailed information about the b_1 meson can be found in [4].

The photoproduction of a $\omega\pi^0$ system recoiling off a proton is written as

$$\gamma(\lambda_\gamma, p_\gamma)p(\lambda_1, p_p) \to \Big[\omega(\lambda_\omega p_\omega)\pi^0(p_\pi)\Big]p(\lambda_2, p_{p'}) \tag{1.4}$$

where, the helicities (λ) of each particle with spin[2] are defined in its helicity reference frame, which is the rest frame of the $\omega\pi^0$ system, where the x-axis is defined to be the direction opposite the recoiling proton (p'). In this two-particle scattering, there are three Mandelstam variables that characterize the kinematics of high-energy

---

[2] π^0 is a spin 0 particle, hence has no λ.

particle collisions. Mandelstam variables are typically denoted as s, t, and u channels. The three Mandelstam variables corresponding to the photo production of $\omega\pi^0$ system at GlueX are shown in Equation 1.5. At GlueX specific case, the reaction predominantly proceeds through the t-channel.

$$\begin{aligned} t &= (p_\gamma - p_{\omega\pi^0})^2 = (p_p - p_{p'})^2 \\ s &= (p_\gamma + p_{p'})^2 = (p_p + p_{\omega\pi^0})^2 \\ u &= (p_\gamma - p_{p'})^2 = (p_p - p_{\omega\pi^0})^2 \end{aligned} \tag{1.5}$$

The photoproduction of b_1 is diagrammatically shown in Figure 1.5. The reaction proceeds through exchanging a virtual particle between its reaction vertices. The exchange mechanism is essential in understanding and predicting the amplitudes of the scattering process. There are two types of exchanges that are allowed in this reaction, unnatural exchange such as a π^0 or natural exchange such as a pomeron $\mathcal{P}$[3]. Therefore, by studying the scattering amplitudes of this reaction one can determine the type of naturality of exchange and hence, can understand the exchange mechanism between the bottom and top vertices. In the photoproduction of b_1 which has been previous measured to decay through unnatural exchange π^0 [9].

---

[3] The scattering cross-section increases with an increase in Center of Mass Energy. To explain this dependence, the Pomeron was introduced as a theoretical construct [23].

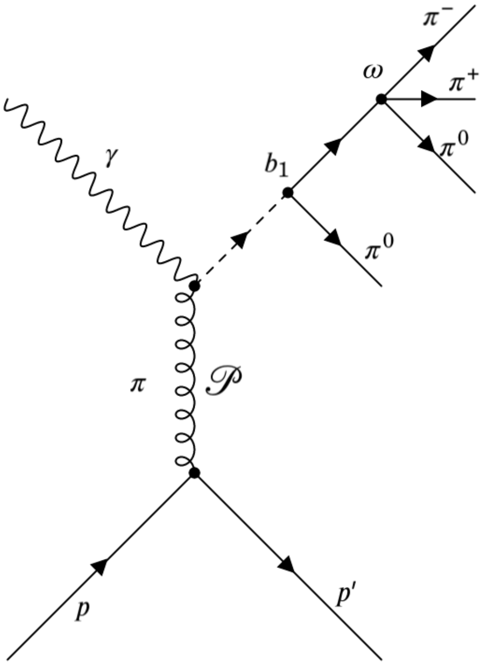

Figure 1.5: Sketch of t-channel photoproduction of the neutral b_1 meson, with its specific decay studied in this thesis.

The intensity ($\mathcal{I}$) distribution for the above-shown reaction in Eq.(1.4) can be explained using an Amplitude Analysis model. The intensity can broken down into amplitudes[4] described by $A_{\lambda_\gamma;\lambda_1\lambda_2}(\Omega, \Omega_H, \Phi)$, where Ω is the solid angle describing the decay kinematics of the $\omega - \pi^0$ system[5], Ω_H is the solid angle that describes decay kinematics of the 3π from $\omega \to \pi^+\pi^-\pi^0$ and Φ being the polarization angle of the photon (γ). These angles will be discussed later in Section 1.2.1. The recipe for computing intensity for photoproduction of $\omega\pi^0$ is adapted from [24].

---

[4] It is also referred to as $\omega\pi^0$ decay amplitudes or simply decay amplitudes.

[5] The decay is described in $\omega\pi^0$ helicity frame, discussed further in Section 1.2.1.

$$
\begin{aligned}
\mathcal{I}(\Omega, \Omega_H, \Phi) &= \frac{d\sigma}{dt dm_{\omega\pi^0} d\Omega d\Omega_H d\Phi} \\
&= \sum_{\lambda_\gamma \lambda'_\gamma \lambda_1 \lambda_2} \kappa A_{\lambda:\lambda_1\lambda_2}(\Omega, \Omega_H) \rho^{\gamma}_{\lambda_\gamma \lambda'}(\Phi) A^{*}_{\lambda_\gamma:\lambda_1\lambda_2}(\Omega, \Omega_H)
\end{aligned}
\tag{1.6}
$$

κ is called the phase space factor for the transition amplitudes A's and is defined as

$$
\begin{aligned}
\kappa &= \frac{1}{(2\pi)^2}\frac{1}{4\pi}\frac{1}{2\pi}\frac{1}{2}\frac{\mathcal{O}^{\frac{1}{2}}(m^2_{\omega\pi^0}, m^2_{\pi^0}, m^2_{\omega})}{16 m_{\omega\pi^0}(s - m_p^2)^2} \\
\mathcal{O}(a, b, c) &= a^2 + b^2 + c^2 - 2(ab + bc + ca)
\end{aligned}
\tag{1.7}
$$

where, m_i^2 is invariant mass squared of corresponding $(\omega\pi^0, \omega, \pi^0)$ system. s is the Mandelstam variable defined in Equation 1.5. $\mathcal{O}$ is called the triangle function.

The summation term in the Equation 1.6, is the transitional probability. Where the transition amplitude can be expanded into its corresponding partial waves which will be discussed in Section 1.3. λ_1, λ_2 are the helicities of the target and the recoiling proton and can take values $\pm\frac{1}{2}$ since it is a spin $\frac{1}{2}$ particle. $\rho^{\gamma}_{\lambda\lambda'}$ corresponds to the spin density matrix of the incoming beam photon (γ) written in the basis of Pauli matrices σ. $\lambda_\gamma, \lambda'_\gamma$ are the photon helicities which can take $+1, -1$. GlueX uses a linearly polarized photon beam in its initial state, however, due to experimental conditions, the photons are partially polarized with a well-measured polarization fraction (P_γ) as a function of its beam energy. To describe a partially linearly polarized beam, a statistical mixture of pure states (Pauli matrices) is used. The spin density matrix for the incoming beam photon is given as

$$\rho^{\gamma}_{\lambda\lambda'}(\Phi) = \frac{1}{2}\Big(\mathrm{I} + P_\gamma(\Phi)\cdot\sigma\Big) \tag{1.8}$$

The final Intensity accounting for a partially linearly polarized beam can be expressed as

$$\begin{aligned}
\mathcal{I}(\Omega,\Omega_H,\Phi) &= \mathcal{I}_0(\Omega,\Omega_H) - P_\gamma \mathcal{I}_1(\Omega,\Omega_H)\cos 2\Phi - P_\gamma \mathcal{I}_2(\Omega,\Omega_H)\sin 2\Phi \\
\mathcal{I}_0(\Omega,\Omega_H) &= \frac{\kappa}{2}\sum_{\lambda_\gamma,\lambda_1\lambda_2} A_{\lambda_\gamma;\lambda_1\lambda_2}(\Omega,\Omega_H)A^*_{\lambda_\gamma;\lambda_1\lambda_2} \\
\mathcal{I}_1(\Omega,\Omega_H) &= \frac{\kappa}{2}\sum_{\lambda_\gamma,\lambda_1\lambda_2} A_{-\lambda_\gamma;\lambda_1\lambda_2}(\Omega,\Omega_H)A^*_{\lambda_\gamma;\lambda_1\lambda_2} \\
\mathcal{I}_2(\Omega,\Omega_H) &= \frac{i\kappa}{2}\sum_{\lambda_\gamma,\lambda_1\lambda_2} \lambda_\gamma A_{\lambda_\gamma;\lambda_1\lambda_2}(\Omega,\Omega_H)A^*_{\lambda_\gamma;\lambda_1\lambda_2}
\end{aligned} \tag{1.9}$$

The total intensity $I(\Omega,\Omega_H,\Phi)$ in Equation 1.9 has now been factored out to have an explicit dependence on the polarization Φ and the decay amplitudes Ω,Ω_H separately. But the polarization angle terms $\sin 2\Phi$ and $\cos 2\Phi$ in the equation can be expressed in its Euler's form and replacing λ_γ with its possible helicity values $[+,-]$, the intensity is reduced to the form

$$\begin{aligned}
\mathcal{I}(\Omega,\Omega_H,\Phi) = \sum_{\lambda_1\lambda_2}\Bigg\{ &\frac{\kappa}{4}(1-P_\gamma)|\tilde{A}_{+:\lambda_1\lambda 2}(\Omega,\Omega_H,\Phi) + \tilde{A}_{-:\lambda_1\lambda 2}(\Omega,\Omega_H,\Phi)|^2 \\
&+ \frac{\kappa}{4}(1+P_\gamma)|\tilde{A}_{+:\lambda_1\lambda 2}(\Omega,\Omega_H,\Phi) - \tilde{A}_{-:\lambda_1\lambda 2}(\Omega,\Omega_H,\Phi)|^2 \Bigg\}
\end{aligned} \tag{1.10}$$

For ease of understanding, the proton helicity λ_1, λ_2 are for now suppressed and will account for its helicity later in Section 1.3.1. Hence, the intensity without proton helicities can be expressed as

$$\begin{aligned}\mathcal{I}(\Omega, \Omega_H, \Phi) = \frac{\kappa}{4}(1 - P_\gamma)|\tilde{A}_+(\Omega, \Omega_H, \Phi) + \tilde{A}_-(\Omega, \Omega_H, \Phi)|^2 \\ + \frac{\kappa}{4}(1 + P_\gamma)|\tilde{A}_+(\Omega, \Omega_H, \Phi) - \tilde{A}_-(\Omega, \Omega_H, \Phi)|^2\end{aligned} \tag{1.11}$$

with $\tilde{A}_\pm(\Omega, \Omega_H, \Phi) = e^{\mp i\Phi} A_\pm(\Omega, \Omega_H)$. $\tilde{A}_\pm$ is called as production phase Φ encoded amplitudes.

1.2.1 Helicity frame & Angular distribution (Ω, Ω_H) of $\omega\pi^0$

As mentioned in the previous section, the decay of the $\omega\pi^0$ is studied in its helicity frame. Therefore, the procedure for computing the decay angles in its helicity frame is outlined in this section. A sketch of the particle vectors and production and decay planes is sketched in Figure 1.6. Angles $\Omega = (\theta, \phi)$ describe the direction of the ω meson in the helicity frame of the $\omega\pi^0$ system. In order to define them, in the γp center-of-mass (C.M) frame, $\vec{z}$ is defined as the unit vector along the $\omega\pi^0$ direction, while $\hat{k}$ is the unit vector in the beam γ direction. x and y-axes are defined by the right-handed coordinate system by the following two equations

$$\begin{aligned}\vec{y} &= \frac{\vec{k} \times \vec{z}}{|\vec{k} \times \vec{z}|} \\ \vec{x} &= \vec{y} \times \vec{z}\end{aligned} \tag{1.12}$$

Then, by performing a Lorentz boost along the direction of b_1 meson, the momentum of $\vec{\omega}$ in $\omega\pi^0$ decay frame with decay angle $\Omega = (\theta, \phi)$ is computed as follows:

$$\begin{aligned} \theta &= cos^{-1}\frac{\vec{\omega}\cdot\vec{z}}{|\vec{\omega}|} \\ \phi &= tan^{-1}\frac{\vec{\omega}\cdot\vec{y}}{\vec{\omega}\cdot\vec{x}} \end{aligned} \tag{1.13}$$

$\Omega_H = (\theta_H, \phi_H)$ describes the kinematics of normal vector to the $\omega \rightarrow \pi^+\pi^-\pi^0$ decay plane. By again performing Lorentz boost and mathematical manipulation the decay angle Ω_H can be expressed as:

$$\begin{aligned} \theta_H &= cos^{-1}(\vec{n}\cdot\vec{z_H}) \\ \phi_H &= tan^{-1}(\frac{\vec{n}\cdot\vec{y_H}}{\vec{n}\cdot\vec{x_H}}) \end{aligned} \tag{1.14}$$

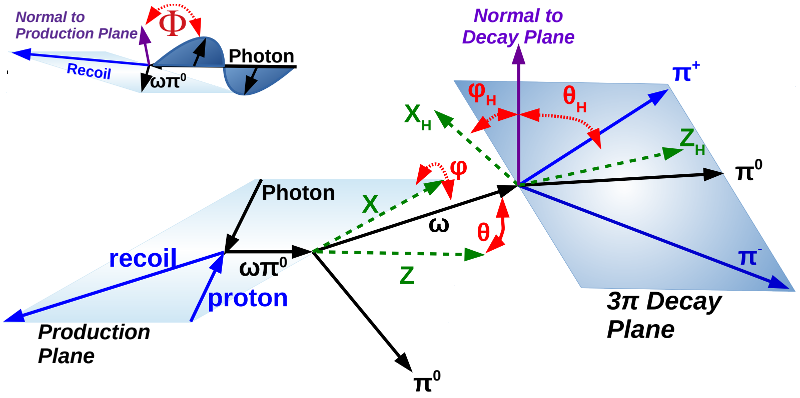

Figure 1.6: The helicity frame of the $\omega\pi$ system is drawn. Φ on the top left denotes the production angle which is the angle between the normal to the production plane and the polarization vector of the beam photon, θ, ϕ describes the kinematics of ω in the $\omega\pi$ decay plane, while θ_H, ϕ_H describes the kinematics of the normal to the 3-pion decay plane.

1.3 Decay amplitudes ($A_{\lambda_\gamma;\lambda_1\lambda_2}$) and the PWA model

Partial Wave Analysis (PWA) is a technique that attempts to fit the production and subsequent decay of a meson by examining not only its mass distribution but also, all angular distributions of the system. The technique is very powerful but requires rather large statistics to be able to identify states. The observed intensity of $\omega\pi^0$ events can be fit in its various decay angles as discussed in the previous section. However, the the $\omega\pi^0$ system decays into a different J^{PC} states. One of the main advantages of PWA is the ability to separate contributions from resonances with different J^P that may be difficult to distinguish by non-resonant backgrounds or interfere with other resonances quantum mechanically. In short, PWA can extract contributions of various J^{PC} states in the observed $\omega\pi^0$ intensity along with its background.

Based on the Intensity defined in Equation 1.11, production phase encoded amplitude factor $\tilde{A}_{\lambda_\gamma} \equiv \tilde{A}_\pm$ encodes the information about various J^{PC} states contributing to $\omega\pi^0$ decay. The production phase encoded amplitude factor can be expressed in its partial waves as an explicit product of $\omega\pi^0$ decay kinematics and its $\omega(3\pi)$ decay kinematics reducing the amplitude expression to,

$$\tilde{A}_{\lambda_\gamma} = \sum_{J_i=1,2,..} \sum_{m=-J_i,..,J_i} T^i_{\lambda_\gamma,m} \sum_{\lambda_\omega=-1,0,1} e^{-\lambda_\gamma i\Phi} D^{J_i*}_{m,\lambda_\omega}(\Omega) F^i_{\lambda_\omega} D^{1*}_{m,0}(\Omega_H) G_{\text{Dalitz}} \mathfrak{F}(p_0)$$

where, $\lambda_\gamma = [+1, -1]$

$$\tilde{A}_\pm = \sum_{J_i=1,2,..} \sum_{m=-J_i,..,J_i} T^i_{\pm,m} \sum_{\lambda_\omega=-1,0,1} e^{\mp i\Phi} D^{J_i*}_{m,\lambda_\omega}(\Omega) F^i_{\lambda_\omega} D^{1*}_{m,0}(\Omega_H) G_{\text{Dalitz}} \mathfrak{F}(p_0) \tag{1.15}$$

where,

λ_γ**:** is the beam photon helicity. $\lambda_\gamma = [+1, -1]$.

$T^i_{\lambda_\gamma,m}$ $(T^i_{\pm,m})$**:** is $\omega\pi^0$ decay amplitude that depends on the relative spin between the ω and π^0 states. $T^i_{\lambda_\gamma,m}$ depends on the naturality of exchange of the reaction (the type of exchange particle). To extract the contribution of natural and unnatural exchanges, the decay amplitudes are expressed in their reflectivity basis. The recipe for expressing the decay amplitudes in reflectivity basis is discussed in the next Section 1.3.1. The decay amplitudes also depend on factors like the beam energy, $M(\omega\pi)$, and momentum transfer (t GeV^2) between the proton and the recoil.

$D^{J_i}_{m,\lambda}(\Omega \ or \ \Omega_H)$**:** is the Wigner function with $\Omega(\theta, \phi)$ and $\Omega_H(\theta_H, \phi_H)$ being decay angles in helicity frame. It describes the decay of $\omega\pi^0$ and ω angular distributions.

$F^i_{\lambda_\omega}$**:** are the ω helicity amplitudes which depends on the relative angular momentum between $\omega - \pi^0$. λ_ω are ω helicities and can take values $\lambda_\omega = [-1, 0, +1]$ They are defined as

$$F^i_{\lambda_\omega} = \sum_{l=0,1,2,3} \langle J_i \lambda_\gamma | l0, 1\lambda_\lambda \rangle \, C^i_l$$

.

For a $J^{PC} = 1^{+-}$ i.e. b_1, the coefficient C_l is nonzero for only even values of orbital angular momentum l [6], reducing the ω helicity amplitude as

$$F^i_{\lambda_\omega} = \langle 1\lambda_\omega | 00, 1\lambda_\omega \rangle \, C^{b_1}_0 + \langle 1\lambda_\omega | 20, 1\lambda_\omega \rangle \, C^{b_1}_2 \qquad (1.16)$$

---

[6] Higher L waves beyond F-wave are not considered in this dissertation.

where this ratio $C_2^{b_1}/C_0^{b_1}$ describes the ratio of the D-wave to the S-wave for the b_1 meson. This ratio will be referred to as D/S ratio or `dsratio` through this dissertation. Chapter 5 and Chapter 6 is dedicated to the extraction of `dsratio` in GlueX experiment.

Previous experiments have reported `dsratio` [25, 26] in their analysis which will be summarized in Section 1.4. `dsratio` have also gained significant theoretical interest. The HadSpec collaboration in 2019 published their first LQCD calculation of coupled $\omega\pi$ and $\phi\pi$ scattering, incorporating coupled S and D-wave $\omega\pi$ in $J^P = 1^+$ [21]. The b_1 was found to couple dominantly to S-wave $\omega\pi$, with a much weaker coupling to D-wave $\omega\pi$. These couplings were extrapolated to the physical value of the light quark masses and reported a `dsratio` of the 1^+ state as

$$\frac{|c^{\text{phys.}}_{\pi\omega\{^3D_1\}}|}{||c^{\text{phys.}}_{\pi\omega\{^3S_1\}}|} = 0.27 \pm 0.20 \tag{1.17}$$

The error is high due to the extrapolation to the physical light quark masses.

$G_{\textbf{Dalitz}}$: is the Dalitz function which describes the distribution of the pions in the $\omega \to \pi^+\pi^-\pi^0$. Detailed Dalitz formalism can be found in [27].

$$|G_{\text{Dalitz}}(z,\vartheta)|^2 = |N|^2(1 + 2\alpha z + 2\beta z^{3/2}\sin(3\vartheta) + 2\gamma z^2) \tag{1.18}$$

where, N is a normalization constant, α, β and γ are parameters predicted from fit performed by JPAC and are shown in Table 1.4. The variables z and ϑ are parameterized using mandelstam quantities like, u, t, s and $m_\pi, M(\omega\pi^0)$. The variables are parameterized as

$$\begin{aligned} z &= \frac{3(t-u)^2 + 9(s_c - s)^2}{4M^2(M-3m_\pi)^2} \\ \tan\vartheta &= \frac{\sqrt{3}(s_s - s)}{(t-u)} \end{aligned} \tag{1.19}$$

where, M is the invariant mass of the 3π system, m_π is the iso-spin averaged pion mass, and $s_c = \frac{1}{3}(M^2 + 3m_\pi^2)$ is the location of the center of the Mandelstam triangle.

	α	β	γ
Low $\phi_{\omega\pi^0}(0)$	0.1212	0.0257	-
High $\phi_{\omega\pi^0}(0)$	0.1201	0.0302	-
Low $\phi_{\omega\pi^0}(0)$	0.1120	0.0230	0.0290
High $\phi_{\omega\pi^0}(0)$	0.1090	0.0260	0.0190

Table 1.4: JPAC calculation of Dalitz parameters for ω decay. JPAC performed two and three parameter fits for the study. For each of the fits yielded minimum and maximum values of parameters for each of the fit. The top row contains the value used in the analysis. Other values are used in systematic studies. The table is adapted from [27].

Finally, the last part of Equation 1.11 can be combined such that $Z^i_m(\Phi, \Omega, \Omega_H) = e^{-i\Phi}\sum_{\lambda_\omega=-1,0,1} D^{J_i*}_{m,\lambda_\omega}(\Omega) F^i_{\lambda_\omega} D^{1*}_{0,\lambda_\omega}(\Omega_H) G_{\text{Dalitz}}$, yielding the final equation for phase rotated decay amplitude in its helicity frame as

$$\tilde{A}_\pm = \sum_{J_i=1,2,..} \sum_{m=-J_i,..,J_i} T^i_{\pm,m} Z^i_m(\Phi, \Omega, \Omega_H) \tag{1.20}$$

$\mathfrak{F}(p_0)$: is called as Blatt-Weisskopf angular momentum barrier factor as formulated in [28]. The factor is included in order to suppress high l waves to domination at relatively low $\omega\pi^0$ masses. Due to kinematics, more excited $\omega\pi^0$ states can be observed when $M(\omega\pi^0)$ has sufficiently high invariant mass. The barrier factors depend on the relative angular momentum l between the ω and π^0 system.

$$\begin{aligned}
\mathfrak{F}_s(z) &= 1 \\
\mathfrak{F}_p(z) &= \sqrt{\frac{2z}{z+1}} \\
\mathfrak{F}_d(z) &= \sqrt{\frac{13z^2}{(z-3)^2+9z}} \\
\mathfrak{F}_f(z) &= \sqrt{\frac{277z^3}{z(z-15)^2+9(2z-5)2}}
\end{aligned} \tag{1.21}$$

where z is called as the breakup momentum and is defined as

$$z = \frac{|m^4_{\omega\pi^0} + m^4_{\omega} + m^4_{\pi^0} - 2m^2_{\omega\pi^0}m^2_{\omega} - 2m^2_{\omega\pi^0}m^2_{\pi^0} - 2m^2_{\omega}m^2_{\pi^0}|}{2m_{\omega\pi^0}P^2_R} \;,$$

with $P_R = 197$ MeV/c.

1.3.1 Reflectivity basis

As mentioned in Section 1.2 Extracting the reflectivity in high energy processes (t channel processes) determines the "naturality" of the exchange particle, providing a deeper understanding of the production mechanisms. Choosing to work on the reflectivity basis separates out the contribution from the 'Natural' and 'Unnatural' exchange processes into its respective reflectivity The reflectivity basis formulation was originally proposed in [29]. The formulation described here is based on the convention from [24] and [30]. To understand the reflectivity basis, the y axis is defined as the direction of the normal vector to the production plane. Then the reflectivity operator, which rotates the eigenstate by π followed by a parity operation.

For an eigenstate having quantum number J and p_z defined in its helicity frame. The reflectivity operator is expressed as

$$\hat{\prod} = \hat{P}R_y(\pi) \tag{1.22}$$

and its corresponding eigenvalue as

$$K = \epsilon(-1)^{2J}$$

where ϵ is call the reflectivity and can take a value $\epsilon = \pm 1$ for bosons.

The relationship between the decay amplitudes in their helicity basis and reflectivity basis is given as

$$\begin{aligned} T^i_{-1m} &= \tau_i(-1)^m \left[{}^{(-)}T^i_{-m} -^{(+)} T^i_{-m} \right] \\ T^i_{+1m} &=^{(-)} T^i_m +^{(+)} T^i_m \end{aligned} \tag{1.23}$$

where τ_i is defined as the naturality of the produced meson system. The relation between the naturality of exchange (τ_e), naturality of produced meson system (τ_e) and the reflectivity is now defined as $\epsilon = \tau_i \tau_e$. For example, if the b_1 system has an unnatural parity which decays through unnatural parity exchange (π^0), then the exchange reflectivity will be $\epsilon = (-1) \times (-1) = +1$.

Now, plugging these into phase-rotated decay amplitude $A_\pm$ in Equation 1.20, the phase-rotated decay amplitude in reflectivity basis takes the form

$$
\begin{aligned}
A_+ &= \sum_{J_i=1,2,..} \sum_{m=-J_i,..,J_i} \left({}^{(-)}T^i_m +^{(+)} T^i_m \right) Z^i_m(\Phi, \Omega, \Omega_H) \\
A_- &= \sum_{J_i=1,2,..} \sum_{m=-J_i,..,J_i} \left(\tau_i (-1)^m \left[{}^{(-)}T^i_{-m} -^{(+)} T^i_{-m} \right] \right) Z^i_m(\Phi, \Omega, \Omega_H)
\end{aligned}
\tag{1.24}
$$

and, plugging these definitions back into the intensity in Equation 1.11

$$
\begin{aligned}
\mathcal{I}(\Omega, \Omega_H, \Phi) = \frac{\kappa}{4}(1 - P_\gamma) \Big| \sum_{J_i=1,2,..} \sum_{m=-J_i,..,J_i} i^{(-)}T^i_m \mathfrak{Im}(Z^i_m) +^{(+)} T^i_m \mathfrak{Re}(Z^i_m) \Big|^2 \\
+ \frac{\kappa}{4}(1 + P_\gamma) | \sum_{J_i=1,2,..} \sum_{m=-J_i,..,J_i} i^{(+)}T^i_m \mathfrak{Im}(Z^i_m) +^{(-)} T^i_m \mathfrak{Re}(Z^i_m) |^2
\end{aligned}
\tag{1.25}
$$

Now, the helicities corresponding to the proton state ($\lambda_1 \lambda_2$) are reintroduced from Equation 1.10. The helicities can be encoded into the decay amplitudes as spin flip. The incoming proton has a helicity of λ_1 and the recoiling proton has a helicity λ_2. Since both the initial and final state are protons the spin can either be flipped ($\lambda_1 = -\lambda_2$) or can have no-spin flip ($\lambda_1 = \lambda_2$). Therefore, by expressing the λ_1, λ_2 into sum over proton spin-flip and non-spin flip k, again using parity invariance

$$
T^i_{m;-\lambda_1-\lambda_2} = \epsilon(-1)^{\lambda_1-\lambda_2} \tag{1.26}
$$

and redefining the amplitudes with $[J_i]^\epsilon_{m,0} =^{(\epsilon)} T^i_{m;+-}$ for non-spin flip and $[J_i]^\epsilon_{m,1} =^{(\epsilon)} T^i_{m;+-}$ for spin-flip the proton helicities to the sum over proton flip (non-flip) is

$$\sum_{\lambda_1,\lambda_2} {}^{(\epsilon)}T^{i}_{m;\lambda_1\lambda_2}\ {}^{(\epsilon^{'})}V^{*i^{'}}_{m^{'};\lambda_1\lambda_2} = (1+\epsilon\epsilon^{'})\sum_{k}[J_i]^{\epsilon}_{m,k}[J^{'}_i]^{(\epsilon^{'})*}_{m^{'},k^{'}} \tag{1.27}$$

Therefore, substituting the above expression for intensity, we have the total intensity can be written as:

$$\begin{aligned}\mathcal{I}(\Phi,\Omega,\Omega_H) = 2\kappa \sum_{k} \\ \Bigg\{(1-P_\gamma)\Bigg[\Big|\sum_{i,m}[J_i]^{(-)}_{m,k}\mathfrak{Im}(Z)\Big|^2 + \Big|\sum_{i,m}[J_i]^{(+)}_{m,k}\mathfrak{Re}(Z)\Big|^2\Bigg] \\ +(1+P_\gamma)\Bigg[\Big|\sum_{i,m}[J_i]^{(+)}_{m,k}\mathfrak{Im}(Z)\Big|^2 + \Big|\sum_{i,m}[J_i]^{(-)}_{m,k}\mathfrak{Re}(Z)\Big|^2\Bigg]\Bigg\}\end{aligned} \tag{1.28}$$

where,

- $[J_i]^{(\epsilon)}_{m,k}$ - complex parameters to be extracted
- k represents the spin-flip (1) or non-flip (0)
- $Z^i_m(\Phi,\Omega,\Omega_H) = e^{-i\Phi}\sum_{\lambda_\omega=-1,0,1} D^{J_i*}_{m,\lambda_\omega}(\Omega)F^i_{\lambda_\omega}D^{1*}_{0,\lambda_\omega}(\Omega_H)G_{\text{Dalitz}}$

As can be observed from Equation 1.28, individual contributions from each nature of exchange corresponding to each J^P state can be extracted independently. Also, there are no kinematic variables that distinguish between the spin-flip ($k=1$) and spin-non-flip ($k=0$) amplitudes and it is anticipated that these two contributions to the intensity will result in a poorly constrained fit. Nevertheless, fit instability seems highly likely for the general case where both $k=0$ and $k=1$ are included for all amplitudes[7]. This has to be revisited in a future analysis. For a $J^P = 1^+$ state, the

---

[7] Since it increases the fit parameters by a factor of two.

final intensity equation in reflectivity basis used for this analysis is shown as

$$\begin{aligned}\mathcal{I}(\Phi,\Omega,\Omega_H) = 2\kappa\Bigg\{ &(1-P_\gamma)\left[\Big|\sum_m [1^+]^{(-)}_m \mathfrak{Im}(Z)\Big|^2 + \Big|\sum_m [1^+]^{(+)}_m \mathfrak{Re}(Z)\Big|^2\right] \\ &+ (1+P_\gamma)\left[\Big|\sum_m [1^+]^{(+)}_m \mathfrak{Im}(Z)\Big|^2 + \Big|\sum_m [1^+]^{(-)}_m \mathfrak{Re}(Z)\Big|^2\right]\Bigg\}\end{aligned} \tag{1.29}$$

By fixing E_γ, M($\omega\pi$), momentum transfer (t [GeV^2]) in ‘thin’ bins one can extract the complex parameter corresponding to 1^+ and its nature of exchange is extracted from fitting the intensity which depends on the decay angles and production angle (5-dimensional fit) in its helicity frame.

1.4 History of PWA of b_1

There has been previous measurements of $b_1(1235)$ made using proton (p), pion (π) and photon beams. However, the latest photoproduction of $b_1(1235)$ dates back to the 1980s. The E852 Collaboration is the most recent experiment that measured and reported the properties of b_1 meson produced through a pion beam.

1.4.1 Photoproduction of b_1

The Omega-Photon [25] studied the photoproduction of $\omega\pi^0$ system near its threshold region. An 80 GeV electron beam from the CERN Super Proton Synchrotron was used to generate polarized photons in the energy range of $20-70$ GeV. The study searched for higher excited states of ρ isovector states. The lightest meson was predicted to have a mass of $\sim$ 1.3 GeV. A spin-parity analysis showed that the $\omega\pi^0$ enhancement is consistent with predominant $J^P = 1^+$ $b_1(1235)$ production, with a $\sim$ 20% $J^P = 1^-$ non-resonant background. The 1^- tail was parameterized as the tail of the $\rho(770)$ isovector meson. The study also found possible contributions from $J^P = 0^-$. The study further concluded that the dominant spin-parity cannot be 0^- since the significant contribution was from ω helicity = ± 1. Finally the study reported a `dsratio` of 0.25 in 1^+ peak of $\sim$ 1.2 GeV, and width 200 MeV. Angular distribution of the $\omega\pi^0$ system in its helicity frame is shown in Figure 1.7. More details on the helicity frame will be discussed in Section 1.2.1.

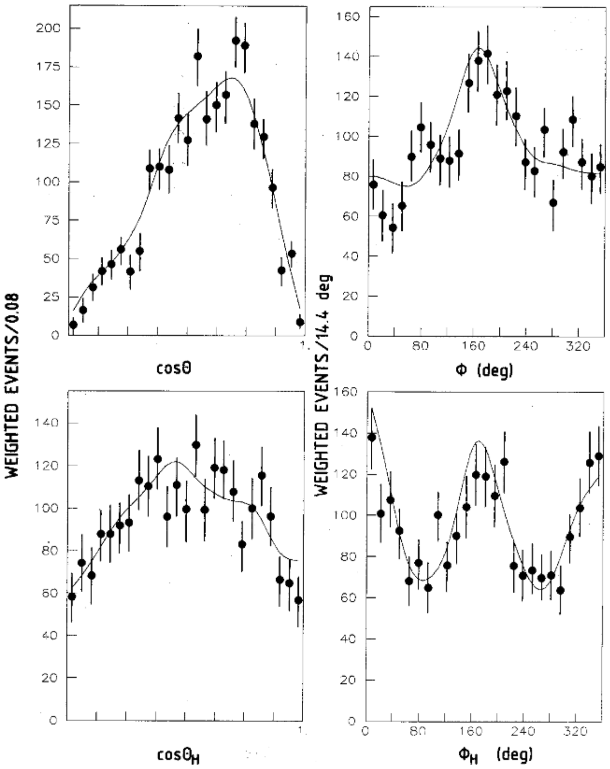

Figure 1.7: Angular distributions of $\omega\pi^0$ system at Omega-Photon Collaboration [25]. The study was suffered from poor statistical precision compared to GlueX photo production.

The other experiment that studied the photoproduction of $\omega\pi^0$ system is SLAC-H-Photon [31]. A total of $306,785$ signal events ($\omega\pi^0$ events) were analyzed in that study. The experiment measured the angular distribution of the production plane relative to the photon polarization vector which showed an inconsistent structure with an s-channel helicity-conserving process. That complements the studies of the Omega-Photon Collaboration studies which resulted in interpreting the $b_1(1235)$ state as an axial vector meson.

1.4.2 The E852 Collaboration Results

The E852 Collaboration [26] published the most recent experimental results for the decay of $b_1^- \to \omega\pi^-$ using negatively charged channel in pion production, $\pi^- p \to \omega\pi^- p$, using $168,000$ $\omega\pi^-$ events using the Multi-Particle Spectrometer setup at BNL. Partial Wave Analysis (PWA) on the $\omega\pi^-$ channel was performed and was concluded that $\omega\pi^-$ data below 1.6 GeVare dominated by the $J^{PC} = 1^{+-}$ resonance i.e. $b_1(1235)$. The experiment also reported the ratio of the D- wave to S-wave amplitudes in $b_1^- \to \omega\pi^-$ to be $|D/S| = 0.269 \pm (0.009)_{\text{stat}} \pm (0.01)_{\text{sys}}$. Similarly, the study also reported the relative phase between the D-wave and the S-wave in $b_1^- \to \omega\pi^-$ to be $\phi(D - S) = 0.184 \pm (0.042)_{\text{stat}\pm(0.07)_{\text{sys}}}$. The D/S ratio reported in the study is the most precise measurement that has been made so far. The study confirmed the ${}^3P_0$ model [32]. The main sources of systematic error considered in the study were the choice of wave sets used to extract the `dsratio` and the mass range ($M(\omega\pi^0)$) selected to extract the `dsratio`. Key features of the study are outlined below in Table 1.5.

Parameter	**Value**	**Remarks**
$\lvert t\rvert$ **range**	$0.1 - 1.5$ GeV^2	Single t bin
$M(\omega\pi^-)$ **range**	$1.155 - 1.315$ GeV	Systematics 60 to 160 in 20 MeV bins
Wavesets included (dominant)	$J^{PC} = 1^{+-}, 1^{--}, 2^{+-}, 3^{--}$	2^{+-} ∼1.6 GeV 3^{--} ∼ 1. 7 GeV seen but no detailed study.
D/S **ratio**	$0.269 \pm (0.009)_{\mathrm{stat}} \pm (0.01)_{\mathrm{sys}}$	
$\phi(D-S)$	$0.184 \pm (0.042)_{\mathrm{stat}} \pm (0.07)_{\mathrm{sys}}$	As predicted in [33]

Table 1.5: Summary of E852 Findings on $b_1(1235)$ state. The main focus here is on the extraction of `dsratio`.

Chapter 2

GlueX Experiment

The chapter provides a brief overview of the GlueX experiment situated at Hall D at the US Department of Energy's Thomas Jefferson National Accelerator Facility (TJNAF) in Newport News, Virginia. It was built as a part of the 12 GeV upgrade to Jefferson Lab. The collaboration consists of approximately 180 members from 30 institutions across 9 countries [34]. The detector was fully commissioned in the spring of 2016. Phase-I of GlueX represents the first 200 days of approved data taken by the Program Advisory Committee of TJNAF, and this data was taken over three-run periods in Spring 2017, Spring 2018, and Fall 2018. The overall data recorded amounts to 300 billion physics events, with a total disk footprint of approximately 4.1 PB (Peta Bytes, Peta = 10^{15}) of data. The results shown in this dissertation are from GlueX-I data.

The primary goal of GlueX is to search and map the spectrum of exotic mesons. To effectively map out the spectrum, the experiment needs to exclusively reconstruct a large number of hadronic states with relatively high efficiency and purity. GlueX is nearly a hermetic detector with high efficiency for the detection of both charged and neutral particles. The detector system is encompassed in a solenoidal magnet of peak magnetic field 2 T that causes charged particles to travel helically within the GlueX detector. This results in higher uniform acceptance at the exchanged momentum (momentum transfer between the γp system) separation. A detailed explanation of the experiments and the detector system can be found in [35] and will be referenced throughout this chapter.

2.1 Continuous Electron Beam Accelerator Facility

The Continuous Electron Beam Accelerator Facility (CEBAF) is a 12 GeV electron accelerator facility at TJNAF. It consists of two linear accelerators and two arcs for recirculation in order to connect the linear accelerators. The electrons are injected through the injector from the north linear accelerator in 4 ns beam bunches. Each linear accelerator is comprised of hundreds of superconducting RF cavities that provide a strong electromagnetic gradient to accelerate the electrons. At the end of the linear accelerators, there is a series of dipole magnets used to separate the RF bunches by energy as the magnetic field strength to curve the beam is dependent on the energy of the electrons. Each arc is composed of five individual beamlines for this purpose. With each pass or linear acceleration the the electron's energy increases by 1090 MeV. Therefore, the arcs provide a range of electron energies that can be delivered to Halls A, B and C. The electrons travel 5.5 passes in the arc to reach Hall - D with a peak energy of 12 GeV. CEBAF is able to deliver up to 250 million electron pulses to the Hall-D tagger every second. A schematic description of the CEBAF is shown in Figure 2.1.

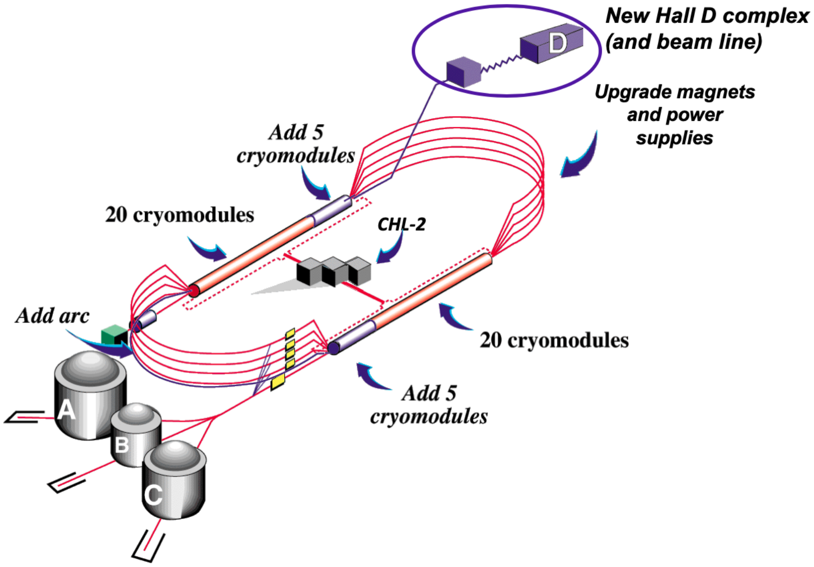

Figure 2.1: Schematic view of the Continuous Electron Beam Accelerator Facility (CEBAF) at TJNAF showing the four experimental halls. The schematic shows the race track accelerator design along with the five pass rings along which different electron momentum is achieved. Hall-D is situated such that the electron reaches 5.5 passes to attain its peak momentum. Figure taken from [35].

2.2 The Detector System at GlueX

The electron from CEBAF enters Hall-D with an energy of 12 GeV. However, GlueX studies photoproduction reactions, and hence, photons have to be produced using the electrons. The experimental setup in Hall-D can be divided into mainly four sectors, namely, (i) the photon beamline, where the polarized photons are produced from the incoming electrons from CEBAF, (ii) the calorimeters, to measure the energy of the particles (iii) charged particle tracking, to determine particle trajectories and (iv) Particle identification. A schematic view of the GlueX is shown in Figure 2.2

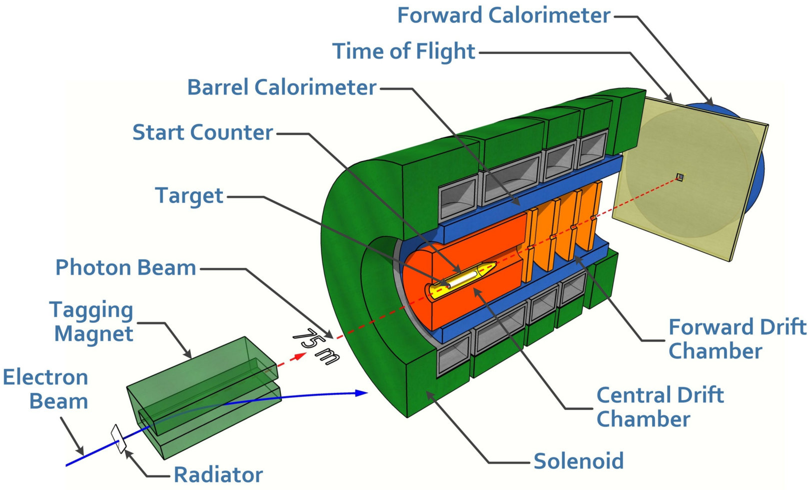

Figure 2.2: Schematic of GlueX detector system. The photon beamline produces a linearly polarized beam of photons. The electrons enter the tagger hall to produce a polarized beam of photons which then travel 75m into the main spectrometer located in the counting-house. Figure adapted from [35].

2.2.1 The Photon Beamline

After 5.5 passes around the accelerator ring, the electrons enter Hall-D with an energy of 12 GeV. Hall-D comprises two buildings, the tagger hall, and the counting-house as in Figure 2.3. The beam enters the tagger hall and impinges on a diamond radiator producing polarized photons. The photon beamline consists of a photon tagger, an electron beam dump, a collimator, the pair spectrometer, and a triplet polarimeter as shown in Figure 2.3.

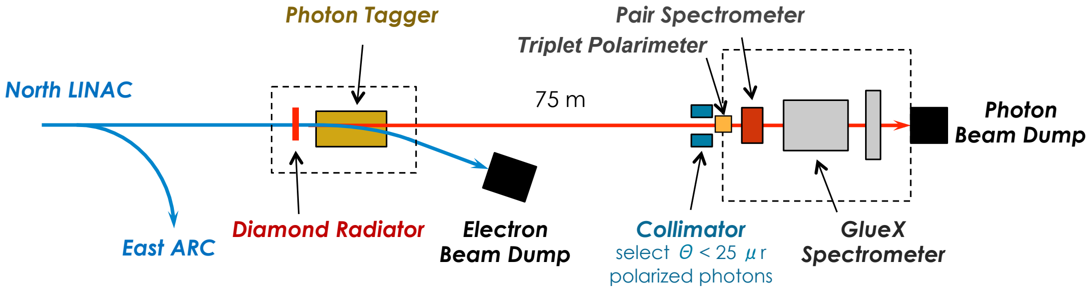

Figure 2.3: Schematic for the GLUEX beamline. Figure reproduced from [34].

Diamond Radiator: This element shown in red in Figure 2.3. The incident electrons from CEBAF strike a 50 μm-thick diamond radiator crystal producing a linearly-polarized photon beam through the bremsstrahlung process. The diamond radiator is mounted on a goniometer[1] in the hall to be aligned in four standard orientations having four different angles of linear polarization: 0°, 45°, 90° and 135°, with respect to the horizontal (floor). Linear polarization parallel to the horizontal (floor) is referred to as PARA (0°, 135°), whereas linear polarization perpendicular to the horizontal is referred to as PERP (45°, 90°). The four polarization orientations allow measurement of polarization-dependent physics observables, such as beam asymmetries, as well as aid in the cancellation of detector systematic effects. The energy range corresponding to maximum linear polarization is termed the coherent peak, and the upper edge of this range is defined as the coherent edge. Fine-tuning the crystal plane adjusts the energy at which the coherent edge occurs as this position is a function of the angle between the beam and the normal to the crystalline plane of the diamond. Nominal GLUEX running results in a coherent peak range of 8.2-8.8 GeV, while the coherent edge is situated at ~9 GeV. Additionally, an aluminum

---

[1] The Goniometer rotates the diamond radiator to different angles allowing different angles of polarization.

radiator that has an amorphous structure is used to produce a photon beam without any linear polarization and hence without any coherent peaks. Photon yields for each of the orientations are shown in Figure 2.4. Details are provided in the following subsections.

Photon Tagger: The photons that are produced through the bremsstrahlung process have to be tagged correctly in order to measure their energies which are determined indirectly by tagging the energy of the scattered electron beam that passes through the diamond radiator. The energy of the radiated photon can be determined by the difference in the measured energy of the electrons in the 'Tagger' and the initial energy of the electron given by the accelerator since the electrons from the accelerator have fixed and known energy prior to interacting with the radiator. A dipole magnet is used to deflect electrons that did not interact with the radiator or lost less than a quarter of their initial energy into a beam dump. The electrons that are deflected to large angles (losing more than a quarter of their initial energy) are directed to an array of scintillation counters known as the Tagger Hodoscope (TAGH) which spans an energy range from 3.0 - 11.6 GeV. In the coherent peak region, scintillators called Tagger Microscope (TAGM) having smaller spatial dimensions are used to achieve better energy resolutions. Both types of scintillators then 'tag' the photons' energy [35].

Since the photon production is done through the scattering process, there is a trajectory that occurs at small polar angles, with respect to the beamline, for the coherent portion of the photon beam. Low-energy photons are deflected at larger angles compared to the high-energy photons which are blocked by the use of the collimator. The coherent portion of the beam spectrum at 12 GeVin energy has an emission angle of less than 15 μrad while the incoherent portion has spread up to 43 μrad from the beamline. The collimator is placed 75 m after the diamond radiator and ~25 m upstream of the target resulting in a nominal collimator aperture of 5 mm.

Triplet Polarimeter (TPOL) From the collimator, the photons approach the Triplet Polarimeter (TPOL) which is used to measure the degree of polarization of the photons. The polarization is measured via the process of triplet production through the reaction $\gamma e^- \rightarrow e^- e^+ e^-$. TPOL contains a thin 75 μm Beryllium foil to trigger the triplet photo-production [36]. The photon interacts with the electron in the Beryllium converter making the electron recoil with the Beryllium atom. The excess energy produces an electron-positron pair. TPOL measures the recoil electron while the Pair Spectrometer (PS) measures the produced pair further down the beamline.

The degree of polarization is calculated using the polarized cross-section, similar to a beam asymmetry measurement. When a photon beam has linear polarization, the production cross-section σ gains a modification to the unpolarized cross-section σ_0 as in Equation 2.30.

$$\sigma = \sigma_0 \Big[1 - P_\gamma \Sigma \cos(2\phi) \Big] \tag{2.30}$$

where, σ and σ_0 are the polarized and unpolarized triplet cross-sections, respectively, P_γ is the degree of photon beam polarization, Σ is the beam asymmetry for this process, and ϕ is the azimuthal angle of the recoil electron trajectory. The degree of photon beam polarization P_γ is determined by fitting the ϕ distribution to the above equation. This is a destructive measurement, however, the overall fraction of intercepted photons is small enough that the measurement can be performed while the experiment is running.

Pair Spectrometer (PS): This device is used primarily to determine the beam flux within the coherent peak. The PS reconstructs the energy of a beam photon by detecting the electron-positron pair produced by the TPOL photon. The determination of the photon beam flux is used to calibrate the energies delivered by the tagging system. The PS detectors cover a momentum range for the electrons and positrons that correspond to photon energies between 6.0 - 12.4 GeV. The photon flux yield from the PS and the degree of polarization from TPOL are shown in Figure 2.4.

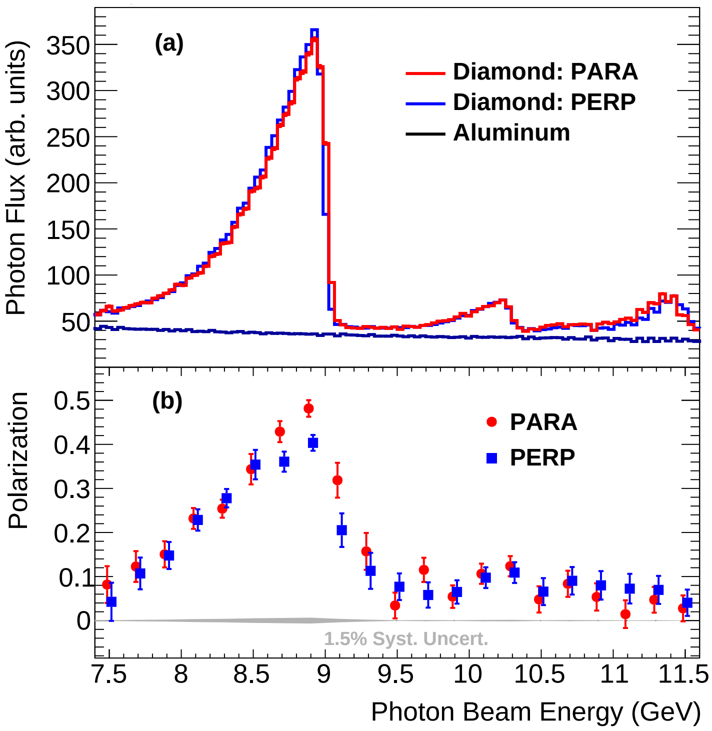

Figure 2.4: Polarized Photon flux measured by Pair Spectrometer and degree of polarization measured by Triplet Polarimeter for 2016 commissioning run period. One can observe the primary coherent peak at $\sim$ 8.8 GeV. Secondary peaks corresponding to the higher harmonics from the crystal planes can also be observed in the figure. Figure from [35].

Target system: The target consists of three major components, namely, (i) the cryocooler, (ii) a condenser, and (iii) the target cell. GlueX uses Liquid Hydrogen (LH_2) as its target. LH_2 is contained within a cell made of 100 μm thick aluminium polyimide sheet made into a conical structure. The overall length of the target system is 30 cm and diameter 2 cm and located at 50 cm in z w.r.t the detector coordinate system. The temperature of the target is constantly maintained and monitored at around 20 K using cryocooler and condensing systems. At the standard operating pressure of 19 psia[2], the boiling point of Liquid Hydrogen (LH_2) is 1 K greater than the operating temperature, reducing boiling within the target cell and thereby resulting in more stable density [35].

2.2.2 Charged Trackers

Gaseous Charged Trackers or Drift Chambers provide excellent position, timing, and energy deposition information of the charged particles in GlueX. Drift chambers are filled with a unique mixture of argon and carbon dioxide which is monitored constantly during the process of data taking. The trackers are called drift chambers because the charged particles passing through the drift chamber ionize the gas around their path. This induces a current which is then measured by the electronics. The motion of the charged particles in the magnetic field, along with its timing, can be used to determine the momentum of the particle. There are two Drift Chambers in GlueX, namely, the Central Drift Chamber and Forward Drift Chamber.

Reconstructing charged particles is key in GlueX. Cuts on the energy deposited in the trackers along with timing and position information could determine the type

---

[2] psia: pounds per square inch absolute

of particle along with matching a subsequent shower in corresponding calorimeters.

Central Drift Chamber (CDC) The CDC as shown in Figure 2.2 is a cylindrical straw-tube detector located in the upstream half of the solenoid and is the first layer around the target and the Start Counter, which is described in Section 2.2.3. The polar angle acceptance of CDC is from 6° to 168°, with its optimal performance from 29° to 132°. It is composed of 28 layers of 1.5 *m* long, 1.6 *cm* diameter straws, totalling 3522 straws. Each straw is composed of a mylar tube with an anode made from 20 μm diameter gold-plated tungsten. The inner wall of each straw behaves as a cathode ensuring a uniform electric field around the wire. The straw is used to add rigidity and support the tension in the wire. A 50/50 mix of argon and carbon dioxide is filled in the straw at 1 atm pressure. The wires inside the straw are kept at $\sim$1250 V. When a charged particle passes through a given straw, the gas mixture becomes ionized and a signal pulse is generated between the signal wire (anode) and the ground (cathode). The CDC has a spatial resolution of 130 μm, and if a charged particle passes within 4 *mm* of one of the straws, each straw has an efficiency over 98%. The alignment of these straws is a major calibration effort that is taken every run period as seen in [35]. Detailed information about CDC can be found in [35, 37].

Forward Drift Chamber (FDC): FDC as drawn in Figure 2.2 is a disk-like tracker that is located in the downstream half of the solenoid and is used to track charged particles in the forward direction. The FDC has a polar angle acceptance from 1° to 10° around the beam line. FDC handles a high volume of tracks as well as spiralling trajectories due to the nearness to the electromagnetic background surrounding the beam line. There are a series of four packages with six wire chambers in each package arranged to form different tracking layers. Each chamber has a plane of sense and signal wires sandwiched between two cathodes which are used to determine the spatial and timing information of the charged particle. A 40/60 mix of argon and carbon dioxide is filled in each of the chambers. Each chamber is rotated by 60° with respect to its neighbouring chambers maximizing coverage and resulting in a position resolution as low as 60 μm. More information about the FDC can be found in [35].

2.2.3 Particle Identification Detector (PID)

Identifying the type of particles is key to reconstructing hadronic reactions. While the Particle ID can be inferred from measurements from other detectors (combination of trackers and calorimeters) in Hall-D, GlueX has two dedicated detectors to perform Charged Particle Identification.

Start Counter (SC): The SC is sketched in Figure 2.2, and it surrounds the target region and covers about 90% of the solid angle for the particles originating from the center of the target. The SC can handle photon intensities of up to 10^8 photons/s in the coherent peak, and accurately associates the beam photons with the correct RF bunch. It has a cylindrical shape with a cone-shaped tip consisting of 30 narrow scintillator paddles supported by ROHACELL foam support structure. This segmentation allows for operation at such high beam intensities. Beam bunches enter the target every 4 ns and thus the resolution of the SC is sufficiently high ($\sim$ 230 ps) to accurately identify the corresponding bunch for each event. Energy deposited in the SC provides a dE/dx measurement used in particle identification. When combined with the track momentum information from the tracking detectors, the dE/dx value from the SC is sensitive enough to separate protons from charged mesons up to a track momentum of $p = 0.9$ GeV/c. Further information on SC can be found in [35, 38].

Time Of Flight (TOF) The TOF is shown in Figure 2.2. It is a planar-type detector made of scintillating bars and is located directly upstream of the FCAL, The TOF is used to determine the flight time of the charged particles. It is composed of two planes of scintillator paddles with PMTs on both ends of each paddle. Each plane consists of 38 paddles with each paddle of length 252 *cm* and width 6 *cm*, and four shorter paddles with one-sided readout to leave a hole around the beamline, and thereby avoiding the high data rates. Additionally, a Lucite shield is placed around the beam hole to further lower the interacting rates. The TOF reads the time at which the charges particle passes through it with an accuracy of ~ 80 *ps*. In conjunction with the time from the accelerator (RF time) and its momentum, a particle's flight time and path length traveled are determined. The detector is able to differentiate between charged pions and kaons up to 2.5 GeVin momentum.

2.2.4 Calorimeters at GlueX

Calorimeters are detectors that measure the energy deposited by a particle traversing them or stopping in them. In GlueX, calorimeters are mainly used to detect photons and their corresponding energy in the final state of a reaction. There are two calorimeters in GlueX: the Barrel Calorimeter and the Forward Calorimeter, which when combined, provide nearly a 4π solid angle coverage as the majority of the reactions are boosted forward due to fixed target interactions. The transition region from BCAL to FCAL has poor reconstruction efficiency, and as a result, a fiducial cut is applied to exclude particles near the transition region.

Barrel Calorimeter (BCAL) The BCAL is diagrammed in Figure 2.2. It is a $10M cylindrical shell detector built and designed by the University of Regina Group. The BCAL is made up of 48 modules, as depicted in Figure 2.5. Each module alternates layers of scintillating fibres (184 layers) and lead (185 layers). Particles hitting the fibres produce photons that travel through the fibres to Silicon PhotoMultipliers (SiPM) connected to the fibres on either side of the BCAL. Each module is further segmented into four sectors in the direction of ϕ and is attached to 10 SiPMs on either side of the BCAL. Each module is further segmented radially into four layers by summing up various SiPMs. Layer 1 is made only by the first inner layer of SiPMs. Layer 2 is summed over the next two SiPMs radially. In contrast, layer 3 is summed over the following three layers and layer 4 represents the sum over the outer four layers of SiPMs, as shown with different colours in Figure 2.5 (d). Each module, therefore, contains a total of 40 SiPMs segmented into four radial and four azimuthal sectors with a total of 16 readout channels on either side of the BCAL. Therefore, the BCAL comprises a total of 3840 SiPMs, readout by 1536 Flash - Analog to Digital Converter (FADC) on both sides of the BCAL. Each of the readout channels allows measurement of the position along with the timing of the particle that interacted in the BCAL. The energy of the incident particle is directly proportional to the light collected in the SiPM. The gains of the SiPMs have to be precisely calibrated for every run period to ensure accurate measurement of energy. Gain calibrations are done every run period which will be discussed later in Chapter 3. A summary of the properties of BCAL is presented in Table 2.1.

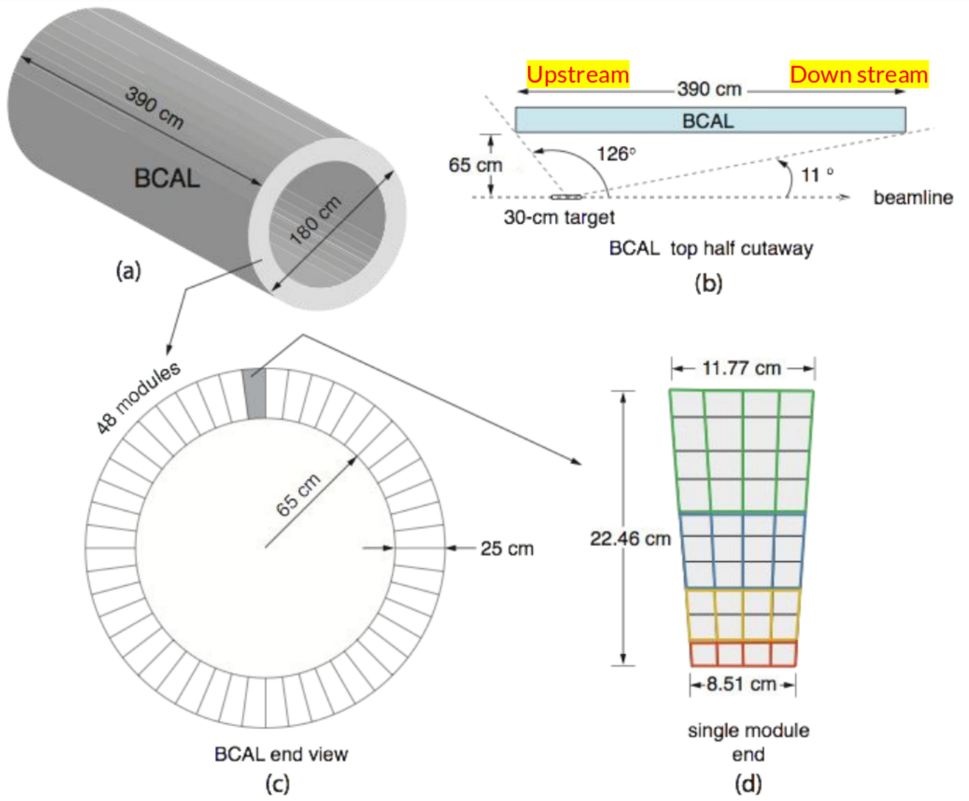

Figure 2.5: Sketch of Barrel Calorimeter (BCAL) readout. (a) A 3D rendering of the BCAL; (b) top-half cutaway (partial side view) of a BCAL module showing its polar angle coverage and location with respect to the LH_2 target; (c) end view of the BCAL depicting all 48 azimuthal modules and (d) an end view of a single module showing the readout segmentation. More details can be found in [35, 39].

Forward Calorimeter (FCAL): The FCAL is shown in Figure 2.2 and is located in the forward region of the detector. The FCAL has polar acceptance from 1° to 11° with a full 2π azimuthal coverage. The FCAL consists of a circular array of 2800 long lead glass scintillating blocks each with dimensions 4×4 cm^2 and 45 cm long. A particle, typically an electron, positron or photon, enters the detector and interacts with the nuclei of the atoms in the block through bremsstrahlung or pair production. This results in an 'electromagnetic shower' in the block. These electromagnetic showers emit Cherenkov photons which are produced within the lead glass blocks. The light

Property	**Value**
Number of Modules	48
Module length	390 cm
Module inner/outer widths	84.0 mm/118.3 mm
Pb-Scintillator matrix thickness	221.9 mm
Inner/outer Al plate thickness	8 mm/31.75 mm
Module azimuthal bite	7.5°
Total number of fibers	685000
Lead sheet thickness	0.5 mm
Kurarary SCSF-78MJ multi-clad fiber	1.0 mm
Fiber pitch radial/lateral	1.22 mm/1.35 mm
Weight fractions (% Pb:SF:Glue)	86.1 : 10.5 : 3.4
Effective density	4.88 g/cm^3
Effective Radiation Length	1.45 cm
Effective Moliere radius	3.63 cm
Effective Atomic Weight	71.4
Effective Atomic Number	179.9
Sampling fraction	0.095
Total Weight	28 tonnes
Energy resolution ($\frac{\sigma(E)}{\sqrt{E}}$)	$\frac{5.2\%}{\sqrt{E}} \otimes 3.6\%$
Timing resolution ($\sigma(t)$)	200 ps @ 1 GeV
Position resolution ($\sigma(z)$)	3 cm

Table 2.1: Summary of Barrel Calorimeter (BCAL).

emitted by these interactions is detected by the μ-metal shielded Photo Multiplier Tubes (PMT)s attached to the end of each of the blocks. The light collected by the PMT is proportional to the initial energy of the incoming particle. FCAL has a positional resolution of 1 cm and a photon energy resolution $\sigma_\gamma = \frac{5.6}{\sqrt{E}}\% \otimes 3.5\%$ for a broad range of particle energies. More information about FCAL can be found in [35, 40].

2.2.5 Trigger and Data Acquisition

During the nominal data taking in GlueX, there are four types of triggers in the Data Acquisition (DAQ) system: (i) PS triggers for photon beam flux calculations, (ii) a random trigger used for estimating the background events, and (iii) LED triggers are synchronized to the LED light pulses in the calorimeters (used for calorimeter calibrations and monitoring) and (iv) physics event triggers, described below. The random trigger is chosen to have a rate of 100 Hz, while the LED trigger is chosen to have a 10 Hz rate. During GlueX-I running, the PS trigger has a rate around 3 kHz. The total trigger rate during GlueX-I data taking was around 40 kHz.

The trigger system at GlueX consists of electronics hosted on 55 VXS crates along with the readout electronics [41]. The energy data from both the FCAL and BCAL are digitized by the FADC modules. The digitized information is summed and passed on to the Crate Trigger Processor (CTP). The CTPs pass their information to the Global Trigger Crate (GTP) where it is combined by the subsystem processors. A GTP then applies a conditional formula to decide whether to trigger or not. The GTP typically follows two formulas for the nominal physics triggers and they are,

$$\Big(2 \times E_{\mathrm{FCAL}} + E_{\mathrm{BCAL}} > 1\ \mathrm{GeV}\Big) \ \cap\ \Big(E_{\mathrm{FCAL}} > 0\ \mathrm{GeV}\Big) \tag{2.31}$$

$$E_{\mathrm{BCAL}} > 1.2\ \mathrm{GeV} \tag{2.32}$$

Equation 2.31 is used for events that are highly boosted in the forward direction while Equation 2.32 is for events with large transverse energy. At nominal GlueX operations photon flux is of the order of $1.5 \times 10^7 \gamma/s$ in the coherent peak region.

Chapter 3

BCAL Service contribution

3.1 Introduction

As detailed in Section 2.2.4, BCAL provides information towards the reconstruction of the detected particle's energy, which is directly related to the amount of light detected by each SiPM. Therefore, it is vital to match the gains of all SiPMs along with the FADC attached at the end of each channel. As a collaborator in GlueX and the institutional member that built the BCAL, the gain calibration in BCAL is performed by the Regina group since GlueX became online in 2017, as part of our service contribution to the Collaboration. This chapter summarizes the results of gain calibration in BCAL since the fall of 2018 and until the summer of 2020.

3.2 BCAL gain calibration

The gains in FADC readouts are used to set the energy scale of the BCAL. The absolute energy scale of all the channels is set to match the energy of well-known physics samples. A conventional shower will deposit energy in more than one channel in the BCAL, making it important to balance the gains of each channel relative to one another. By adjusting the gains, the energy resolution associated with an incident photon shower will also be minimized since more than one channel is used to reconstruct a cluster. Before performing the gain calibrations, several low-level calibrations, such as the timing calibration [42] and attenuation length calibrations [42, 43] are performed [39].

When a cell fires in the BCAL, the upstream channel and its corresponding downstream channel provide hit-level information, as shown in Figure 2.5. The calibration procedure assumes that the gains of the SiPM between the upstream and its corresponding downstream channel varies by a ratio called the *gain ratio*. This ratio is extracted as a result of all the low-level calibrations.

Two complimentary methods of gain calibration were initially explored, one was a method of bootstrapped gain calibration based solely on the shape of the invariant mass spectra from the detector response and does not require a beam of known energy. This method was adapted from [44], however, a second iterative method was proven to be more robust for calibration. The methods are compared and discussed in detail at [45]. Both techniques rely on having large statistics of inclusive $\pi^0 \rightarrow 2\gamma$ events. Since a sample of photons with known energy is not available, π^0 samples are used as a reference for calibration since its mass can be reconstructed in the BCAL and compared with its precisely known value in the PDG [4]. A brief description of the iterative method is presented below.

3.2.1 Gain calibration procedure

The gain calibration in the BCAL is an iterative procedure using inclusive π^0 events. This method offers large statistics in the energy range of interest (0.5 - 3 GeV). The gains for the FADCs channels in the first three layers of the BCAL are determined in every run period using this procedure. However, the photons that decay from the π^0 events ($\pi^0 \rightarrow 2\gamma$) do not have enough energy to penetrate into the 4^{th} layer of the BCAL. Therefore, channels in that layer are calibrated using cosmic muons [46]. A detailed description of the procedure for gain calibration in the BCAL can be found in [47], and is briefly summarized below:

1. π^0 inclusive reactions (eg. $\gamma p \rightarrow \omega p \rightarrow \pi^+\pi^-\pi^0 p$) with at least one charged

track are chosen for calibration.

2. The energy of the photons (E_1, E_2) is determined by the SiPM attached to the end of each channel in the BCAL. The z position of the photon shower is reconstructed from the timing information from the Time to Digital Converter (TDC)s, attached at the end of each channel in the BCAL. The vertex of the reaction is deduced from the tracks of the charged particles.

3. For every event, channels with greater than 50% (or $> 30\%$ for Layer 3 channels) for either E_1 or E_2 are selected for calibration to assign the reconstructed π^0 mass. An energy cut ($E_{1\text{or}2} > 0.4$ GeV) is applied further purify the π^0 samples. This results in a higher signal-to-background ratio during the fitting process.

4. Using the reconstructed information found in earlier steps, the invariant mass of the π^0 is reconstructed [39], using the equation

$$m^2 = 2E_1E_2(1 - \cos\phi)$$

where ϕ is the angle between the two decaying photons (γ_1 and γ_2).

5. The 2γ mass distribution (measured π^0 mass) for each of the channels is then formed, and fitted using a Gaussian function for the signal and a second order polynomial function for background

$$N_0 e^{(-\frac{1}{2}((x-\mu)/\sigma)^2)} + ax^2 + bx + c$$

. An example of the fitted π^0 mean, μ, and its width, σ, is shown in Figure 3.1.

6. The ratio of the mean π^0 mass to the PDG mass of π^0 (0.135 GeV) is formed. This ratio is applied as a correction to the existing gains for the channels.

7. The procedure is reiterated until the mean π^0 mass is within 1% and the tolerance $(\frac{\sigma_{\pi^0}}{\mu_{\pi^0}})$ of is less than 1%.

Layer 4 channels are calibrated using cosmic muons. The cosmic muon calibrations are fairly constant and were done only twice during the entire GlueX Phase-I data-taking period. After each iteration, the fit mean versus the channel number is plotted to look for convergence. Figure 3.2 shows the fit mean at the start of the gain calibration for the summer 2020 run period.

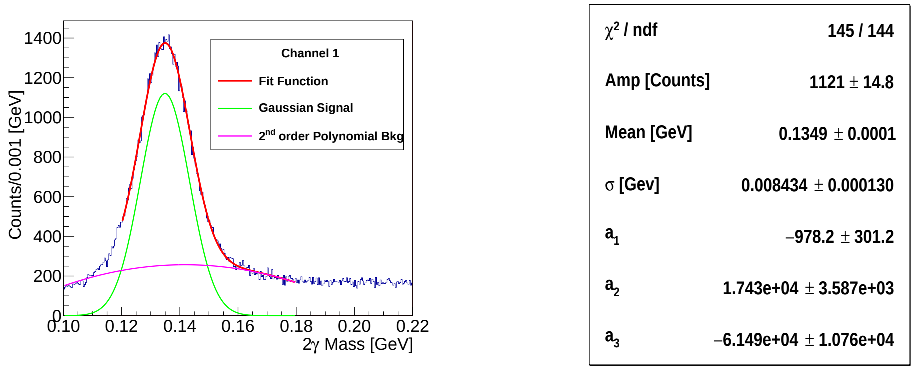

χ^2 / ndf	145 / 144
Amp [Counts]	1121 ± 14.8
Mean [GeV]	0.1349 ± 0.0001
σ [Gev]	0.008434 ± 0.000130
a_1	−978.2 ± 301.2
a_2	1.743e+04 ± 3.587e+03
a_3	−6.149e+04 ± 1.076e+04

(a) **(b)**

Figure 3.1: The plot on the left (a) is an example of 2γ (π^0) mass distribution after the cuts discussed in the procedure for channel 1 (Module 1, Layer 1, Sector 1) in the BCAL. Likewise, all 768 channels have similar distributions (signal-to-noise ratio layer 2 > layer 1 > layer 3, due to the readout summing scheme) procedure which are fit (red color) using a single Gaussian (green) and a second order polynomial (magenta). On the right (b) the corresponding fit parameters are shown. The extracted mean is divided with M(π^0) GeV to form the ratio that is then multiplied with the existing gains as correction for the next iteration.

It is also important to ensure that there is an improvement in the resolution of the 2γ (π^0) mass distribution as the iterations proceed. Figure 3.3 shows the improvement of resolution between the start and end of spring 2020 calibration.

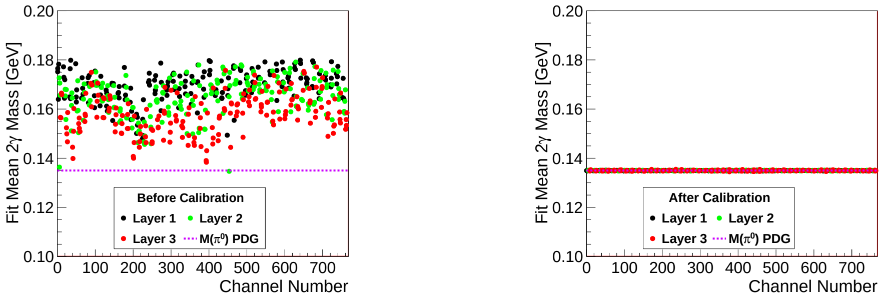

(a) **(b)**

Figure 3.2: The figure on the left shows the mean π^0 mass extracted from the fits for all the channels in the first three layers (each color represents a different layer in the BCAL) of the BCAL before the start of summer 2020 calibration. The magenta dotted line corresponds to the PDG value of the π^0 mass of ~ 0.135 GeV. The plot on the right shows the fit mean of the channels after 19 iterations. The gains for each of the channels have converged within 1% of π^0 true mass.

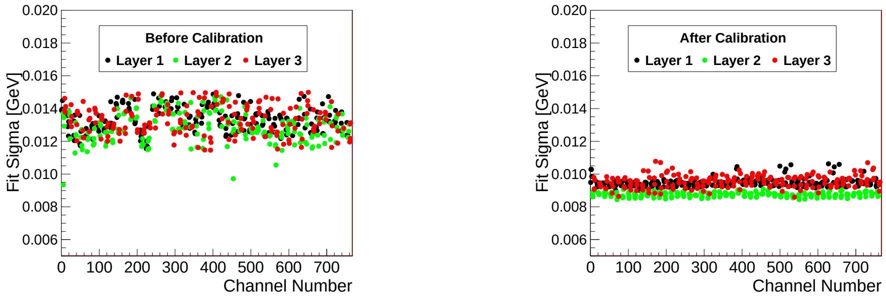

(a) **(b)**

Figure 3.3: The figure on the left shows the mean π^0 resolution extracted from the fits for all the channels in the first three layers (each color represents a different layer in the BCAL) of the BCAL before the start of spring 2020 calibration. The plot on the right shows the same after 19 iterations. One can observe tightening of the resolution in the end of 19^{th} iteration.

Finally, as mentioned in the procedure, $\frac{\sigma(\pi^0)}{\mu(\pi^0)}$ is calculated for all the channels as a figure of merit for convergence. Figure 3.4 shows convergence of overall measured $\frac{\sigma(\pi^0)}{\mu(\pi^0)}$ as a function of iteration during calibration.

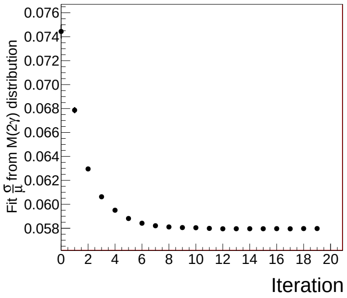

Figure 3.4: The figure shows the ratio $\frac{\sigma_{\pi^0}}{\mu_{\pi^0}}$ as a function of iteration. The ratio has to be stable within 1% in order to have sufficiently converged gains.

Once the gains for every channel have sufficiently converged, a non-linearity in the measured energy of the incoming particle in the BCAL is noticeable. This non-linearity is explained in the next section.

3.2.2 Nonlinear energy correction

After the FADC gains are calibrated using the procedure outlined above, there still exists a nonlinearity in reconstructed π^0 mass as a function of shower energy. The response of BCAL is nonlinear in the order of a few percent ($\sim 1-2\%$). A few key causes of this nonlinear response are explained below,

Saturation of SiPM pixels: Non-linearity of SiPMs due to saturation is a known feature of these optical sensors [48] and the relation between the number of incident photons and the number of fired pixels is given by

$$N_{\text{fire}} = M\Big(1 - e^{\epsilon N_\gamma / M}\Big) \tag{3.33}$$

where, N_{fire} is the average number of pixels of the SiPM that fire when N_γ optical photons impinge on a SiPM array. The photon detection efficiency (PDE) is denoted by ϵ and M is the number of pixels of the SiPM array. The true number of hits can be approximated as $N_{\text{True}} \approx \epsilon N_\gamma$, which is proportional to the number of incident photons. Inverting Eq. (3.33) gives,

$$N_{\text{true}} = -M\Big(\log\left(1 - N_{\text{fire}}/M\right)\Big) \tag{3.34}$$

In Layer 1, there is only one SiPM sensor array with $M = 16 \times 3600 = 57000$ pixels. Layers 2, 3, and 4 have two, three, and four sensor outputs summed into a single channel. The light collected by each light guide approximately uniformly illuminates the surface of the sensors. For the BCAL, the SiPM pixels per count is calculated to be 0.478 pixel/count [49, 50]. However, the data prefer a value for SiPM pixel/count of 0.25 which is nearly half of what is calculated [51, 52]. SiPM saturation correction is done on a hit-by-hit basis and mainly affects higher energies.

Saturation of FADC electronics: The light intensity in the sensors is directly proportional to the energy of the incident particle. This results in FADC integral saturation. Therefore, a correction (scale up) is applied to FADC amplitude based on its integral count [39].

The above-mentioned corrections have been implemented and mostly account for high-energy corrections. The main cause of low energy corrections is explained below,

Shower Leakage and non-linearity as a function of 'z' position in the BCAL: The distribution of energy leakage can be modelled as a function of z position in the BCAL. This is because the sampling thickness effectively increases at shallow angles, which affects the effective threshold for the generation of secondaries and this can complicate the interpretation of simulated results. A detailed study on energy leakage can be found at [39] and energy dependence as a function of z was studied in [53]. In this study, a detailed comparison between data and MC was made. This results in identifying and correcting most of the nonlinearity in the BCAL.

To account for the nonlinearities in measuring energies in the BCAL, the following steps are followed.

1. Consider two-photon showers in the BCAL in an event;
2. Reconstruct the invariant mass of the two-photon showers (E_1 and E_2)[1]
3. If the reconstructed invariant mass is between 0.07 GeVand 0.25 GeVand if the difference in photon energies is within 100 MeV, then record their corresponding invariant mass and the mean energy of the two showers.

The plots in Figure 3.5 represent the invariant mass of π^0 as a function of mean photon energy (GeV). The points in Figure 3.5a are energies before applying the empirical nonlinear corrections. Then an empirical function shown in Equation 3.35 which corrects the measured energy (E_{raw}) is fit to the distribution. The corrected energy value E_{corr} after the applying empirical corrections[2] is shown in the Figure 3.5b

$$\frac{m_{\pi^0}^{\text{recon}}}{m_{\pi^0}^{\text{PDG}}} = [0] - [1]e^{[2]E+[3]} - \frac{[4]}{[5] + [6]e^{-[7]E+[8]}} \tag{3.35}$$

---

[1] We choose π^0 events decaying into two γ; E_1 and E_2 correspond to the two decay photons from the decaying π^0.

[2] These applied corrections are made by fitting a curve to in Figure 3.5a.

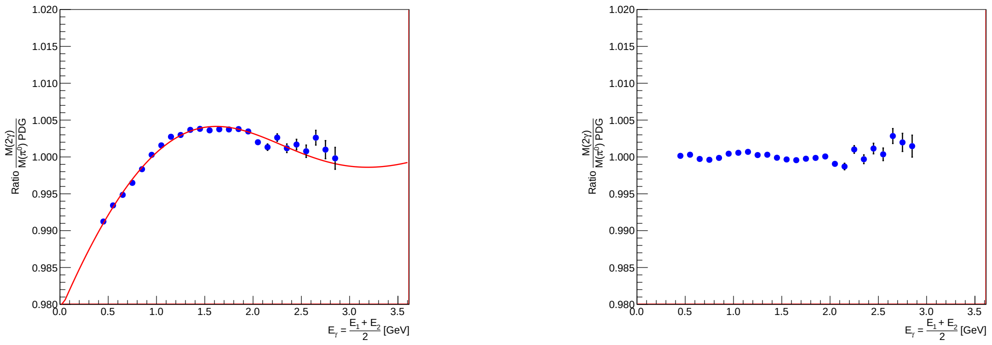

(a) Uncorrected Energies

(b) Corrected energies

Figure 3.5: Ratio of reconstructed invariant mass π^0 to the PDG value of π^0 as a function of photon energy. The large error bars at higher energies are due to a lack of statistics of high energetic photons in the BCAL.

With these empirical nonlinear corrections, the BCAL is calibrated for every run period.

3.2.3 Calibration summary since fall 2018

Fall 2018: This dataset corresponds to the end of GlueX Phase-I data period. The effect of SiPM saturation correction in data and the non-linearity in measuring energy as a function of z in the BCAL was studied in detail. The calibration for fall 2018 and the SiPM saturation study can be found in [51].

Spring 2019: The dataset corresponds to the PrimEx experiment [54]. The experiment had a magnetic field turned off which in turn increased the background in the BCAL. A detailed report for calibration has been written and can be found at [55].

Fall 2019 to fall 2020: The total data taken during the fall of 2019 and spring of 2020 are split into 12 batches of approximately equal statistics. Some of these batches have different beam currents and some sub-batches have special run conditions. Therefore, each of these batches was calibrated separately and sequentially such that the gains from a preceding batch become the seed for the next one. A summary of the calibration is shown in Figure 3.6.

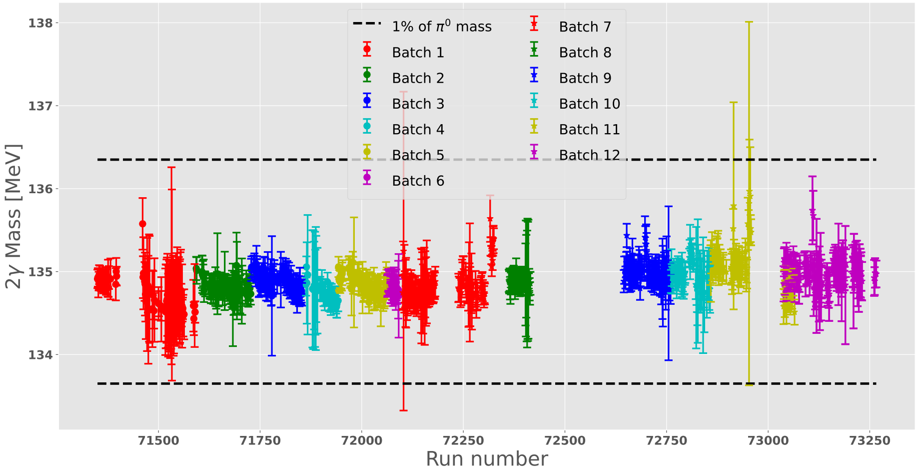

Figure 3.6: Reconstructed 2γ Mass [MeV] as a function of run number for various batches after the nonlinear corrections. Colors correspond to the various batches of runs in the run period. The errors in each point are statistical and depend on the total events in the run. Runs having non-physics triggers are removed. Points with large error bars represent relatively short-duration runs.

At the end of each calibration, the results are presented for approval to the Calorimetry Working Group (CALWG) and to the GlueX Physics Coordinator. Once approved, the calibration constants are uploaded to the `Calibration Constants DataBase` which is then used for physics analysis by the collaborators. The calibration for subsequent run periods (since fall 2021) has been handed over to a new graduate student with continual assistance when needed.

Chapter 4

Analysis of $\gamma p \rightarrow \omega \pi^0 p$ at GlueX

CEBAF typically runs for two seasons (run periods) in a year. The spring run period corresponds to the run between January and April, while the fall run period corresponds to the run between September and December of each year. This analysis was performed for the GlueX Experiment (GlueX) Phase-I data set, which was collected using a linearly polarized photon beam on its LH_2 target. The overall dataset was taken over a period of two years (2017–2018) and split into three run periods. The electron beam used to produce the photon beam was delivered at an average current from 150-250 nA.

	Spring 2017	**Spring 2018**	**Fall 2018**
Luminosity [pb^{-1}]	21.8	63.0	40.1
Fraction of GlueX Phase-I	17.4%	50.4%	32.1%

Table 4.1: Summary of GlueX-Phase-I data. The results shown in this thesis correspond to the data taken during the shown run periods.

GlueX Phase-I data amounts to about 1400 physics quality runs[1] with a total disk footprint of 3 petabytes in raw data mode (EVIO) [56]. After sufficient calibrations, the raw data is processed in various reconstruction launches, resulting in more than 500 terabytes (TB) of reconstructed data. The reconstructed format in GlueX is called Reconstructed Events STorage (REST) files. REST files are ROOT files containing event-level information on various reconstructed quantities such as shower information in the calorimeters, and track information from trackers in a GlueX specific data structure [35]. The full set of REST data comprises events that can be further cleaned for individual reactions. Therefore, one can filter out the final state of interest by using a "reaction filter" process which is run in parallel for many reactions where users provide their reaction's configuration through a web interface

---

[1] A GlueX run is defined as a data taking period of about ~ 2 hours each.

which is periodically downloaded to a configuration file for an "analysis launch". This dissertation focuses on the reaction $\gamma p \rightarrow \omega\pi^0 p$ with specific interest in extracting the contribution of b_1 meson. $b_1 \rightarrow \omega\pi^0$ has the highest branching fraction [4].

Generation of Monte-Carlo events: In order to understand the detector response and any systematics associated with the analysis methodology, a Monte Carlo (MC) sample along with GlueX data is simulated mimicking detector response and run conditions during the data taking process. This way, any bias/systematics during the data analysis can be studied in detail. The exact details of the Signal Monte Carlo events will be discussed in Section 5.3. In the following sections, side-by-side comparisons will be made for various data analysis cuts between GlueX Phase-I data and generated Signal MC events.

4.1 Event Selection of $\omega\pi^0$

The analysis starts by matching events to the final state reaction of interest and creating possible particle combinations from the reconstructed tracks and showers from the REST data. In this case, a beam photon is detected by the tagger as described in Section 2.2.1 and in the final state, two positively charged tracks (the π^+ and the recoil proton) and one negatively charged track (π^-) are detected by the trackers along with four neutral showers detected by the calorimeters. The selection criterion is applied for exclusivity and particle identification, then a kinematic fit is performed as discussed in the next Section 4.4. If the kinematic fit converges for a combination of tracks and showers, that event is stored in a ROOT tree for further analysis.

The analysis cuts can be classified broadly into two categories, (i) Stage-I cuts and (ii) Stage-II cuts. Stage-I cuts are performed during the analysis launches, which are mostly 'loose' and are applied across most of the channels that are analyzed. Stage-II cuts are performed on the ROOT files from the analysis launch productions. These are cuts, that are applied after the "reaction filter" process. These, cuts are done using the "DSelectors" which is GlueX specific framework to analyze output from the "reaction filter".

4.2 Stage-I cuts

TOF Cuts Timing cuts are applied to make sure that the tracks in the detectors come from the corresponding RF bunch. The timing cuts shown in Table 4.2 are applied to the system with the best timing information available. For instance, a hit in the TOF will have no timing cuts applied on the FCAL or SC. Since the detectors occupy different angular regions, a track with hits in the BCAL will probably not hit the FCAL or TOF. The timing cuts are redone after the kinematic fit has updated the momentum and vertex information. Plots corresponding to timing cuts in BCAL is shown in Figure A.1.

PID	**BCAL RF Δt (ns)**	**TOF RF Δt (ns)**	**FCAL RF Δt (ns)**	**SC RF Δt (ns)**
γ	±1.0	–	±2.5	–
π^+	±1.0	±0.5	±2.0	±2.5
π^-	±1.0	±0.5	±2.0	±2.5
p	±1.0	±0.5	±2.0	±2.5

Detector Subsystem	**BCAL**	**TOF**	**FCAL**	**SC**
Timing Resolution	234 ps	105 ps	380 ps	150 ps

Table 4.2: Selection Cuts on Δt_{RF} for different particle species in SC, TOF, BCAL and FCAL. The labels in blue color correspond to Stage-II cuts which are stricter than Stage-I cuts. A larger cut is used for photons in the calorimeters due to the time needed for the electromagnetic showers to evolve and get detected in the photosensors which results in a larger Δt_{RF}.

dE/dx cuts on charged particles Cuts are placed on the energy loss of each charged track. Different species of charged particles lose energy in a medium at different rates based on their rest mass. This can be exploited to differentiate various charged particles. Cuts on energy loss on p and charged $\pi^{\pm}$ in CDC tracking detector are placed as shown in Table 4.3 and Figure A.2. The cuts on track energy loss are kept loose and follow the Stage-I set of cuts.

PID	**CDC dE/dx (keV/cm)**
p	$dE/dx > e^{-4p+2.25} + 1.0$
$\pi^{\pm}$	$dE/dx < e^{-7p+3.0} + 6.2$

Table 4.3: dE/dx cut in the CDC for protons and charged pions

4.3 Accidental Subtraction

As mentioned earlier, photons impinge on the target, in beam bunches. Each beam bunch is separated by 4.008 ns from adjacent bunches. Contributions to the final state products may arise due to matching particles to the wrong beam bunch, so a background subtraction has to be done in order to suppress tagged photon contributions from the 'wrong' beam bunches. To this end, beam photons are characterized by its corresponding beam bunch Δt_{RF}, where Δt_{RF} is defined as :

$$\Delta t_{\text{RF}} = t_{\text{beam tagger}} - t_{\text{RF}} \tag{4.36}$$

where, t_{RF} is the event time from the final state particles and $t_{\text{beam tagger}}$ is the beam photon time at target.

A sample Δt_{RF} distribution is shown in Figure 4.1, where the central peak at 0 ns represents the events reconstructed using the correct beam bunch (prompt), while peaks on either side represent events assigned to wrong beam bunch (accidentals). Accidentals can also leak into the prompt signal peak. Therefore, the yield contributions due to accidental beam bunches (up to four beam bunches on either side of the prompt peak) are calculated and subtracted from the prompt peak yield. This is done by applying weights on an event-by-event basis. The events corresponding to the prompt peak are given a weight of 1.0, while events corresponding to accidentals are given a weight of $-\frac{1}{8}$ as shown in Figure 4.1.

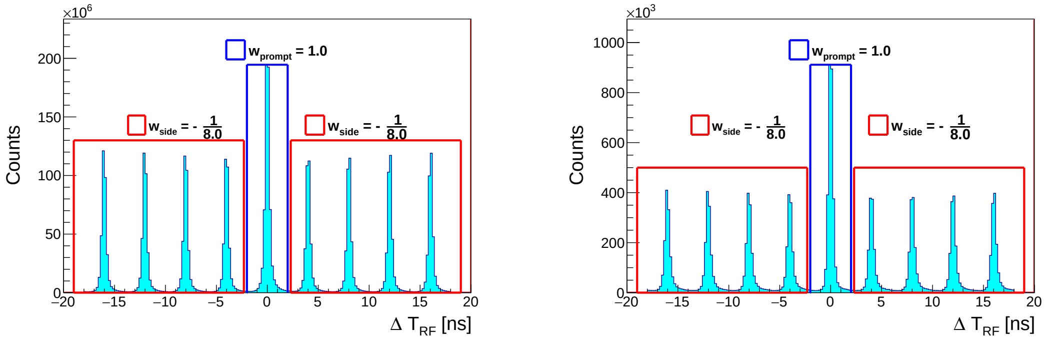

(a) **(b)**

Figure 4.1: Accidental Subtraction of beam bunch based on its RF time. The figure on the left (a) corresponds to GlueX data, and the figure on the right (b) corresponds to Simulated Monte Carlo (MC) sample.

4.4 Stage-II cuts

***t* cuts:** t is defined as the four-momentum transfer squared between the target proton and the recoiling proton as defined in Equation 1.5. A cut on $|t|$ separates different production mechanisms. This has been studied in detail in [57]. Differential cross-section studies show that there are two production mechanisms corresponding to two $|t|$ slope production [57] in the region $0.1 < |t| < 1.0$ and $1. < |t| < 3.0$. Therefore, a cut is made on $|t|$ that is shown in Figure 4.2.

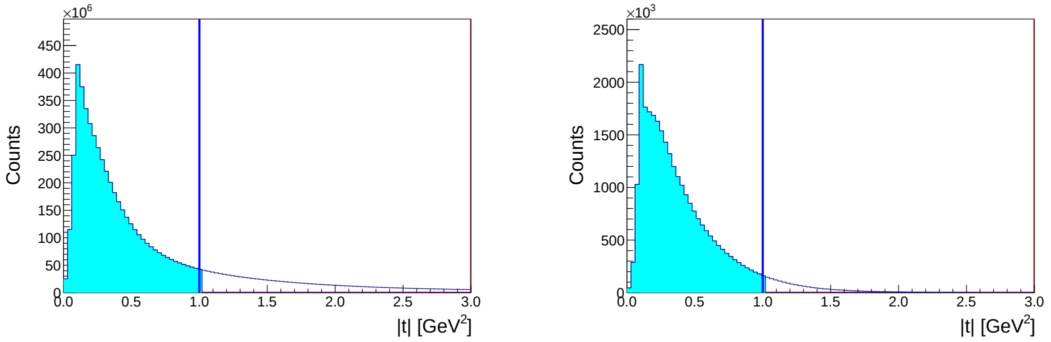

(a) **(b)**

Figure 4.2: $|t|$ Selection cuts. Shaded region in cyan corresponds to the selected $|t|$ region. The plot on the left corresponds to GlueX Phase-I data and the plot on the right corresponds to the Signal MC.

Beam Energy Cut: As mentioned in Chapter 2, GlueX uses a polarized photon beam with its coherent peak energy ranging between 8.2−8.8 GeV. In order to extract the polarization dependence of the physics observables, a cut is placed on this energy range. Signal MC events are also generated only in this beam energy range. The cut is summarized in Figure 4.3.

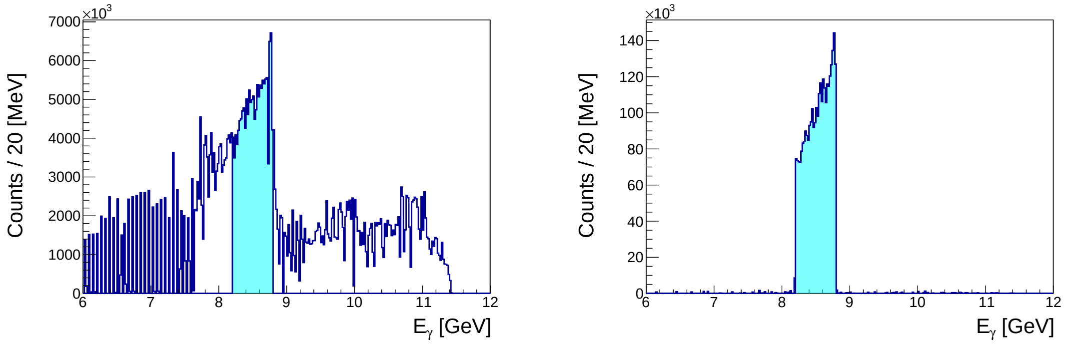

Figure 4.3: Photo beam energy spectrum. The coherent peak region, where polarization is maximum is chosen for PWA. The distribution on the left corresponds to GlueX Phase-I while the distribution on the right corresponds to Signal MC.

Missing Mass square ($M_{\mathbf{Miss}}$) cut: The missing mass squared is defined as

$$MM^2 = (p_\gamma + p_p - \Sigma p_f)^2 \tag{4.37}$$

where, p_γ and p_p are the four momentum of the initial state, *i.e.* the beam photon and the target proton. The p_f refers to the four momenta of the measured final state particles. The distribution peaks around zero as this is an exclusive reaction where all the final state particles are detected. To ensure the purity of the final state, a cut on this quantity is made between $-0.05 < MM^2 < 0.05$ GeV^2. The cut is shown in Figure 4.4.

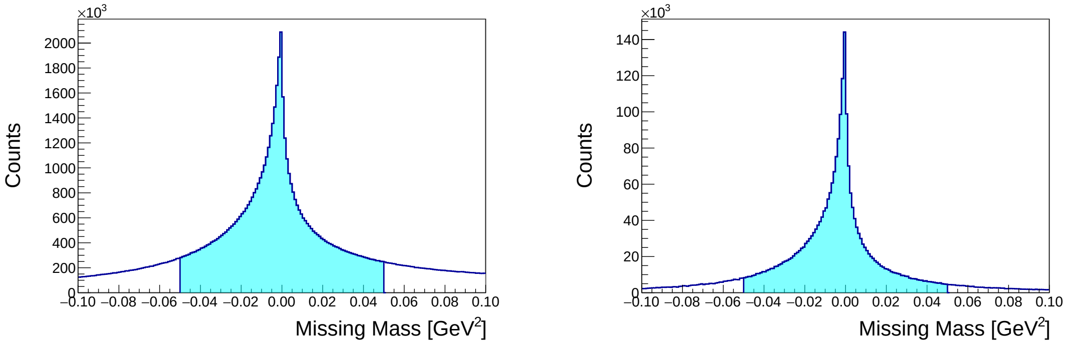

Figure 4.4: Shaded region in cyan corresponds to selection based on Missing Mass squared for photo production of $\omega\pi^0$ events in GlueX. The distribution on the left corresponds to GlueX Phase-I data (left) while the distribution on the right corresponds to the generated Signal MC events.

Confidence Level cuts: In GlueX, the initial state is very well known, with the target proton at rest and the incident photon energy measured to a high precision of roughly $10 - 25$ MeVresolution. Using this information, the resolution of measured tracks and photon showers can further be improved using the process of Kinematic Fitting (KinFit)[58, 59]. In the reaction of interest Equation 1.4, all final state particles momenta and energies are measured, the KinFit is defined as the χ^2 minimization, where χ^2 is the absolute difference between the measured and fitted observables. χ^2 is calculated by solving the system of equation shown in (4.38)

$$\chi^2 = (y_{\text{fit}} - y_{\text{meas}})^T V_y^{-1} (y_{\text{fit}} - y_{\text{meas}}) + 2\lambda^T \mathbf{f} \tag{4.38}$$

where, $y's$ are the measured and the fitted observables and V_y is the covariance matrix of the measured observables y_{meas}, λ is the set of unknown constant Langrangian multipliers and $\mathbf{f}$ is the set of constraint equations to be satisfied. The KinFit varies with the value of each observable to obtain the minimal χ^2. The KinFit used imposes energy-momentum conservation between the initial and final state particles as

$$\vec{p_\gamma} + \vec{p_p} - \Sigma \vec{p_f} = 0 \tag{4.39}$$

In addition to energy and momentum conservation, the KinFit also imposes constraints on particles to come from their parent decay vertex and have a total invariant mass of the parent. This mass constraint is applied to reconstruct π^0 particles from $\pi^0 \to 2\gamma$. However, this constraint is not applied in reconstruction of $\omega \to 3\pi$, since the invariant mass is relatively large, and to minimizing any bias in selection. The quality of the kinematic fit is determined from the χ^2 of the fit formed with the number of degrees of freedom. The following cut is based on KinFit metrics:

$$\begin{aligned} \chi^2/NDF &< 2.25 \\ \text{KinFit CL} &> 0.01 \end{aligned} \tag{4.40}$$

The cut is visually shown in Figure 4.5. This cut has to be examined carefully in future systematic studies.

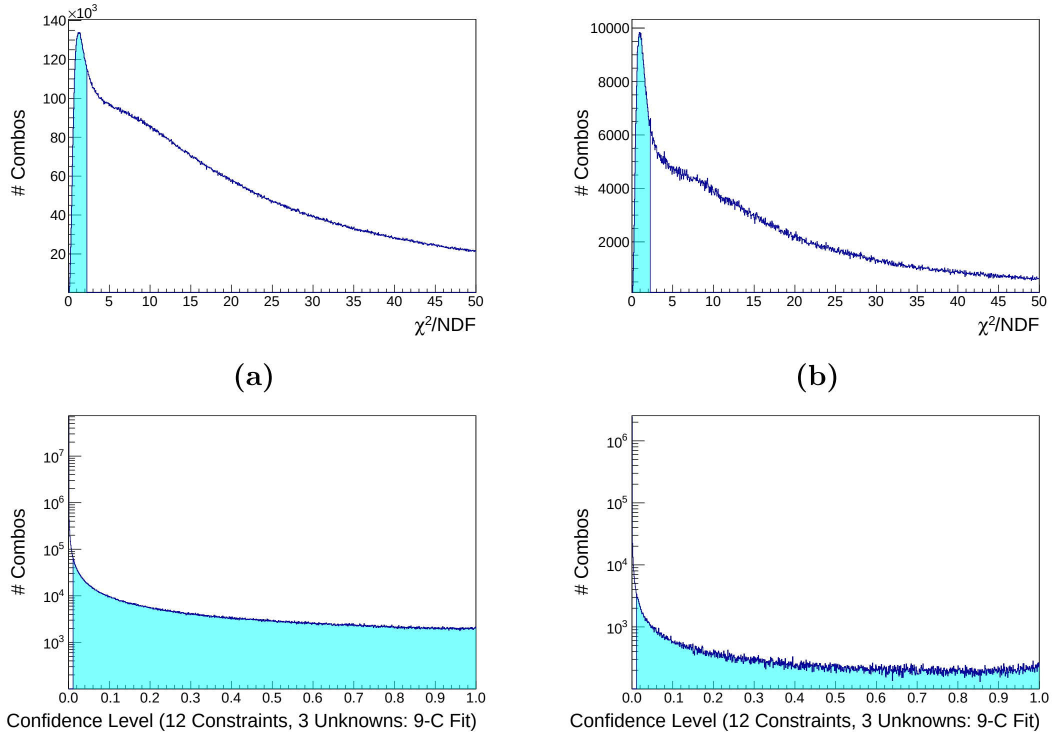

(a) **(b)**

(c) **(d)**

Figure 4.5: Kinematic Fits. The plots in the top row show the χ^2/NDF distribution. Plots in the bottom row show the Confidence level for the same. The shaded region is selected for PWA. Selection is based on kinematic fitting. The distributions on the left correspond to GlueX Phase-I data (left) while the distributions on the right correspond to generated Signal MC events.

4.5 Two-dimensional ω side band subtractions

The final state particles for the photo production reaction of $\omega\pi^0$ at GlueX as in Equation 4.41 has a proton (p) two π^0, and two charge pions $\pi^\pm$. Since there are two neutral pions, one associated with ω decay and the bachelor π^0. A two-dimensional side band subtraction is applied to select the most compelling combinations that make up a $\omega\pi^0$ event.

$$\begin{aligned} \gamma p \ &\rightarrow \omega\ \pi_2^0\ p \\ \omega \ &\rightarrow \ \pi^+\pi^-\pi_1^0 \end{aligned} \tag{4.41}$$

A two-dimensional sideband subtraction is applied on the two possible $\pi^+\pi^-\pi^0$ mass combinations. The two neutral pions π_1^0 and π_2^0 are indexed, then the three pion mass $M_1(3\pi)$ and $M_2(3\pi)$ are formed as shown in Figure 4.6 with $M(\pi^+\pi^-\pi_1^0)$ on x-axis and $M(\pi^+\pi^-\pi_2^0)$ on y-axis. Each combination of $\pi^+, \pi^-, \pi_1^0, \pi_2^0$ is given a weight based on its position in the two-dimensional distribution. If both the invariant masses $M(\pi^+\pi^-\pi_1^0)$ and $M(\pi^+\pi^-\pi_2^0)$ are close to the nominal ω mass of 783 MeV, the invariant mass closer to the PDG[4] ω mass value is chosen. These have a weight of 1.0. This yields the angled shape selection near the ω mass in Figure 4.6. If in a combination, the invariant mass $M(\pi^+\pi^-\pi_1^0)$ falls in the range of ω mass and invariant mass of $M(\pi^+\pi^-\pi_2^0)$ is outside the range of ω mass, then the combination is given a weight of 1.0. If in a combination, the invariant mass $M(\pi^+\pi^-\pi_1^0)$ falls in the side band region of ω mass, are given a weight of -0.5. If in a combination, both the invariant masses of $M(\pi^+\pi^-\pi_1^0)$ and $M(\pi^+\pi^-\pi_2^0)$ falls in the side band region of ω mass, then the combination is given a weight of -0.625. Finally, combinations having $M(\pi^+\pi^-\pi_2^0)$ in the ω region are removed (weight of 0.0). This weighting, allows us to estimate the number of near true $\omega\pi^0$ events while removing effectively the non-ω background.

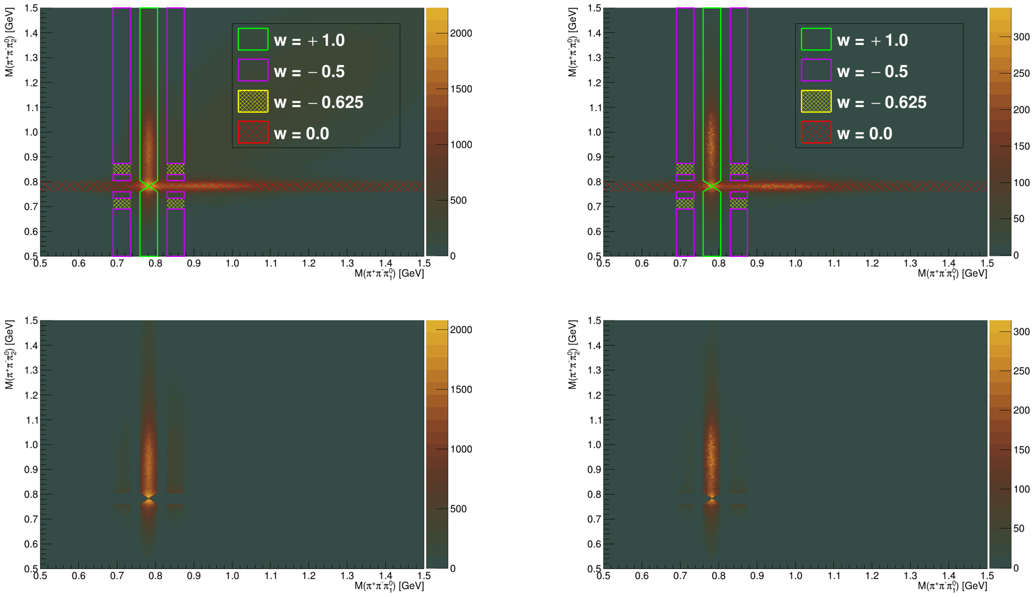

Figure 4.6: Two-dimensional side band subtraction to account for ω events. The top row shows various weights being applied in two-dimensional ω distribution. The bottom row shows the two-dimensional ω distribution after subtractions. The plots on the left correspond to GlueX Phase-I data while the plots on the right correspond to Signal MC events. The subtraction scheme is adapted from [60].

4.6 Distributions after cuts

The weights for every event are applied in the following way. For each combination that passes all the selection cuts, a weight is assigned which is defined as the product of the accidental weight factor and two-dimensional ω weight factor (AccWeight × omega2DWeight) where AccWeight is Accidental subtraction from Section 4.3 and omega2DWeight is the two-dimensional omega side band subtraction from Figure 4.6. When creating the input for the fitting software (AmpTools [61]), these weights are also written for each combination. These weights are used by AmpTools to effectively account for 4π events while performing PWA.

In order to demonstrate the effective signal selection from data, mass distribution of reconstructed π^0 and 4π events as a function of various cuts are summarized in Figure 4.7 and Figure 4.8.

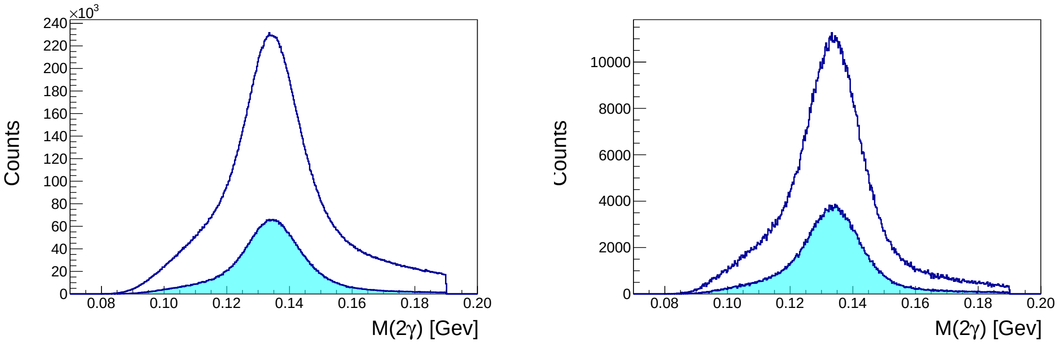

Figure 4.7: The measured invariant mass of the two final state photons before and after the kinematic fit. The plot on the left corresponds to the GlueX Phase-I while the plots on the right correspond to Signal MC events.

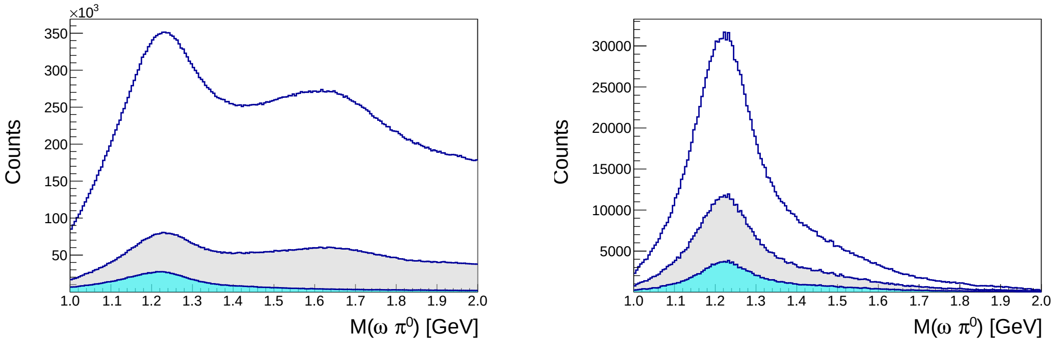

Figure 4.8: The invariant mass of the $\omega\pi^0$ state at various analysis cuts. The unshaded distribution corresponds to mass of $\omega\pi^0$ after χ^2/NDF cut. The gray-shaded region corresponds to $M(\omega\pi^0)$ distribution after the accidental subtraction, and finally, the cyan-shaded region corresponds to $M(\omega\pi^0)$ distribution after the two-dimensional ω cut. Each distribution is made with incremental cuts. The plot on the left corresponds to the GlueX Phase-I data while the plot on the right corresponds to Signal MC events.

4.7 Angular distribution of $\omega\pi^0$ events

With all the data selection made, one can compute the angular distribution of $\omega\pi^0$ in its helicity frame as discussed in Section 1.2.1. One can plot the five decay angle distributions. The five-dimensional intensity is then used in the Partial Wave Analysis (PWA) model and is fit using `AmpTools` which will be discussed in the next chapter. The effect of the detector acceptance and data analysis cuts made can be seen in Figure 4.9. Phasespace MC is generated and is compared to the same after detector acceptance and data analysis cuts to extract efficiency.

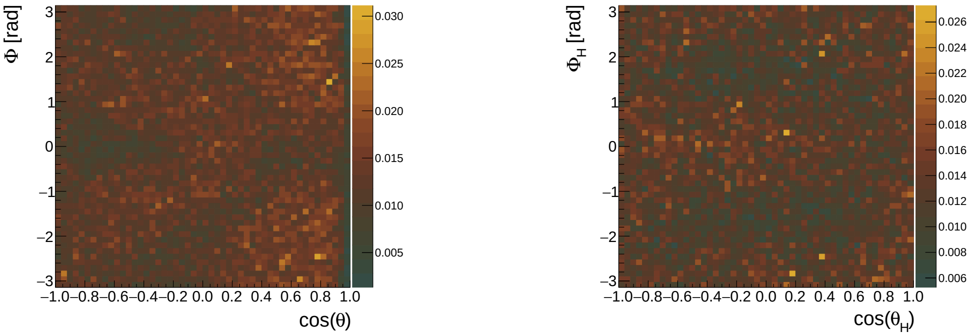

Figure 4.9: Efficiency of data analysis cuts and detector acceptance on helicity angles. The generated phasespace sample has flat distribution in all the decay angles. This efficiency motivated to generate a phasespace MC sample which is at least 10 times larger for performing PWA.

In this chapter a detailed explanation on data selections was presented, effectively selecting out $\omega\pi^0$ events. Once the event selections are made, the distribution of intensity in the five-dimensional decay angles, namely $[\theta, \theta_H, \Phi, \Phi_H, \Phi_{\text{prod}}]$ are computed. Figure 4.10 shows the angular distribution for GlueX Phase-I data and Signal MC samples after all selection cuts.

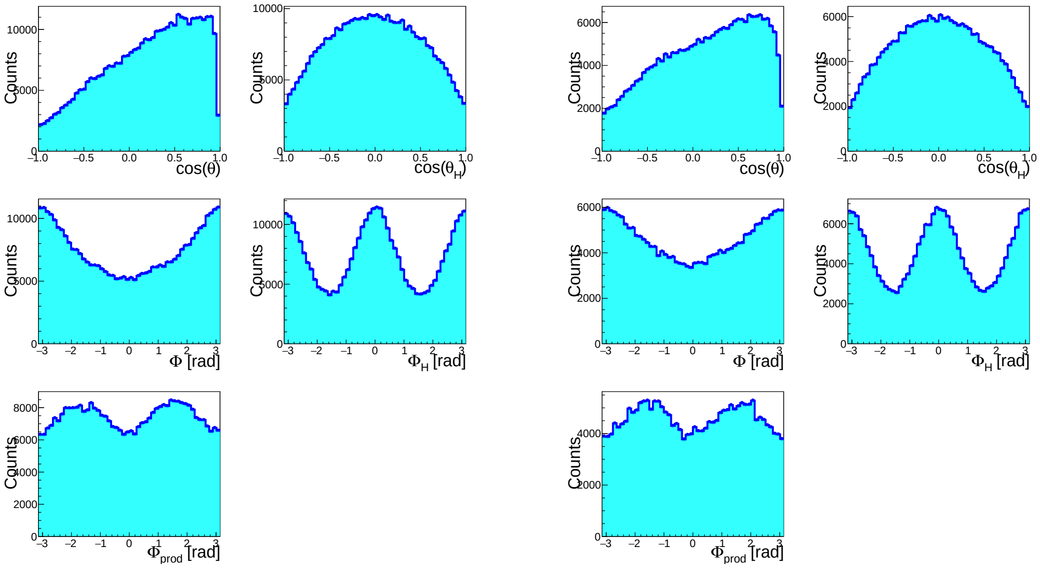

(a) **(b)**

Figure 4.10: Plots of angular distribution of $\omega\pi^0$ events in its helicity frame. The figure on the left corresponds to the GlueX Phase-I data while the figure on the right corresponds to Signal MC events. The five angles namely, $[\theta,\, \theta_H,\, \Phi,\, \Phi_H,\, \Phi_{\text{prod}}]$ are plotted in each of the figure. $[\theta,\, \theta_H]$ are plotted as $\cos(\theta)$ and $\cos(\theta_H)$. The distribution in five dimensions is then fit according to the PWA model discussed in Section 1.3.

Chapter 5

Partial Wave Analysis of $\omega\pi^0$ system at GlueX

5.0.1 Extended Unbinned Maximum Likelihood fitting

The amplitude analysis model that was discussed in Section 1.3 serves as the model to be fit to the observed GlueX Phase-I data. The amplitude analysis model can be expressed as a function of x (observables) i.e. $\vec{x}(\theta, \Phi, \theta_H, \Phi_H)$ and containing m parameters θ i.e. complex production parameters. Extended unbinned maximum likelihood fitting builds upon the fundamental principles of maximum likelihood estimation (MLE). Maximum Likelihood fitting optimizes to obtain the best estimates for the values of parameters θ, and does so by searching the m-dimensional parameter space for the value that maximizes the likelihood. In the case of unbinned data, each individual data point contributes to the likelihood function without any prior grouping or discretization. The likelihood function is constructed based on a chosen probability distribution function (PDF) that represents the underlying distribution of the continuous data. The likelihood function is a product of individual probabilities associated with each data point, reflecting the assumption of independence among the data. For a data sample containing N samples, the extended maximum likelihood as a function of its parameter can be written as

$$\mathcal{L} = \frac{e^{-\mu}\mu^N}{N!} \prod_{i=1}^{N} \mathcal{P}(\mathbf{x_i}; \theta) \tag{5.42}$$

where, $\mathcal{P}$ is the n-dimensional probability density. One can express the probability density $\mathcal{P}$ in terms of total number of observed events in terms of the intensity ($\mathcal{I}(\mathbf{x} : \theta)$) and the efficiency ($\eta(\mathbf{x})$). Intensity ($\mathcal{I}$) is defined as the total number of signal events per unit phase space and efficiency (η) is defined as the efficiency for observing events in x observable space. The relation between probability density, intensity, and efficiency is written as

$$
\begin{aligned}
\mathcal{P}(\mathbf{x}:\theta) &= \frac{1}{\mu}\mathcal{I}(\mathbf{x}:\theta)\eta(\mathbf{x}) \\
\mu &= \int \mathcal{I}(\mathbf{x}:\theta)\eta(\mathbf{x})d\mathbf{x}
\end{aligned}
\tag{5.43}
$$

where μ is the total number of observed events predicted by the model from the set of θ parameters. One can now minimize the likelihood for the probability density using the unbinned extended maximum likelihood technique. This happens to be useful in selecting the most significant model which will be explained in Section 5.2. Substituting the probability density function in Equation 5.42 with Equation 5.43, $-2\ln\mathcal{L}$ becomes

$$
-2\ln\mathcal{L}(\theta) = -2\left(\sum_{i=1}^{N}\ln\mathcal{I}(\mathbf{x};\theta) - \mu\right) + c_1 \tag{5.44}
$$

For the photo production of $\omega\pi^0$ at GlueX, there are five observables $x = (\theta, \theta_H, \phi, \phi_H, \Phi)$ as shown in Figure 4.10, which are encoded in a five-dimensional vector, to describe the intensity distribution. To normalize the probability density, the integral μ has to be computed. Since computing the integral analytically is not possible, a Monte Carlo integration is done over a uniform distribution in the multi-dimensional phasespace that spans the domain of the intensity function. This sample will be referred to as 'phasespace' MC. For a sample size of M_g generated phasespace Monte Carlo events, the average integral value can be computed as

$$
\left\langle\mathcal{I}(\mathbf{x};\theta)\eta(\mathbf{x})\right\rangle = \frac{1}{M_g}\sum_{i=1}^{M_a}\mathcal{I}(\mathbf{x};\theta) \tag{5.45}
$$

where, M_a is the size of the accepted phasespace Monte Carlo after detector acceptance, and M_g is the total number of generated phasespace. Using the ratio of $\frac{M_a}{M_g}$ in various bins of phasespace, the total acceptance is computed and corrected for when presenting the results.

One can now plug in the intensity function given in Equation 1.28 from Section 1.3.1 with different $[J^i]_m^{(\epsilon)}$ as its fit parameters (θ). An example of this will be discussed in Section 5.1.

5.0.2 AmpTools

The software package used for this maximum likelihood fitting is called AmpTools (`AmpTools`), developed by the group at Indiana University with amplitudes written in GlueX software `halld_sim` repository [61].

5.0.3 Phasespace Monte Carlo

To compute the numerical integrals describe above, a sample of phasespace MC was generated through the GlueX reconstruction pipeline with and without acceptance effects. Information about the phasespace samples generated for the study is summarized in Table 5.1.

Run Period	**Spring 2017**	**Spring 2018**	**Fall 2018**	**Total**
Events generated	50M	150M	100M	300M

Table 5.1: Summary of generated phasespace MC events for analyzing GlueX Phase-I Data / Signal MC. The phasespace was generated with a t-slope of 3 GeV^2 to approximately match the data.

`AmpTools` takes as input both the generated phasespace MC with and without acceptance effects to account for acceptance correction as described in Equation 5.45.

5.0.4 Error Estimation

`AmpTools` uses the `MINUIT` [62] package for its minimization. In `MINUIT`, the errors on each parameter are the amount of variation in the parameter that increases $-2\log\mathcal{L}(\theta)$ by 1, which corresponds to a 1σ Gaussian uncertainty variation. Various studies [30, 57] using `AmpTools` in a high dimensional parameter space have reported that it consistently underestimates the errors on each of the fit parameters. The fit results reported in this dissertation have errors estimated using an independent parameter scan. However, it is found that in most cases, the errors returned by `MINUIT` and independent parameter scans are consistent with one another in most cases[1]

5.1 The Intensity Model for polarized $\omega\pi^0$ photoproduction

The intensity ($I(\Omega, \Omega_H, \Phi_{\text{prod}})$) from Equation 1.28 describes the PWA model to explain the intensity of $\omega\pi^0$ events in its helicity frame. For ease of reference, the equation is once again written here:

$$\begin{aligned} I(\Phi,\Omega,\Omega_H) = 2\kappa \sum_k \\ \Bigg\{ (1-P_\gamma)\left[\Big| \sum_{i_N,m} [J_i]^{(-)}_{m,k} \mathfrak{Im}(Z) \Big|^2 + \Big| \sum_{i_N,m} [J_i]^{(+)}_{m,k} \mathfrak{Re}(Z) \Big|^2 \right] \\ +(1+P_\gamma)\left[\Big| \sum_{i_N,m} [J_i]^{(+)}_{m,k} \mathfrak{Im}(Z) \Big|^2 + \Big| \sum_{i_N,m} [J_i]^{(-)}_{m,k} \mathfrak{Re}(Z) \Big|^2 \right] \end{aligned} \tag{5.46}$$

---

[1] There is a discrepancy between `MINUIT` reported errors on fit fraction on various J^{PC} and independently extracted errors on fit fraction. This variation is well within 5%.

`AmpTools`, minimizes $-2\ln(\mathcal{L})$ for the intensity $\mathcal{I}(\mathbf{x};\theta)$. The parameters θ in the `AmpTools` when applied to the intensity of $\omega\pi^0$ events corresponds to the complex production parameters $[J_i]_m^{(\epsilon)}$ in the above Equation 5.46. The intensity is described in a $\mathbf{x}$ dimensional space, spanned by $\mathbf{x} = [\Omega(\theta,\Phi), \Omega_H(\theta_H,\Phi_H), \Phi_{[\text{prod}]}]$.

One can use `AmpTools` to compute the parameters ($\theta = [J_i]_m^{(\epsilon)}$) that best describe the intensity observed in its five decay angles. For a given range in $M(\omega\pi^0)$, t and Beam Energy (E_γ), a set of waves with various J^{PC} states are fit using `AmpTools` to extract the production parameters for various J^{PC} states in these bins. The possible quantum numbers for the b_1 state are summarized below in Table 5.2.

$J^{PC} = 1^{+-} b_1(1235)$	Both reflectivity ($\epsilon = [-1,+1]$)
l up to $l = 2$	S, D-wave
$m = [-J, J]$	$[-1, 0, 1]$

Table 5.2: Table summarizing the quantum numbers for $J^{PC} = 1^{+-}$ state encoded in `AmpTools`

The intensity for this waveset $[1^{+-}]^{(\pm)}$ in `AmpTools` is given as:

$$\begin{aligned}\mathcal{I}(\Phi,\Omega,\Omega_H) = 2\kappa\Bigg\{(1-P_\gamma)\Bigg[&\Big|\sum_{m=-1,0,1}[1^+(S)]_m^{(-)}\mathfrak{Im}(Z_m^{(S)}) + [1^+(D)]_m^{(-)}\mathfrak{Im}(Z_m^{(D)})\Big|^2 \\ &+\Big|\sum_{m=-1,0,1}[1^+(S)]_m^{(+)}\mathfrak{Re}(Z_m^{(S)}) + [1^+(D)]_m^{(+)}\mathfrak{Re}(Z_m^{(D)})\Big|^2\Bigg] \\ +(1+P_\gamma)\Bigg[&\Big|\sum_{m=-1,0,1}[1^+(S)]_m^{(+)}\mathfrak{Im}(Z_m^{(S)}) + [1^+(D)]_m^{(+)}\mathfrak{Im}(Z_m^{(D)})\Big|^2 \\ &+\Big|\sum_{m=-1,0,1}[1^+(S)]_m^{(-)}\mathfrak{Re}(Z_m^{(S)}) + [1^+(D)]_m^{(-)}\mathfrak{Re}(Z_m^{(D)})\Big|^2\Bigg]\Bigg\}\end{aligned} \tag{5.47}$$

The amplitudes between S and D waves are constrained since the ratio between these is well defined as the property of the decay for 1^{+-} state [21, 26]. Therefore, the total number of parameters corresponding to D-wave can be reduced further.

5.1.1 Encoding of the DS ratio

As mentioned, ratio of D to S wave amplitudes (`dsratio`) is defined as a "scale factor" as a fit parameter which can take a value between 0 to 1. The ratio scales the amplitudes between S and D amplitudes and is referred to as `dsratio`. There could also be a phase between the S and D wave parameters defined as ϕ_{D-S}. The Equation 5.47 now reduces to:

$$\begin{aligned}\mathcal{I}(\Phi,\Omega,\Omega_H) = 2\kappa\Bigg\{ (1-P_\gamma)\Bigg[& \Bigg|\sum_{m=-1,0,1}[1^+(S)]^{(-)}_m\Bigg(\mathfrak{Im}(Z^{(S)}) + D/S\ e^{i\phi_{D-S}}\mathfrak{Im}(Z^{(D)})\Bigg)\Bigg|^2 \\ & + \Bigg|\sum_{m=-1,0,1}[1^+(S)]^{(+)}_m\Bigg(\mathfrak{Re}(Z^{(S)}) + D/S\ e^{i\phi_{D-S}}\mathfrak{Re}(Z^{(D)})\Bigg)\Bigg|^2\Bigg] \\ +(1+P_\gamma)\Bigg[& \Bigg|\sum_{m=-1,0,1}[1^+(S)]^{(+)}_m\Bigg(\mathfrak{Im}(Z^{(S)}) + D/S\ e^{i\phi_{D-S}}\mathfrak{Im}(Z^{(D)})\Bigg)\Bigg|^2 \\ & + \Bigg|\sum_{m=-1,0,1}[1^+(S)]^{(-)}_m\Bigg(\mathfrak{Re}(Z^{(S)}) + D/S\ e^{i\phi_{D-S}}\mathfrak{Re}(Z^{(D)})\Bigg)\Bigg|^2\Bigg]\Bigg\}\end{aligned} \tag{5.48}$$

This set of amplitudes of the waveset contains a total of 14 free parameters (NPAR) to be fit against the observed intensity distribution. In principle, the `dsratio` ratio should be consistent across all reflectivites and spin projections (m) that contribute to the b_1. However, one can use scale factors for six different D/S ratios across different reflectivites and spin projections (m). In theory, all the six ratios extracted must have the same value.

Extending the procedure, more J^{PC} states can be added to form more complex wavesets. Various combinations of wavesets then can be used to fit the PWA model.

5.1.2 Mass Independent fits

Performing fits in a model-independent manner is always preferred since it makes minimal assumptions about the structure of data in various angular bins. The fits are performed assuming no dependence in mass $M(\omega\pi^0)$. The data is split into various bins in $\omega\pi^0$ mass and will be fit individually, without including a mass dependence in fitting the PWA model. This allows extraction from individual partial waves contributing to the overall decay of the $\omega\pi^0$ system without making prior assumptions about properties such as the resonance masses and decay widths of possible mesonic states decaying into $\omega\pi^0$. However, independent fits have proven to be unstable when including higher spin states and are extremely sensitive to the wavesets used in the fit. The stability of the fits also, depends on the mass binning of $M(\omega\pi^0)$. However, throughout this dissertation, mass-independent fits are only considered and were used to perform PWA fits. This will be revisited in future analyses.

5.2 Model selection strategy

Selecting the ‘ideal’ set of waves $[J^{PC}]_m^{(\epsilon)}$ is one of the most challenging steps in performing a Partial Wave Analysis (PWA). In principle, the sum over partial waves amplitudes is an infinite sum, and all partial waves that are physically allowed should be included during fitting. However, for practical reasons only a finite subset of physically allowed partial waves are usually considered for fitting. The choice of wavesets is mainly motivated by the underlying physics. In spite of the physics intuition in selecting the waves, the choice of wavesets is still not unique. To select the most significant set of wavesets statistical methods have to be used to compare among different waveset models. Methods used to compare various wavesets are summarized below.

5.2.1 Likelihood Ratio Test (LRT)

LRT is a statistical method used to compare the goodness of fit between two nested statistical models. It is commonly employed in hypothesis testing to assess whether a more complex model significantly improves the fit compared to a simpler model.

A general recipe of how the LRT is performed for selecting the most significant waveset is summarized below:

1. Formulate two competing models: The null model (model having the least number of wavesets that best describe the data) and the alternative model (more complex model having a larger number of wavesets or more free parameters to fit). The null model is usually a special case or a simplified version of the alternative model.

2. Estimate the model parameters: For both the null and alternative models, estimate the parameters by minimizing $-2\ln\mathcal{L}(\mathbf{x};\theta)$. This term is referred to as NLL.

3. Compute the LRT statistic: The LRT statistic is calculated by comparing the

NLL of the two models. It is the difference in the logarithm of the likelihoods between the alternative and null models per increase in the number of free parameters. Mathematically, it can be expressed as

$$LRT = \frac{\Delta NLL}{\Delta NPAR} = \frac{NLL_{\text{alternate}} - NLL_{\text{null}}}{NPAR_{\text{alternate}} - NPAR_{\text{null}}} \tag{5.49}$$

4. Determine the statistical significance: The increase in LRT greater than 1 would mean that the alternative model contributes significantly to improving the fit result and has to be considered. The model with the greatest significance will have the largest LRT with respect to the null model.

The LRT allows for model selection by providing a formal statistical framework to compare and evaluate different models based on their goodness of fit to the observed data.

5.2.2 Akaike Information Criterion (AIC)

Akaike Information Criterion (AIC) is a statistical measure used for model selection and comparison. It was developed by the Japanese statistician Hirotugu Akaike [63]. The AIC provides a way to balance the goodness of fit for a model and its complexity, helping to identify the most appropriate model among a set of competing models.

The AIC is based on the concept of information theory and the principle of parsimony, which favors simpler models. It takes into account both the quality of fit and the number of parameters in a model, penalizing overly complex models that may overfit the data. The aim is to find a model that provides a good fit while avoiding unnecessary complexity.

The formula for AIC is as follows:

$$\mathrm{AIC} = \frac{2 \times \mathrm{NLL} + 2 \times \mathrm{NPAR}}{N} \tag{5.50}$$

where, NLL is the Negative Log Likelihood for minimization, NPAR is the number of free parameters in the fit, lastly, N is the total number of events used in fitting. The normalization with the significantly large N makes even a small decrease in AIC proving its significance.

The AIC value can be interpreted as a measure of the relative amount of information lost by the model. Lower AIC values indicate better-fitting models with a better balance between fit and complexity. Thus, the model with the lowest AIC value is often selected as the most appropriate model among the options considered.

When comparing models using AIC, it is essential to use the same dataset and the same type of analysis for consistency. Different models can be compared by calculating their respective AIC values and selecting the model with the lowest value. The difference in AIC values between models can also provide insight into the relative strength of evidence for one model over another. A difference of 2 or more in AIC values is generally considered as substantial evidence in favor of the model with the lower AIC.

However, it's important to note that the AIC is not an absolute measure of model quality. It is a relative measure for model comparison within a specific dataset. Furthermore, the AIC does not provide information about the validity of the assumptions underlying the models or the appropriateness of the chosen variables.

5.2.3 Bayesian Information Criterion (BIC)

BIC, also known as the Schwarz criterion, is a statistical measure used for model selection and comparison [64]. Similar to the Akaike Information Criterion (AIC), the BIC provides a way to balance the goodness of fit and the complexity of a model. However, the BIC applies a stronger penalty for model complexity than the AIC.

The BIC is based on Bayesian principles, which favors simpler explanations when multiple competing explanations are possible. It addresses the trade-off between model complexity and fit by considering both the likelihood of the data given the model and the number of parameters in the model.

The formula for BIC is as follows:

$$\mathrm{BIC} = \frac{2 \times \mathrm{NLL} + 2 \times \ln(N) \times \mathrm{NPAR}}{N} \tag{5.51}$$

Similar to the AIC, lower BIC values indicate better-fitting models with a better balance between fit and complexity. However, the BIC tends to prefer simpler models more strongly than the AIC. This preference for simplicity is reflected in the stronger penalty term, $\ln(N)$, which increases with larger sample sizes. Consequently, the BIC is more likely to select a model with fewer parameters compared to the AIC.

When comparing models using the BIC, the model with the lowest BIC value is generally preferred as the most appropriate model among the options considered. As with the AIC, the difference in BIC values between models can provide insights into the relative strength of evidence for one model over another.

However, like the AIC, it is important to note that the BIC is not an absolute measure of model quality. It is a relative measure for model comparison within a specific dataset and analysis. Additionally, the BIC does not assess the validity of underlying assumptions or the appropriateness of chosen variables.

5.3 Signal MC generation

In order to test the developed PWA model, a test sample has to be created with well known initial conditions. Various Input/Output (`I/O`) checks can then be performed on the data sample to ensure that the fit procedure consistently result with what was initially generated. A Signal Monte Carlo (MC) model sample was generated using the wavesets found in Table 5.3 and the relative strength of the amplitudes was based on a preliminary fit to the GlueX Phase-I data with the same model. The S and D wave decays of the 1^+ wave are constrained to have a `dsratio` of 0.27 across all spin projections m. Also, the states 1^+ and 1^- are generated such that they have non zero amplitudes only for positive reflectivites ($[1^+, 1^-]^+$). 1 Million signal events were generated using an event generator that includes appropriate beam properties, final state kinematics and angular distributions and is passed through the GlueX reconstruction software in order to account for detector response. The Signal MC was made to roughly match the distribution seen in GlueX data. This can be verified visually in Figure 4.10 from Section 4.7. The exact values of parameters used for generating Signal MC is shown in Table B.1 in Appendix B.2.1. This Signal MC sample can now be tested by fitting various combinations of wavesets to assess the effect of fitting with more waves that were not part of the Signal MC generation. The model selection strategy that will allow to choose the most significant set of waves to describe this distribution must converge to exactly the same set of waves that were used to generate the Signal MC. This serves as a robust `I/O` check for the fit methodology. Figure 5.1 shows the angular distribution along with the Mass distribution of $M(\omega\pi^0)$ for the Signal MC events.

J^P	Name	Mass [GeV]	Width(Γ) [GeV]	l	m	Refl (ϵ)	D/S	ϕ_{D-S}
1^+	b_1	1.229	0.142	0, 2	-1, 0, 1	+	0.27	0
1^-	$\rho(1450)$	1.465	0.400	1	-1, 0, 1	+	N/A	N/A

Table 5.3: Properties of Signal MC events. Refl refers to the reflectivity of the J^{PC} state. The ρ has a possible decay to 4π topology as reported in [65].

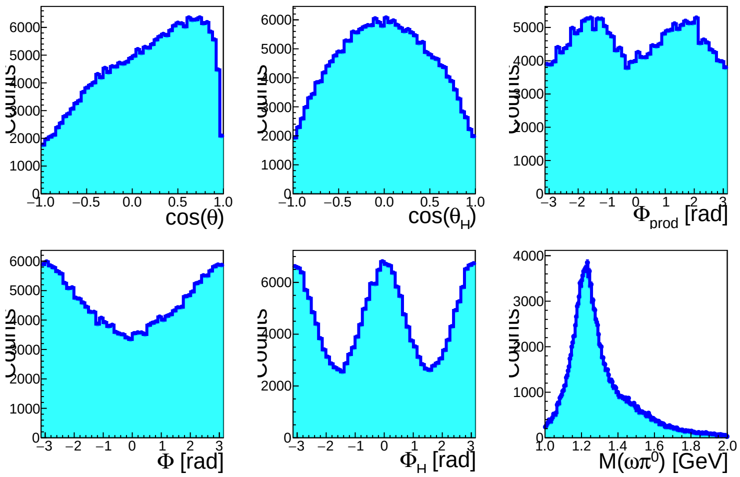

Figure 5.1: Angular distribution and mass distribution for Signal MC events. Data is binned in bins of $M(\omega\pi^0)$ and will be fit using PWA containing a set of waves across its mass bins. The data is further split based on its t [GeV^2] value as well. The angular distribution shown in the figure correspond to a slice of $M(\omega\pi^0)$ with its mean at b_1 mass and width within Γ(140) MeV.

5.4 Validating fit methodology using Signal MC

In order to validate the fit procedure, the signal MC is fit with combinations of wavesets. To extract effective contribution of a $[J^{PC}]^{(\epsilon)}$, the results are presented in terms of a "fit fraction" for each amplitude used in a fit. Each amplitude has a production coefficient with a real part and its corresponding imaginary part. The "fit fraction" is defined as the total fraction (intensity) contributing to the over all observed intensity for that amplitude. The fit fraction is related to the magnitude of complex fit parameter corresponding to the state. The fit fraction for a given $[J^{PC}]_m^{(\epsilon)}$ is defined as:

$$[\mathrm{FF}_J]^{(\epsilon)} = \frac{[\mathcal{I}_J(\mathbf{x};\theta)]^{(\epsilon)}}{\Big\langle \mathcal{I}(\mathbf{x};\theta)\eta(\mathbf{x}) \Big\rangle} \tag{5.52}$$

where, $[\mathcal{I}_J(\mathbf{x};\theta)]^{(\epsilon)}$ is the intensity of the $[I]^{(\epsilon)J}$ wave as given in Equation 5.46 and the denominator is the total intensity computed in Equation 5.45. In an ideal situation, the fit fraction corresponding to the spin states that were used in generating the signal MC has to match up and any additional waves should have little to no contribution. By performing this systematic fit study, one can evaluate the effect of adding additional waves that are not part of the original event generation. As mentioned before, the overall mass distribution ($M(\omega\pi^0)$) is segmented into 80 MeV wide bins. In each of the bins, 25 independent fits are made each time with randomized starting parameters, and the result with the best minimum NLL is chosen as the final solution in that mass bin. This ensures that no solution is stuck in a local minimum and other local solutions in the parameter space (θ). Therefore, for each of the wavesets tested, fit fractions in each mass bin are extracted and studied in detail. Table 5.4 outlines the various binning followed for this study along with the combinations of waves explored. It is worthwhile to note again that the signal MC was made purely with the waveset $[1^+, 1^-]^+$.

	Range	**Bin Width**	**Number of bins**		
Mass $M(\omega\pi^0)$ [GeV]	1.035 - 1.755	80 MeV	9		
t range [GeV^2]	0.15 - 1.0	(0.15 - 0.30), (0.30 - 0.50), (0.50 - 1.00)	3		
`dphase` ϕ_{D-S}	**0.0**	The value is fixed during fit			
N randomized fits	**25**				
Fit Name	$[J^P]^{(\epsilon)}$	l	m	**Decay**	**NPARS**
`1p`	$[1^+]^{\pm}$	$0(S), 2(D)$	[-1, 0, 1]	$\omega\pi^0$	11
`1p1m`	$[1^+]^{\pm}$	$0(S), 2(D)$	[-1, 0, 1]	$\omega\pi^0$	23
	$[1^-]^{\pm}$	$1(P)$	[-1, 0, 1]	$\pi^0\pi^+\pi^-\pi^0$	27
`0m1p1m`	$[0^-]^{\pm}$	$1(P)$	0	$a_0\pi$	27
	$[1^+]^{\pm}$	$0(S), 2(D)$	[-1, 0, 1]	$\omega\pi^0$	
	$[1^-]^{\pm}$	$1(P)$	[-1, 0, 1]	$\pi^0\pi^+\pi^-\pi^0$	
`1p1m2m`	$[1^+]^{\pm}$	$0(S), 2(D)$	[-1, 0, 1]	$\omega\pi^0$	47
	$[1^-]^{\pm}$	$1(P)$	[-1, 0, 1]	$\pi^0\pi^+\pi^-\pi^0$	
	$[2^-]^{\pm}$	$1(P), 3(F)$	[-1, 0, 1]	$a_{0/2}\pi$	
`1p1mPos`	$[1^+]^{+}$	$0(S), 2(D)$	[-1, 0, 1]	$\omega\pi^0$	13
	$[1^-]^{+}$	$1(P)$	[-1, 0, 1]	$\pi^0\pi^+\pi^-\pi^0$	

Table 5.4: Table summarizing conditions for independent PWA fits for Signal MC

Fit fractions extracted for various J^P states in the five sets of waveset combinations are paneled in Figure 5.2. Each row of plots (from top to bottom) correspond to the different waveset combinations used for fitting. The dominance of $[1^+]^{(+)}$ is evident in the b_1 mass region across all t-bins and across all of the wavesets. In the higher mass region around the $\rho(1450)$ mass $[1^-]^{(+)}$ dominates the fit fraction over all of wavesets. This proves that the fitting procedure is robust in extracting the most dominant states. It can also be seen that, in the waveset `1p1m2m`, the $[2^-]$ states start to contribute in the low mass region which was not part of the generated model and is against intuition. By construction, the PWA model includes a barrier factor [28] as discussed in Equation 1.21 which suppresses contribution from higher l waves in the low mass region. This is due to the multiplicity of solutions. Therefore, a effective way of selecting the most significant waveset has to be deployed.

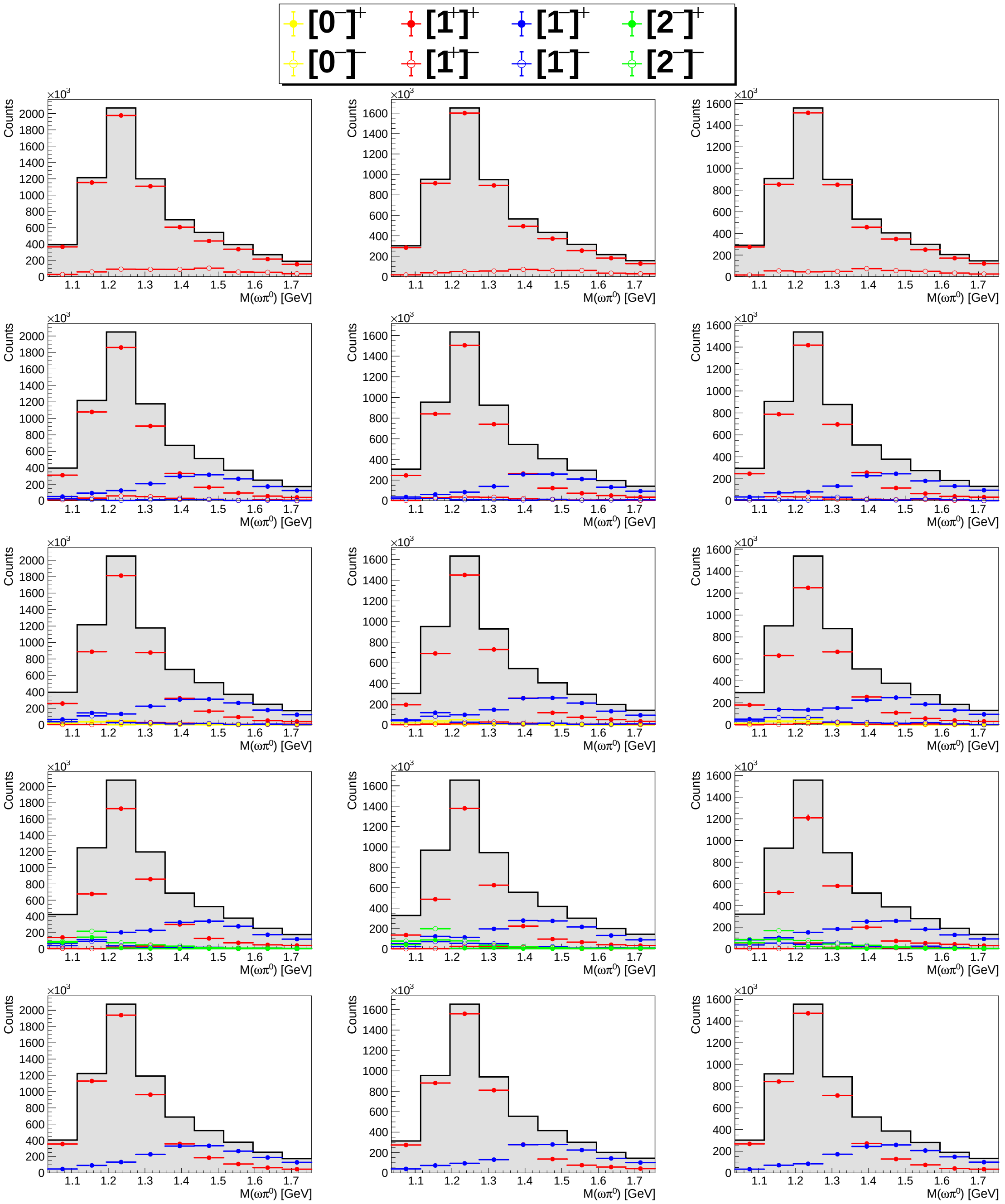

$0.15 < |t| < 0.30$ GeV^2 $\quad$ $0.30 < |t| < 0.50$ GeV^2 $\quad$ $0.50 < |t| < 1.00$ GeV^2

Figure 5.2: Fit Fraction extracted for various J^{PC} in Signal MC. The plots in the three columns corresponds to three t-bins. The plots on each row correspond to various wavesets in the order listed in Table 5.3

5.4.1 Selecting the most significant model

In order to select out the most significant model out of the wavesets used for fitting, the three-model selection criterion was used, namely LRT, AIC and BIC. For each bin in mass and t-range, 25 independent fits are performed for each of the wavesets from Table 5.4 with each fit having randomized initial fit parameters. Since data in each bin have sufficient statistics, LRT will be considered as the most important metric for choosing the most significant model. The waveset `1p` is considered as the null model, the bare minimum model that could describe the angular distribution as shown in Appendix B.1.1. The fit extracted for corresponding J^P state in its angular distribution is shown in Appendix B.1. The metrics, AIC and BIC are minimum for the most significant model. Figure 5.3 shows the results for choosing the most significant model.

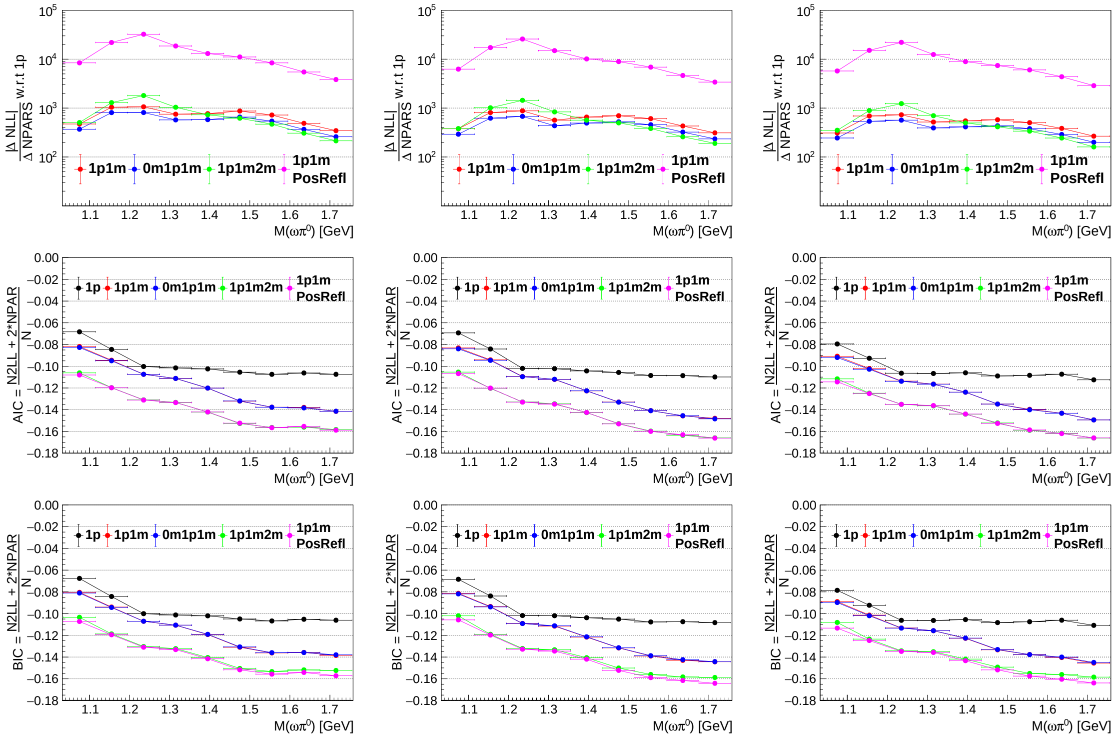

$0.15 < |t| \leq 0.30$ GeV^2 $0.30 < |t| \leq 0.50$ GeV^2 $0.50 < |t| \leq 1.00$ GeV^2

Figure 5.3: The figure summarizes the model selection strategy followed for selecting the most significant model. The figures in the three columns correspond to the three different t bins. The plots on each rows Top row plots shows the LRT with `1p` as its null model, performed across various wavesets. The middle row and third row plots show AIC and BIC for different wavesets throughout the nine mass bins. The results do converge into the original waveset that was used to generate the Signal MC.

It can be seen from the results in Figure 5.3, the following inferences along with its explanation are summarized below

- The increase in Negative Log Likelihood (NLL) for the waveset `1p1mPos` compared to `1p` waveset, is the maximum out of all the explored combinations. It is worth to note that the increase in the number of free parameters for fitting between the `1p1pmPosRefl` (NPARS = 13) and `1p` (NPARS = 11) is ΔNPARS = 2 and is consistently higher than other wavesets throughout the mass and t-bins.

- The increase in NLL especially in the b_1 resonance region is the maximum for `1p1mPos`, clearly favouring the waveset that was originally used for generating the Signal MC. It is to be noted that the absolute NLL between `1p1mPos` and `1p1m2m` is of the same order of magnitude. Even though by increasing the number of free parameters for fitting to NPARS = 47 for the waveset `1p1m2m` with ΔNPARS = 36, the effective increase in the NLL per NPARS is minimal by at least an order of magnitude less than that of `1p1mPos`. This is observed across various t-bins.
- Comparing the AIC and BIC for the various wavesets, `1p1mPos` has the loweset AIC and BIC across all mass bins and across the three t bins. AIC by construction will favour a more complex model but it can be observed that `1p1m2m` being the most complex model performs nearly the same as the `1p1mPos`. It can also be noted that taking into account all the three metrics, it can be concluded that the most significant model is `1p1mPos`, the waveset that was originally used to generate the Signal MC. Hence, the model selection strategy can now be extended to data.

5.4.2 Results for the most significant model `1p1mPos`

After choosing, the most significant model, `1p1mPos` in this case, the parameter `dsratio` can be extracted across all the mass bins. Figure 5.4 shows the fit fractions corresponding to `1p1mPos` along with the extracted `dsratio` across all the mass bins. The extracted `dsratio` in the higher mass bins has larger error due to its decreased dominance relative to the $[1^-]$ $\rho(1450)$. The variations in `dsratio` even though agree within the errors, is extremely sensitive to the waveset being used. Though the extracted `dsratio` is strictly consistent especially in the b_1 mass region ($M(b_1)$). As the mass of $M(\omega\pi^0)$ goes higher, the effective dominance of 1^+ state goes down, and `dsratio` is defined with respect to the amplitudes corresponding to D-wave and S-wave. Therefore, when scaling to the fit fraction, the effective dependence of this ratio gets squared making the measurement very sensitive to statistical fluctuation. The variation in higher mass region has to be studied in detail in future studies.

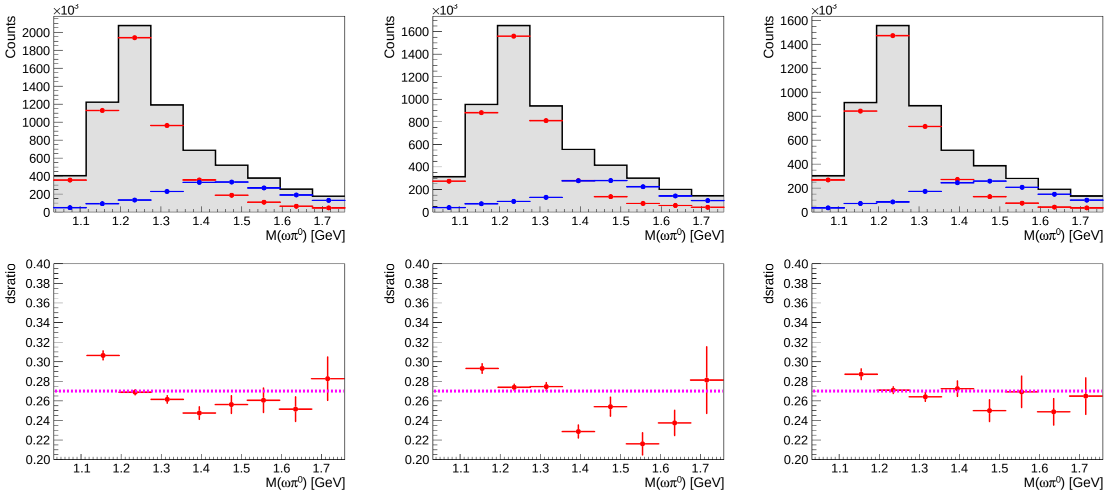

$0.15 < |t| \leq 0.30$ GeV^2 $0.30 < |t| \leq 0.50$ GeV^2 $0.50 < |t| \leq 1.00$ GeV^2

Figure 5.4: The top row of plots shows the fit fractions for in the three t-bins for the most significant model waveset `1p1mPos`. The second row of plots shows the extracted `dsratio` across the mass range in the three t-bins. The magenta line is the `dsratio` with which the Singal MC was generated.

It is not trivial to compare directly the generated and the extracted fit parameters. The extracted fit amplitudes depend on the total number of events (signal) used. Additionally the Signal MC, after passing through the detector response, could have altered the amplitudes. However, one can compare the relative phase between the fit parameters that were initially generated to what is extracted in the end. Comparisons are made between relative phases of extracted fit parameters ($[1^+]^{(+)}(S)$) and $[1^-]^{(+)}$ in Appendix B.2.1.

5.5 PWA fits to GlueX Phase-I data

The PWA model is fit to the full GlueX Phase-I[2] data following to those described for the Signal MC. A total of six combinations of wavesets are explored with increasing complexity. Details of the wavesets are summarized in Table 5.5. It can be seen that by adding higher J^P states, the number of free parameters (NPARS) increases significantly. Therefore, not all the m projections and reflectivities from these higher J^P states are added while fitting. It can be seen that in the waveset combination `1p1m2m2piso`, only positive reflectivity from 2^- and 2^+ are included. Similarly, m projections only up to $m = [-1, 0, 1]$ are included even though for a $2^\pm$ state the possible end projection $m = [-2, -1, 0, 1, 2]$ are possible. This is done mainly because of the fact that their previous experiments [26] have found little significance when including higher m projections. The final set of combinations of waves named 'All allowed J^P waves' contains all possible J^P states up to $J = 3$ and $L = 3$. Also, to restrict the total number of free parameters, only certain reflectivities and m projections for some J^P states are included. Additionally, an isotropic background that does not interfere with any of the other amplitudes in the model is also included. Nevertheless, a more systematic study will be required in the future in individual bins of $M(\omega\pi^0)$ by having more combinations[3] of wavesets to be included, and evaluate other possible contribution.

---

[2] A systematic study was performed to ensure all data periods and orientations yielded results within its statistical precision.

[3] Adding more waves should have strong physics motivation.

	Range	**Bin Width**	**N bins**		
Mass $M(\omega\pi^0)$ [GeV]	1.035 - 1.755	80 MeV	9		
t range [GeV^2]	0.15 - 1.0	(0.15 - 0.30), (0.30 - 0.50), (0.50 - 1.00)	3		
`dphase` ϕ_{D-S}	**0.0**	The value if fixed during fit			
N randomized fits	**25**				
Fit Name	$[J^P]^{(\epsilon)}$	l	m	**Decay**	**NPARS**
`1p`	$[1^+]^\pm$	$0(S), 2(D)$	[-1, 0, 1]	$\omega\pi^0$	11
`1p1m`	$[1^+]^\pm$	$0(S), 2(D)$	[-1, 0, 1]	$\omega\pi^0$	26
	$[1^-]^\pm$	$1(P)$	[-1, 0, 1]	$\pi^0\pi^+\pi^-\pi^0$	
`0m1p1m`	$[0^-]^\pm$	$0(P)$	0	$a_0\pi$	30
	$[1^+]^\pm$	$0(S), 2(D)$	[-1, 0, 1]	$\omega\pi^0$	
	$[1^-]^\pm$	$1(P)$	[-1, 0, 1]	$\pi^0\pi^+\pi^-\pi^0$	
`1p1m2m2piso`	$[1^+]^\pm$	$0(S), 2(D)$	[-1, 0, 1]	$\omega\pi^0$	45
	$[1^-]^\pm$	$1(P)$	[-1, 0, 1]	$\pi^0\pi^+\pi^-\pi^0$	
	$[2^-]^+$	$1(P), 3(F)$	[-1, 0, 1]	$a_{0/2}\pi$	
	$[2^+]^+$	$2(D)$	[-1, 0, 1]	$a_{1/2}\pi, \rho\pi$	
	Isotropic Bkg	Uniform background			
`1p1m2m2p3miso`	$[1^+]^\pm$	$0(S), 2(D)$	[-1, 0, 1]	$\omega\pi^0$	51
	$[1^-]^\pm$	$1(P)$	[-1, 0, 1]	$\pi^0\pi^+\pi^-\pi^0$	
	$[2^-]^+$	$1(P), 3(F)$	[-1, 0, 1]	$a_{0/2}\pi$	
	$[2^+]^+$	$2(D)$	[-1, 0, 1]	$a_{1/2}\pi$	
	$[3^-]^+$	$3(F)$	[-1, 0, 1]	$a_{1/2}\pi$	
	Isotropic Bkg	Uniform background			
All allowed J^P waves	$[0^-]^\pm$	$0(P)$	$0^{(+)}$	$a_0\pi$	77
	$[1^+]^\pm$	$0(S), 2(D)$	[-1, $0^{(+)}$, 1]	$\omega\pi^0$	
	$[1^-]^\pm$	$1(P)$	[-1, $0^{(+)}$, 1]	$\pi^0\pi^+\pi^-\pi^0$	
	$[2^-]^\pm$	$1(P), 3(F)$	[-1, $0^{(+)}$, 1]	$a_{0/2}\pi$	
	$[2^+]^\pm$	$2(D)$	[-1, $0^{(-)}$, 1]	$a_{1/2}\pi$	
	$[3^-]^\pm$	$3(F)$	[-1, $0^{(-)}$, 1]	$a_{1/2}\pi, \rho\pi$	
	$[3^+]^\pm$	$2(D)$	[-1, $0^{(-)}$, 1]	Possible state	
	Isotropic Bkg	Uniform background			

Table 5.5: Table summarizing the conditions for independent PWA fits for GlueX Phase-I data.

The fit fraction corresponding to various combinations as shown in Table 5.5 is shown in Figure 5.5. Each row of plots (from top to bottom) corresponds to different waveset combinations used for fitting. A clear dominanace of $[1^+]^{(+)}$ is evident in the b_1 mass region across all t-bins and across all combinations of wavesets. The dominanace of $[1^+]^{(+)}$ can be seen even when all possible wavesets up to $J^P = 3$ are added in the fit. However, including higher J^P states has a significant effect on the extracted fit fraction of $[1^+]^{(+)}$ state. And as seen in the Signal MC case, higher J^P states having high l give unstable fits especially in the lower mass region of $M(\omega\pi^0)$ due to the multiplicity of solutions. Hence, the model selection strategy discussed and validated using Signal MC case is applied to GlueX Phase-I data.

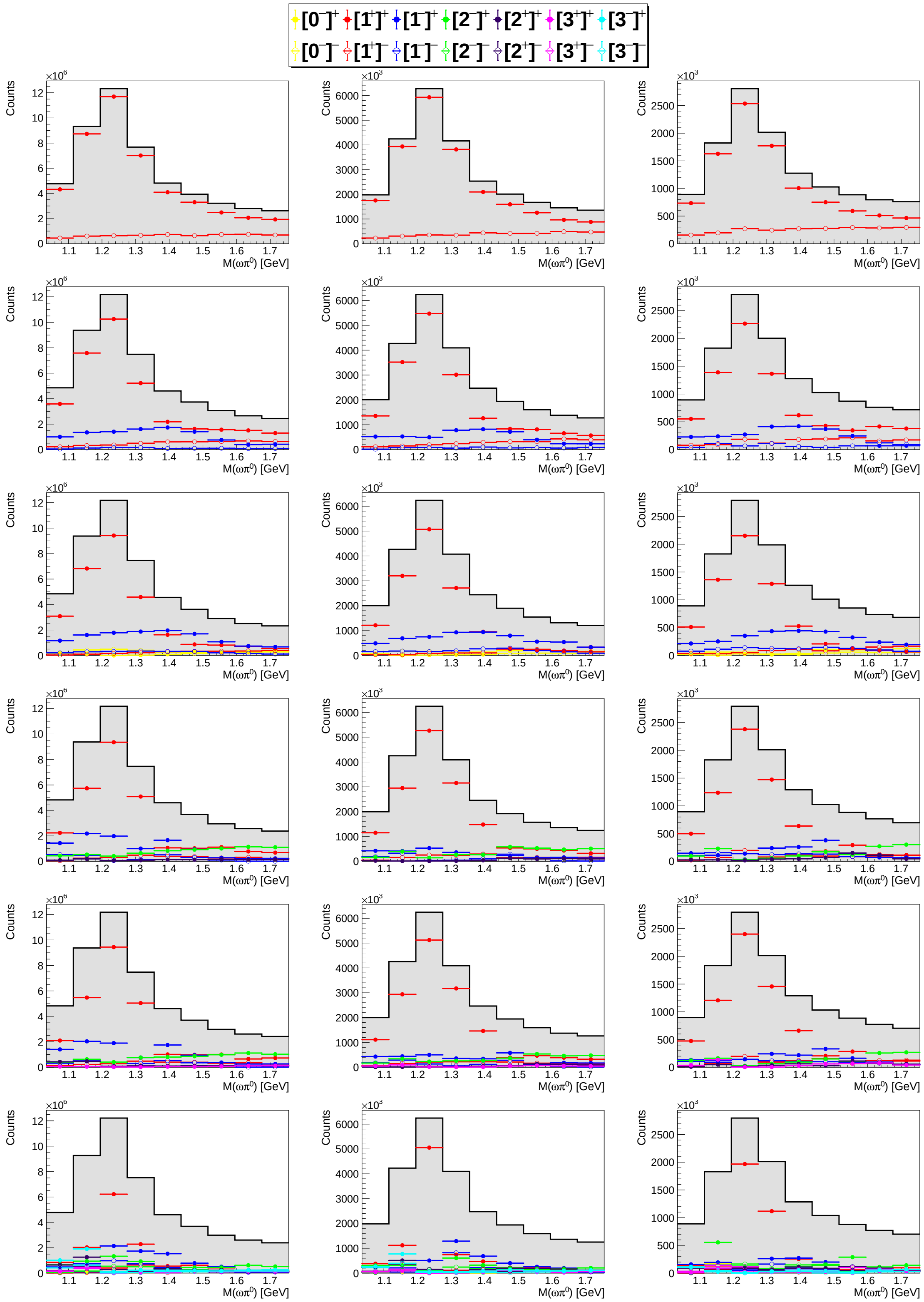

$0.15 < |t| < 0.30$ GeV^2 $\quad$ $0.30 < |t| < 0.50$ GeV^2 $\quad$ $0.50 < |t| < 1.00$ GeV^2

Figure 5.5: Fit Fraction extracted for various J^{PC} in GLUEX Phase-I data. The plots in the three columns correspond to three t-bins. The plots on each row correspond to various wavesets in the order listed in Table 5.5

5.5.1 Model selection for GlueX Phase-I data

The model selection strategy is applied to various combinations of waves. Following a similar procedure to Signal MC, `1p` serves as the null model against which all the other models are evaluated. Also, the angular distributions for each bin in mass and t are also tracked, and summarized in Appendix B.3. Figure 5.6 shows the results for model selection.

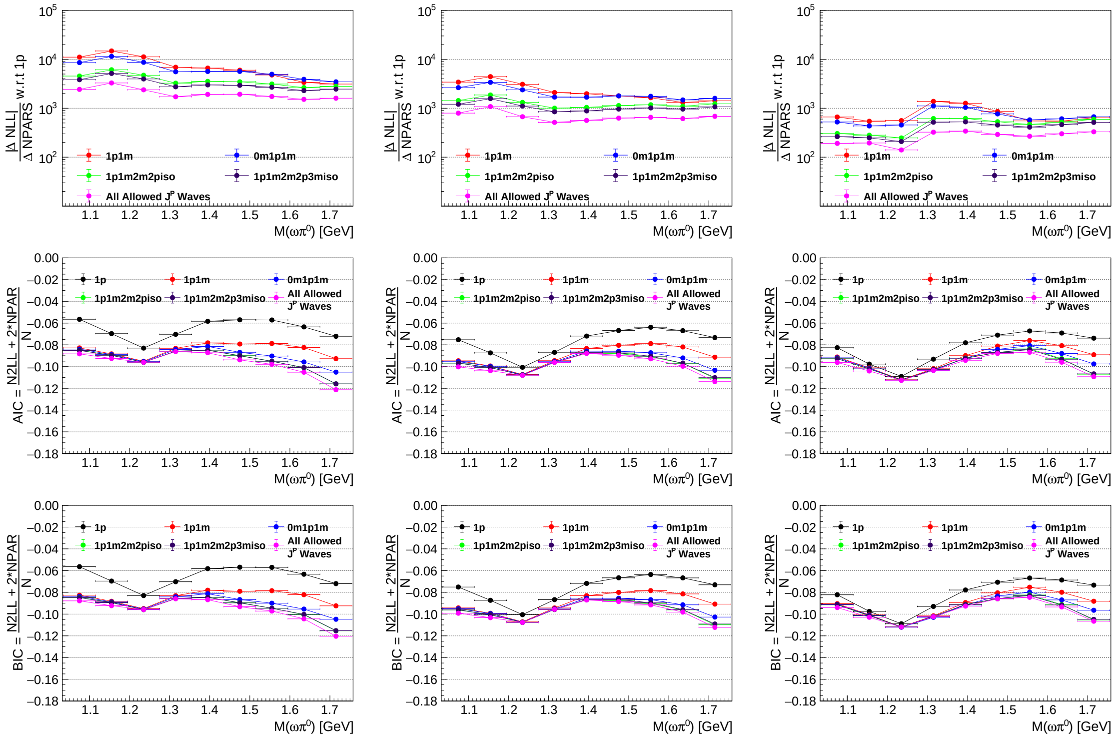

$0.15 < |t| \leq 0.30$ GeV^2 $0.30 < |t| \leq 0.50$ GeV^2 $0.50 < |t| \leq 1.00$ GeV^2

Figure 5.6: The figure summarizes the model selection strategy followed for selecting the most significant model. The figures in the three columns correspond to the three different t bins. Top row plots show the LRT with `1p` as its null model, performed across various wavesets. The middle row and third-row plots show AIC and BIC for different wavesets throughout the nine mass bins.

Selecting a single model (set of waveset) is not straightforward as in the case of Signal MC. It can be seen from Figure 5.6 that the various combinations of wavesets explored varies in its significance across the mass bins and t bins. A general inference can be observed in LRT in Figure 5.6 (top row), namely that the difference in ΔNLL is less than an order of magnitude across the board. Similar observations can be made for AIC and BIC that, the significance for various model changes as the mass $M(\omega\pi^0)$ increases. A detailed discussion about the inferences and their explanation is given below.

Results in lower $M(\omega\pi^0)$ range (b_1 range): Comparing the Likelihood Ratio Test in the low mass region in Figure 5.6, it can be observed that, the most significant model (waveset) in this region is `1p1m` and is closely followed by `01p1m` indicating that only low J^P states contribute significantly in that region. This can also be observed across the AIC and BIC, where the metrics are nearly equal for all the wavesets being used[4] indicating that adding more J^{PC} state does not improve the fitting of the model. This can also be seen from the angular distribution fits in Appendix B.3. Up to a mass of $M(\omega\pi^0) \leq 1.355$ GeV, the AIC and BIC across different wavesets are equal within their statistical precision. And, the LRT for `1p1m` is the maximum in this region. This behavior is very compelling, since the model's significance AIC and BIC does not change significantly by including a waveset having $NPAR = 26$ or $NPAR = 77$. Hence, one can conclude that the most significant waveset in the low mass region of $M(\omega\pi^0)$, ~ 1.35 GeV is `1p1m`, and that provides a complete description of GlueX Phase-I data.

---

[4] with an exception of the `1p` waveset.

Results in high $M(\omega\pi^0)$ range: The GlueX Phase-I data prefer to have a more complex model in the high $M(\omega\pi^0)$ range. On comparing the model selection metric LRT in the mass range $M(\omega\pi^0) > 1.355$ GeV, the gap between simpler models and more complex models starts to decrease as mass ($M(\omega\pi^0)$) increases. This behavior is observed in all the t bins as well, suggesting that a more complex model is needed to describe the data. The AIC (second row) prefers the most complex model which includes all allowed $J < 4$ states. This is where the competing nature (trade-off nature) of AIC and BIC becomes evident. The BIC prefers a more complex model but not as complex as the model including all allowed J^P states. The BIC prefers a model waveset `1p1m2m2p3miso` to be chosen. In order to choose the ideal model in this region, LRT has to be maximum, while both AIC and BIC have to be minimum. Motivated by this strategy, the waveset `1p1m2m2p3miso` is chosen as the waveset that best describes data in the high region of $M(\omega\pi^0) > 1.355$ GeV[5]

Therefore, for the region in low $M(\omega\pi^0) \leq 1.355$ GeV, the model `1p1m` will be considered, and for the region in high $M(\omega\pi^0) > 1.355$ GeV the model `1p1m2m2p3miso` across all t bins will be considered for extracting fit fractions.

5.5.2 Intensity of $b_1(1^{+-})$ in GlueX Phase-I data

By selecting the appropriate model corresponding to the mass region $M(\omega\pi^0)$, one can look into the overall intensity of $b_1(1^{+-})$ observed across its mass bins. The extracted intensity of the b_1 in the three t-bins is shown in Figure 5.7

---

[5] This strategy is not applied on a bin-by-bin basis because having distinct waveset describing various mass bins in close proximity lacks physics motivation.

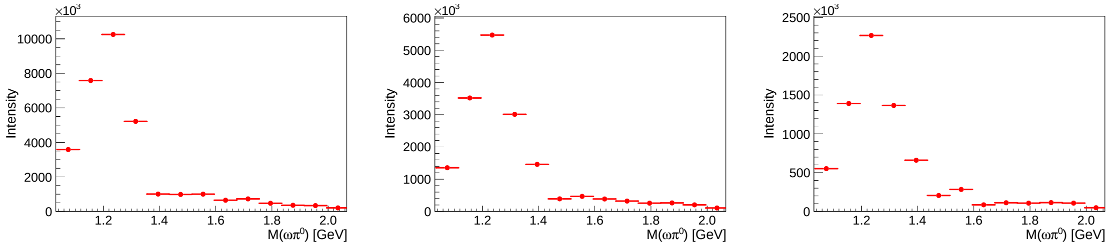

$0.15 < |t| < 0.30$ GeV^2 $0.30 < |t| < 0.50$ GeV^2 $0.50 < |t| < 1.00$ GeV^2

Figure 5.7: Extracted intensity of $b_1(1^{+-})$ for GLUEX Phase-I data. Mass bins until 2 GeV are shown. One can observe the spectra of 1^{+-} state across the t bins have similar line shapes and this can be extended to other J^P states as done in [26]. The other J^P states are not as stable as 1^+. It may require more systematic studies and is beyond the scope of this dissertation, hence, other J^P state's line shapes are not shown here.

This is the first significant step towards computing the total cross-section of the photoproduction of the state b_1 at GLUEX. The cross-section for the state b_1 can be computed as

$$\sigma = \frac{N}{\epsilon \times \text{Flux} \times \text{Target} \times \mathcal{B}(b_1(1235) \to \omega\pi^0) \times \mathcal{B}(\omega \to \pi^+\pi^-\pi^0) \times \mathcal{B}(\pi^0 \to 2\gamma)} \tag{5.53}$$

where, σ is the cross-section for photoproduction of b_1, N is the intensity of b_1 (coherently summed over all partial wave contributions from Figure 5.7), ϵ is the efficiency., flux is the total polarized tagged flux, $\mathcal{B}$ is the branching ratio for the decay chains, and target is the target thickness. What has been demonstrated is the recipe to compute the yield N by performing a PWA on the $\omega\pi^0$ and extracting the effective contribution of b_1 meson from it.

As discussed earlier the main challenge in PWA is to choose the most significant set of waves that best fits GLUEX data. The next step beyond this dissertation is to perform a systematic study in the chosen mass bin width to ensure the stability of extracted yield. Furthermore, detector systematic studies have to be done to ensure there are no biases in the data selection procedure[6].

It can be seen from Figure 5.7, that the b_1 resonance is narrow in the region $1.155 < M(\omega\pi^0) < 1.315$. As discussed in Section 1.2 the `dsratio` for b_1 is a measure of its decay mechanism. Extracting `dsratio` in the mass region of $1.155 < M(\omega\pi^0) < 1.315$ is crucial in understanding the b_1. Hence, a detailed and systematic study is performed in extracting the `dsratio` in the b_1 region, as described in the next chapter.

---

[6] It is usually observed that the main systematic in PWA is choosing the best waveset.

Chapter 6

Systematic study in neutral b_1 region

In the previous chapter, the yield of the $b_1(1245)[1^{+-}]$ state was extracted in the mass range $1.0 < M(\omega\pi^0) < 2.0$ GeV. The b_1 has a unique decay property that is referred to as the `dsratio` and defined as the ratio of its D-wave ($l = 2$) to its S-wave ($l = 0$) as described previously. Extracting the `dsratio` in the photoproduction of the b_1 at GlueX is crucial to understanding the decay dynamics of $b_1 \to \omega\pi^0$. This chapter focuses on the extraction of `dsratio` in the mass region $1.155 < M(\omega\pi^0) < 1.315$ GeV. Additional figures that are relevant to this chapter has been presented in Appendix C. The choice of this mass region was motivated by its reported width (Γ) of 140 MeV and the previous measurement at E852 experiment at Brookhaven National Laboratory (BNL) [26]. The `dsratio` is extracted under various conditions assessing the systematic uncertainties from the GlueX Phase-I data. The default extraction conditions are presented in Table 6.1.

Cut Name	**Selection**	**Systematic Remarks**
$M(\omega\pi^0)$ [GeV]	$1.155 - 1.315$ GeV	Systematics performed
$\|t\|$ [GeV^2]	$[(0.15 - 0.30), (0.30 - 0.50), (0.50 - 1.00)]$ GeV^2	Systematically studied fit variation across t range
Fit Waves	Combinations of $0^-, 1^+, 1^-, 2^-$	Systematics performed
Beam Energy [GeV]	$8.2 - 8.8$ GeV	Systematics performed
Dalitz Parameters (α, β, γ)	$\alpha = 0.1212; \beta = 0.02570; \gamma = 0.0$	Systematics performed based on [27]
Polarization Fraction (P_γ)	$\sim$ 35%	Systematics performed
Event Selection	Default as given in Chapter 4	No systematics performed
`dphase`	Fixed to 0.0	Studied a floating `dphase`

Table 6.1: Table summarizing default data selection and systematics for extracting `dsratio`.

For the systematic studies performed, the errors corresponding to `dsratio` are defined as

$$\Delta_{\text{sys}} = \sqrt{\frac{\sum_i^N (\texttt{dsratio}_i - \texttt{dsratio}_{ref})^2}{N-1}} \tag{6.54}$$

where, N is the total number of systematic variations made and $\texttt{dsratio}_{ref}$ is the "nominal value", which will be discussed in Section 6.2.

6.1 Fitting across all four polarization orientations

As mentioned in Section 2.2.1, GlueX switches between four orientation angles of the photon beam. As the value of `dsratio` does not depend on the polarization orientation, this affords a major consistency check for the extraction method. If the four values agree with statistical precision, the datasets can be combined into a single set, thereby improving the statistical precision. The extraction conditions are shown in Table 6.1, for the waveset `1p1m`. The errors reported on the fit parameters are from `MINUIT`. The results for the extracted `dsratio` are shown in Figure 6.1 and results are tabulated in Table 6.2. The fit fractions for the `1p1m` waveset are shown in Figure C.1. The extracted `dsratio` across all four orientations is shown in Figure 6.1. The dashed lines and corresponding error band in the figure correspond to the mean and standard deviation of the four `dsratio` extracted from the four different orientations. The extracted `dsratio` in the four orientations falls within the uncertainties reported by `MINUIT` and is stable across all orientations.

Fit Parameter	$0.15 < \lvert t\rvert < 0.30$ GeV^2				$0.30 < \lvert t\rvert < 0.50$ GeV^2				$0.50 < \lvert t\rvert < 1.00$ GeV^2			
	PARA 0°	PERP 45°	PERP 90°	PARA 135°	PARA 0°	PERP 45°	PERP 90°	PARA 135°	PARA 0°	PERP 45°	PERP 90°	PARA 135°
D/S Ratio	0.2553 ± 0.0016	0.2549 ± 0.0016	0.2553 ± 0.0016	0.2586 ± 0.0016	0.2667 ± 0.0021	0.2674 ± 0.0021	0.2645 ± 0.0021	0.2651 ± 0.0021	0.2352 ± 0.0031	0.2331 ± 0.0031	0.2391 ± 0.0031	0.2400 ± 0.0031
Fit Fraction $[\mathbf{1}^{+}]^{+}$	83.87% ± 2.41%	81.96% ± 2.41%	79.32% ± 2.41%	82.15% ± 2.41%	86.24% ± 3.53%	84.66% ± 3.53%	84.41% ± 3.53%	86.34% ± 3.53%	72.93% ± 4.83%	76.01% ± 4.83%	76.21% ± 4.83%	76.15% ± 4.83%
Fit Fraction $[\mathbf{1}^{+}]^{-}$	2.45% ± 2.33%	4.63% ± 2.33%	6.68% ± 2.33%	4.16% ± 2.33%	3.64% ± 2.15%	4.52% ± 2.15%	4.41% ± 2.15%	2.89% ± 2.15%	9.62% ± 2.75%	8.35% ± 2.75%	8.20% ± 2.75%	6.64% ± 2.75%
Fit Fraction $[\mathbf{1}^{-}]^{+}$	10.77% ± 1.55%	12.31% ± 1.55%	13.24% ± 1.55%	11.78% ± 1.55%	7.93% ± 2.41%	9.06% ± 2.41%	9.01% ± 2.41%	8.62% ± 2.41%	14.79% ± 1.93%	12.88% ± 1.93%	11.24% ± 1.93%	11.78% ± 1.93%
Fit Fraction $[\mathbf{1}^{-}]^{-}$	2.86% ± 1.64%	1.05% ± 1.64%	0.81% ± 1.64%	1.91% ± 1.64%	2.20% ± 1.44%	1.76% ± 1.44%	2.12% ± 1.44%	2.12% ± 1.44%	2.65% ± 1.86%	2.75% ± 1.86%	4.33% ± 1.86%	5.4% ± 1.86%

Table 6.2: Table summarizing fit result across various orientations.

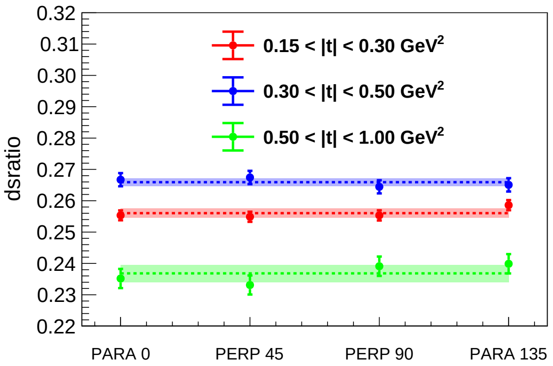

Figure 6.1: Extracted `dsratio` across different orientations of the polarization by fitting the waveset `1p1m`. Colors correspond to t-bins.

In conclusion, the four orientations can be combined into a single data set, and PWA fits are then applied to this. From here on in the analysis was carried out on the combined data set with the four polarization orientations fit simultaneously.

6.2 Statistical precision

The full dataset was split into three t bins, as shown in Table 6.1. In order to compute the statistical precision in measuring `dsratio`, a likelihood scan is performed. To this end, a waveset of `1p1mPos` is chosen ($[1^+, 1^-]^{(+)}$) and is used for PWA fits[1]. Then, the `dsratio` is fixed across a range between 0.2 to 0.4, in steps of 0.005. Results from 25 randomized fits were used as starting parameters for each fit in the scan, with all parameters in the model floating except the `dsratio`. Subsequently, the difference in $-2\ln(\mathcal{L})$ from these scans is plotted against the fixed `dsratio`. Spline interpolation is used to precisely determine the minimum and the error. The left and right error of this distribution is extracted separately, and the error is computed as the value of

---

[1] The waveset is the best fit in describing data as shown in Section 6.3.

`dsratio` when $\Delta - 2\ln(\mathcal{L})$ is 1.0, which corresponds to an uncertainty of 1σ. Results of the scans for Signal MC are shown in Figure 6.2 and results of GlueX Phase-I data are shown in Figure 6.3. The results for the parameter scan are tabulated in Table 6.3.

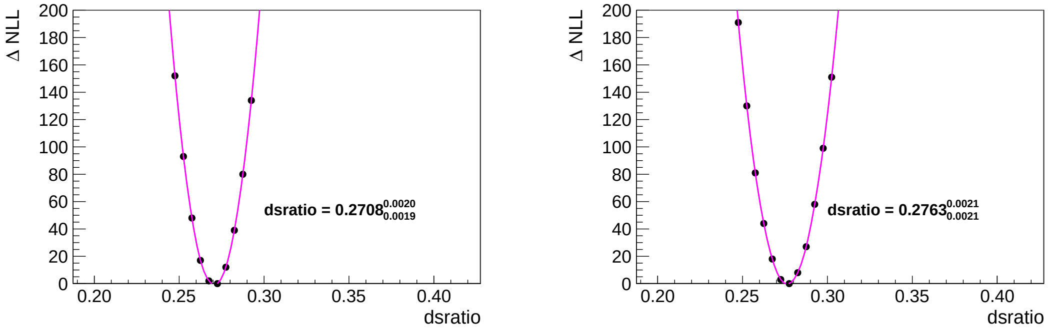

$0.15 < |t| < 0.30$ GeV^2 $\quad$ $0.30 < |t| < 0.50$ GeV^2

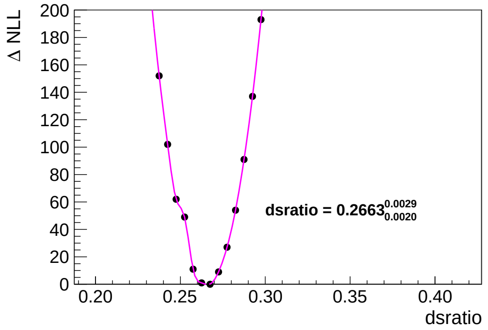

$0.50 < |t| < 1.00$ GeV^2

Figure 6.2: Statistical precision in extracting `dsratio` for the Signal MC, in three t-bins. The magenta line is the spline interpolation line used to extract the minimum and the left and right statistical errors from the distributions.

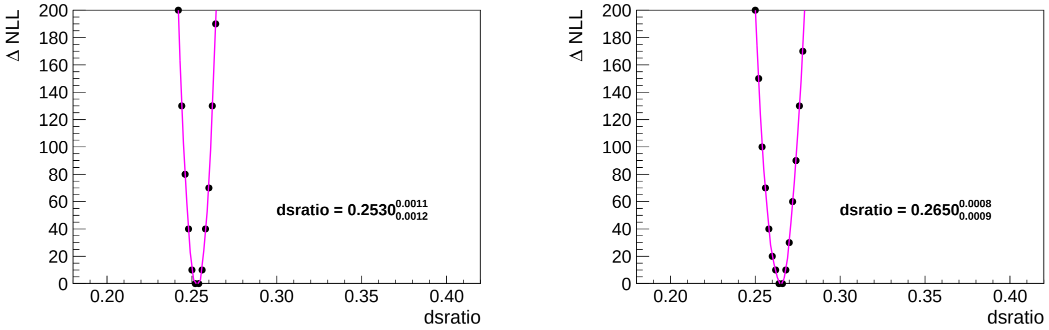

$0.15 < |t| < 0.30$ GeV^2 $\quad$ $0.30 < |t| < 0.50$ GeV^2

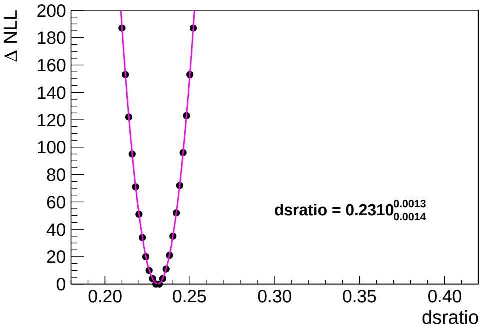

$0.50 < |t| < 1.00$ GeV^2

Figure 6.3: Statistical precision in extracting `dsratio` for the GlueX Phase-I data, in three t-bins. The magenta line is the spline interpolation line used to extract the minimum and the left and right statistical errors from the distributions.

	Extracted `dsratio`	
$\|t\|$ **range** GeV^2	**GlueX Phase-I data**	**Signal MC**
$0.15 < \|t\| < 0.30$	$0.2530^{0.0011}_{0.0012}$	$0.2708^{0.0020}_{0.0019}$
$0.30 < \|t\| < 0.50$	$0.2650^{0.0008}_{0.0008}$	$0.2763^{0.0021}_{0.0021}$
$0.50 < \|t\| < 1.00$	$0.2310^{0.0013}_{0.0014}$	$0.2663^{0.0029}_{0.0020}$

Table 6.3: Extracted `dsratio` and its correponding statistical error from `dsratio` parameter scan. The results tabulated here will be used as a *benchmark* value for `dsratio` and its corresponding statistical error.

The parameter scans also reject any minima that can be found in the `dsratio` parameter space as seen in Figure 6.3. It can be noted that the third t-bin has "lower" `dsratio` compared to the other two t bins, which are still under investigation. A detailed study of extracting `dsratio` as a function of t is presented in Section 6.5. This is against physics intuition since, the `dsratio` is a decay property of the b_1 but $|t|$ is a production variable and hence, `dsratio` should not depend on $|t|$.

6.3 Fit wave systematics

The procedure for choosing the best waveset was discussed in Section 5.5. In this section, focus has been given to a subset of waves that potentially contribute to the overall angular distribution in the b_1 mass region. As seen in the results from Section 5.5, the waveset `1p1m` is the most significant one indicating only small $J = 1$ states contribute to this mass region. Hence, the waveset of choice used in this section will mostly be combinations of small $J^P \leq 2$ states. Following the data selection procedure outlined in Table 6.1 and the steps in Section 5.5, the best waveset is chosen for the Signal MC first, to demonstrate the procedure, and then to the data set. The associated systematic errors are computed at the end of this section.

6.3.1 Choosing the best waveset in Signal MC

Table 6.4 shows the combination of J^P used to perform PWA on the Signal MC. It is worth reminding that the Signal MC was generated using $[1^+, 1^-]^{(+)}$ only, and the model selection strategy must converge on the waveset `1p1mPos`. For each of the combinations of waves, 25 randomized fits are performed and the results are extracted. Then, the model selection strategy from Section 5.2 is carried out and the corresponding metrics, namely LRT, AIC and BIC are computed and presented in

Figure 6.4. In Table 6.4 contains the two wavesets named `OmNeg1pPos1mPosisoSepDS` and `1p1mPosSepDS` which have separate `dsratio` defined for the three m projections $m = [-1, 0, 1]$ for the 1^+ state. Ideally, the `dsratio` should be independent of m projections and should yield a consistent `dsratio` across these projections, however, they are allowed to be independent here, so that stable m projection amplitudes may provide a more stable determination of the `dsratio`.

Waveset Name	**Remarks**	**Wave sets**			**NPARS**
		$[J^P]^\epsilon$	m	L	
`1p`	-	$[1^+]^\pm$	$-1, 0, 1$	S, D	11
`0m1p`	-	$[0^+]^\pm$	0	P	15
		$[1^+]^\pm$	$-1, 0, 1$	S, D	
`1p1m`	-	$[1^+]^\pm$	$-1, 0, 1$	S, D	23
		$[1^-]^\pm$	$-1, 0, 1$	P	
`0m1p1m`	-	$[0^+]^\pm$	0	P	27
		$[1^+]^\pm$	$-1, 0, 1$	S, D	
		$[1^-]^\pm$	$-1, 0, 1$	P	
`0m1p1miso`	-	Same as above + Isotropic Bkg			28
`0mNeg1pPos1mPosiso`	-	$[0^+]^-$	0	P	14
		$[1^+]^+$	$-1, 0, 1$	S, D	
		$[1^-]^+$	$-1, 0, 1$	P	
		Isotropic Bkg			
`1p1mPos`	-	$[1^+]^+$	$-1, 0, 1$	S, D	12
		$[1^-]^+$	$-1, 0, 1$	P	
`0mNeg1pPos1mPosisoSepDS`	Seperate `dsratios` for 3 m	Same as `0mNeg1pPos1mPosiso`			16
`1p1mPosSepDS`	Seperate `dsratios` for 3 m	Same as `1pPos1mPos`			14

Table 6.4: Summary of wavesets used to extract `dsratio` in b_1 region from Signal MC.

As seen in Figure 6.4, the most significant waveset is `1p1mPos`[2] which agrees with the waveset used for generating the Signal MC. It is also, worth noting that the second most significant set of waves is `0mNeg1pPos1mPosiso` in LRT. Both these wavesets

---

[2] The waveset name convention is from Table 6.4.

are highlighted along the x-axis Figure 6.4. Now, this methodology can be extended to GlueX Phase-I data.

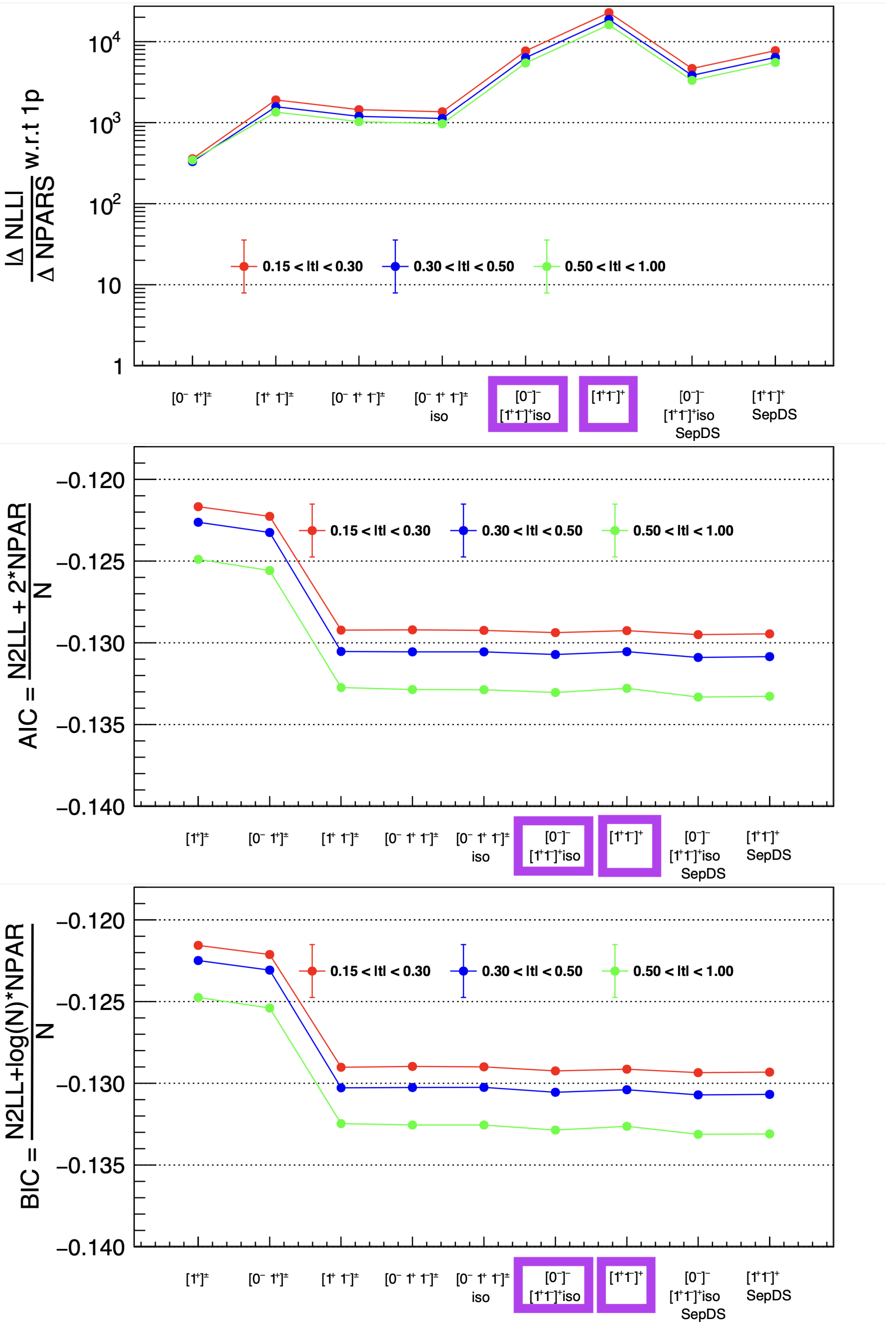

Figure 6.4: Model selection strategy for extracting `dsratio` for Signal MC. The line is used to guide eye.

6.3.2 Choosing the best wave sets in GlueX Phase-I data

Table 6.5 shows the combination of J^P used to perform PWA on GlueX Phase-I data. For each of the wavesets, 25 randomized fits are performed and the results are extracted. Figure 6.5 shows the results of the model selection strategy.

Waveset Name	**Remarks**	**Wave sets**			**NPARS**
		$[J^P]^\epsilon$	m	L	
`1p`	-	$[1^+]^\pm$	$-1, 0, 1$	S, D	14
`0m1p`	-	$[0^+]^\pm$	0	P	18
		$[1^+]^\pm$	$-1, 0, 1$	S, D	
`1p1m`	-	$[1^+]^\pm$	$-1, 0, 1$	S, D	26
		$[1^-]^\pm$	$-1, 0, 1$	P	
`0m1p1m`	-	$[0^+]^\pm$	0	P	30
		$[1^+]^\pm$	$-1, 0, 1$	S, D	
		$[1^-]^\pm$	$-1, 0, 1$	P	
`0m1p1miso`	-	Same as above + Isotropic Bkg			31
`0mNeg1pPos1mPosiso`	-	$[0^+]^-$	0	P	17
		$[1^+]^+$	$-1, 0, 1$	S, D	
		$[1^-]^+$	$-1, 0, 1$	P	
		Isotropic Bkg			
`1p1mPos`	-	$[1^+]^+$	$-1, 0, 1$	S, D	15
		$[1^-]^+$	$-1, 0, 1$	P	
`0mNeg1pPos1mPosisoSepDS`	Seperate `dsratios` for 3 m	Same as `0mNeg1pPos1mPosiso`			19
`1pPos1mPosSepDS`	Seperate `dsratios` for 3 m	Same as `1p1mPos`			17
`1p1m2mPos`		$[1^+]^\pm$	$-1, 0, 1$	S, D	46
		$[1^-]^\pm$	$-1, 0, 1$	P	
		$[2^-]^+$	$-2, -1, 0, 1, 2$	D, F	
`1p1m2mPos2pPosiso`		$[1^+]^\pm$	$-1, 0, 1$	S, D	45
		$[1^-]^\pm$	$-1, 0, 1$	P	
		$[2^-]^+$	$-1, 0, 1$	P, F	
		$[2^+]^+$	$-1, 0, 1$	D	
		Isotropic Bkg			

Table 6.5: Summary of wavesets used to extract `dsratio` in b_1 region in GlueX Phase-I data.

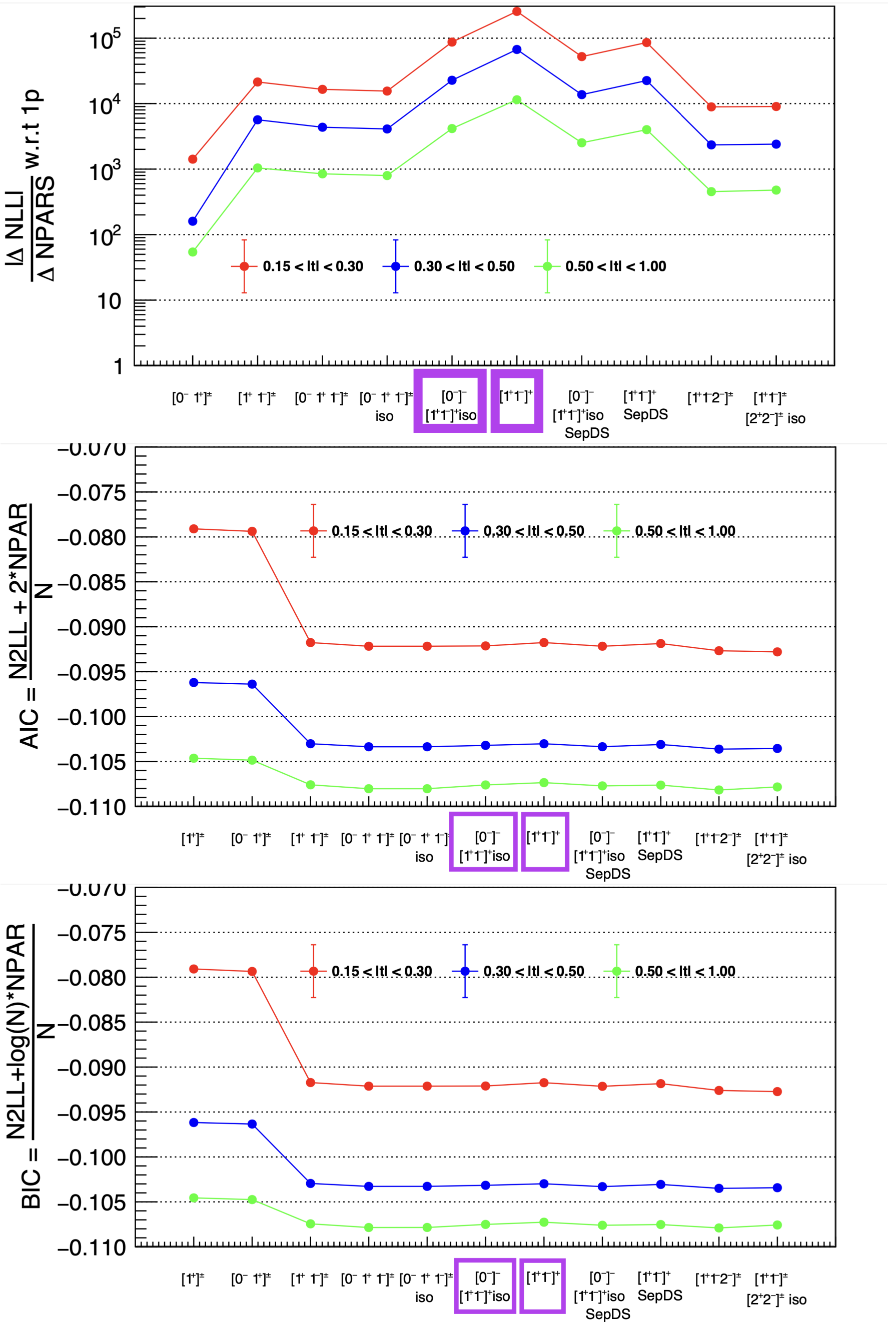

Figure 6.5: Model selection strategy for extracting `dsratio` for GlueX Phase-I data.

As seen in Figure 6.5, the most significant waveset out of all the wavesets explored is `1p1mPos`[3] as highlighted along the x-axis in the figure. A key observation made in the figure is that the metric LRT across wavesets is not as large as seen in Signal MC, especially in the $|t|$ range $0.50 < |t| < 1.00$ GeV^2. The difference in LRT for `0mNeg1pPos1mPosiso` is closely followed to that of the waveset `1p1mPos`. The other two model selection metrics, AIC and BIC, do not change significantly as well for the combination of waves used in the study. Nevertheless, the maximum LRT waveset of `1p1mPos` is chosen as the best waveset that describes GlueX Phase-I data. Appendix C.2.1 shows the extracted `dsratio` for the various combinations of wavesets used.

6.3.3 Fit wave systematics result

In order to calculate the systematic uncertainty caused by the choice of wavesets used in measuring the `dsratio`, Equation 6.54 is utilized with the wavesets having LRT greater than 1000. The summary of systematic errors is presented in Table 6.6 and the results are plotted in Figure 6.6.

Wavesets	$\|t\|$ bins GeV^2					
	$0.15 < \|t\| < 0.30$		$0.30 < \|t\| < 0.50$		$0.50 < \|t\| < 1.00$	
	Signal MC	GlueX Phase-I data	Signal MC	GlueX Phase-I data	Signal MC	GlueX Phase-I data
`1p1m`	0.2674	0.2509	0.2791	0.2616	0.2661	0.2330
`0m1p1miso`	0.2946	0.2874	0.3097	0.2810	0.3048	0.2508
`1p1mPos`	0.2682	0.2531	0.2787	0.2644	0.2657	0.2309
`0mNeg1pPos1mPosiso`	0.2933	0.2962	0.3078	0.2874	0.3025	0.2531
Benchmark `dsratio`	**0.2708**	**0.2530**	**0.2763**	**0.2650**	**0.2663**	**0.2310**
Systematic Uncertainity	**0.0210**	**0.0325**	**0.0246**	**0.0165**	**0.0311**	**0.0173**

Table 6.6: Systematic uncertainty due to choice of wavesets in extracting `dsratio`.

---

[3] The waveset name convention is from Table C.2.

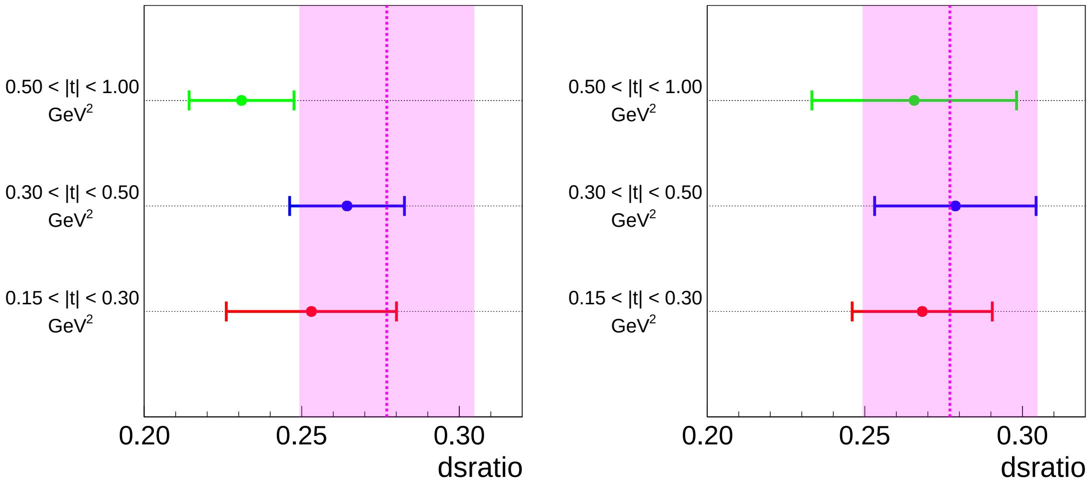

Figure 6.6: Systematic uncertainty due to choice of wavesets in extracting `dsratio`. The plot on the left corresponds to GlueX Phase-I data, while the figure on the right corresponds to Signal MC. The points in the graph are the benchmark `dsratio` values from Table 6.3 and systematic uncertainties from Table 6.6. The dashed magenta line and band in the figure correspond to the current PDG value [4].

The following conclusions are drawn from the following fit wave systematic study:

- The `dsratio` for the high t bin $0.50 < |t| < 1.00$ GeV^2 is consistently lower than the other two t bins. This is further studied in the next sections.

- By adding a 0^- state, the `dsratio` increases, which means the effective S wave amplitude contribution decreases. This effect is particular for the 0^- state and can be seen in both Signal MC and GlueX Phase-I data. This is still under investigation, and it is possible that when adding 0^- state there is interference in the cross terms in the intensity Equation 1.25 which causes ambiguities in the extracted solutions.

- The largest systematic error comes from the waveset choice, which is ~ 10 times larger than the statistical error.

6.4 Mass ($M(\omega\pi^0)$) range systematics

Another important systematic is associated with the mass range $M(\omega\pi^0)$ chosen for the PWA fit. The nominal value of $1.155 < M(\omega\pi^0) < 1.315$ GeV is motivated by previous studies made by E852 [26]. The width of this mass bin was studied. The PWA model does not make any assumptions about the mass dependence of $M(\omega\pi^0)$. Therefore, a study is made by varying the width of mass range $M(\omega\pi^0)$, for the chosen waveset `1p1mPos`.

6.4.1 Mass range systematics in Signal MC

The mass range $M(\omega\pi^0)$ is systematically decreased in a symmetric fashion from $1.149 - 1.310$ GeV/c^2 to $1.200 - 1.260$ GeV/c^2 in steps of 20 MeV. A total of six variations were studied and the extracted `dsratio` result is shown in Figure 6.7. It can be seen that the variation of `dsratio` as a function of the chosen mass range has minimal effect compared to that of the choice of waveset used.

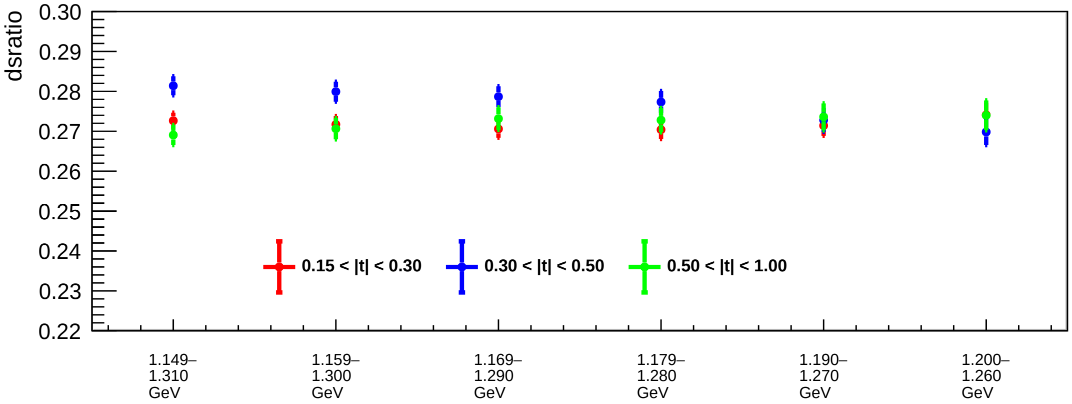

Figure 6.7: Extracted `dsratio` with varying mass bin in Signal MC. It can be seen that the variation across all three t bins and mass bins is minimal. The errors shown are from `MINUIT`. As the mass width becomes smaller, the statistical error reported by `MINUIT` increases.

6.4.2 Mass range systematics in GlueX Phase-I data

Following similar mass range variation as in Signal MC, the mass range $M(\omega\pi^0)$ is systematically decreased from $1.149 - 1.310$ GeV/c^2 to $1.200 - 1.260$ GeV/c^2 in steps of 20 MeV. Additionally, an asymmetrical binning is also made to evaluate the effect of the higher mass region in extracting the `dsratio`. This is mainly because the data show larger variation in `dsratio` as a function of mass binning and is affected the most at the higher mass region as shown in Figure 6.8

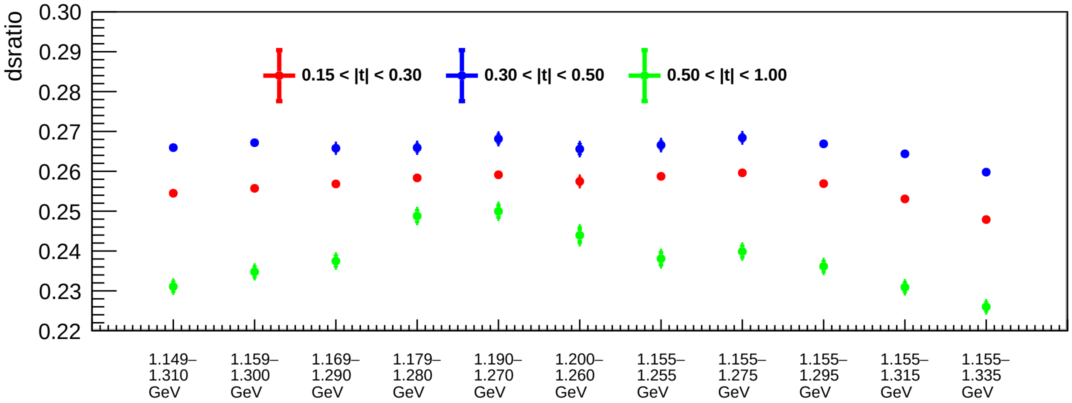

Figure 6.8: The extracted `dsratio` is plotted from varying the mass bins in GlueX Phase-I data. It can be seen that the extraction of `dsratio` shows the largest variation to this cut variation at the highest $|t|$ bins.

6.4.3 Systematic mass bin width study

The results for this systematic study are summarized in Table 6.7, and the results are plotted in Figure 6.9. The following conclusions can be made from this systematic study.

Mass Bin [$M(\omega\pi^0)$**GeV**]	**Bin Width**	$\lvert t\rvert$ bins GeV^2					
		$0.15 < \lvert t\rvert < 0.30$		$0.30 < \lvert t\rvert < 0.50$		$0.50 < \lvert t\rvert < 1.00$	
		Signal MC	GlueX Phase-I data	Signal MC	GlueX Phase-I data	Signal MC	GlueX Phase-I data
$1.150 \leq M(\omega\pi^0) < 1.310$	160	0.2726	0.2545	0.2814	0.2659	0.2691	0.2311
$1.160 \leq M(\omega\pi^0) < 1.300$	140	0.2717	0.2557	0.2799	0.2672	0.2706	0.2348
$1.170 \leq M(\omega\pi^0) < 1.290$	120	0.2706	0.2568	0.2787	0.2658	0.2732	0.2375
$1.180 \leq M(\omega\pi^0) < 1.280$	100	0.2704	0.2583	0.2773	0.2659	0.2728	0.2488
$1.190 \leq M(\omega\pi^0) < 1.270$	80	0.2714	0.2591	0.2728	0.2681	0.2736	0.2500
$1.200 \leq M(\omega\pi^0) < 1.260$	60	0.2741	0.2575	0.2698	0.2656	0.2740	0.2440
$1.155 \leq M(\omega\pi^0) < 1.255$	100	-	0.2587	-	0.2666	-	0.2381
$1.155 \leq M(\omega\pi^0) < 1.275$	120		0.2596		0.2684		0.2399
$1.155 \leq M(\omega\pi^0) < 1.295$	140		0.2569		0.2669		0.2361
$1.155 \leq M(\omega\pi^0) < 1.315$	160		0.2531		0.2644		0.2309
$1.155 \leq M(\omega\pi^0) < 1.335$	180		0.2479		0.2598		0.2260
Benchmark `dsratio`		**0.2708**	**0.2530**	**0.2763**	**0.2650**	**0.2663**	**0.2310**
Systematic Uncertainity		**0.0018**	**0.0048**	**0.0045**	**0.0025**	**0.0068**	**0.0104**

Table 6.7: Systematic uncertainty due to mass range of $M(\omega\pi^0)$.

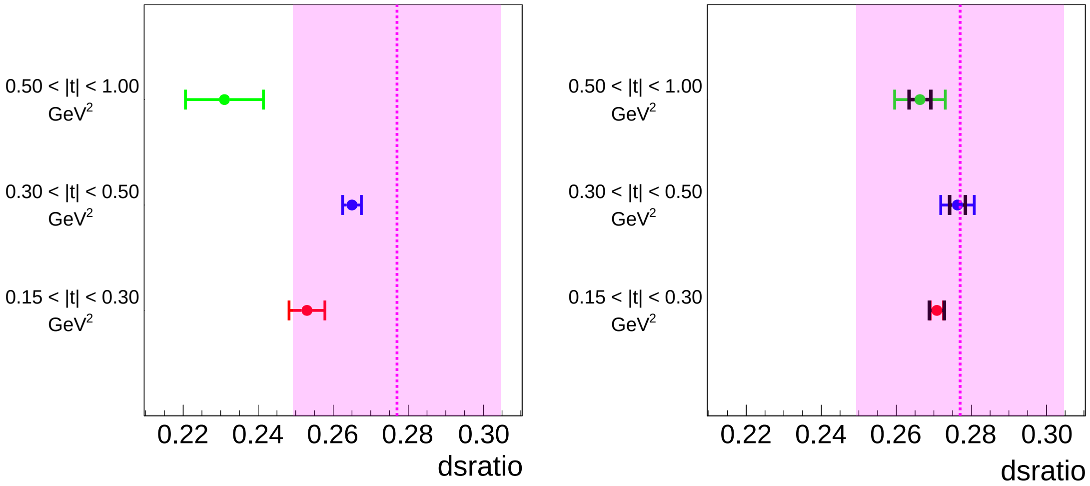

Figure 6.9: Systematic uncertainty due to width of $M(\omega\pi^0)$ in extracting `dsratio`. The plot on the left corresponds to GlueX Phase-I data, while the figure on the right corresponds to Signal MC. Points and errors are from benchmark and systematic uncertainty from Table 6.7. The black error bars correspond to the statistical error extracted from the parameter scan shown in Table 6.3. The dashed magenta line and band in the figure correspond to the current PDG value [4].

Stability of fit procedure: The Signal MC is consistent within the allowed statistical precision when the width of the mass bin is systematically varied. Therefore, the fitting procedure is free of any bias in extracting `dsratio` based on the width of the mass bin.

`dsratio` in low t bins: In the case of GlueX Phase-I data, in the first two t bins, namely, $0.15 < |t| < 0.30$ GeV^2 and $0.30 < |t| < 0.50$ GeV^2, the extracted `dsratio` shows little variation expect when the width of the mass bin is increased significantly (to 180 MeV). This can be explained by the fact that the fits are made with an assumption that there is no mass $M(\omega\pi^0)$ dependence. This effect yields a systematic error of about ~ 0.005 in extracting `dsratio` in the corresponding two low t bins. This can further be improved by considering a piece-wise hybrid mass-dependent formulation [30], where the intensity equation from Equation 1.28 is rewritten as:

$$
\begin{aligned}
& I(\Phi,\Omega,\Omega_H) = 2\kappa \\
& \Bigg\{(1-P_\gamma)\left[\left|\sum_{i,m}[J_i]^{(-)}_m F^{(-)}_i(M,\vec{x})\mathfrak{Im}(Z)\right|^2 + \left|\sum_{i,m}[J_i]^{(+)}_m F^{(+)}_i(M,\vec{x})\mathfrak{Re}(Z)\right|^2\right] \\
& +(1+P_\gamma)\left[\left|\sum_{i,m}[J_i]^{(+)}_m F^{(+)}_i(M,\vec{x})\mathfrak{Im}(Z)\right|^2 + \left|\sum_{i,m}[J_i]^{(-)}_m F^{(-)}_i(M,\vec{x})\mathfrak{Re}(Z)\right|^2\right]\Bigg\}
\end{aligned}
\tag{6.55}
$$

where, $F^{(\pm)}_i(M,\vec{x})$ is the mass distribution equation which is characterized by $\vec{x}$ additional parameters. In the mass region of interest, an assumption is made that b_1 is the dominant resonance and is modelled by a relativistic Breit-Wigner formulation. The other J^P contributions are simultaneously fit along the same $\omega\pi^0$ mass range in a mass-independent fashion, with unique complex parameters for each mass bin.

This should improve the stability of `dsratio` further, however, the variation is of the order of 0.005, which is an order of magnitude less than the systematic error due to the choice of wavesets used. Hence, this is left to be implemented and studied in future analyses by the GlueX Collaboration.

`dsratio` in high t bin: The `dsratio` from GlueX Phase-I data in the high t bin, $0.50 < |t| < 1.00$ GeV^2, is consistently lower than that of the other t bins. It can be seen from Figure 6.8 that the extracted `dsratio` is strongly affected by this mass range variation. As the width of the mass bin decreases, the `dsratio` in the highest t bin converges to the value measured in the other two low t bins. As the width of the mass bin increases, the extracted `dsratio` decreases. By increasing the width of the mass bin, the b_1 signal effectively dilutes. A cut on invariant mass of recoiling proton (p) and the bachelor π^0, $M(p\pi^0)$ will reduce baryonic contribution if any, under the b_1 peak. But the high t bin has stronger dependence in the extraction of `dsratio` which leads to a systematic study in understanding the dependence of extracting `dsratio` as a function in $|t|$ as discussed in the next Section 6.5

6.5 Fit across various $|t|$ bins

The extracted `dsratio` should not have any dependence in $|t|$ as it is a production variable. However, throughout the analysis, there seems to be a strong correlation between extracting `dsratio` in various $|t|$ bins. As the t range increases the extracted `dsratio` decreases as shown in Figure 6.6 and Figure 6.9. In order to understand the dependence, a study was made by performing 25 randomized fits in each fine $|t|$ bin from 0.15 GeV^2 to 1.00 GeV^2 in a total of 39 bins such that there is roughly equal statistics in each of the t bin. The most significant waveset `1p1mPos` is used with conditions following Table 6.1. In this section only results from GlueX Phase-I data are discussed. A similar study was made for Signal MC and is reported in Appendix C.3. Figure 6.10 summarizes the results of the study.

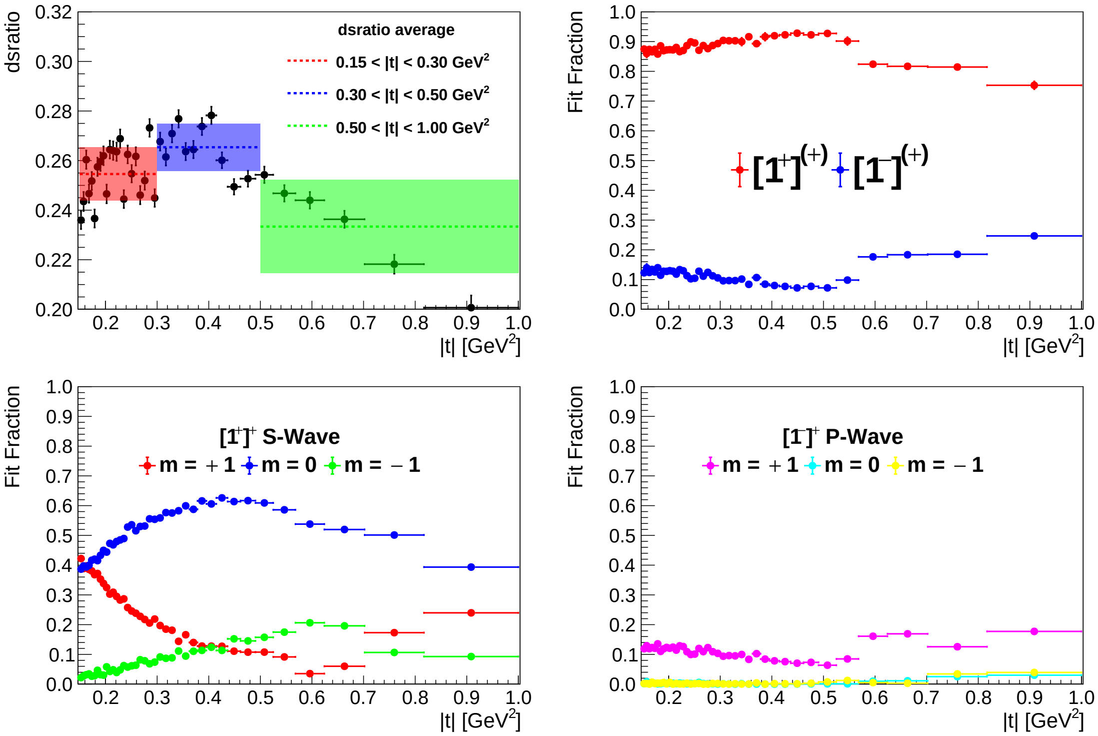

Figure 6.10: Extracted `dsratio` in fine t bins for GlueX Phase-I data. For the extracted `dsratio` on the top left plot, the different colored lines and band correspond to the statistical mean and variation of the extracted `dsratio` combined into the three t bins. The remaining plots are the fit fractions corresponding to various $[J^P]_m$ states.

From Figure 6.10 following conclusions can be drawn from the study

- In the t bins up to $|t| \leq 0.5$ GeV^2 the extracted `dsratio` has statistical variations consistent within its allowed errors. However, for $|t| > 0.5$ GeV^2, the extracted `dsratio` strongly decreases until $|t| = 1.00$ GeV^2.

- This decrease in `dsratio` is correlated with an increase in the $[1^-]$ fit fraction as seen in top right plot in Figure 6.10. For $|t| > 0.5$ GeV^2 the fit fraction corresponding to $[1^-]^{(+)}$ increases monotonically. This could indicate that a different waveset combination could describe the data better than just `1p1mPos`. Hence, a waveset combination of `0mNeg1pPos1mPosiso` was chosen as it was the second best performing from the waveset selection strategy discussed in Section 6.3.2. The result is summarized in Appendix C.4. The study showed that by introducing a 0^- state an overall increase is seen in the extraction of `dsratio`. But the behaviour still remains such that for higher t range, the extracted `dsratio` is lower, and the fit fraction corresponding to 1^- state increases strictly beyond $|t| > 0.5$ GeV^2. This means that the chosen waveset is not the primary reason for this correlation.

- The plot on the bottom left in Figure 6.10 shows the individual fit fractions corresponding to the state $[1^+]^{(+)}$, with the different colors correspond to the three m projections $m = [-1, 0, 1]$. It can be seen that beyond $|t| > 0.5$ GeV^2, an inversion is observed in dominance between the states $m = -1$ and $m = 1$. The m projection $m = +1$ decreases in its dominance while $m = -1$ increases in its dominance. This is due to the fact that the Φ angle in the angular distribution is the sensitive angular parameter that is responsible for this behaviour. The visible change in the distribution of this angle Φ for various t is shown in Appendix C.5. Using Equation 1.28, the angular variable Φ is encoded in the Wigner D Functions discussed in Section 1.3.

- `dsratio` can be defined independently for each m projection in each reflectivity corresponding to $[1]^+$ state. Ideally, `dsratio` has to be consistent across the different m projections. Therefore, a study was made by having three independent `dsratio` corresponding to the three m projections[4]. The result is summarized in Appendix C.6. The result of the study showed that the `dsratio` corresponding to the most dominant m projection $m = 0$ was only reliable across the t range, and monotonically decreased as a function of t. The extracted `dsratio` across the three orientations in the region of high statistics are consistent with one another. The most dominant m projection $m = 0$ shows similar behaviour where `dsratio` decreases in higher t bins.

Finally, this leaves the potential next step, that is, to study any baryonic/non-baryonic($M(p\pi^0)$) resonance background in this region. This can be done by placing cut on the invariant mass of $M(\pi^0 p)$, recoiling proton (p) and the bachelor pion (π^0). A systematic study should be performed by placing a cut $M(\pi^0 p) > 1.5$ GeV, $M(\pi^0 p) > 1.6$ GeV and $M(\pi^0 p) > 1.7$ GeV, and is currently underway but is not included in this thesis. This will remove any non-baryonic backgrounds and is the subject of future systematic study.

In conclusion, the dependence of extracting `dsratio` is still under investigation and hence, the results cannot be combined into a single t bin. The results will be reported separately for the three t bins.

6.6 Systematics by varying Beam Energy

The default data selection has a cut on the incoming photon beam energy. For the default cut of $8.2 < E_\gamma < 8.8$ GeV, the polarization fraction is about ~ 0.35.

---

[4] There is no negative reflectivity amplitudes in the waveset `1p1mPos`.

Hence, varying this cut and studying the systematic effect in extracting the `dsratio` is performed in this section. When the beam energy cut is varied the corresponding polarization fraction also changes accordingly. Hence, for the variable cuts explored in this study, the corresponding polarization fraction for the different orientations is outlined in Table 6.8.

Beam Energy [GeV]	**Width [MeV]**	**Polarization Fraction**			
		PARA_0	PERP_45	PERP_90	PARA_135
8.2 - 8.8	600	0.3410	0.3352	0.3355	0.3402
8.3 - 8.8	500	0.3457	0.3378	0.3436	0.3401
8.4 - 8.8	400	0.3437	0.3367	0.3378	0.3457
8.5 - 8.8	300	0.3468	0.3372	0.3359	0.3472
8.20 - 8.75	550	0.3501	0.3435	0.3425	0.3470
8.20 - 8.70	500	0.3465	0.3425	0.3417	0.3468
8.20 - 8.65	450	0.3465	0.3422	0.3420	0.3465

Table 6.8: Table summarizing various beam energy ranges and their corresponding polarization fraction.

6.6.1 Beam Energy systematics in Signal MC

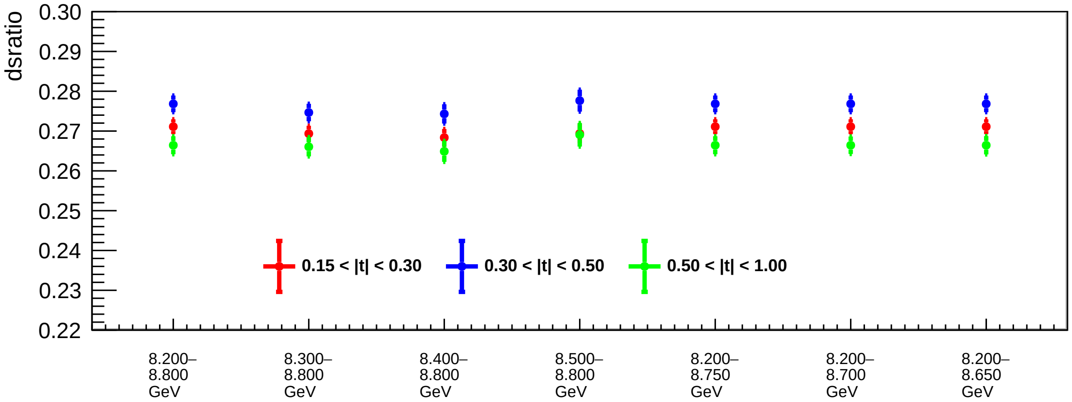

Figure 6.11: Extracted `dsratio` with varying Beam Energy cut in Signal MC. It can be seen that the variation across all three t bins and mass bins is minimal. The errors shown are from `MINUIT`.

6.6.2 Beam Energy systematics in GlueX Phase-I data

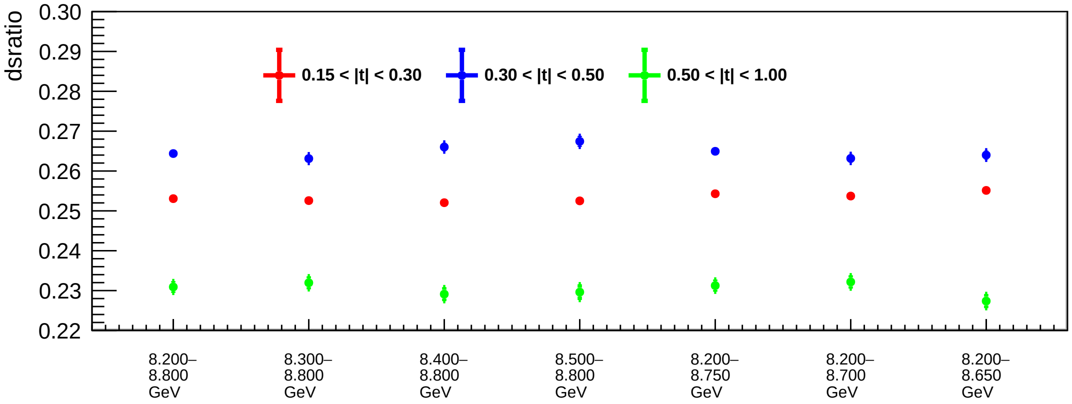

Figure 6.12: Extracted `dsratio` with varying Beam Energy cut in GlueX Phase-I. It can be seen that the variation across all three t bins and mass bins is minimal, but the extracted `dsratio` in the highest t bin is still lower than the other two lower t bins.

The result of the systematic study is tabulated in Table 6.9.

Beam Energy [GeV]	**Width [MeV]**	$\lvert t\rvert$ bins GeV^2					
		$0.15 < \lvert t\rvert < 0.30$		$0.30 < \lvert t\rvert < 0.50$		$0.50 < \lvert t\rvert < 1.00$	
		Signal MC	GlueX Phase-I data	Signal MC	GlueX Phase-I data	Signal MC	GlueX Phase-I data
8.2 - 8.8	600	0.2711	0.2531	0.2768	0.2644	0.2664	0.2309
8.3 - 8.8	500	0.2694	0.2526	0.2747	0.2631	0.2661	0.2320
8.4 - 8.8	400	0.2684	0.2521	0.2743	0.2660	0.2649	0.2291
8.5 - 8.8	300	0.2694	0.2525	0.2776	0.2674	0.2691	0.2296
8.20 - 8.75	550	0.2711	0.2543	0.2768	0.2650	0.2664	0.2312
8.20 - 8.70	500	0.2711	0.2537	0.2766	0.2632	0.2662	0.2322
8.20 - 8.65	450	0.2710	0.2551	0.2769	0.2640	0.2665	0.2273
Benchmark `dsratio`		**0.2708**	**0.2530**	**0.2763**	**0.2650**	**0.2663**	**0.2310**
Systematic Uncertainty		**0.0013**	**0.0012**	**0.0016**	**0.0015**	**0.0017**	**0.0019**

Table 6.9: Systematic uncertainty due to Beam Energy cut

6.6.3 Systematic Beam Energy cut results.

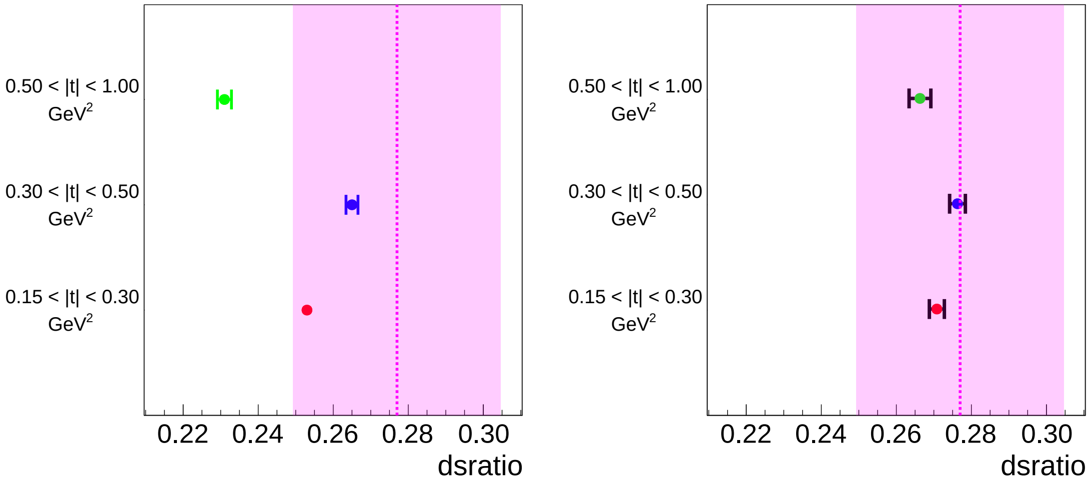

Figure 6.13: Systematic uncertainty due to beam energy cut in extracting `dsratio`. The plot on the left corresponds to GlueX Phase-I data, while the figure on the right corresponds to Signal MC. Points and errors are from benchmark and systematic uncertainty from Table 6.9. The black error bars correspond to the statistical error extracted from the parameter scan shown in Table 6.3. The dashed magenta line and band in the figure correspond to the current PDG value [4].

6.7 Systematics by varying the Dalitz Parameters

The factor G_{Dalitz} from Section 1.2 in Equation 1.18 describes the Dalitz distribution of the pions in $\omega \to \pi^0\pi^+\pi^-$ decay, and is a scalar function of the Mandelstam variables as shown in Equation 1.19. The Joint Physics Analysis Center (JPAC) revisited the dispersion analysis of the $\omega \to 2\pi$ decay amplitude and the $\omega\pi^0$ transition form factor. Within the framework of the Khuri-Trieman equation, the Dalitz plots distributions and integrated decay widths were presented in detail [27]. JPAC reported four sets of possible solutions for the Dalitz distribution. These four solutions are applied as a systematic in extracting the `dsratio`. The four sets of solutions for α, β and γ are presented in Table 6.10 and its corresponding extracted `dsratio` is tabulated. Figure 6.14 shows the `dsratio` across the four solutions presented by JPAC in [27].

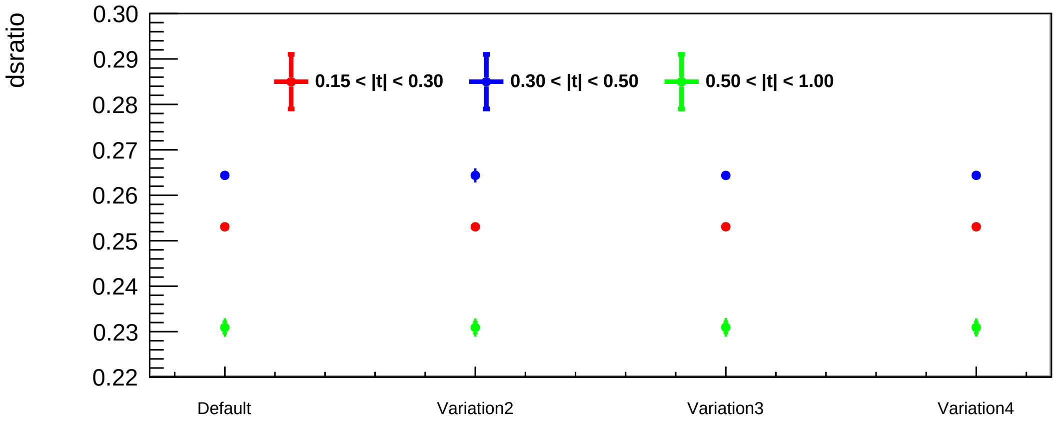

Figure 6.14: Extracted `dsratio` for various Dalitz parameters combination

Variation Name	Remarks	Dalitz Parameters			GlueX Phase-I data		
		α $\times 10^3$	β $\times 10^3$	γ $\times 10^3$	$0.15 < \lvert t \rvert < 0.30$	$0.30 < \lvert t \rvert < 0.50$	$0.50 < \lvert t \rvert < 1.00$
Default	2 param fit	121.2	25.7	-	0.2531	0.2644	0.2309
Varation 2		120.1	30.2	-	0.2530	0.2643	0.2309
Variation 3	3 param fit	112	23	23	0.2530	0.2645	0.2308
Variation 4		109	26	19	0.2531	0.2644	0.2308
Benchmark `dsratio`					**0.2530**	**0.2650**	**0.2310**
Systematic Uncertainty					**0.0007**	**0.0008**	**0.0009**

Table 6.10: Systematic uncertainty due to Dalitz parameters variation. It can be seen that varying the Dalitz parameters for the four different solution presented by JPAC [27] have minimal effect on extracting `dsratio`.

It can be concluded that the variation in extracting in `dsratio` by varying the Dalitz parameter has a minimal effect. The result is presented in Figure 6.15.

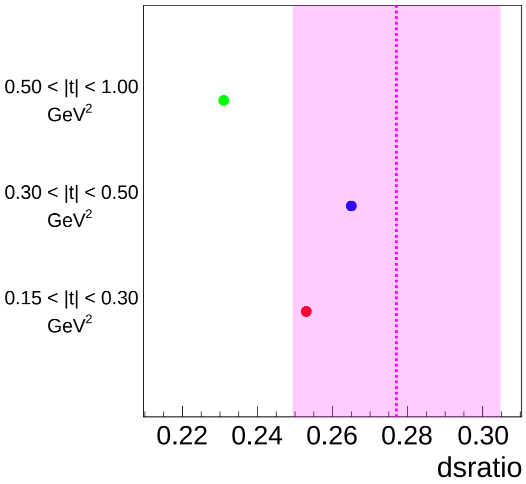

Figure 6.15: Extracted `dsratio` with varying Dalitz parameters in GlueX Phase-I. Points and errors are from benchmark and systematic uncertainty from Table 6.10. It can be seen that the variation across all three t bins and mass bins is minimal. Still the extracted `dsratio` in the highest t bin is lower than the other two lower t bins. The magenta dashed line and band in the figure correspond to the current PDG value [4].

6.8 Summary of Systematic Uncertainties

Table 6.11 shows the estimated systematic uncertainties along with the total statistical uncertainty determined in extracting `dsratio` for both Signal MC and GlueX Phase-I data. There could be a systematic correlation between the different cuts applied. The correlation between the cuts required a more detailed study and is beyond the scope of this dissertation. In this work, the contributions are assumed to be uncorrelated and were thus added in quadrature to determine the total uncertainty.

Cut Name	$\lvert t\rvert$ bins GeV^2					
	$0.15 < \lvert t\rvert < 0.30$		$0.30 < \lvert t\rvert < 0.50$		$0.50 < \lvert t\rvert < 1.00$	
	Signal MC	GLUEX Phase-I data	Signal MC	GLUEX Phase-I data	Signal MC	GLUEX Phase-I data
Fit Waves	0.0210	0.0325	0.0246	0.0165	0.0311	0.0173
Mass bin	0.0018	0.0048	0.0045	0.0025	0.0068	0.0104
Beam Energy	0.0013	0.0012	0.0016	0.0015	0.0017	0.0019
Dalitz Parameter	-	0.0007	-	0.0007	-	0.0007
Benchmark `dsratio`	**0.2708**	**0.2530**	**0.2763**	**0.2650**	**0.2663**	**0.2310**
Statistical Uncertainty Δ_{stat}	0.0020 0.0019	0.0011 0.0012	0.0021 0.0021	0.0008 0.0008	0.0029 0.0020	0.0013 0.0014
Systematic Uncertainty Δ_{sys}	**0.0211**	**0.0329**	**0.0251**	**0.0168**	**0.0319**	**0.0203**

Table 6.11: Total systematic uncertainty for extracting `dsratio`

The summary of extracted `dsratio` is shown in Figure 6.16. The extracted ratio from GLUEX Phase-I data agrees with the current PDG value reported in [4] across all the t bins, with the highest t bin value being systematically lower than that of PDG and the other two t, which should be investigated in future GLUEX analyses.

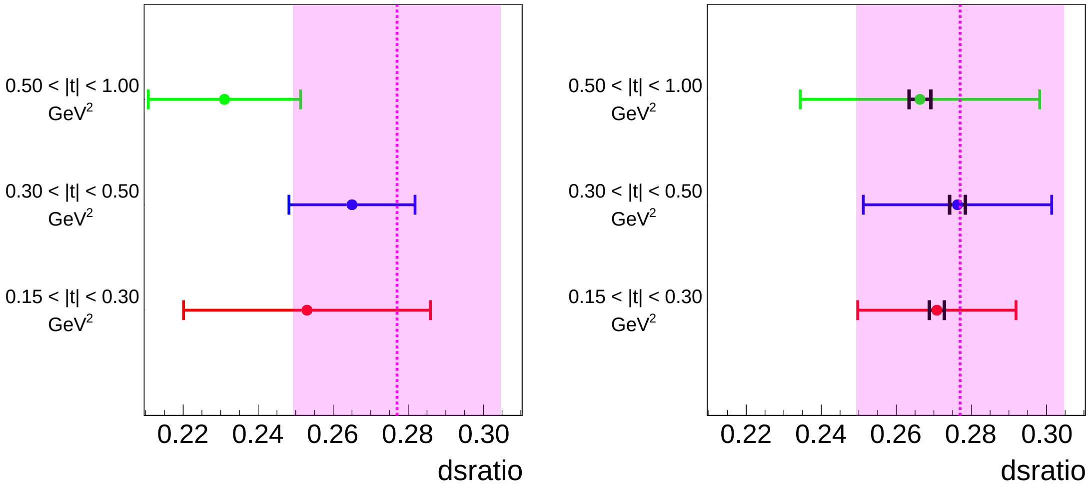

Figure 6.16: The extracted `dsratio` after accounting for systematic studies presented in this chapter. The plot on the left corresponds to GLUEX Phase-I data, while the figure on the right corresponds to Signal MC. Points and errors are from reference and systematic uncertainty from Table 6.11. The black error bars correspond to the statistical error extracted from the parameter scan shown in Table 6.3. The magenta dashed line and band in the figure correspond to the current PDG value [4].

The following conclusions are drawn from the systematic study:

- The most dominant waveset is $[1^+]$ in the explored $M(\omega\pi^0)$ region is in its positive reflectivity. This concludes that unnatural parity π^0 exchange is dominant in this photoproduction reaction as discussed in Section 1.3.1.

- The dataset corresponding to the four orientations yielded consistent `dsratio` results, allowing fits to be performed on all four orientations simultaneously.

- The statistical error on `dsratio` was extracted using a parameter scan. It is also confirmed that the extracted `dsratio` has no other minimum in its parameter space.

- The largest systematic found in extracting the `dsratio` is from the choice of waveset used for performing fits. The systematic error corresponding to the choice of waveset is at least ~ 10 times the statistical error.

- Fit fractions for various m projections for the $[1^+]^{(+)}$ state were extracted across various t bins. An inversion of dominance between the states $m = -1$ and $m = 1$ is observed for $|t|$ beyond $|t| > 0.5\text{GeV}^2$. This is because Φ angle (Ω) is the angular distribution that is sensitive to $|t|$ variation.

- Finally, the overall systematic errors are similar to the reported PDG error [4], hence making the results reported in this thesis competitive with previous measurements.

Chapter 7

AI-assisted tracker design for the EIC

7.1 Introduction

This chapter delves into the design of the tracker for the upcoming Electron-Ion Collider (EIC) experiment. Initially, we present the EIC experiment's objectives and detector requirements, along with the associated EIC Comprehensive Chromodynamics Experiment (ECCE) proto-collaboration in Section 7.2. The section includes details of the proposed ECCE tracker technologies. In Section 7.4, we introduce the concept of Multi Objective Optimization (MOO) and its key terminologies. Section 7.5 details the application of MOO to design the ECCE tracker, outlining the goals, the optimized detector systems, and the timeline of optimization. The outcomes of two significant optimization phases are presented at the end of the section. Appendix D includes additional results from tracking studies conducted during the optimization process. Most of the work discussed here has been previously published [66], and therefore, only key points are summarized in this chapter.

7.2 EIC Experimental program

The Electron-Ion Collider (EIC) [67] is a large-scale next-generation particle accelerator facility conceived by U.S nuclear and accelerator physicists and proposed to be built at Brookhaven National Laboratory on Long Island, New York by the U.S Department of Energy between the late 2020s and early 2030s. This colossal effort is jointly led by Brookhaven National Laboratory (BNL) and Thomas Jefferson National Accelerator Facility (TJNAF) along with its worldwide collaborators (EIC User Group) [67]. EIC will enable the study of the properties of nucleons and nuclei with unprecedented accuracy, by colliding electrons with protons and ions in an extensive range of energies and with high luminosity. Its high-design luminosity and highly polarized beams are beyond state-of-the-art and its realization will likewise push the frontiers of particle accelerator science and associated technologies.

EIC will be realized with the following design requirements.

- Peak luminosity between 10^{33} cm^{-2}s^{-1} and 10^{34} cm^{-2}s^{-1} and an integrated luminosity of 100 fb^{-1}
- Highly polarized leptons (electrons $\sim 70\%$) and hadrons (protons $\sim 70\%$) beams
- Variety of ion beams ranging from light nuclei like deuterons to heavy nuclei such as gold, lead or uranium
- Tunable $e + p$ center of mass energies ranging from 20-100 GeV(possibly upgrading to 140 GeV)

EIC will be utilizing the existing RHIC beamline, with a newly added electron injector. Figure 7.1 shows a sketch of the conceived EIC facility at BNL.

7.2.1 Physics Goals

EIC operates with a wide range of center-of-mass energies which will allow measurements that bridge the past and present experiments and the exploration of new kinematic regions. Figure 7.2 shows the expected EIC kinematic range capabilities. EIC would contribute to address fundamental questions in Quantum ChromoDynamics (QCD), highlighted below.

Origin of nucleon mass: The nucleon mass problem has been one of the longstanding questions in the field of hadron structure. Interestingly, constituent masses of quarks in a proton make only about 1% of its total measured mass. While QCD considers the Higgs mechanism to explain the mass problem, it only is responsible for a small fraction of the proton mass. The proton mass composition can be better understood by the trace anomaly of the QCD energy-momentum tensor [68]. EIC aims to study the origin of nucleon mass by performing measurements of quarkonia's exclusive production (J/ψ and Y) close to the production threshold. This physics

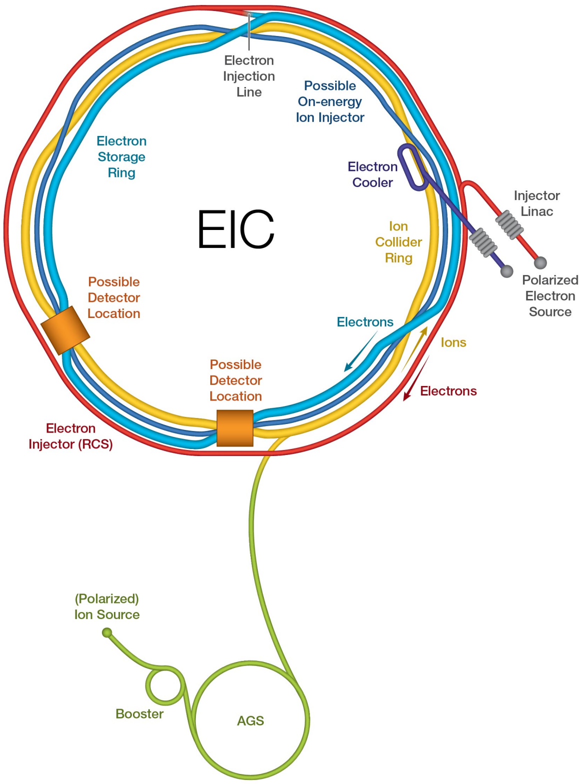

Figure 7.1: This sketch illustrates the proposed electron-ion collider, utilizing the existing RHIC beamline. The "AGS" denotes the "alternating gradient synchrotron" for ion acceleration. The EIC proposal includes two interaction points. Figure adapted from [67].

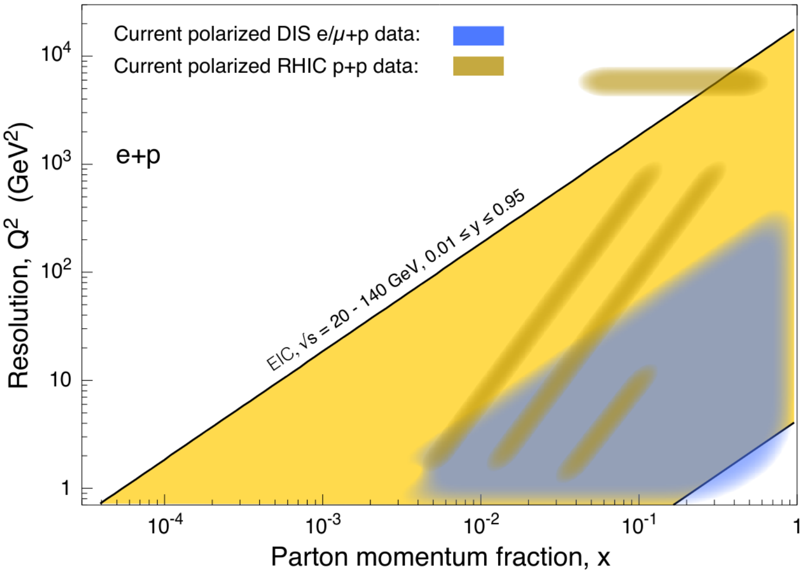

Figure 7.2: This figure illustrates the $x - Q^2$ coverage of the EIC and other $e/\mu - p$ and $p - p$ experiments. The variables x and Q^2 represent the momentum fraction of the struck parton and the square of momentum transfer, respectively. Diagonal lines denote lines of constant inelasticity y, and these variables are related through $Q^2 \approx sxy$. Figure adapted from [67].

goal demands EIC to have a precise reconstruction of electron's energy at low Q^2 (central) region and precise reconstruction of protons at small angles (forward-going direction)

Origin of spin of nucleons: Efforts to understand the contributions of quarks and gluons to nucleon spin have spanned several decades. It's known that quark/anti-quark spins, gluon spins, and parton angular momenta all contribute. However, traditional models and experiments have found that about 60% of the nucleon's spin originates from quark/anti-quark and gluon spins [69–73]. The remaining 40%, believed to be from Parton Orbital Angular Momentum (POAM), will be investigated by the EIC with its access to the full kinematic range. This task necessitates a precise electromagnetic calorimeter for polarized DIS studies. More theoretical details can be found in [74].

Structure of nucleons, nuclei and mesons: The nuclear physics community has long sought to understand the three-dimensional structure of the nucleon, encoded in Transverse Momentum-Dependent Parton distributions (TMDs). Previous experiments have provided insight but were limited by kinematic range and statistical precision [75–79]. The EIC will enhance these measurements, offering high precision and a broad kinematic range [80], made possible by excellent particle identification (PID) and large data sets. Additionally, EIC will delve into spatial distributions of quarks and gluons via their Generalized Parton Distributions (GPDs) through Deeply virtual Compton Scattering (DVCS) processes and deeply virtual meson production. This will provide insight into the Total Angular Momentum (OAM) of quarks and gluons, enhancing our understanding of GPDs and enabling maps of parton distributions down to 0.1 fm performing studies for protons in the range $0.04 \leq t < 1.5\ GeV^2$.

Understanding nuclear effects: At EIC electrons are collided with a range of atomic nuclei, This enables us to study the collisions with the nucleus compared to single nucleons. These interactions are described by nuclear Parton Distribution Functions (nPDFs) which depend on the value of x. At EIC the cross-section ratio of $e-$ion collisions to its expected behaviour from a collection of individual nucleons are studied for a range of values of x. EIC will make measurements with high precision on nPDFs due to its large kinematic range and high luminosity,

EIC will also provide insights about the transport properties of quark-gluon plasma and cold QCD through jet measurements. Jet measurements will constrain polarized and unpolarized parton distribution functions, probing gluon transverse momentum-dependent distributions. It will also contribute to QCD Hadronization, shower evolution, and cold nuclear matter effects. This jet reconstruction imposes very strict requirements on the vertex reconstruction resolution (pointing resolution) and minimum detectable momentum (to a few hundred MeV).

The physics goals are continuously evolving as the design concepts are getting molded towards a mature design phase. More information can be found at [67, 81].

7.3 Detector requirements in EIC

The physics program requires EIC to measure event and particle kinematics (x, Q^2, y, p_T, z, ϕ, θ)[1] reconstructed with high precision. To access the full $x-\mathrm{Q}^2$ plane at different center-of-mass energies and having strongly asymmetric beam-energy combinations, the detector must be able to reconstruct events over a wide span of polar angle (θ) and pseudorapidity (η). Therefore, these aspects dictate the detector requirements for EIC. A schematic of the EIC conceptual detector is shown in Figure 7.3.

Electron-Ion Collider (EIC) physics program imposes the following critical detector requirements.

- EIC will be a 4π hermetic detector with low mass (material) inner tracking
- Primary detector will cover an η between -4 to 4 to measure electrons, photons, hadrons and jets. It also requires strong auxiliary detectors in both the far forward and backward region
- EIC detectors should have radiation hardness comparable to that of LHC ones

---

[1] x, y and z are momentum fractions. p_T is transverse momentum and ϕ & θ reconstructed quantities.

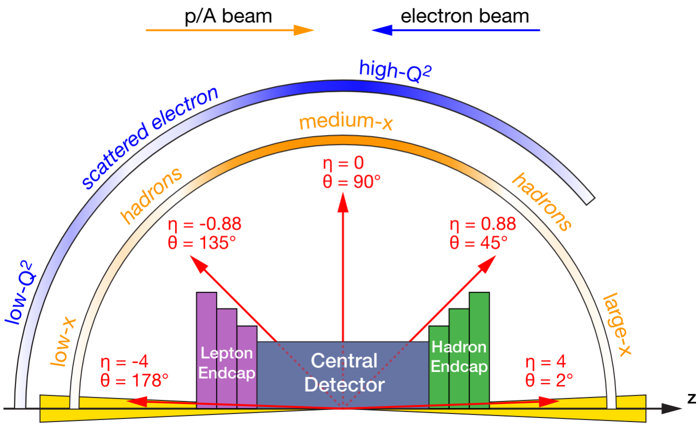

Figure 7.3: This schematic portrays the EIC detector's pseudorapidity range, mapping scattered electron and hadron distributions to their pseudorapidity across different $x - \mathrm{Q}^2$ regions. It links polar angle (θ) and pseudorapidity (η) via $\eta = -\ln\tan\theta/2$. The positive z direction or "forward" region contrasts the negative z or "backward" region. The central region ($-0.88 \leq \eta \leq 0.88$) is flanked by the transition region and the end cap region.

- Momentum resolution of trackers
  - Central tracker; $\sigma_{p_T}/p_T(\%) = 0.05p_T \otimes 0.5$
  - Forward tracker (hadron-going); $\sigma_{p_T}/p_T(\%) = 0.1p_T \otimes (1-2)$
  - Backward tracker (electron-going); $\sigma_{p_T}/p_T(\%) = 0.1p_T \otimes (0.5)$
- Impact parameter ($\mathrm{DCA_{2D}}$) resolution of tracker $\sigma_{xy} \sim 20/p_T \otimes 5\ \mu$ m
- Calorimeter Energy resolution
  - Electromagnetic Central region; $\sigma(E)/E \approx 10\%/\sqrt{E} \otimes (1-3)\%$
  - Electromagnetic Backward region; $\sigma(E)/E \approx 2\%/\sqrt{E} \otimes (1-3)\%$
  - Hadronic Forward region; $\sigma(E)/E \approx 50\%/\sqrt{E} \otimes 10\%$
- Excellent PID for 3σ $\pi/K/p$ separation up to 50 GeV/c in the forward region, up to 10 GeV in the central detector region, and up to 7 GeV in the backward

Full detector requirements are summarized in the EIC yellow report [67].

7.3.1 The ECCE proto-collaboration

The EIC Comprehensive Chromodynamics Experiment (ECCE), an international consortium of over 90 institutions, was chosen by DPAP in March 2022 to build the first detector for the EIC. After the decision, ECCE was expanded to include more experts, forming a new collaboration named ePIC. ECCE's proposed detector, based on the existing BABAR 1.5T magnet and the PHENIX hadronic calorimeter, aims to offer comprehensive energy coverage and optimized far forward detection. The detector is expected to be operational at the onset of EIC operations. For more details about the collaboration and its structure, refer to [82, 83].

7.3.1.1 ECCE Detector System

The ECCE detector extends approximately 40 m and consists of a central detector around the interaction point and regions in far-forward and far-backward directions [67]. It relies on the central detector for achieving EIC's physics goals, requiring hermeticity and proficient particle identification (PID) over a broad phase space.

The detector utilizes the BABAR superconducting solenoidal magnetic, in use by the sPHENIX experiment, which can reach a 1.5T magnetic field and sustain a high field of 1.4T[2]. The central detector includes a tracking system for charged particle reconstruction, PID sub-detectors, and calorimeters for particle flow data crucial to certain event topologies, such as those containing jets.

---

[2] ePIC developments have led to an increase in the magnetic field to 1.7T.

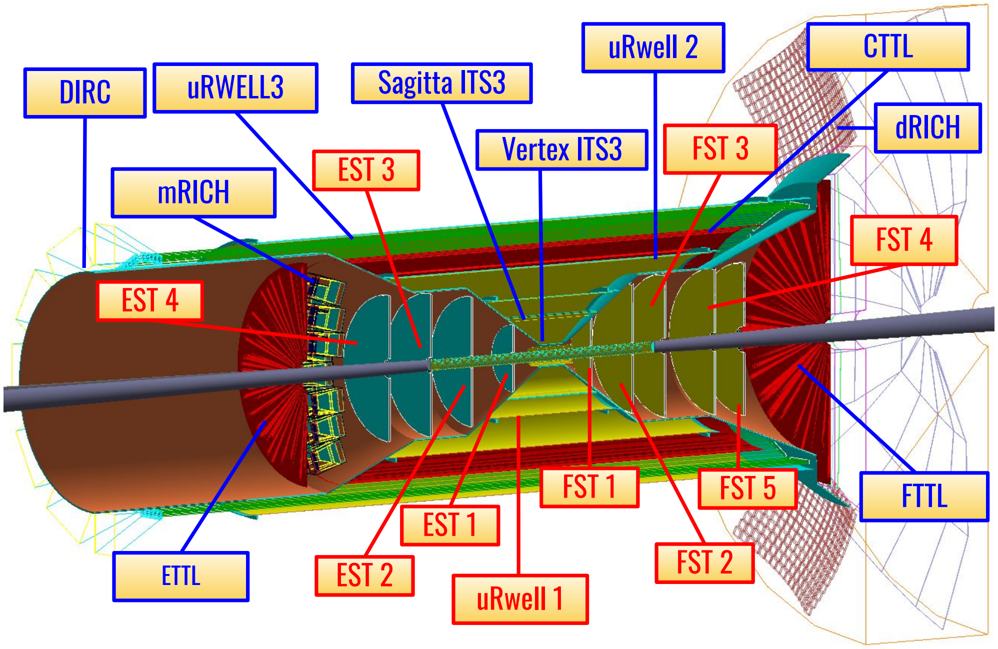

Figure 7.4: GEANT4 visualization of the proposed ECCE tracker [83].

7.3.1.2 ECCE Tracker

The ECCE tracker detector, one of the first AI-optimized sub-detectors at the EIC, consists of a silicon vertex/tracking detector and a micro-Rwell-based gas tracker. The silicon detector includes 5 barrel layers, 5 hadron endcap disks, and 4 electron endcap disks, while the gas tracker consists of 3 barrel layers.

Silicon Tracking system: The silicon vertex/tracking system uses ITS-3 type sensors with a pixel pitch at 10 μm and an average material budget per layer of $0.05\% X_0$. The detector design will be imported from the EIC eRD104 and eRD111 studies. The leading technology candidate for the ECCE silicon tracking detector is the new Monolithic Active Pixel Sensor (MAPS) under prototype sensor design and characterization [84, 85]. Other explored technologies include Depleted MAPS

(DMAPS) [86].

Gas Tracking system: The μRwell gas tracking layers, offering better spatial resolution and lower production costs compared to GEMs, will form three barrel tracking layers further out from the beam pipe than the silicon layers. The strip pitch for all 3 layers will be 400 μm.

AC-LGAD based tracking layers: Track reconstruction also uses position information provided by the AC-coupled Low Gain Avalanche Detector (AC-LGAD) based Time of Flight (ToF) subsystem in ECCE [82]. AC-LGAD sensors require additional R&D to demonstrate and characterize their performance

7.4 Multi Objective Optimization (MOO)

Multi Objective Optimization (MOO) minimizes or maximizes multiple objective functions subject to a set of constraints. It can be mathematically defined as:

$$\begin{aligned} \min / \max \ \mathbf{f_m}(\mathbf{x}), m = 1, \ldots, M \\ \text{s.t. } \mathbf{g_j}(\mathbf{x}) \leq 0,, j = 1, \ldots, J \\ \mathbf{h_k}(\mathbf{x}) = 0,, k = 1, \ldots, K \\ x_i^L \leq x_i \leq x_i^U,, i = 1, \ldots, N \end{aligned} \tag{7.56}$$

where the aim is to optimize objective functions $f_m(x)$, depending on design parameters x_i, subject to constraints $g_j(x)$ and $h_k(x)$.

MOO is resolved using two methods: Scalarization, which combines multiple objectives into a single one to minimize/optimize, and Pareto methods, which keep objectives independent, optimizing them simultaneously. Pareto methods are best for conflicting objectives and yield multiple solutions.

Various fields such as chemical engineering [87], data mining [88] and molecular design [89] have widely adopted MOO.

7.4.1 Fundamental Concepts

Figure 7.5 illustrates the central concept of MOO. The goal is to find optimal design points that provide the best performance in its objective space. The points in the objective space map to corresponding points in the design space.

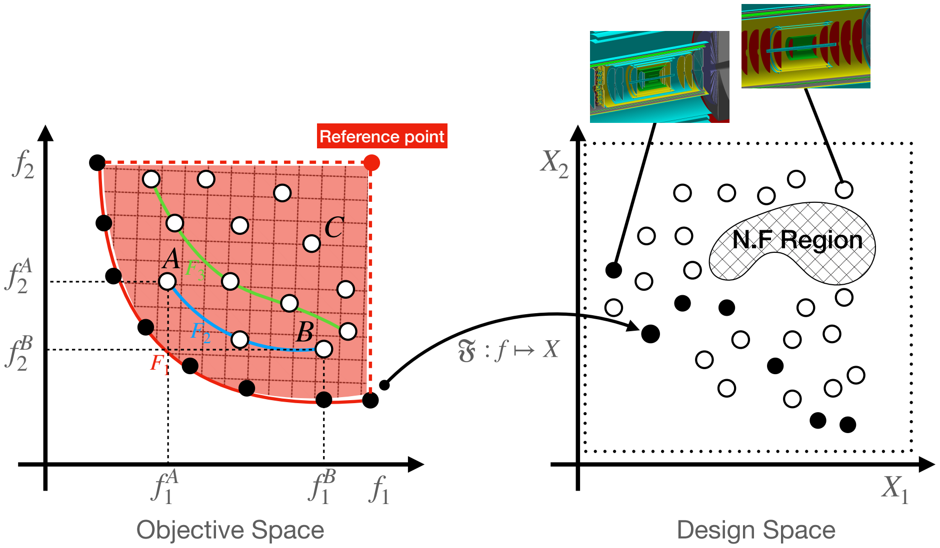

Figure 7.5: Relationship between the design space (x_i) with 2 design parameters and the objective space ($f_m(x)$) with 2 objective functions. N.F Region corresponds to a subspace in design where the design solutions are not feasible.

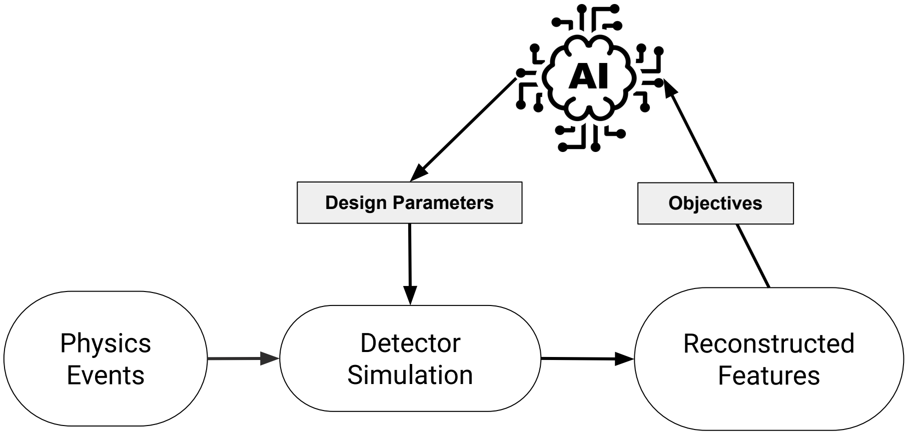

Figure 7.6: In AI-assisted detector design, we first generate physics events of interest, such as single π^+ events with varying momentum (p) and pseudo-rapidity (η). These events are introduced into the detector with specific design parameters. We reconstruct and analyze the simulated detector response to determine the figures of merit (objectives). These objectives are input to a MOO algorithm to guide the selection of the next design parameters to explore. This iterative process continues until we achieve optimal performance across all objectives. (Image taken from [66]).

7.4.1.1 MOO for Detector Design

Optimizing the design of large-scale detectors like ECCE is complex due to the multidimensional design parameter space and computationally intensive simulations. Traditionally, optimization was manual or brute-force, optimizing one figure of merit at a time. This is a problem well-suited for MOO.

Figure 7.6 shows an AI-assisted workflow for detector design. The main steps are:

- **Identify Objectives:** Determine potential objectives and their calculation methods.

- **Identify Parameters:** Identify optimizable detector subsystems and their parameters, and define their variation range.

- **Encode Design Criteria:** Reduce parameter number through parameterization, and encode constraints into it.
- **Automate Analysis:** Build a robust analysis pipeline for simulating detector response and extracting objectives, including checks to prevent unfeasible solutions and fitting procedure to avoid underfitting or overfitting.
- **Integrate MOO Algorithms:** Couple the objectives with a MOO algorithm and loop back to injecting the detector parameters for simulation.

7.4.2 Multi Objective Evolutionary Algorithm (MOEA)

An Evolutionary Algorithm (EA) aims to identify the global optimum for a specific problem, simulating evolution to achieve this. EAs excel in discovering the global optimum for intricate, non-linear optimization problems that traditional methods find challenging or costly to solve. Their robustness to noise and ability to find solutions in discontinuous search spaces underscore their utility. Key components of an EA include a population of potential solutions, a fitness function assessing each solution's quality, and genetic operators that spawn new solutions from existing ones. Various types of EA exist, such as Genetic Algorithms (GA), Evolutionary Strategies (ES), Differential Evolution (DE), and Particle Swarm Optimization. A comprehensive review of population initialized techniques of Evolutionary Algorithm (EA) is available in [90]. Genetic algorithms (GAs) [91], a category of Evolutionary Algorithm (EA) inspired by natural evolution, are employed for finding approximate solutions to optimization and search problems, forming the basis for the NSGA-II algorithm discussed subsequently.

NSGA-II algorithm: NSGA-II (Non-dominated Sorting Genetic Algorithm II), introduced by Kalyanmoy Deb in 2002 [92], is a renowned multi-objective optimization algorithm designed to identify the Pareto front of such problems. It extends the original NSGA by employing a mix of genetic operators—selection, crossover, and mutation—to produce a population of solutions. It ranks these solutions using a non-dominated sorting process based on Pareto dominance, a comparison measure of solutions concerning different objectives. This sorting is employed during offspring selection. NSGA-II's pseudo-code and full schematic are detailed below and in Fig. 7.7, respectively.

Algorithm 1 Steps of NSGA-II.

```
procedure NSGA-II
    Input: Population size, number of generations, crossover rate, mutation rate, and fitness functions
    Output: Pareto optimal solutions
    Initialize population $P$ with random solutions
    Evaluate the fitness of each individual in population $P$
    Sort the population $P$ into different levels of non-domination
    for $i = 1$ to number of generations do
        Select individuals for reproduction based on their non-domination level
        Apply crossover operator to produce offspring
        Apply mutation operator to introduce random changes to the offspring
        Evaluate the fitness of the offspring
        Combine population $P$ and offspring to form population $Q$
        Sort population $Q$ into different levels of non-domination
        Select the best individuals respecting constraints (if any)from population $Q$ to form the new population $P$
    end for
    Return the Pareto optimal solutions in the final population $P$
end procedure
```

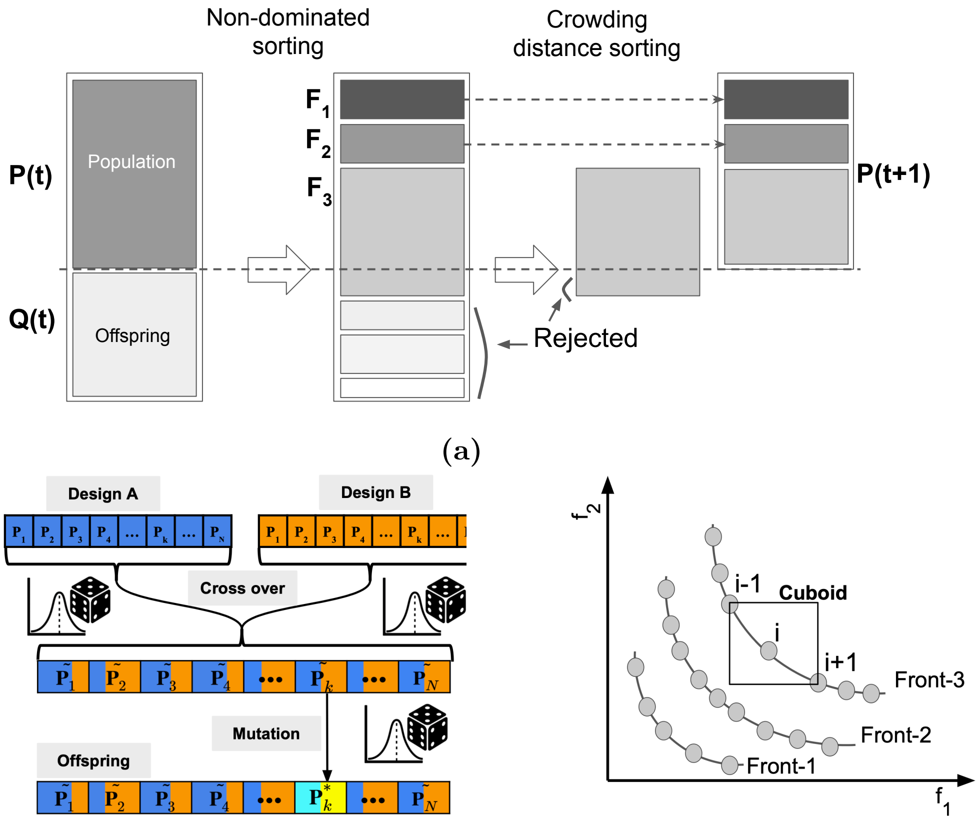

(a)

(b)

(c)

Figure 7.7: NSGA workflow: (a) adapted from [66], illustrates NSGA-II. Offspring Q_t are generated from an N-sized design population using a Genetic Algorithm (GA). The offspring and the parent population merge into R_t, which is sorted into non-dominated fronts F_s, with F_1 being the most optimal. Population size is then restored using the crowding distance metric. (b) Demonstrates a simple Genetic Algorithm, where crossover and potential mutation of two design points yield offspring. (c) Showcases the crowding distance calculation, an NSGA-II principle maintaining diversity by selecting uncluttered solutions in the objective space.

With a complete picture of MOEA algorithm and MOO for detector design, one can now design an end-to-end pipeline which can be used for detector design optimization. The developed pipeline is summarized in Fig 7.8.

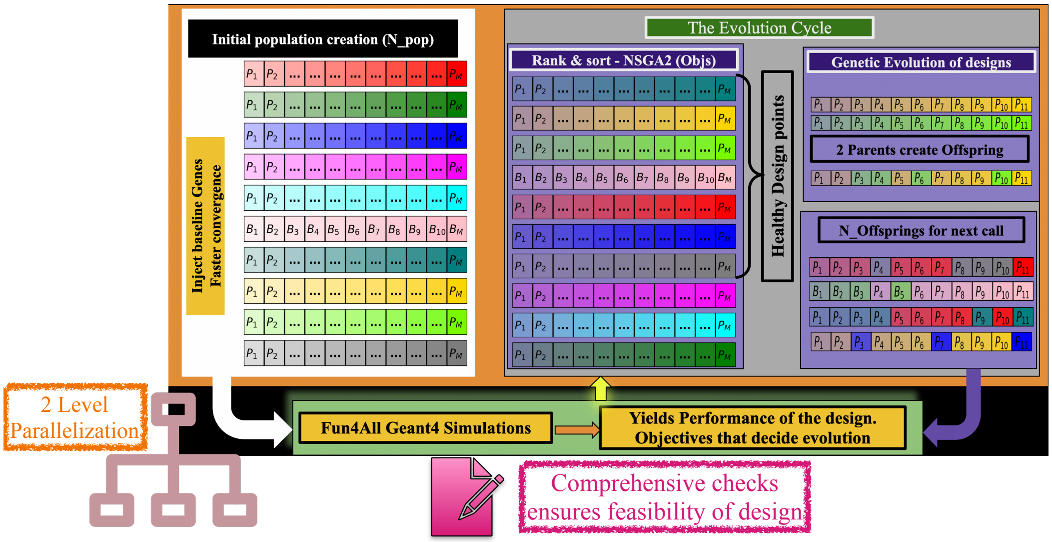

Figure 7.8: MOEA-based detector optimization pipeline: An initial population of detector design parameters is generated and each is used to simulate detector responses with GEANT4. Leveraging the inherent parallelization of MOEA, a 2-level parallelization, as discussed in [66], is implemented. Objectives are evaluated and passed to the evolution cycle where they're sorted using the NSGA-II algorithm to produce new offspring. The process iterates until a termination criterion is met.

7.4.3 Multi Objective Bayesian Optimization (MOBO)

Multi Objective Bayesian Optimization (MOBO) is a multi-objective variant of Bayesian Optimization (BO), enhancing it to optimize for multiple objectives. It aims to find a Pareto front, representing optimal trade-offs between different objectives (see Appendix D.0.2). MOBO utilizes a multi-objective acquisition function to guide the Pareto front search. It employs a trade-off balance between exploration and exploitation of the search space. MOBO uses a probabilistic Pareto front model, like a Gaussian Process (GP), to facilitate new solutions. The GP model, trained on current solutions, predicts the Pareto front at new points. The acquisition function then selects points expected to enhance the Pareto front.

qNEHVI Quantile-based Normalized Expected Hypervolume Improvement (qNEHVI) [93] is based on the hypervolume concept. In this work, we use qNEHVI as the acquisition function to guide the Pareto front search, focusing on improving less explored regions by dividing the Pareto front into different regions. qNEHVI is computationally efficient [94], making it ideal for solving problems with numerous objectives and constraints, like detector design optimization requiring intensive simulations.

Algorithm 2 Pseudo code for qNEHVI based MOBO

```
procedure QNEHVI
    Input: Initialize population P with SOBOL initializer
    Output: Optimal solution
    for $i = 1$ to iteration number do
        Evaluate, sort solutions in P and calculate hypervolume indicator
        Divide solutions into quantiles, select quantile with lowest hypervolume
        Select solution with highest EHVI and update P respecting constraints
    end for
    Return points with highest acquisition function value as optimal solution
end procedure
```

7.5 AI-assisted Detector Design

Optimizing the EIC detector carries significant implications for performance and cost [95]. As discussed in [67], Artificial Intelligence (AI) enables complex combinatorial searches and handles multi-objective, multidimensional problems, identifying correlations within design parameters. ECCE incorporated these AI methods during the detector proposal phase, initially steering design choices and later fine-tuning parameters [95]. An AI pipeline was implemented to facilitate the sequential design optimization, aligning with the different ECCE working groups [83] in a post hoc decision-making process. This sequential approach involved multiple optimizations leading to the final ECCE tracker design, each surpassing its predecessor. Hence, a base reference design exists for each optimization. These optimizations were classified into two phases: Phase-I, the early stage, and Phase-II, the later stage with more realistic simulations primarily on tracking support structures.

7.5.1 Tracker simulation using Fun4All

The simulation and detector response was processed using the Fun4All framework [96–98]. ECCE-EIC core software employed daily, weekly builds, and tagged production releases [99]. The framework's development was steered by the need for swift data processing. Its modular design allows for independent development and easy integration of different detector subsystems. Numerous event generators like HIJING [100], PYTHIA [101], Sartre [102], single particle and others are supported through the EIC-smear interface and Fun4All. Various detector system macros are bundled through central simulation macros, facilitating detector design modifications. The Fun4All framework outputs events in root files at different reconstruction levels.

7.5.2 Objective Functions

Several key detector response metrics were identified in the EIC yellow report [67] to fulfill the EIC physics program. Reconstruction performance (Kalman Filter efficiency) was among the objectives considered for optimization. A comprehensive list of the objectives used throughout the optimization is summarized in Table 7.1.

Objectives	**Definition**
Momentum Resolution ($\frac{dp}{p}$ [%])	$\frac{dp}{p} = \frac{p_{\text{reco}} - p_{\text{true}}}{p_{\text{true}}}$
Theta Resolution ($d\theta$ [mRad])	$d\theta = \theta_{\text{reco}} - \theta_{\text{true}}$
Phi Resolution ($d\phi$ [mRad])	$d\theta = \theta_{\text{reco}} - \theta_{\text{true}}$
Kalman Filter Inefficiency	No of tracks that failed to be reconstructed.
Theta Resolution at PID ($d\theta_{\text{PID}}$ [mRad])	$\theta_{proj} = \tan^{-1}\left(\frac{(\vec{p}_{reco} - \vec{p}_{true}) \cdot (\vec{p}_{true} \times \vec{z})}{\lvert\vec{p}_{true}\rvert \lvert(\vec{p}_{true} \times \vec{z})\rvert}\right)$
Phi Resolution at PID ($d\phi_{\text{PID}}$ [mRad]	$\phi_{proj} = \tan^{-1}\left(\frac{(\vec{p}_{reco} - \vec{p}_{true}) \cdot (\vec{p}_{true} \times \vec{z}) \times \vec{p}_{true}}{\lvert\vec{p}_{true}\rvert \lvert(\vec{p}_{true} \times \vec{z}) \times \vec{p}_{true}\rvert}\right)$
Vertex resolution (DCA_{2D}) [μm]	Spatial separation between the primary vertex and the reconstructed track projected back to the z-axis.

Table 7.1: Various objectives used during optimizations. Note that not all the objectives are used simultaneously during a given optimization. Utmost 3 objectives were simultaneously optimized for any given optimization

The EIC inner tracker spans a pseudo rapidity η range between -3.5 to 3.5, covering various detector systems (Figure 7.4). Consequently, the objectives must be optimized across all regions, with a focus on the transition region between different detectors in the central and end cap areas. The tracker design must also optimize performance across a momentum range of $0.5 - 30$ GeV. Objectives are defined in bins of η and momentum (p) for each design point. For each point, N events of π^- tracks are simulated across a momentum and η range and analyzed in their respective bins.

For example, to evaluate the **global momentum resolution**, we:

1. Simulate N tracks of π^- particles across a range of momentum p and pseudo-rapidity η for a given design point.
2. Bin the data in momentum p and pseudo-rapidity η. A distribution is created in each bin using the momentum resolution defined in Table 7.1.
3. Fit the distributions with a double Gaussian distribution, ensuring the mean of the distribution is consistent. A comparison between single and double Gaussian

fits is summarized in [66].

4. Define the resolution as
$$\sigma_{DG} \sim \frac{A_1\sigma_1 + A_2\sigma_2}{A_1 + A_2}, \tag{7.57}$$
with σ_{DG} as the resolution calculated with σ_1 and σ_2 being the standard deviations extracted from the double Gaussian fits, scaled with their corresponding amplitudes A_1 and A_2.

5. Compare new resolutions in each bin to those of the baseline design, providing a ratio $R(f)_{p,\eta}$ in each bin.

6. Build a global figure of merit with a weighted sum of these ratios for both the relative momentum and the angular resolutions:
$$R(f) = \frac{1}{N_\eta}\sum_\eta \left(\frac{\sum_p w_{p,\eta} \cdot R(f)_{p,\eta}}{\sum_p w_{p,\eta}}\right), \tag{7.58}$$
where f is one of the metrics from Table 7.1, and the weight $w_{p,\eta} = 1/\sigma^2(f_{p,\eta})$ is calculated in each η, p bin, proportional to the inverse of the variance of the objective functions f. This procedure is detailed in [66].

The performance of a design solution can be visualized using petal diagrams, which depict the performance of each objective and global objectives simultaneously. More on petal diagrams can be found in [103].

7.5.3 The Optimization Workflow

An automated optimization workflow has been implemented on JLab's scientific computing clusters [104]. This workflow, composed of two parts, is modular, facilitating deployment on different scientific computing clusters.

7.5.3.1 The Pipeline

MOO Algorithm Block: Two algorithms, MOEA and MOBO, were implemented. They take the prior performance of design solutions and suggest new design points. The MOO block uses `pymoo` [103] for the MOEA pipeline and `Ax-BoTorch` for the MOBO pipeline. Design solutions are run in parallel, with MOEA being naturally parallelizable and MOBO not parallelized for this study[3]. Performance studies of MOEA are reported in [66].

Simulation Block: This block simulates the detector response for a given design point using the Fun4All framework GEANT4 simulation. To accommodate parallel operation, an explicit multi-processing wrapper was created. A schematic of this operation is found in [66], and the average time taken to simulate N events is shown in Figure 7.9c. Design feasibility checks are also performed before running a simulation.

---

[3] Parallelization is feasible for MOBO, but was not necessary for this study. Performance studies for MOBO will continue as part of future work.

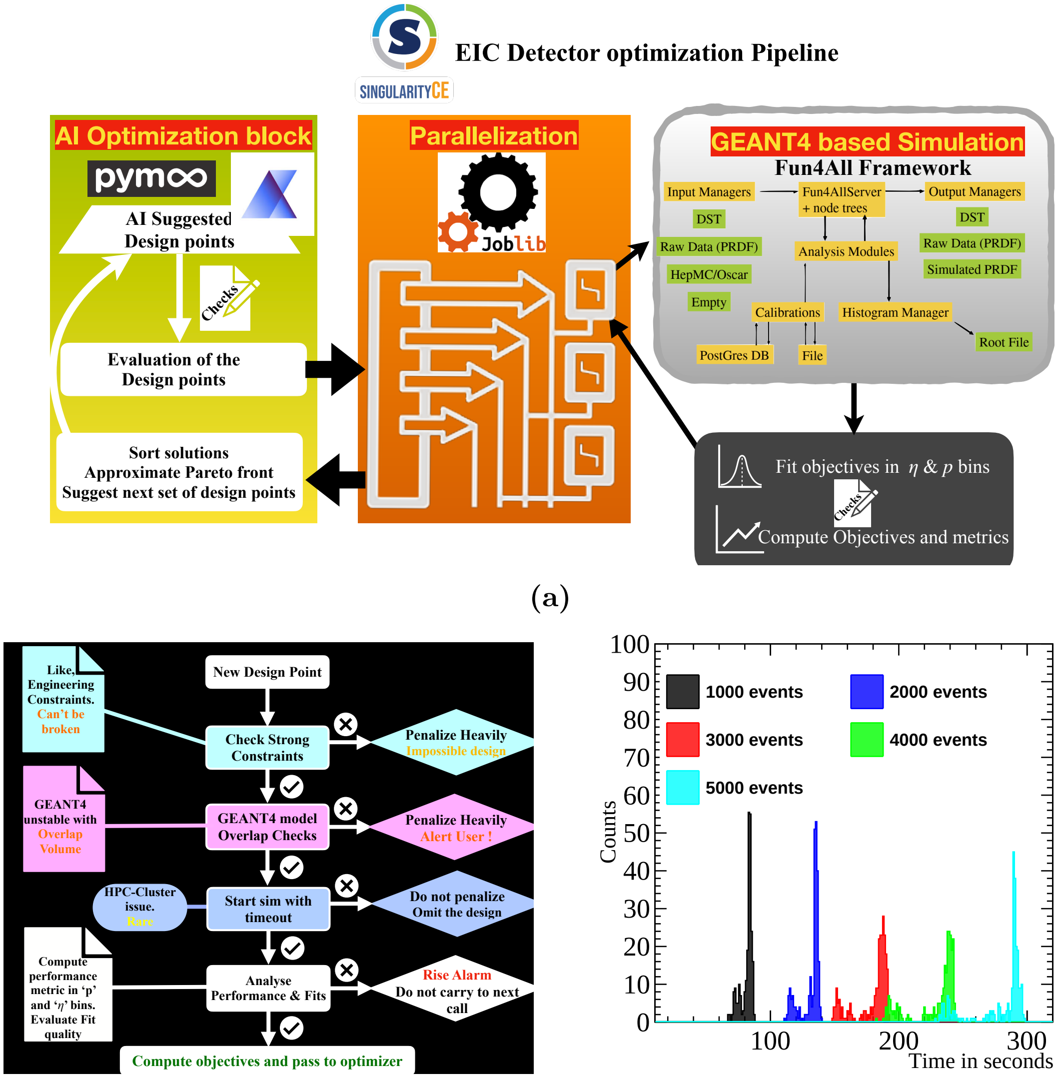

(a)

(b)

(c)

Figure 7.9: **(a)** Summary of AI optimization pipeline. **(b)** Series of checks performed throughout all optimizations. **(c)** Average time taken to simulate N events in Fun4All framework on a single core. For simulating a single design solution multiple instances of Fun4All are initiated each with 5000 events.

Analysis Block: Here, simulated detector responses are analyzed and objectives are computed. Ratios are formed with a baseline design and fed back into the algorithm block to suggest new design points. Stability checks are also performed on the extracted objectives.

Design Criteria Encoding and Checks: Design criteria encoding is crucial for optimization. For example, the inner radius of the disk tracker (Figure 7.4) depends on the radii of the beam pipe and can be parameterized as a function of the 'z' position. This reduces the total number of design parameters and ensures no potential detector overlaps. Checks for overlaps and hard constraints are performed to ensure only feasible designs are simulated.

Checkpoints and Monitoring: Checkpoints are created at every iteration, allowing for easy monitoring and control over the optimization process. The optimization pipeline is summarized in Figure 7.9.

Parallel Pipelines and Continual Optimization The optimization process is iterative. At any given time, N candidate configurations are studied, creating an optimization pipeline resulting in a Pareto front of solutions. This new information aids in the steering of the design, rejecting some configurations and identifying new reference points. New optimization pipelines are defined based on these alternatives, and the process is iterated. The interaction between the ECCE Teams working on Physics(PWG), Detector(DWG), and Computing(CWG) is enhanced by AI during the design process. The parallel pipelines in the continual optimization process are shown in Figure 7.10.

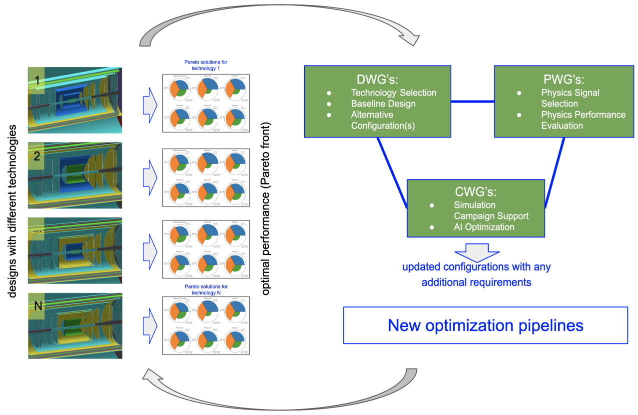

Figure 7.10: Flowchart illustrating the collaboration among various Working Groups for continuous optimization. Each optimization pipeline generates a list of design solutions, proposed by the AI Working Group to detector experts, guiding the design process. Each sequential optimization strives to enhance the previous iteration, making the use of ratio-defined objectives intuitive. Image taken from [66].

7.5.4 Optimization: Phase-I

Phase I optimization, spanning June to September 2021, began with a simplified GEANT4 detector implementation, such as detector modules on a basic aluminum conical support structure. The optimization pipelines included a symmetric arrangement of detectors with simple geometric models for DIRC and AC-LGAD-based TOF detectors. Figure 7.11 shows a GEANT4 visualization of the Phase-I tracker.

In these pipelines, we evaluated various inner tracker technologies using the MOEA method (Section 7.4.2). This process provided performance insights for each configuration, guiding the choice of barrel and disk technologies. Configuration 4 was eventually chosen as the new baseline for Phase-II optimizations. We also compared two main designs for disk trackers, with the smaller pixel size design offering superior performance.

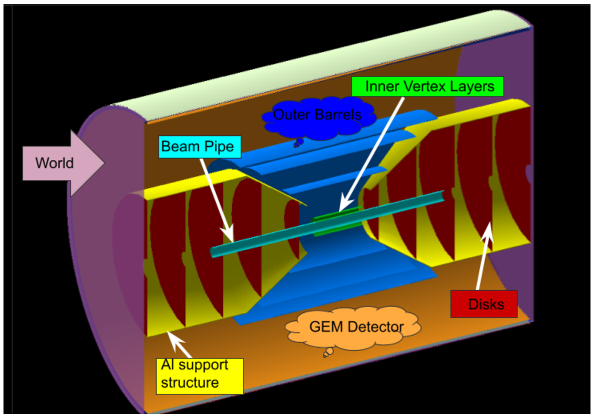

Figure 7.11: GEANT4 visualization of the Phase-I optimized tracker, featuring simplified silicon disks and an aluminum support structure.

Configuration	Combination
1	2 Vtx (ITS3) + 2 Sagitta (ITS2) + 2 Outer (ITS2)
2	2 Vtx (ITS3) + 2 Sagitta (ITS3) + 2 Outer (ITS2)
3	2 Vtx (ITS3) + 2 Sagitta (ITS2) + 2 Outer (μRwell)
4	2 Vtx (ITS3) + 2 Sagitta (ITS3) + 2 Outer (μRwell)

Table 7.2: The EIC yellow report's base configuration [67] featured two vertex layers, two middle (Sagitta) layers, and two closely-spaced outer layers for redundancy. Various technologies were explored for their performance potential.

The optimization pipeline, primarily based on pion (π^-) particle gun samples, was found to yield consistent results with both π^- and π^+ simulations. The kinematic range explored is presented in Table 7.3. Given the symmetric detector design across the hadron-going and electron-going directions, optimization was performed only in the hadron-going direction. Simulations assumed a 100% hit efficiency for all tracking layers.

Kinematic variable	**Minimum**	**Maximum**
Momentum p	1 GeV	30 GeV
Pseudorapidity η	0.0	3.5

Table 7.3: Table summarizing the overall kinematic range used in the process of optimization. A total of 15 momentum (p) bins (equally spaced) and 3 pseudorapidities (η) bins (central region, transition region, and hadron-going region) were used in the optimization.

Objectives Three key objectives[4] guided the optimization process: (i) momentum resolution ($\frac{\Delta p}{p}$), (ii) angular resolution ($d\theta$), and (iii) Kalman Filter Inefficiency (KFInEff). By comparing these metrics to baseline configurations, we identified sets of optimal solutions through parallel pipeline execution.

Encoding design criteria The tracker detector geometry in Figure 7.11 has a fixed cone angle from the support structure of 36.5°, linking the barrel layers' length and radius. This structure also prescribes the maximum disk layer radius as a function of its 'z' position, leading to a simple optimization problem parametrization. Moreover, to avoid overlaps, we define design parameters incrementally from previous layers. For instance, barrel layer radii follow an incremental pattern (r_0, $r_0 + \Delta r_1$, $r_0 + \Delta r_1 + \Delta r_2$, ... , $r_0 + \Delta r_1 + ... + \Delta r_6$). The same approach applies to disk layer design parameters.

During Phase I, we optimized up to 11 design parameters, including radii of 6 barrel layers and 'z' positions of 5 disk trackers, while ensuring no overlaps between detectors. There were four constraints, organically developed in collaboration between the AI and tracker detector working groups:

- Maximum radius of second vertex layer: 15 cm.

---

[4] See Table 7.1 for definitions

- Maximum radius of outermost barrel layer: 51 *cm*.
- Maximum radius of second sagitta layer (4^{th} layer): 45 *cm*.
- Maximum absolute 'z' position of the final disk: 125 *cm*.

MOEA algorithm was used to carry out these optimizations. Refer to Table 7.4 for detailed parameters.

Description	**Symbol**	**Value**
Algorithm used	MOEA	NSGA-II
# Objectives	M	3
# Offspring	O	30(50)
# design Parameters	D	11
# calls (tot. budget)	-	200
# Cores	-	same as offspring
# Charged π^- tracks	N_{trk}	80k
Population Size	N	100

Table 7.4: Hyperparameters used in optimization, with values in parentheses indicating the maximum used in alternate pipelines. Checkpoints provide snapshots of ongoing optimization, while a two-tier parallelization accelerates the process (see Figure 7.8 for details).

Outcome of optimization This phase of optimization provided key insights into the effective combination of ITS3 and μRwell barrel detectors, meeting physics requirements while minimizing technology risks. Each optimization yielded a set of Pareto optimal solutions. A representative optimal solution from each pipeline is depicted in Figure 7.12. Phase-I optimizations offered valuable insights into the optimal technological choices to meet the Physics Working Group's requirements. Solutions favored larger cylinder radii and extended disk placements along the 'z' direction. Initially assuming symmetry between forward and backward directions, later findings revealed less space for disk trackers in the backward direction, expanding the optimization parameter space. The inclusion of additional detectors, such as TTL, led naturally to Phase-II optimizations.

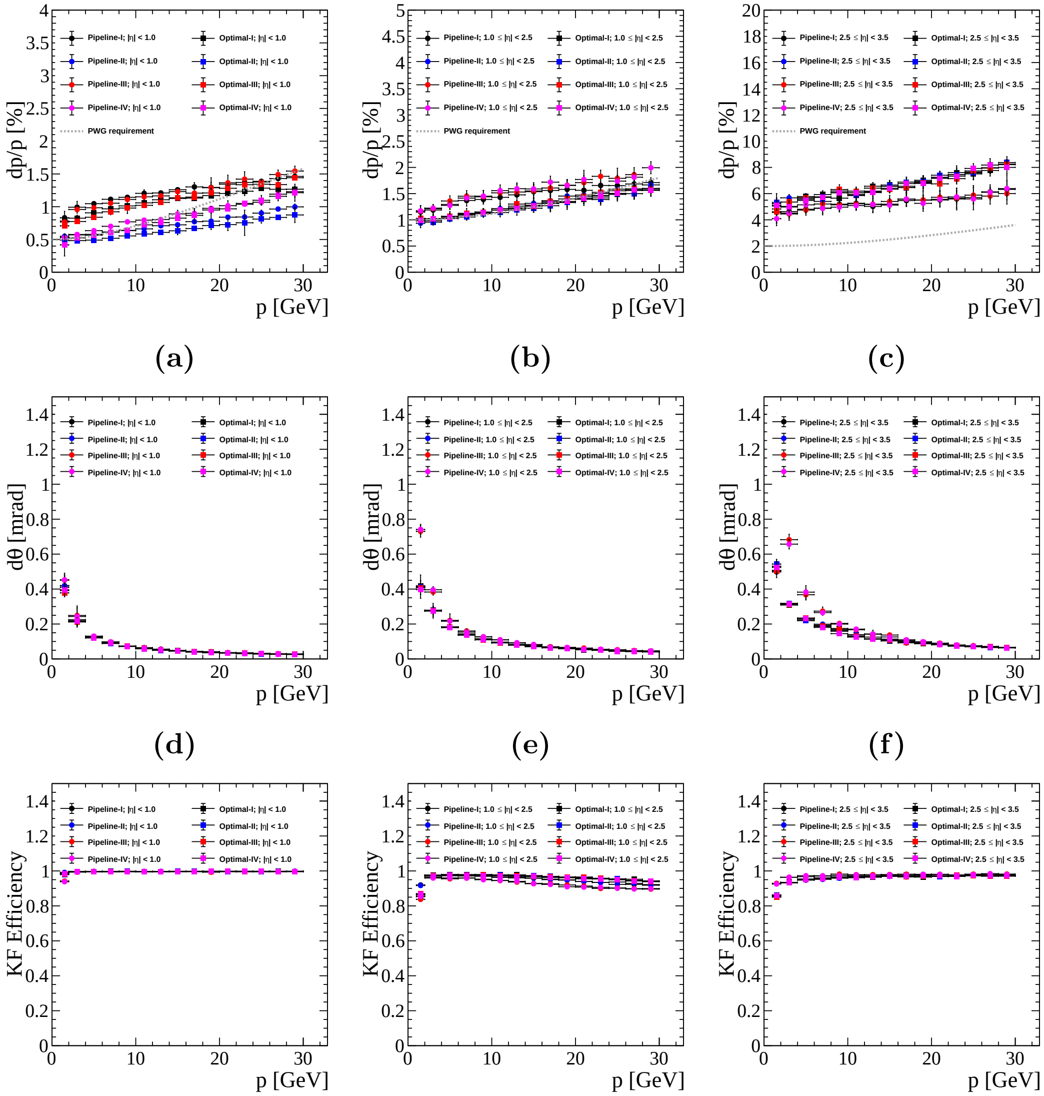

(a) (b) (c)

(d) (e) (f)

(g) (h) (i)

Figure 7.12: Top row represents momentum resolutions, the second, angular resolution (θ), and the third, Reconstruction Efficiency. Plots illustrate the performance of four pipelines across three pseudorapidities (η) bins: central, transition, and end cap regions. Given the tracker's symmetric design, absolute η is optimized.

7.5.5 Optimization: Phase-II

Phase II optimization, running from Sept-2021 to Nov-2021, incorporated a more realistic support structure and finer simulations of PID and TTL detectors. More rigorous engineering constraints were applied, such as sensor size for the MAPS detector (ITS3). This phase introduced an asymmetric detector arrangement in endcap regions, with a maximum of 4 EST disks electron-going and 5 FST disks hadron-going. The varied spatial arrangement allowed for adjustable angles subtended by detectors. A comprehensive parameterization was developed based on the support cone structure (Figure 7.13). More details can be found in [66]. Key results from Phase II are summarized below.

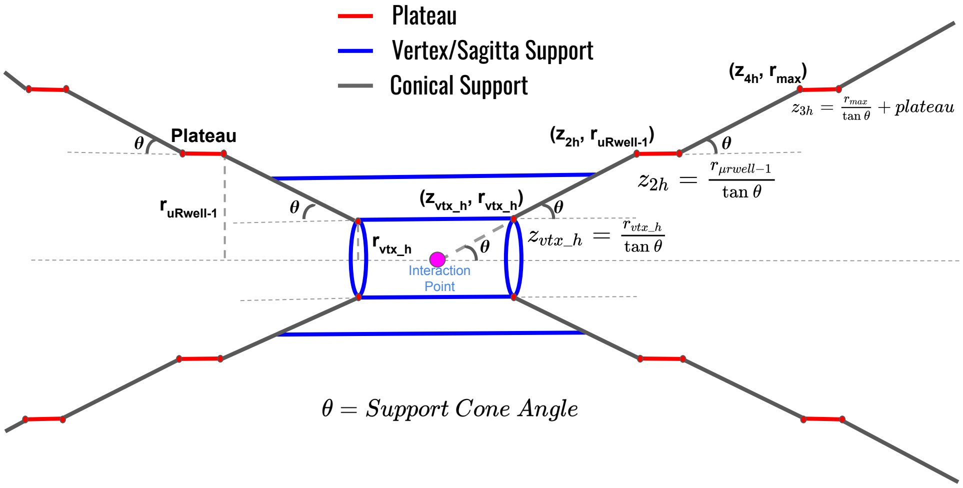

Figure 7.13: Parametrization of the Inner Tracker Support Cone: Defined by five variables: θ (projection angle), r_{vtx} (vertex support radius), $r_{\mu rwell-1}$ (μRwell-1 radius), plateau length, and r_{max} (maximum inner tracker radius). A detailed explanation can be found in [66].

Objectives During this phase, up to three objectives were concurrently optimized across various pipelines. These included: (i) Momentum resolution ($\frac{\delta p}{p}$), (ii) Angular resolutions ($d\theta$) at PID locations, (iii) Kalman Filter Inefficiency (KFInEff), and (iv) Vertex Resolutions ($\mathrm{DCA}_{\mathrm{2D}}$). Ratios formed from baseline configurations facilitated parallel pipeline execution to find optimal solutions.

Encoding design criteria The optimization process utilized a parametrization based on the tracker's support structure. Predominantly, the optimization considered the support cone angle, cylindrical tracker radii, disk tracker 'z' locations, and TTL detectors. Details of the total design parameters used for optimization are found in Table 7.5.

	design pars	**objectives**
ECCE tracker design (non-projective)	5 disks z (hadron endcap) and 4 disks z (electron end cap) location, 2 μRwell layers Radius	momentum resolution; angular resolution; Kalman filter efficiency; (pointing resolution)
ECCE ongoing R&D design (projective)	Angle Tracking Support (θ), 2 TTL z-location, 1 uRwell-1 Radius, 3 FST disks, 2 EST disks (9 parameters);	momentum resolution; angular resolution; Kalman filter efficiency; (angular resolution at dRICH; pointing resolution)

Table 7.5: Dimensionality of the optimization pipeline: Constraints include (i) beam envelope dimensions compatibility with inner radii of endcap disks and barrel's inner vertex layer; (ii) alignment of barrel layer lengths and disks' outer radii with Al-shell support. These reflected in the GEANT4 design, are verified for overlaps during optimization. Parentheses denote additional exploratory objectives.

The design optimization includes two types of geometrical constraints: (a) *strong constraints* like a 10 cm minimum distance between disks, which mustn't be violated, and (b) *soft constraints*, which can be slightly violated to control sensor coverage. For instance, the difference between the outer and inner radii of each disk should be a sensor cell size multiple, but minor post-hoc adjustments are allowed for practical detector geometry. Two additional constraints are reflected in the GEANT4 design: (i) Compatibility of endcap disks' inner radii and barrel's inner vertex layer with the beam envelope dimensions, and (ii) compatibility of barrel layer lengths and disks' outer radii with the tracking support structure. Finally, potential overlaps among modules are checked throughout the optimization.

Outcome of optimization Each optimization generates trade-off solutions. Figure 7.14 illustrates the convergence of the final proposed ECCE design, using hypervolume as a performance metric. The diagram visualizes the three objective values of a Pareto front solution. This figure also compares the proposed ECCE tracker performance to the EIC Yellow Report.

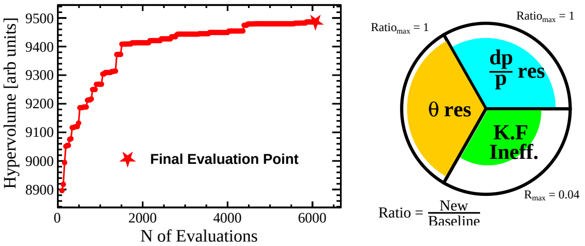

Figure 7.14: Hypervolume depicting optimization convergence. As referenced in Section 7.4 and Appendix. D.0.1, hypervolume improvement fell below tolerance, concluding the optimization. The right plot presents the performance of the final evaluated design (red star).

Phase II yielded two designs: (i) the Non-projective tracker proposed by ECCE, and (ii) the Projective design optimizing support material budget. The Non-projective design was mainly proposed due to the project timeline, whereas the Projective design, labelled “Ongoing R&D”, continues to be explored — the corresponding design is displayed in Figure 7.15 (left). Phase II, which included support cone angle parametrization (as explained in Figure 7.13), explored a cone angle projective to the dRICH detector. This design (Figure 7.15) minimized the tracker’s support material budget by concentrating material within a narrow polar angle (θ), as evident in Figure 7.16. The two resultant geometries from this phase are summarized in Figure 7.15.

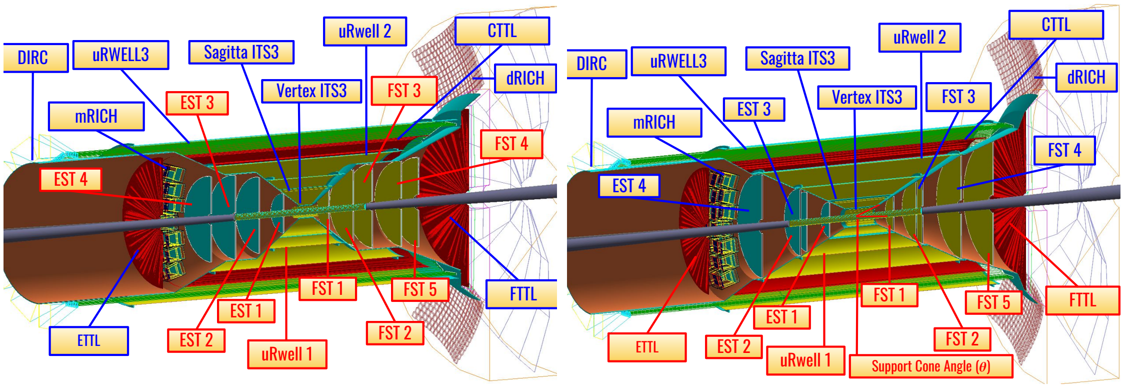

Figure 7.15: Non-projective (left) and ongoing R&D projective (right) designs: The figures show ECCE non-projective and projective designs. Red labels indicate optimized sub-detectors; blue labels mark fixed ones due to constraints. The non-projective design (left) resulted from inner tracker layers optimization with a fixed support structure. The projective design (right) aimed to reduce readout and service impacts on tracking resolution. Refer to [66] and [83] for further details.

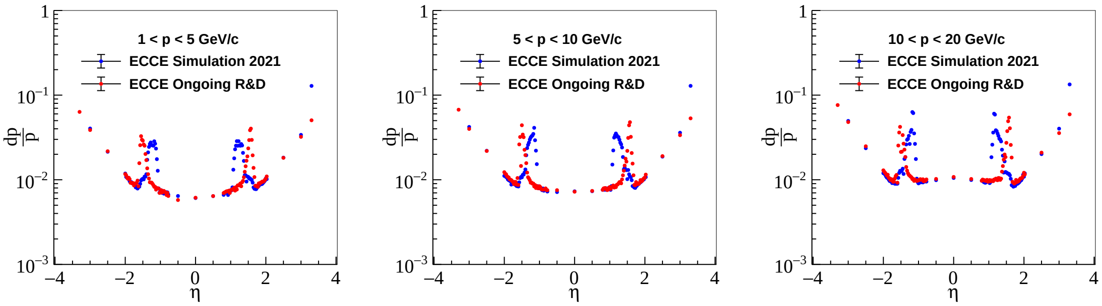

Figure 7.16: Momentum resolution scan for charged pions in pseudo-rapidity bins across different momentum values. Solid points represent the projective design, star points the non-projective design. The projective design narrows the tracking dead area to a smaller η range.

7.5.6 Optimization: Phase-III

Phase III, transitioning from the ECCE concept to the ePIC detector, will expand optimization to include more design parameters and kinematics, using a more realistic geometry. A proof-of-concept optimization model and visualization framework were developed for future EIC detector optimization. However, increased complexity demands more evaluations for convergence, leading to high latency for MOEA methods. To address this, a MOBO algorithm-based pipeline will be designed to find optimal designs with fewer calls. A web application was also created to interactively navigate through the solutions, accessible at AI4EIC-Detector-Optimization-MOBO. Work on the ePIC design optimization is anticipated to progress beyond the completion of the thesis.

Chapter 8

Conclusions and future work

8.1 Summary

Hadron spectroscopy involves the study of strong nuclear interactions. The GlueX experiment has collected the world's largest photoproduction dataset for the $\omega\pi^0$ system just in its first phase of data taking. The GlueX program will thus achieve improved purity in search for mesons and baryons containing strange quarks.

Gain calibration efforts in BCAL at GlueX from 2018 to 2021 were presented in Chapter 3. Additional studies that were made to improve calibrations in the BCAL can be found in technical reports [52] and [53]. Further studies to improve the detector resolution using Machine Learning (ML) methods were explored and have been reported internally within the research group. Several technical notes summarizing the calibration efforts have been written during the course of the thesis [51, 55].

The physics objective of this dissertation was to study the photoproduction reaction $\gamma p \to \omega\pi^0 p$ in GlueX and perform PWA to study the properties of the axial vector b_1 meson in its neutral state. Understanding the decay of b_1 meson will help in carrying out PWA of even more complicated channels. Since the neutral b_1 decays predominantly through $\omega\pi^0$, a portion of events in that $\omega\pi^0\pi^0$ system came from the $b_1\pi^0$ decay, as predicted by theory, which in turn, could have decayed from a more complicated channel. To select out the $\omega\pi^0$ strategic data analysis cuts are made which were discussed in detail in Chapter 4.

An amplitude analysis model was developed to describe the intensity of $\omega\pi^0$ events as described in Chapter 1. The data analysis included selection of $\omega\pi^0$ events, followed by a Partial Wave Analysis (PWA) analysis using `AmpTools` on the reaction $\gamma p \to \omega\pi^0 p$, that was presented in Chapter 5. In order to select the combinations of waves used in PWA, a model selection strategy using LRT and information criteria (AIC and BIC) was deployed. A recipe to compute the yield of b_1 meson using PWA was illustrated in a mass range between $1.0 - 2.0$ GeV in bins of 80 MeV, in three t ranges. The fits to data show good agreement in all its angular distributions. In the mass region between $1.0 - 1.30$ GeV, the $[J^P]^{(\epsilon)}$ state of $[1^+]^{(+)}$ was found to be the most dominant wave. The second most dominant wave in this region was found to be $[1^-]^{(+)}$ with no resonant structure. PWA shows that the b_1 production mechanism is through unnatural parity exchanges since the contribution from $[1^+]^{(-)}$ was found to have an insignificant contribution to the overall intensity. In the higher mass region between $1.3 < M(\omega\pi^0) < 2.0$, more J^P states, and especially the higher J^P states are required to better describe its intensity in the higher mass region between. These observations agree with the results reported by previous experiments. In particular, the E852 Collaboration [26] had reported an enhancement in the higher mass region at ~ 1650 MeV which in an exotic 2^{+-} wave. Furthermore, that study also reported the dominance of ρ_3 in the 3^{--} wave at ~ 1690 MeV.

A more detailed look at the b_1 mass region was presented in Chapter 6, where the main focus was to understand the decay of the b_1 meson and specifically extract the `dsratio` of b_1 through PWA. Out of all the systematic studies performed, the choice of waves is found to be the most dominant systematic. Furthermore, the extraction of `dsratio` was found to be strongly correlated as a function of $|t|$. This is currently attributed to any non-baryonic/non-baryonic($M(p\pi^0)$) resonance backgrounds under the b_1 peak. The extracted `dsratio` is mainly dominated by systematic errors, and the statistical precision with GlueX Phase-I data is at least an order of magnitude better than previously reported E852 Collaboration results. In conclusion, the extracted `dsratio` across the three $|t|$ bins is found to be consistent within one another as well as the current PDG value of 0.277 ± 0.027 [4].

In this dissertation, the relative phase between the D-wave and the S-wave in b_1 (`dphase`) was fixed to be zero. Studies have been made with allowing the relative phase between the D-wave and the S-wave to vary. However, in the current formulation of the amplitude analysis model, this generates ambiguities in the solution with both parameters allowed to vary. Figure 8.1 shows the result of a 2-d parameter scan between the `dsratio` and `dphase`. The result suggests a correlation between the parameters which is unexpected.

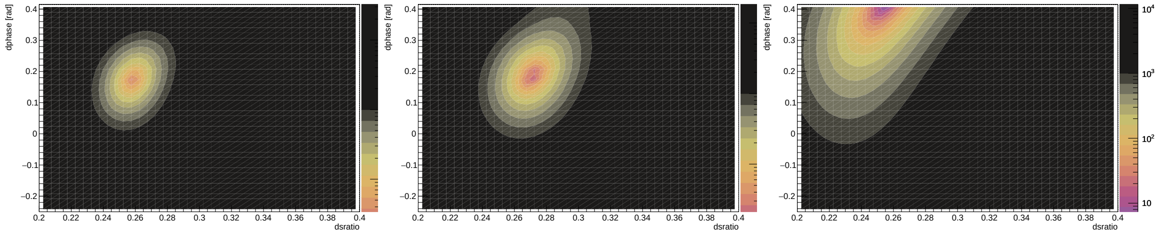

Figure 8.1: 2D parameter scan on GlueX Phase-I data. Just like the parameter scan performed in Section 6.2, a 2D parameter scan between `dsratio` and `dphase` with waveset `1p1mPosRefl` across three $|t|$ bins was performed. It was found there there are at least two minimum solutions in the middle figure, and solutions converge with a higher `dphase` in the last figure.

Finally, a novel methodology for optimizing the tracking system at EIC Comprehensive Chromodynamics Experiment (ECCE) was presented in detail in Chapter 7. This is one of the first methods to integrate current optimization algorithms like MOEA and MOBO to full GEANT4 based detector simulation. A proposal to extend the study to the current ePIC detector system is also presented along with a procedure to extend the methodology to to any HEP detector design experiments. The work led to an ECCE collaboration paper [66] and the work has been presented at several conferences and a workshop.

The iterative nature of the ECCE tracker's optimization process is depicted in Figure 8.2. Each optimization phase informs the next, creating a continuous cycle of improvement.

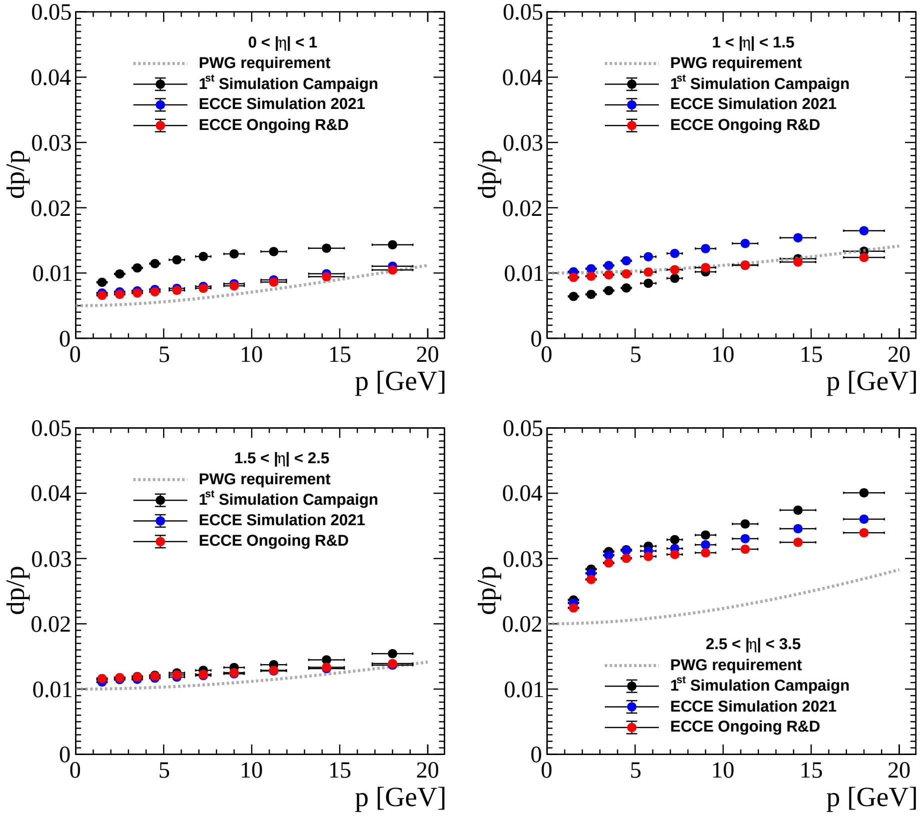

Figure 8.2: Momentum resolutions across four η bins. Left to right: $|\eta| < 1.0$ (barrel), $1.0 \mid \leq \eta < \mid 1.5$ (transition region), $1.5 \leq |\eta| < 2.5$ and $2.5 \leq \eta < 3.5$ (end-caps). Black points: first simulation campaign (preliminary phase-I design with undeveloped support structure); blue: final ECCE detector proposal; red: ongoing R&D for support structure optimization. Except for the transition region, all η bins show improved performance over the preliminary design. The transition region's performance difference is due to its lack of realistic material budget simulation. The projective design's improvement is also visible in this region. (Figure adapted from [66]).

The developed framework enables comprehensive system optimization, suitable for the newly formed ePIC collaboration to refine the detector system. It allows extending the design optimization to a larger sub-detector system and integrating physics analyses into the optimization process as additional objectives. Plans are in place to further AI-driven detector optimization, particularly the tracking system and PID sub-detectors.

8.2 Future Studies

8.2.1 Future Studies on PWA of neutral b_1 meson

In the immediate future, studies have been proposed to reduce the systematic uncertainty in measuring `dsratio`. To begin with, the non-baryonic resonance contribution under the b_1 peak has to be studied. This can be done by applying the $M(\pi^0 p) > 1.5$ GeV cut and assessing the systematic variation of this cut on `dsratio`. Secondly, the systematic uncertainty due to the width of the mass bin used in extracting `dsratio` can be reduced by performing a hybrid mass dependence fit as discussed earlier in Section 6.4.2. Finally, systematics due to analysis cuts have to be examined. For instance, the χ^2/NDF of KinFit cut is currently too strict and it can be relaxed to see its systematic effect. The other selection cut to be studied will be the two-dimensional ω-side band cut. A variation in this cut will help in understanding the non-omega resonance contributions. However, initial studies appear to indicate that these variations will have minimal influence compared to the ones included in this dissertation.

The procedure to extract b_1 yield in various mass bins has been illustrated in this dissertation. Six combinations of waveset were used to perform PWA to extract the

b_1 yields. More combinations of wavesets (up to $J < 4$) could be studied with special attention in the higher mass regions. The contribution of higher J^P states as reported by other experiments should be studied. Finally, once the yields are extracted for the b_1 meson, they can be applied in calculating the differential cross-section as shown in Equation 5.53. For differential cross-section measurements, external systematics such as detector acceptance should be studied. For example, the tracking efficiency and the photon detection efficiency in the calorimeters (FCAL & BCAL), have to be studied mainly to account for the normalization of the overall extracted yield.

With all these systematics done, it will be a leap forward in understanding the b_1 meson at GlueX and creating the pathway to performing a full PWA on the $b_1\pi$ channel which will facilitate the study of the properties of the lightest hybrid meson $\pi_1(1600)$.

8.2.2 Future Studies on AI-assisted detector design

A complex detector geometry and larger statistical physics sample necessitate an advanced optimization workflow. We present a conceptual workflow in Figure 8.3 that can be adapted for more distributed optimization. The distribution level depends on the detector geometry's complexity (time taken by GEANT4 simulations) and physics inputs.

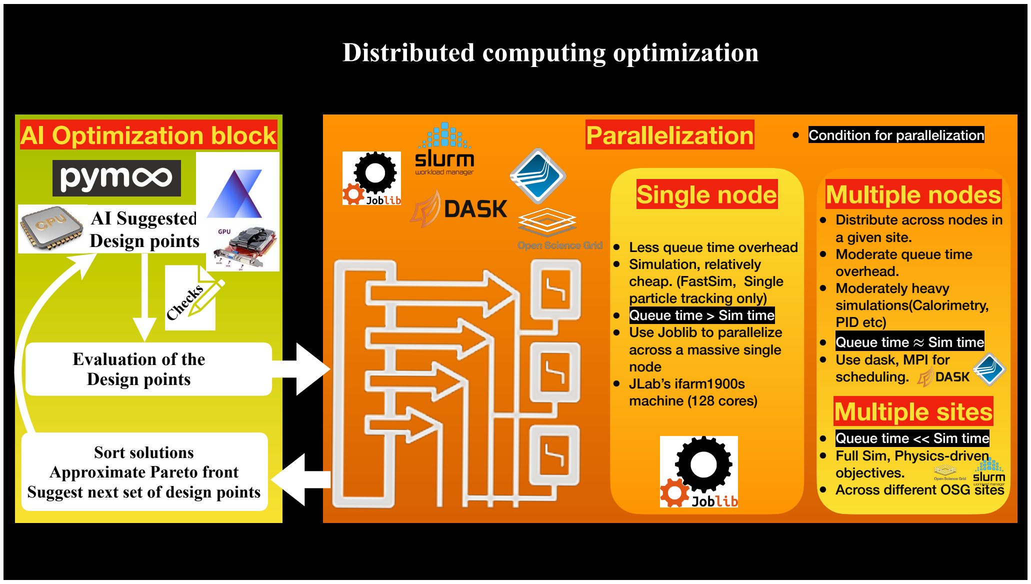

Figure 8.3: Schematic of future optimization workflow, illustrating adaptable AI and parallelization components based on the time overhead from GEANT4 simulations.

Queue time refers to the duration before job execution starts, and *simulation time* denotes the time required for simulating a specific design point with particular statistics (N). Physics reaction simulations also add to the simulation time. A workflow manager can be devised based on these parameters. In this dissertation, simulations utilized a π^- particle gun, resulting in a longer Queue time than the simulation time. Jobs were parallelized using `joblib` within a single node at TJNAF. If Queue time is similar to simulation time, jobs can be scheduled across multiple nodes at TJNAF using `swif2`[1]. If the Queue time is significantly shorter than the simulation time, jobs can be parallelized across various sites under `OSG` [105].

---

[1] A `SLURM` wrapper at TJNAF

Bibliography

[1] MissMJ Wikimedia Commons. *Standard Model of Particle Physics*. 2019. URL: `https://commons.wikimedia.org/wiki/File:Standard_Model_of_Elementary_Particles.svg`.

[2] M. Gell-Mann. "A schematic model of baryons and mesons". In: *Physics Letters* 8.3 (1964), pp. 214–215. ISSN: 0031-9163. DOI: `https://doi.org/10.1016/S0031-9163(64)92001-3`. URL: `https://www.sciencedirect.com/science/article/pii/S0031916364920013`.

[3] G Zweig. "An SU_3 model for strong interaction symmetry and its breaking; Version 2". In: (1964). DOI: `10.17181/CERN-TH-412`. URL: `http://cds.cern.ch/record/570209`.

[4] R. L. Workman et al. "Review of Particle Physics". In: *PTEP* 2022 (2022), p. 083C01. DOI: `10.1093/ptep/ptac097`.

[5] Claude Amsler. "Mesons". In: *The Quark Structure of Hadrons: An Introduction to the Phenomenology and Spectroscopy*. Cham: Springer International Publishing, 2018, pp. 9–27. ISBN: 978-3-319-98527-5. DOI: `10.1007/978-3-319-98527-5_2`. URL: `https://doi.org/10.1007/978-3-319-98527-5_2`.

[6] E2m Wikimedia Commons. *Meson nonet - spin 0 / 1*. 2008. URL: `https://commons.wikimedia.org/wiki/File:Meson_nonet_-_spin_0.svg`.

[7] P. A. Zyla et al. “Review of particle physics”. In: *to be published in Prog. Theor. Exp. Phys.* 8 (2022), p. 083C01.

[8] Jozef J. Dudek et al. “Toward the excited isoscalar meson spectrum from lattice QCD”. In: *Phys. Rev. D* 88 (9 Nov. 2013), p. 094505. DOI: `10.1103/PhysRevD.88.094505`. URL: `https://link.aps.org/doi/10.1103/PhysRevD.88.094505`.

[9] C.A. Meyer and E.S. Swanson. “Hybrid mesons”. In: *Progress in Particle and Nuclear Physics* 82 (2015), pp. 21–58. ISSN: 0146-6410. DOI: `https://doi.org/10.1016/j.ppnp.2015.03.001`. URL: `https://www.sciencedirect.com/science/article/pii/S0146641015000162`.

[10] Philip R. Page, Eric S. Swanson, and Adam P. Szczepaniak. “Hybrid meson decay phenomenology”. In: *Phys. Rev. D* 59 (3 Jan. 1999), p. 034016. DOI: `10.1103/PhysRevD.59.034016`. URL: `https://link.aps.org/doi/10.1103/PhysRevD.59.034016`.

[11] D. R. Thompson et al. “Evidence for Exotic Meson Production in the Reaction $\pi^- p \to \eta\pi^- p$ at 18GeV/c”. In: *Phys. Rev. Lett.* 79 (9 Sept. 1997), pp. 1630–1633. DOI: `10.1103/PhysRevLett.79.1630`. URL: `https://link.aps.org/doi/10.1103/PhysRevLett.79.1630`.

[12] S. U. Chung et al. “Evidence for exotic $J^{\mathrm{PC}}= 1^{-+}$ meson production in the reaction $\pi^- \vec{p}\ \eta\pi^- p$ at 18GeV/c”. In: *Phys. Rev. D* 60 (9 Oct. 1999), p. 092001.

DOI: `10.1103/PhysRevD.60.092001`. URL: `https://link.aps.org/doi/10.1103/PhysRevD.60.092001`.

[13] G.S. Adams et al. “Confirmation of the 1^{-+} meson exotics in the $\eta\pi^0$ system”. In: *Physics Letters B* 657.1 (2007), pp. 27–31. ISSN: 0370-2693. DOI: `https://doi.org/10.1016/j.physletb.2007.07.068`. URL: `https://www.sciencedirect.com/science/article/pii/S037026930700809X`.

[14] A. Abele et al. “Exotic $\eta\pi$ state in $p\bar{d}$ annihilation at rest into $\pi^-\pi^0\eta p_{spectator}$”. In: *Physics Letters B* 423.1 (1998), pp. 175–184. ISSN: 0370-2693. DOI: `https://doi.org/10.1016/S0370-2693(98)00123-3`. URL: `https://www.sciencedirect.com/science/article/pii/S0370269398001233`.

[15] A. Abele et al. “Evidence for a$\eta\pi$-P-wave in $p\bar{p}$-annihilations at rest into $\pi^0\pi^0\eta$”. In: *Physics Letters B* 446.3 (1999), pp. 349–355. ISSN: 0370-2693. DOI: `https://doi.org/10.1016/S0370-2693(98)01544-5`. URL: `https://www.sciencedirect.com/science/article/pii/S0370269398015445`.

[16] E. I. Ivanov et al. “Observation of Exotic Meson Production in the Reaction $\pi^- p \to \eta^{'}\pi^- p$ at 18GeV/c”. In: *Phys. Rev. Lett.* 86 (18 Apr. 2001), pp. 3977–3980. DOI: `10.1103/PhysRevLett.86.3977`. URL: `https://link.aps.org/doi/10.1103/PhysRevLett.86.3977`.

[17] Yu. Khokhlov. “Study of $X(1600)$ 1^{-+} hybrid”. In: *Nuclear Physics A* 663-664 (2000), pp. 596c–599c. ISSN: 0375-9474. DOI: `https://doi.org/10.1016/S0375-9474(99)00663-6`. URL: `https://www.sciencedirect.com/science/article/pii/S0375947499006636`.

[18] C. Adolph et al. “Odd and even partial waves of $\eta\pi^-$ and $\eta^{'}\pi^-$ in $\pi^- p \rightarrow \eta^{'}\pi^- p$ at $191 GeV/c$”. In: *Physics Letters B* 740 (2015), pp. 303–311. ISSN: 0370-2693. DOI: `https://doi.org/10.1016/j.physletb.2014.11.058`. URL: `https://www.sciencedirect.com/science/article/pii/S0370269314008685`.

[19] M. G. Alekseev et al. “Observation of a $J^{\mathrm{PC}} = 1^{-+}$ Exotic Resonance in Diffractive Dissociation of 190 GeV/c π^- into $\pi^-\pi^-\pi^+$”. In: *Phys. Rev. Lett.* 104 (24 June 2010), p. 241803. DOI: `10.1103/PhysRevLett.104.241803`. URL: `https://link.aps.org/doi/10.1103/PhysRevLett.104.241803`.

[20] A. Rodas et al. “Determination of the Pole Position of the Lightest Hybrid Meson Candidate”. In: *Phys. Rev. Lett.* 122 (4 Jan. 2019), p. 042002. DOI: `10.1103/PhysRevLett.122.042002`. URL: `https://link.aps.org/doi/10.1103/PhysRevLett.122.042002`.

[21] Antoni J. Woss et al. “Decays of an exotic 1^{-+} hybrid meson resonance in QCD”. In: *Phys. Rev. D* 103 (5 Mar. 2021), p. 054502. DOI: `10.1103/PhysRevD.103.054502`. URL: `https://link.aps.org/doi/10.1103/PhysRevD.103.054502`.

[22] B. Collick et al. “Primakoff Production of the $B^+(1235)$ Meson”. In: *Phys. Rev. Lett.* 53 (25 Dec. 1984), pp. 2374–2377. DOI: `10.1103/PhysRevLett.53.2374`. URL: `https://link.aps.org/doi/10.1103/PhysRevLett.53.2374`.

[23] S. Yazaki. “Inclusive distributions near the central region in a dynamical pomeron coupling model”. In: *Nucl. Phys. B* 49 (1952), pp. 71–76. DOI: `10.1016/0550-3213(72)90586-X`.

[24] V. Mathieu et al. “Moments of angular distribution and beam asymmetries in $\eta\pi^0$ photoproduction at GlueX”. In: *Phys. Rev. D* 100 (5 Sept. 2019), p. 054017. DOI: `10.1103/PhysRevD.100.054017`. URL: `https://link.aps.org/doi/10.1103/PhysRevD.100.054017`.

[25] M. Atkinson et al. “A Spin Parity Analysis of the $\omega\pi^0$ Enhancement Photoproduced in the Energy Range 20-GeV to 70-GeV”. In: *Nucl. Phys. B* 243 (1984), pp. 1–28. DOI: `10.1016/0550-3213(84)90382-1`.

[26] M. Nozar et al. “A Study of the reaction pi- p —> omega pi- p at 18-GeV/c: The D and S decay amplitudes for b(1)(1235) —> omega pi”. In: *Phys. Lett. B* 541 (2002), pp. 35–44. DOI: `10.1016/S0370-2693(02)02194-9`. arXiv: `hep-ex/0206026`.

[27] JPAC Collaboration. et al. “$\omega \to 3\pi$ and $\omega\pi^0$ form factor revisited”. In: *The European Physical Journal* (June 2020). DOI: `https://doi.org/10.1140/epjc/s10052-020-08576-6`.

[28] Frank von Hippel and C. Quigg. “Centrifugal-Barrier Effects in Resonance Partial Decay Widths, Shapes, and Production Amplitudes”. In: *Phys. Rev. D* 5 (3 Feb. 1972), pp. 624–638. DOI: `10.1103/PhysRevD.5.624`. URL: `https://link.aps.org/doi/10.1103/PhysRevD.5.624`.

[29] S. U. Chung and T. L. Trueman. “Positivity conditions on the spin density matrix: A simple parametrization”. In: *Phys. Rev. D* 11 (3 Feb. 1975), pp. 633–646. DOI: `10.1103/PhysRevD.11.633`. URL: `https://link.aps.org/doi/10.1103/PhysRevD.11.633`.

[30] Marie Schertz Amy. “Partial Wave Analysis of the $\omega\pi^-$ Final State Photoproduced at GlueX”. 2022. DOI: `https://doi.org/10.21220/j3sa-a765`.

[31] James E. Brau et al. “Production and Decay Properties of the $\omega\pi^0$ State at 1250-MeV/c^2 Produced by 20-GeV Polarized Photons on Hydrogen”. In: *Phys. Rev. D* 37 (1988), p. 2379. DOI: `10.1103/PhysRevD.37.2379`.

[32] W. Roberts and B. Silvestre-Brac. “General method of calculation of any hadronic decay in the $^3P_0$ model”. In: (1992). DOI: `10.1007/BF01641821`. URL: `https://doi.org/10.1007/BF01641821`.

[33] T. Barnes, N. Black, and E. S. Swanson. “Meson-meson scattering in the quark model: Spin dependence and exotic channels”. In: *Phys. Rev. C* 63 (2 Jan. 2001), p. 025204. DOI: `10.1103/PhysRevC.63.025204`. URL: `https://link.aps.org/doi/10.1103/PhysRevC.63.025204`.

[34] GlueX Collaboration. *GlueX Experiment.* URL: `%7Bhttps://gluex.org%7D`.

[35] S. Adhikari et al. “The GlueX beamline and detector”. In: *Nuclear Instruments and Methods in Physics Research Section A: Accelerators, Spectrometers, Detectors and Associated Equipment* 987 (2021), p. 164807. ISSN: 0168-9002. DOI: `https://doi.org/10.1016/j.nima.2020.164807`. URL: `https://www.sciencedirect.com/science/article/pii/S0168900220312043`.

[36] M. Dugger et al. “Design and construction of a high-energy photon polarimeter”. In: *Nuclear Instruments and Methods in Physics Research Section A: Accelerators, Spectrometers, Detectors and Associated Equipment* 867 (2017), pp. 115–127. ISSN: 0168-9002. DOI: `https://doi.org/10.1016/j.nima.`

2017.05.026. URL: `https://www.sciencedirect.com/science/article/pii/S0168900217305715`.

[37] N.S. Jarvis et al. "The Central Drift Chamber for GlueX". In: *Nuclear Instruments and Methods in Physics Research Section A: Accelerators, Spectrometers, Detectors and Associated Equipment* 962 (2020), p. 163727. ISSN: 0168-9002. DOI: `https://doi.org/10.1016/j.nima.2020.163727`. URL: `https://www.sciencedirect.com/science/article/pii/S0168900220302771`.

[38] E. Pooser et al. "The GlueX Start Counter Detector". In: *Nuclear Instruments and Methods in Physics Research Section A: Accelerators, Spectrometers, Detectors and Associated Equipment* 927 (2019), pp. 330–342. ISSN: 0168-9002. DOI: `https://doi.org/10.1016/j.nima.2019.02.029`. URL: `https://www.sciencedirect.com/science/article/pii/S0168900219302128`.

[39] T.D Beattie et al. "Construction and performance of the barrel electromagnetic calorimeter for the GlueX experiment". In: *Nuclear Instruments and Methods in Physics Research Section A: Accelerators, Spectrometers, Detectors and Associated Equipment* 896 (2018), pp. 24–42. DOI: `https://doi.org/10.1016/j.nima.2018.04.006`.

[40] K. Moriya et al. "A measurement of the energy and timing resolution of the GlueX Forward Calorimeter using an electron beam". In: *Nuclear Instruments and Methods in Physics Research Section A: Accelerators, Spectrometers, Detectors and Associated Equipment* 726 (2013), pp. 60–66. ISSN: 0168-9002. DOI: `https://doi.org/10.1016/j.nima.2013.05.109`. URL: `https://www.sciencedirect.com/science/article/pii/S0168900213007201`.

[41] David J. "Abbott et al. "A 250 MHz Level 1 Trigger and Distribution System for the GlueX experiment". In: (Nov. 2009). DOI: `10.1109/RTC.2009.5321659`. URL: `https://www.osti.gov/biblio/1088381`.

[42] B. D. Leverington et al. "Performance of the prototype module of the GlueX electromagnetic barrel calorimeter". In: *Nucl. Instrum. Meth. A* 596 (2008), pp. 327–337. DOI: `10.1016/j.nima.2008.08.137`.

[43] T.D. Beattie and A.P. Fischer and S.T. Krueger and G.J. Lolos and Z. Papandreou and E.L. Plummer and A.Yu. Semenov and I.A. Semenova and L.M. Sichello and L.A. Teigrob and E.S. Smith. "Light yield of Kuraray SCSF-78MJ scintillating fibers for the Gluex barrel calorimeter". In: *Nuclear Instruments and Methods in Physics Research Section A: Accelerators, Spectrometers, Detectors and Associated Equipment* 767 (2014), pp. 245–251. ISSN: 0168-9002. DOI: `https://doi.org/10.1016/j.nima.2014.08.038`. URL: `https://www.sciencedirect.com/science/article/pii/S0168900214009735`.

[44] R.T. Jones et al. "A bootstrap method for gain calibration and resolution determination of a lead-glass calorimeter". In: *Nuclear Instruments and Methods in Physics Research Section A: Accelerators, Spectrometers, Detectors and Associated Equipment* 566.2 (2006), pp. 366–374. ISSN: 0168-9002. DOI: `https://doi.org/10.1016/j.nima.2006.07.061`. URL: `https://www.sciencedirect.com/science/article/pii/S0168900206013556`.

[45] William Mcginley. "Development of the Barrel Calorimeter Reconstruction and Measurement of the Beam Asymmetry (Sigma) for π^0 and η mesons with the GlueX Experiment". In: (Nov. 2019). DOI: `10.1184/R1/10293638.v1`. URL: `https://kilthub.cmu.edu/articles/thesis/Development_of_`

the_Barrel_Calorimeter_Reconstruction_and_Measurement_of_the_Beam_Asymmetry_Sigma_for_Pi0_and_Eta_mesons_with_the_GlueX_Experiment/10293638.

[46] C. Hensche et al. *Cosmic muon calibration of the Barrel Calorimeter using Geant4 fine-structure simulation GlueX Experiment Document 3849-v2*. Tech. rep. URL: https://halldweb.jlab.org/doc-private/DocDB/ShowDocument?docid=3849.

[47] W. McGinley. *BCAL Gain Calibration GlueX Experiment Document 2901-v4*. Tech. rep. URL: https://halldweb.jlab.org/DocDB/0029/002901/004/bcal_calib.pdf.

[48] A. Ghassemi and K. Sato and K. Kobayashi. *MPPC Technical Note Report Cat. No. KAPD9005E01, Hamamatsu.* 2022. URL: %7Bhttps://www.hamamatsu.com/content/dam/hamamatsu-photonics/sites/documents/99_SALES_LIBRARY/ssd/mppc_kapd9005e.pdf%7D.

[49] E. S. Smith. *Saturation in BCAL SiPMs*. 2018. URL: %7Bhttps://halldweb.jlab.org/DocDB/0037/003737/004/SiPM_saturation.pdf%7D.

[50] F. Barbosa et al. “Silicon photomultiplier characterization for the GlueX barrel calorimeter”. In: *Nuclear Instruments and Methods in Physics Research Section A: Accelerators, Spectrometers, Detectors and Associated Equipment* 695 (2012). New Developments in Photodetection NDIP11, pp. 100–104. ISSN: 0168-9002. DOI: https://doi.org/10.1016/j.nima.2011.11.059. URL: https://www.sciencedirect.com/science/article/pii/S0168900211021036.

[51] K. Suresh et al. π^0 *Gain Calibration For Fall and Spring 2018 Run Period GlueX Experiment Document 4001-v1*. Tech. rep. URL: `https://halldweb.jlab.org/doc-private/DocDB/ShowDocument?docid=4001`.

[52] B. Crompvoets and M. M Dalton and D. Ross and E. S. Smith. *Experimental Determination of Saturation in the BCAL SiPMs*. 2019. URL: `%7Bhttps://halldweb.jlab.org/DocDB/0041/004135/003/SiPM_test_saturation.pdf%7D`.

[53] K. Suresh and M. M. Dalton E. S. Smith and Z. Papandreou. *Detailed study on z dependence in the process of reconstruction of* π^0 *events in the BCAL.* URL: `https://halldweb.jlab.org/doc-private/DocDB/ShowDocument?docid=4139`.

[54] A. Gasparian et al. *"Precision Measurement of the* η *Radiative Decay Width via the Primakoff Effect (PR12-10-011)"*. Tech. rep. URL: `https://www.jlab.org/exp_prog/proposals/10/PR12-10-011.pdf`.

[55] K. Suresh et al. *BCAL gain calibrations (Spring 2019) GlueX Experiment Document 4297-v6*. Tech. rep. URL: `https://halldweb.jlab.org/doc-private/DocDB/ShowDocument?docid=4297`.

[56] *JLab Data Acquisition Group, CODA Online Data Formats*. URL: `%7Bhttps://coda.jlab.org/drupal/system/files/eventbuilding.pdf%7D`.

[57] Ahmed Marwan Abdelrahman Foda. "Photoproduction of the $b_1(1235)$ Meson off the proton at E_γ - $6 - 12$ GeV". URL: `https://ourspace.uregina.ca/handle/10294/14330`.

[58] A. G. Frodesen, O. Skjeggestad, and H. Tofte. *Probability and Statistics in Particle Physics*. Bergen, Norway: Universitetsforlaget, 1979. ISBN: 978-82-00-01906-0.

[59] Paul Mattione. *Least Squares Kinematic Fitting of Physics Reactions*. Tech. rep. URL: `https://halldweb.jlab.org/doc-private/DocDB/ShowDocument?docid=2112`.

[60] S. U. Chung et al. "Spin-parity analysis of the B meson". In: *Phys. Rev. D* 11 (9 May 1975), pp. 2426–2440. DOI: `10.1103/PhysRevD.11.2426`. URL: `https://link.aps.org/doi/10.1103/PhysRevD.11.2426`.

[61] Matthew Shepherd et al. *mashephe/AmpTools: Version 0.14.5*. Version v0.14.5. Nov. 2022. DOI: `10.5281/zenodo.7336113`. URL: `https://doi.org/10.5281/zenodo.7336113`.

[62] F and James. "MINUIT: Function Minimization and Error Analysis Reference Manual". In: (1998). CERN Program Library Long Writeups. URL: `https://cds.cern.ch/record/2296388`.

[63] Malcolm Forster and Elliott Sober. "AIC Scores as Evidence: A Bayesian Interpretation". In: *Philosophy of Statistics*. Ed. by Prasanta S. Bandyopadhyay and Malcolm R. Forster. Vol. 7. Handbook of the Philosophy of Science. Amsterdam: North-Holland, 2011, pp. 535–549. DOI: `https://doi.org/10.1016/B978-0-444-51862-0.50016-2`. URL: `https://www.sciencedirect.com/science/article/pii/B9780444518620500162`.

[64] P. Stoica and Y. Selen. “Model-order selection: a review of information criterion rules”. In: *IEEE Signal Processing Magazine* 21.4 (2004), pp. 36–47. DOI: `10.1109/MSP.2004.1311138`.

[65] D. P. Barber et al. “Photoproduction of ρ' (1.2) and ρ' (1.6) in the Final States $\pi^+\pi^-\pi^+\pi^-$ and $\pi^+\pi^-\pi^0\pi^0$”. In: *Z. Phys. C* 4 (1980), p. 169. DOI: `10.1007/BF01421795`.

[66] C. Fanelli et al. “AI-assisted optimization of the ECCE tracking system at the Electron-Ion Collider”. In: *Nuclear Instruments and Methods in Physics Research Section A: Accelerators, Spectrometers, Detectors and Associated Equipment* 1047 (2023), p. 167748. ISSN: 0168-9002. DOI: `https://doi.org/10.1016/j.nima.2022.167748`. URL: `https://www.sciencedirect.com/science/article/pii/S0168900222010403`.

[67] R. Abdul Khalek and al et al. *Science Requirements and Detector Concepts for the Electron-Ion Collider: EIC Yellow Report*. 2021. DOI: `10.48550/ARXIV.2103.05419`. URL: `https://arxiv.org/abs/2103.05419`.

[68] Xiangdong Ji. “QCD Analysis of the Mass Structure of the Nucleon”. In: *Phys. Rev. Lett.* 74 (7 Feb. 1995), pp. 1071–1074. DOI: `10.1103/PhysRevLett.74.1071`. URL: `https://link.aps.org/doi/10.1103/PhysRevLett.74.1071`.

[69] Matthias Burkardt and Abdullah Jarrah. *Quark Orbital Angular Momentum in the MIT Bag Model*. 2010. DOI: `10.48550/ARXIV.1011.1041`. URL: `https://arxiv.org/abs/1011.1041`.

[70] Christine A. Aidala et al. “The spin structure of the nucleon”. In: *Rev. Mod. Phys.* 85 (2 Apr. 2013), pp. 655–691. DOI: `10.1103/RevModPhys.85.655`. URL: `https://link.aps.org/doi/10.1103/RevModPhys.85.655`.

[71] Daniel de Florian et al. “Evidence for Polarization of Gluons in the Proton”. In: *Phys. Rev. Lett.* 113 (1 July 2014), p. 012001. DOI: `10.1103/PhysRevLett.113.012001`. URL: `https://link.aps.org/doi/10.1103/PhysRevLett.113.012001`.

[72] European Muon Collaboration (EMU). “A measurement of the spin asymmetry and determination of the structure function g1 in deep inelastic muon-proton scattering”. In: *Physics Letters B* 206.2 (1988), pp. 364–370. ISSN: 0370-2693. DOI: `https://doi.org/10.1016/0370-2693(88)91523-7`. URL: `https://www.sciencedirect.com/science/article/pii/0370269388915237`.

[73] Elke-Caroline Aschenauer, Alexander Bazilevsky, and et. al. *The RHIC SPIN Program: Achievements and Future Opportunities.* 2015. DOI: `10.48550/ARXIV.1501.01220`. URL: `https://arxiv.org/abs/1501.01220`.

[74] R.L. Jaffe and Aneesh Manohar. “The g1 problem: Deep inelastic electron scattering and the spin of the proton”. In: *Nuclear Physics B* 337.3 (1990), pp. 509–546. ISSN: 0550-3213. DOI: `https://doi.org/10.1016/0550-3213(90)90506-9`. URL: `https://www.sciencedirect.com/science/article/pii/0550321390905069`.

[75] A. Airapetian et al. “Single-Spin Asymmetries in Semi-Inclusive Deep-Inelastic Scattering on a Transversely Polarized Hydrogen Target”. In: *Phys. Rev. Lett.* 94 (1 Jan. 2005), p. 012002. DOI: `10.1103/PhysRevLett.94.012002`. URL: `https://link.aps.org/doi/10.1103/PhysRevLett.94.012002`.

[76] M. Alekseev, V.Yu. Alexakhin, and et al. “Collins and Sivers asymmetries for pions and kaons in muon–deuteron DIS”. In: *Physics Letters B* 673.2 (2009), pp. 127–135. ISSN: 0370-2693. DOI: `https://doi.org/10.1016/j.physletb.2009.01.060`. URL: `https://www.sciencedirect.com/science/article/pii/S0370269309000884`.

[77] X. Qian et al. “Single Spin Asymmetries in Charged Pion Production from Semi-Inclusive Deep Inelastic Scattering on a Transversely Polarized ^{3}He Target at $Q^2 = 1.4 - -2.7$ GeV^2”. In: *Phys. Rev. Lett.* 107 (7 Aug. 2011), p. 072003. DOI: `10.1103/PhysRevLett.107.072003`. URL: `https://link.aps.org/doi/10.1103/PhysRevLett.107.072003`.

[78] L. Adamczyk et al. “”Transverse single-spin asymmetry and cross section for π^0 and η mesons at large Feynman x in $p^\uparrow + p$ collisions at $\sqrt{s}$=200 GeV””. In: *Phys. Rev. D* 86 (5 Sept. 2012), p. 051101. DOI: `10.1103/PhysRevD.86.051101`. URL: `https://link.aps.org/doi/10.1103/PhysRevD.86.051101`.

[79] A. Adare et al. “Measurement of transverse single-spin asymmetries for J/ψ production in polarized $p + p$ collisions at $\sqrt{s} = 200$ GeV”. In: *Phys. Rev. D* 82 (11 Dec. 2010), p. 112008. DOI: `10.1103/PhysRevD.82.112008`. URL: `https://link.aps.org/doi/10.1103/PhysRevD.82.112008`.

[80] L. Zheng et al. “Accessing the gluon Sivers function at a future electron-ion collider”. In: *Phys. Rev. D* 98 (3 Aug. 2018), p. 034011. DOI: `10.1103/PhysRevD.98.034011`. URL: `https://link.aps.org/doi/10.1103/PhysRevD.98.034011`.

[81] A. Accardi et al. “Electron-Ion Collider: The next QCD frontier”. In: (Aug. 2016). DOI: `10.1140/epja/i2016-16268-9`.

[82] J. K. Adkins and et al. Akiba. *Design of the ECCE Detector for the Electron Ion Collider*. 2022. DOI: `10.48550/ARXIV.2209.02580`. URL: `https://arxiv.org/abs/2209.02580`.

[83] ECCE consortium. *EIC Comprehensive Chromodynamics Experiment Collaboration Detector Proposal*. May 2022. DOI: `10.5281/zenodo.6537588`. URL: `https://doi.org/10.5281/zenodo.6537588`.

[84] G. Aglieri Rinella et al. "First demonstration of in-beam performance of bent Monolithic Active Pixel Sensors". In: (May 2021). arXiv: `2105.13000 [physics.ins-det]`.

[85] Domenico Colella. "ALICE ITS 3: the first truly cylindrical inner tracker". In: (2021). arXiv: `2111.09689 [physics.ins-det]`.

[86] Xuan Li et al. "Forward silicon vertex/tracking detector design and R&D for the future Electron-Ion Collider". In: *Proceedings of Particles and Nuclei International Conference 2021 — PoS(PANIC2021)*. Sissa Medialab, Mar. 2022. DOI: `10.22323/1.380.0084`. URL: `https://doi.org/10.22323%2F1.380.0084`.

[87] Shivom Sharma and Gade Pandu Rangaiah. "Multi-Objective Optimization Applications in Chemical Engineering". In: *Multi-Objective Optimization in Chemical Engineering*. John Wiley & Sons, Ltd, 2013. Chap. 3, pp. 35–102. ISBN: 9781118341704. DOI: `https://doi.org/10.1002/9781118341704.ch3`. eprint: `https://onlinelibrary.wiley.com/doi/pdf/10.1002/9781118341704.ch3`. URL: `https://onlinelibrary.wiley.com/doi/abs/10.1002/9781118341704.ch3`.

[88] Alex A. Freitas. "A Critical Review of Multi-Objective Optimization in Data Mining: A Position Paper". In: *SIGKDD Explor. Newsl.* 6.2 (Dec. 2004), pp. 77–86. ISSN: 1931-0145. DOI: `10.1145/1046456.1046467`. URL: `https://doi.org/10.1145/1046456.1046467`.

[89] George Lambrinidis and Anna Tsantili-Kakoulidou. "Challenges with multi-objective QSAR in drug discovery". In: *Expert Opinion on Drug Discovery* 13.9 (2018). PMID: 29996683, pp. 851–859. DOI: `10.1080/17460441.2018.1496079`. eprint: `https://doi.org/10.1080/17460441.2018.1496079`. URL: `https://doi.org/10.1080/17460441.2018.1496079`.

[90] Borhan Kazimipour, Xiaodong Li, and A. K. Qin. "A review of population initialization techniques for evolutionary algorithms". In: *2014 IEEE Congress on Evolutionary Computation (CEC)*. 2014, pp. 2585–2592. DOI: `10.1109/CEC.2014.6900618`.

[91] Stephanie Forrest. "Genetic algorithms". In: *ACM Computing Surveys (CSUR)* 28.1 (1996), pp. 77–80.

[92] Kalyanmoy Deb et al. "A fast and elitist multiobjective genetic algorithm: NSGA-II". In: *IEEE transactions on evolutionary computation* 6.2 (2002), pp. 182–197.

[93] Samuel Daulton, Maximilian Balandat, and Eytan Bakshy. *Parallel Bayesian Optimization of Multiple Noisy Objectives with Expected Hypervolume Improvement*. 2021. DOI: `10.48550/ARXIV.2105.08195`. URL: `https://arxiv.org/abs/2105.08195`.

[94] Maximilian Balandat et al. "BoTorch: A Framework for Efficient Monte-Carlo Bayesian Optimization". In: *Advances in Neural Information Processing Systems 33*. 2020. URL: `https://proceedings.neurips.cc/paper/2020/hash/f5b1b89d98b7286673128a5fb112cb9a-Abstract.html`.

[95] R. Ent. *EIC Overview and Schedule*. The AI4EIC Workshop - First workshop on Artificial Intelligence for the Electron Ion Collider, http://eic.ai. 2021. URL: `https://indico.bnl.gov/event/10699/contributions/53658/attachments/36955/60868/AI4EIC_EIC_Overview_and_Schedule_090721_post.pptx`.

[96] Chris Pinkenburg. *Fun4All*. URL: `https://www.jlab.org/conferences/eicsw/EICSoftwareMeeting-Pinkenberg-Fun4All.pdf`.

[97] PHENIX Collaboration. *Fun4All framework*. URL: `%7Bhttps://www.phenix.bnl.gov/software/fun4all.html%7D`.

[98] sPHENIX collaboration. *fun4all sPHENIX detectors*. URL: `https://github.com/sPHENIX-Collaboration/coresoftware`.

[99] *ECCE-EIC core software*. URL: `https://github.com/ecce-eic/coresoftware`.

[100] Xin-Nian Wang and Miklos Gyulassy. "HIJING: A Monte Carlo model for multiple jet production in pp, pA, and AA collisions". In: *Physical Review D* 44.11 (1991), p. 3501.

[101] Torbjörn Sjöstrand, Stephen Mrenna, and Peter Skands. "A brief introduction to PYTHIA 8.1". In: *Computer Physics Communications* 178.11 (2008), pp. 852–867.

[102] Tobias Toll and Thomas Ullrich. "The dipole model Monte Carlo generator Sartre 1". In: *Computer Physics Communications* 185.6 (2014), pp. 1835–1853.

[103] J. Blank and K. Deb. "pymoo: Multi-Objective Optimization in Python". In: *IEEE Access* 8 (2020), pp. 89497–89509.

[104] *JLab Scientific Computing*. URL: `https://scicomp.jlab.org/scicomp/home`.

[105] OSG. *OSPool*. 2006. DOI: `10.21231/906P-4D78`. URL: `https://osg-htc.org/services/open_science_pool.html`.

[106] M. Williams, M. Bellis, and C. A. Meyer. *Separating Signals from Non-Interfering Backgrounds using Probabilistic Event Weightings*. 2008. arXiv: `0804.3382 [physics.data-an]`. URL: `https://doi.org/10.48550/arXiv.0804.3382`.

[107] C.M. Fonseca, L. Paquete, and M. Lopez-Ibanez. "An Improved Dimension-Sweep Algorithm for the Hypervolume Indicator". In: *2006 IEEE International Conference on Evolutionary Computation*. 2006, pp. 1157–1163. DOI: `10.1109/CEC.2006.1688440`.

[108] *ECCE Software Documentation*. URL: `https://ecce-eic.github.io`.

Appendix A

APPENDIX : Data Analysis Cuts

A.1 Timing Cuts

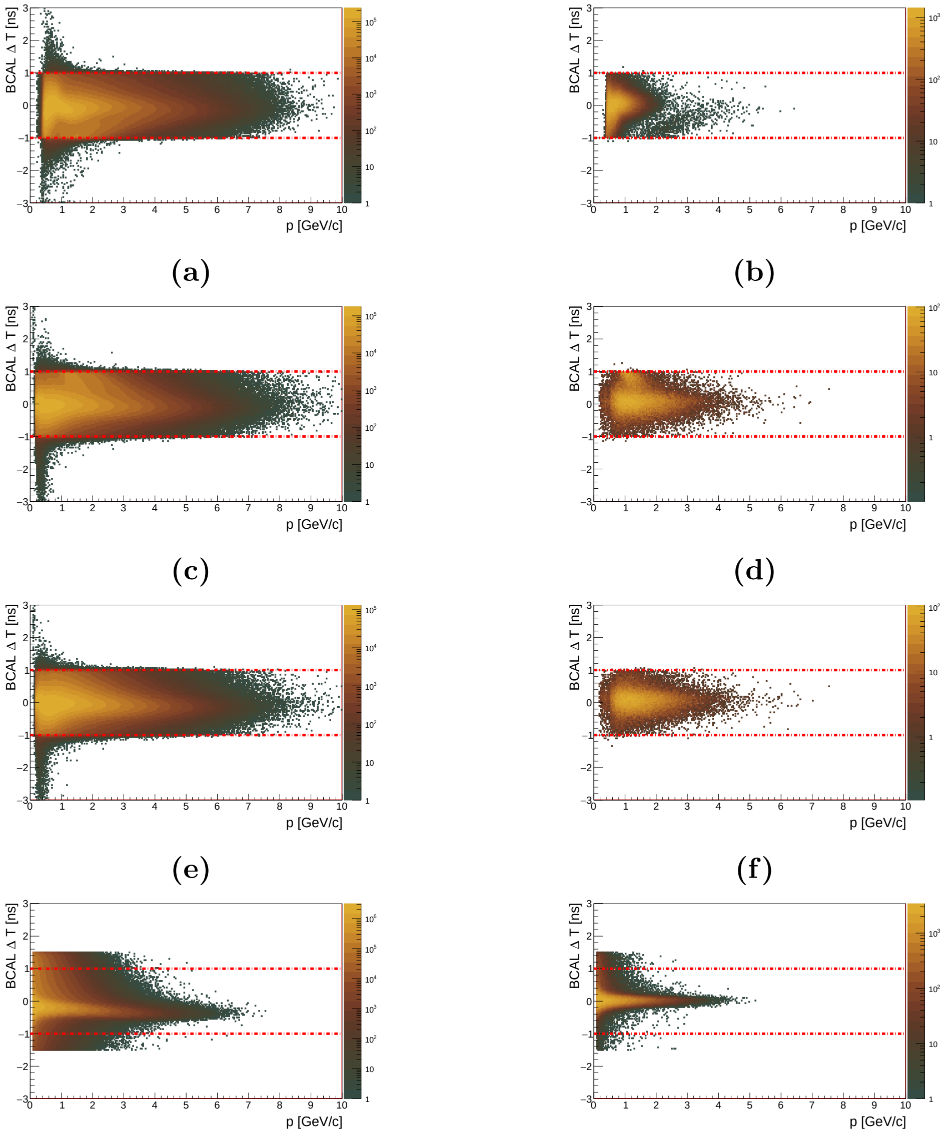

(a) **(b)**

(c) **(d)**

(e) **(f)**

(g) **(h)**

Figure A.1: Timing Cuts for detected final state particles in the BCAL. The plots on the left correspond to GlueX Phase-I data, plots on the right corresponds to Signal MC events. The plots on the top row corresponds to protons p, second row plots corresponds to π^+, while the third row corresponds to π^- and finally the plots on the fourth row corresponds to the photons (γ).

Timing cuts in BCAL:

A.2 Tracking Energy Loss Cuts

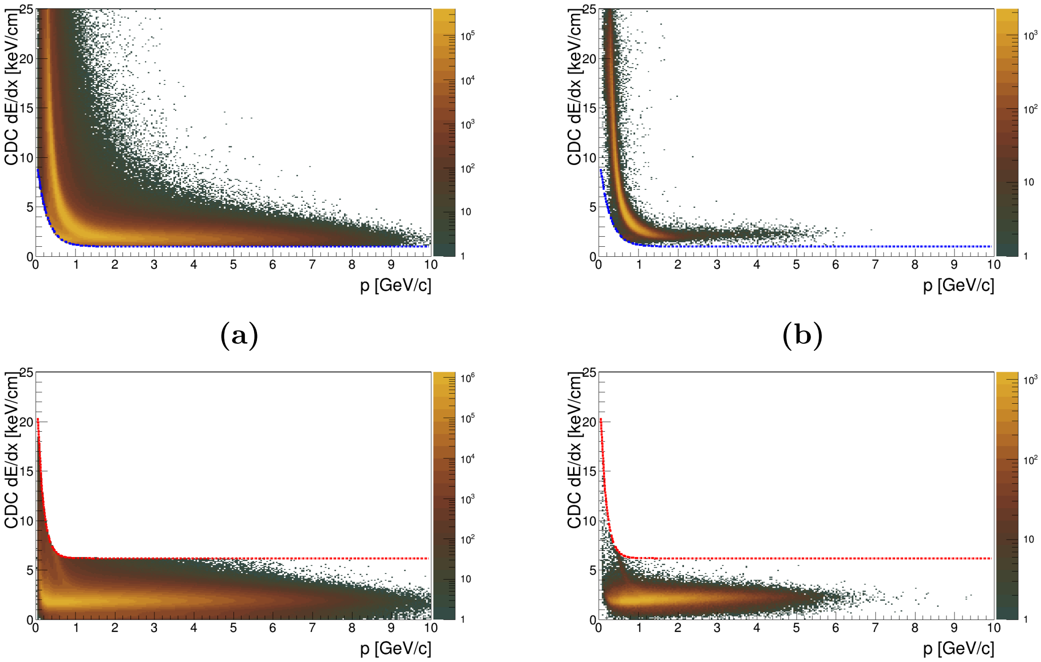

(a) **(b)**

(c) **(d)**

Figure A.2: Selection cuts on charged particles as shown in Section 4.2. The plots on the left corresponds to GlueX Phase-I data, while the plots on the right corresponds to Signal MC events. The plots on the top row corresponds to the dE/dx cut for a proton (p) and the bottom row corresponds to dE/dx for charged pions ($\pi^{\pm}$).

Appendix B

APPENDIX : Mass independent fits for $\omega\pi^0$

B.1 Signal MC angular distributions

Each of J^P states that contribute in describing the angular distributions have to be tracked as well. Throughout all the mass bins, the angular distribution is plotted and checked on how various wavesets describes the five decay angles. Also, an additional quantity $M(p\pi^0)$ is also plotted. $M(p\pi^0)$ is the invariant mass of the proton and the bachelor π^0. The distribution is more useful to look specifically in data for any baryonic resonances and making sure that there is minimal baryonic interference. Since, the fits are mass independent fits, it assumes a flat distribution of $M(\omega\pi 0)$ during its fit. This can also be observed in the $M(\omega\pi^0)$ distribution in the set of following plots. Due to large number of figures arising from each fit, in each t bin, in each mass bin, only the Mass bin $M(\omega\pi^0) = 1.195 - 1.275$ GeV is shown in the following section.

B.1.1 Angular distribution for waveset `1p`

It can be seen that, `1p` cannot fully describe the angular distribution especially in the $\omega\pi^0$ decay angles (Ω) i.e. $\cos(\theta)$ and Φ. However, it does seem to describe other decay angles well. Hence, making it ideal as the null model for comparing other wavesets.

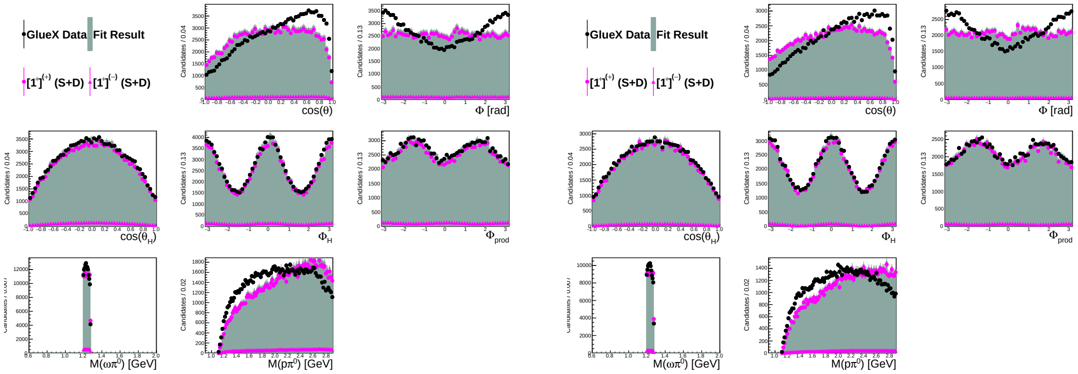

(a) $0.15 < |t| < 0.30$ GeV^2 **(b)** $0.30 < |t| < 0.50$ GeV^2

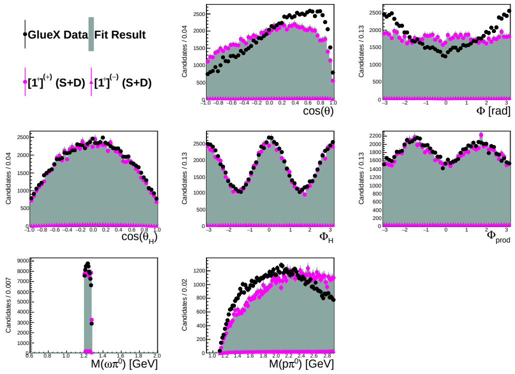

(c) $0.50 < |t| < 1.00$ GeV^2

Figure B.1: Angular distribution for the waveset `1p`

B.1.2 Angular distribution for waveset `1p1m`

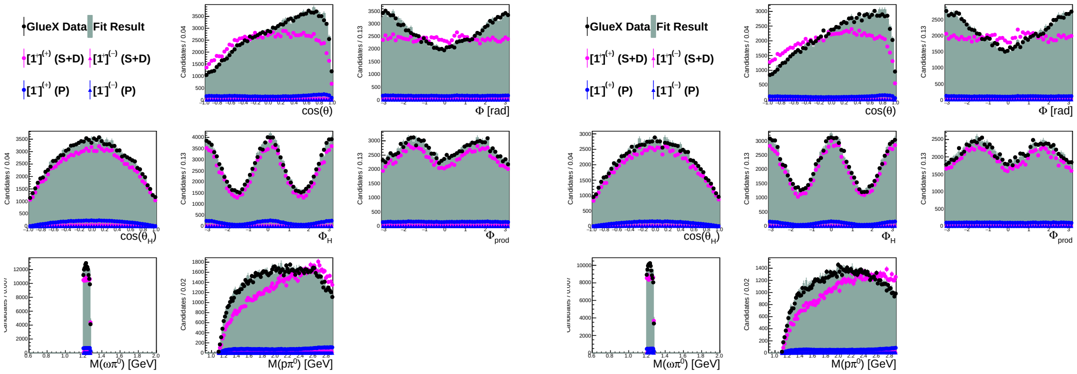

(a) $0.15 < |t| < 0.30$ GeV^2 **(b)** $0.30 < |t| < 0.50$ GeV^2

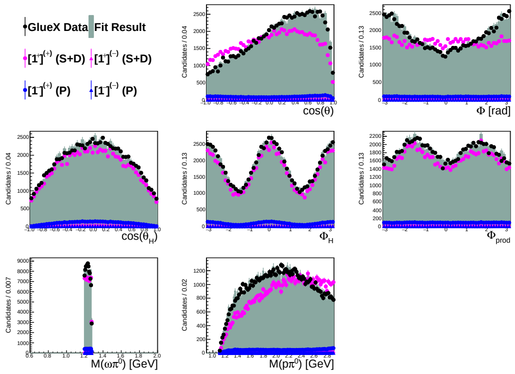

(c) $0.50 < |t| < 1.00$ GeV^2

Figure B.2: Angular distribution for the waveset `1p1m`

B.1.3 Angular distribution for waveset `0m1p1m`

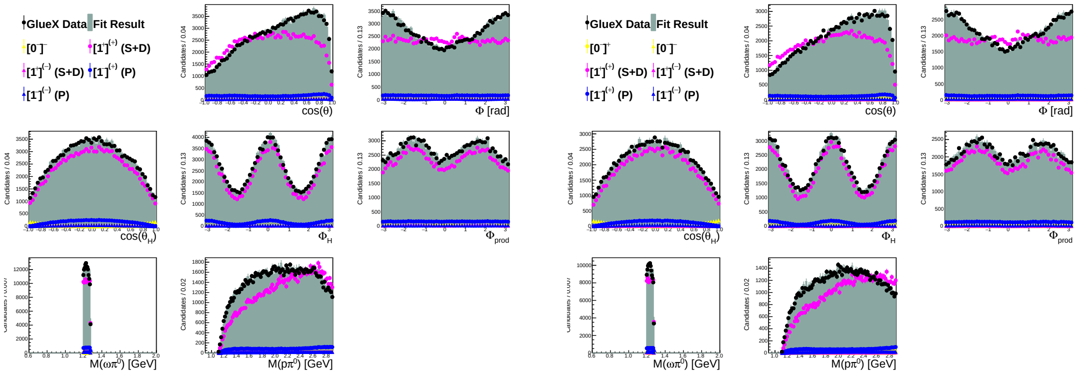

(a) $0.15 < |t| < 0.30$ GeV^2 **(b)** $0.30 < |t| < 0.50$ GeV^2

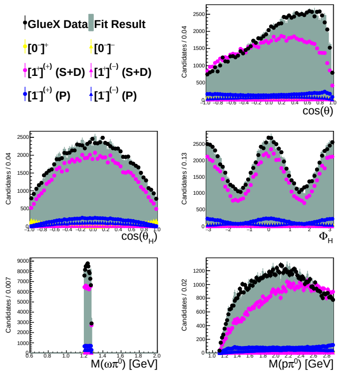

(c) $0.50 < |t| < 1.00$ GeV^2

Figure B.3: Angular distribution for the waveset `0m1p1m`

B.1.4 Angular distribution for waveset `1p1m2m`

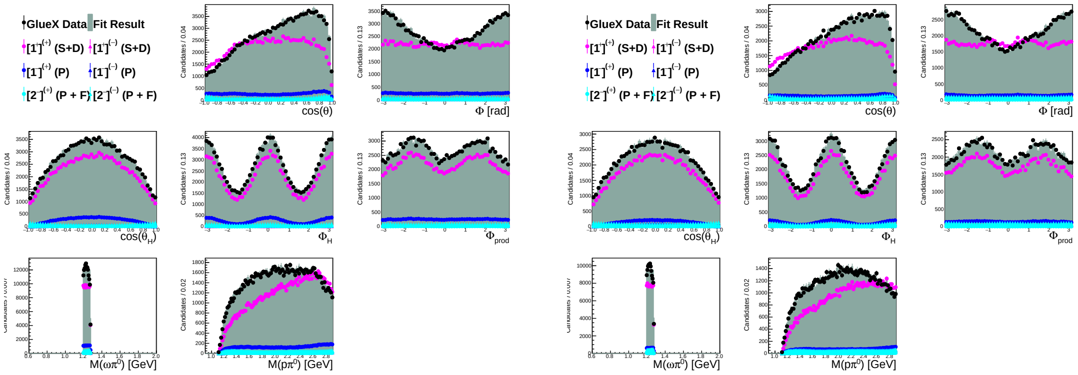

(a) $0.15 < |t| < 0.30$ GeV^2 **(b)** $0.30 < |t| < 0.50$ GeV^2

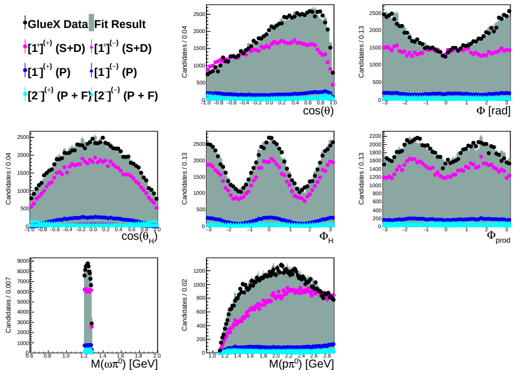

(c) $0.50 < |t| < 1.00$ GeV^2

Figure B.4: Angular distribution for the waveset `1p1m2m`

B.1.5 Angular distribution for waveset `1p1mPosRefl`

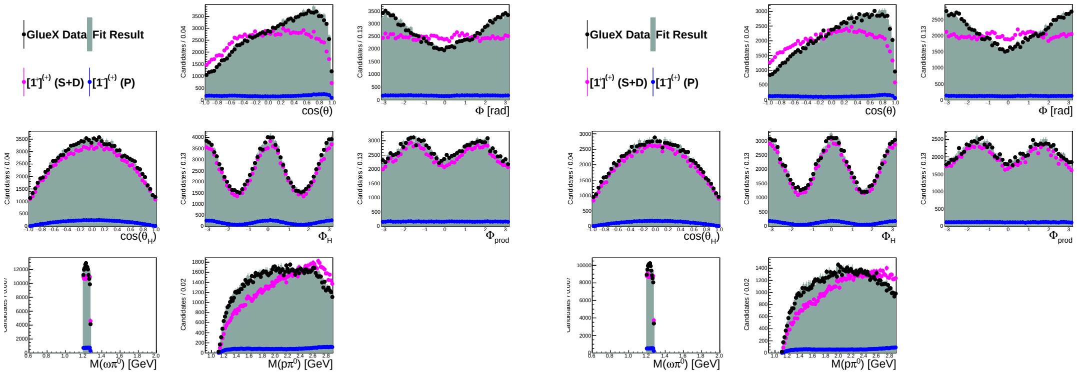

(a) $0.15 < |t| < 0.30$ GeV^2 **(b)** $0.30 < |t| < 0.50$ GeV^2

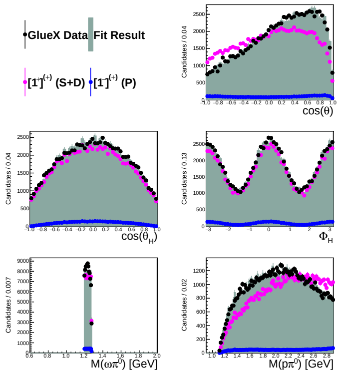

(c) $0.50 < |t| < 1.00$ GeV^2

Figure B.5: Angular distribution for the waveset `1p1mPosRefl`

B.2 Generated Signal MC Parameters

Below is the summary of generated Signal MC

$[J_m^{PC}(l)]^{(\epsilon)}$	**Parameter Name**	**Real Part**	**Imaginary Part**
$[1^+_{+1}(S)]^{(+)}$	1pps	-837.74	720.40
$[1^+_0(S)]^{(+)}$	1p0s	1378.36	0.00
$[1^+_{-1}(S)]^{(+)}$	1pms	-402.51	55.14
$[1^+_{+1}(D)]^{(+)}$	1ppd	-283.21	152.03
$[1^+_0(D)]^{(+)}$	1p0d	364.09	39.66
$[1^+_{-1}(D)]^{(+)}$	1pmd	-53.43	54.23
$[1^-_{+1}(P)]^{(+)}$	1mpp	1652.09	209.66
$[1^-_0(P)]^{(+)}$	1m0p	-224.23	-83.45
$[1^-_{-1}(P)]^{(+)}$	1mmp	129.64	4.58

Table B.1: Table summarizing the parameters and its value used to generate Signal MC. `gen_omegapi` was used to generate the events Signal MC generated events, which then passes through detector response and through full GlueX reconstruction pipeline.

B.2.1 Comparing relative phase (ϕ) between $[1^+]^{(+)}$ and $[1^-]^{(+)}$

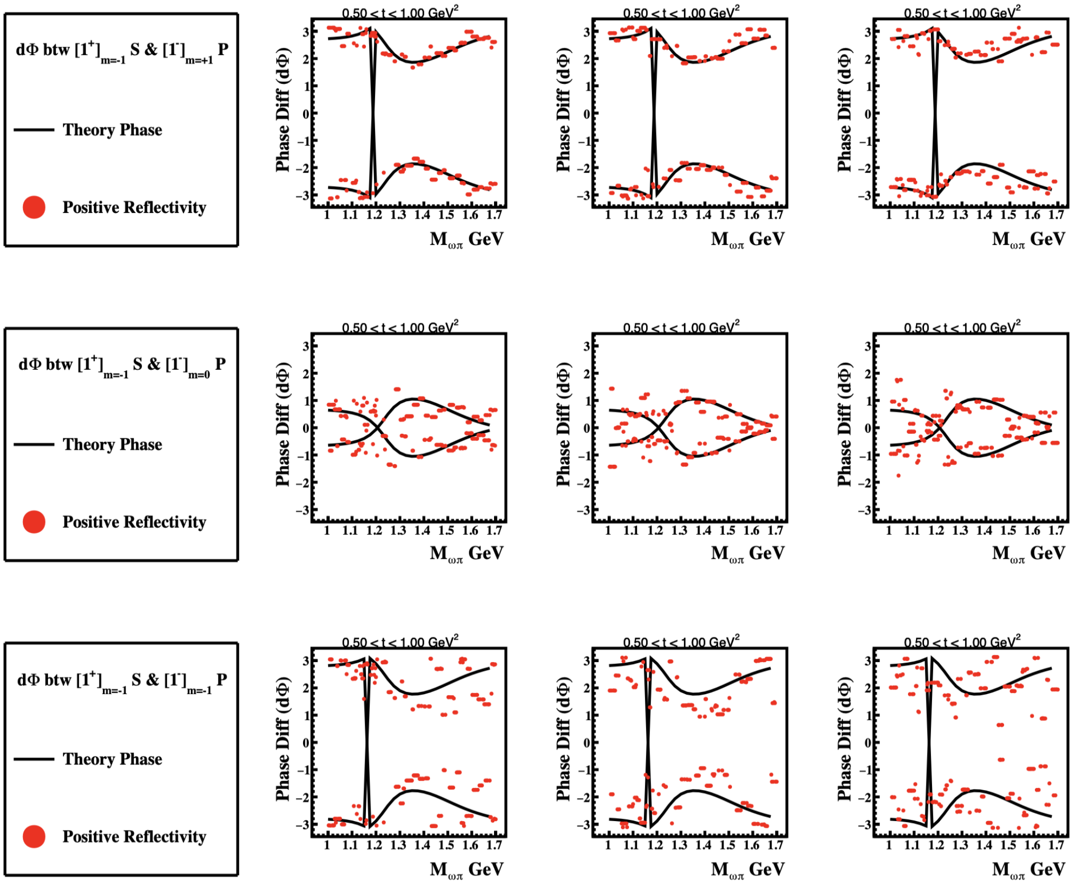

Figure B.6: Relative Phase between $[1^+]_{m=-1}(S)$ and $[1^-](P)$ waves

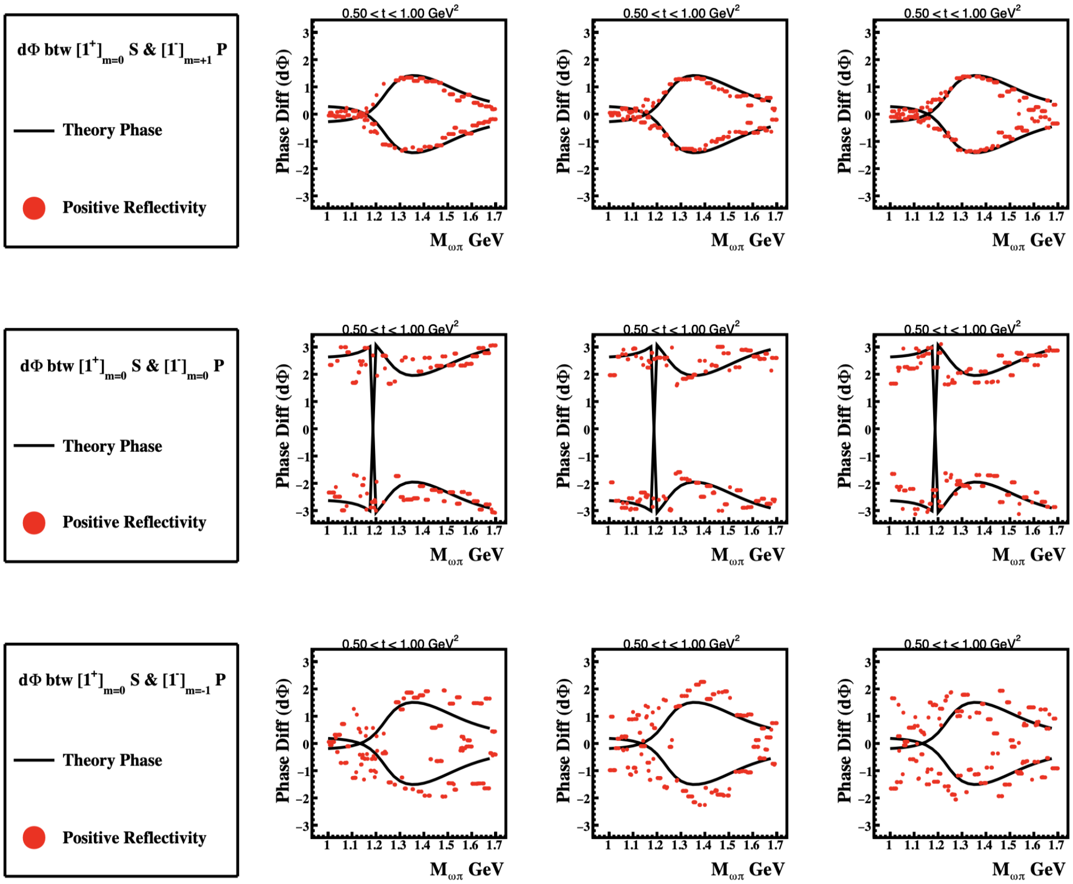

Figure B.7: Relative Phase between $[1^+]_{m=0}(S)$ and $[1^-](P)$ waves

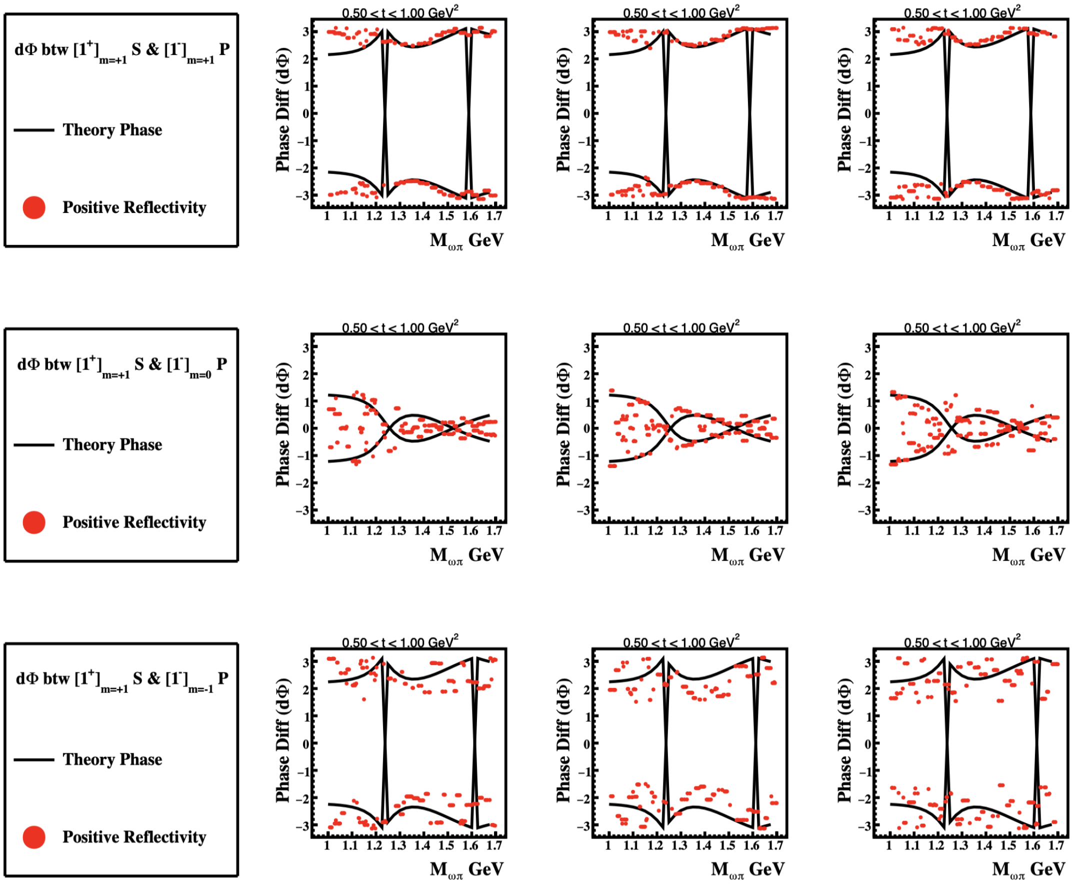

Figure B.8: Relative Phase between $[1^+]_{m=+1}(S)$ and $[1^-](P)$ waves

B.3 GlueX Phase-I data angular distributions in b_1 region

Summary of various contribution of J^P states to the angular distribution while fitting GlueX Phase-I data is summarized in this section. Similar set of plots to that of signal MC shown in Appendix B.1 is shown here. An additional quantity λ is also plotted. λ is a the measure of purity of ω samples in the $\omega\pi^0$ events. It is based on a method for separating signals from non-interfering backgrounds by computing, an event by event quality factor as mentioned in [106]. A typical distribution of λ is such that it strictly increases between 0 to 1. λ is defined such that it is the measure of the angle $\vec{p}_{\pi^+} \times \vec{p}_{\pi^-}$ of ω in its helicity frame. Due to large number of figures arising from each fit, in each t bin, in each mass bin, only the Mass bin $M(\omega\pi^0) = 1.195 - 1.275$ GeV is shown in the following section.Due to large number of figures arising from each fit, in each t bin, in each mass bin, only the Mass bin $M(\omega\pi^0) = 1.195 - 1.275$ GeV is shown in the following section.

B.3.1 Angular distribution for waveset `1p` for GlueX Phase-I data

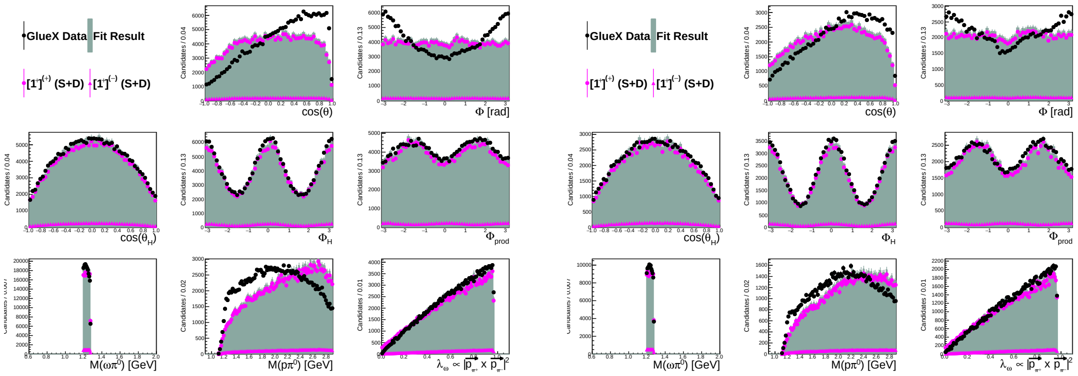

(a) $0.15 < |t| < 0.30$ GeV^2 **(b)** $0.30 < |t| < 0.50$ GeV^2

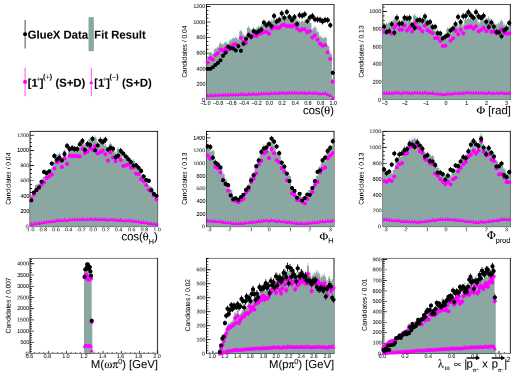

(c) $0.50 < |t| < 1.00$ GeV^2

Figure B.9: Angular distribution for the waveset `1p`

B.3.2 Angular distribution for waveset `1p1m` for GlueX Phase-I data

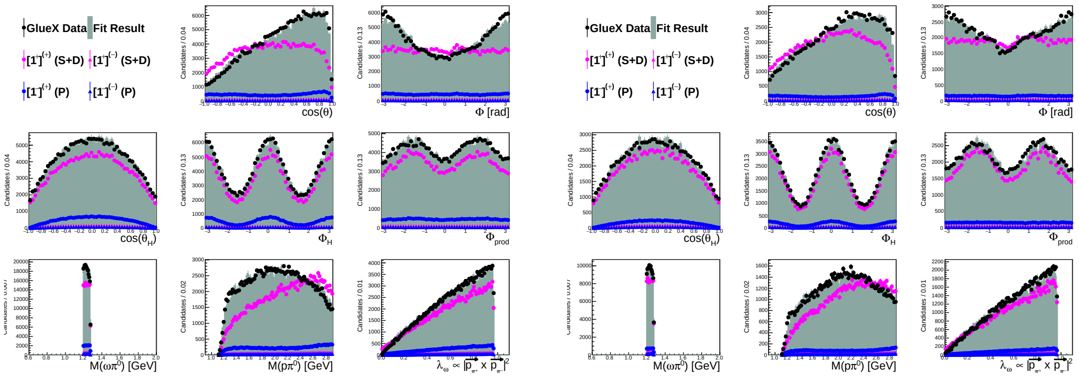

(a) $0.15 < |t| < 0.30$ GeV^2 **(b)** $0.30 < |t| < 0.50$ GeV^2

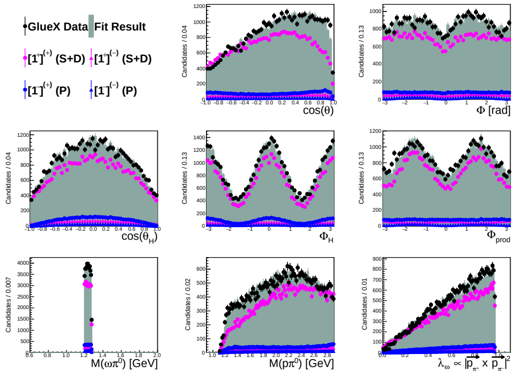

(c) $0.50 < |t| < 1.00$ GeV^2

Figure B.10: Angular distribution for the waveset `1p1m`

B.3.3 Angular distribution for waveset `0m1p1m` for GlueX Phase-I data

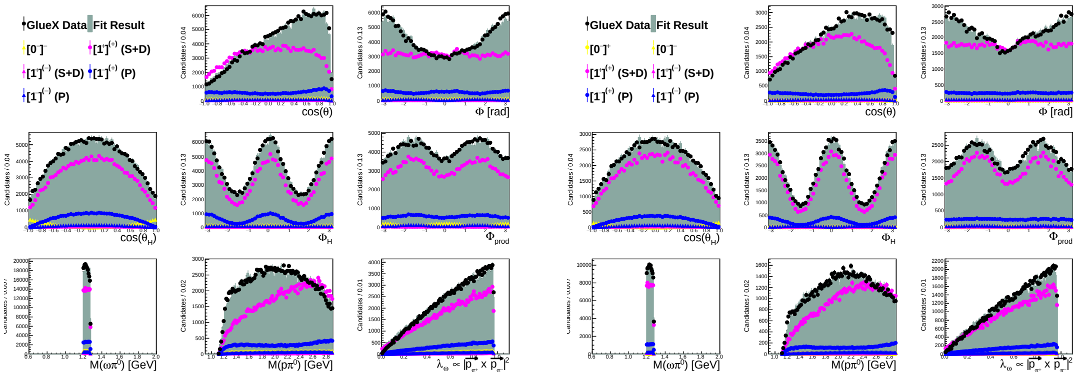

(a) $0.15 < |t| < 0.30$ GeV^2

(b) $0.30 < |t| < 0.50$ GeV^2

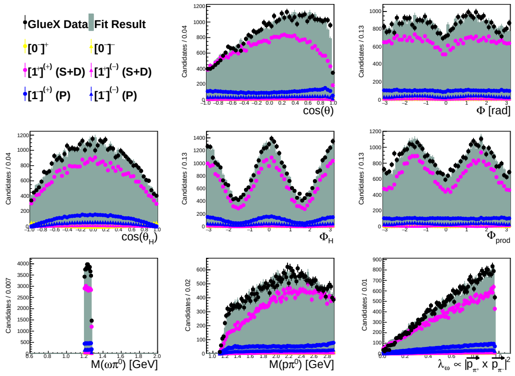

(c) $0.50 < |t| < 1.00$ GeV^2

Figure B.11: Angular distribution for the waveset `0m1p1m`

B.3.4 Angular distribution for waveset `1p1m2m2piso` for GlueX Phase-I data

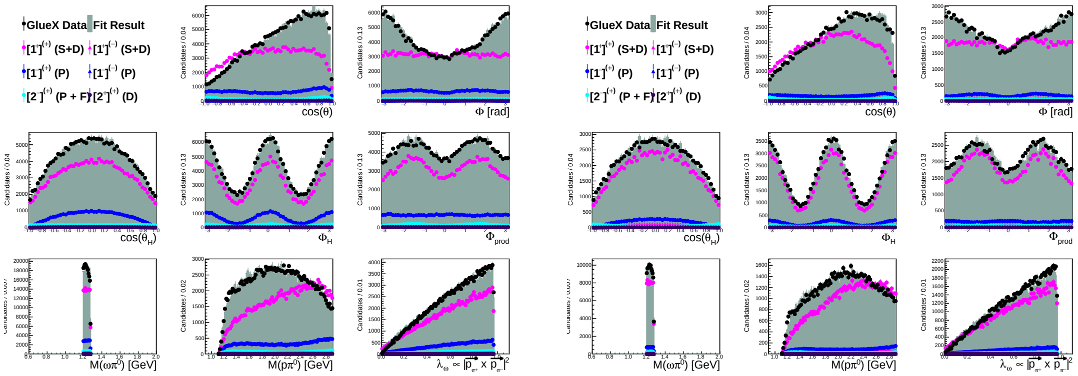

(a) $0.15 < |t| < 0.30$ GeV^2 **(b)** $0.30 < |t| < 0.50$ GeV^2

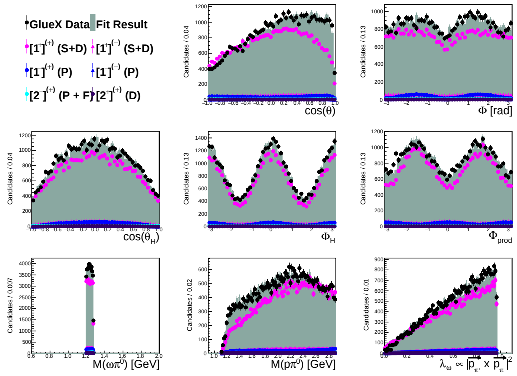

(c) $0.50 < |t| < 1.00$ GeV^2

Figure B.12: Angular distribution for the waveset `1p1m2m2piso`

B.3.5 Angular distribution for waveset `All Waves` for GlueX Phase-I data

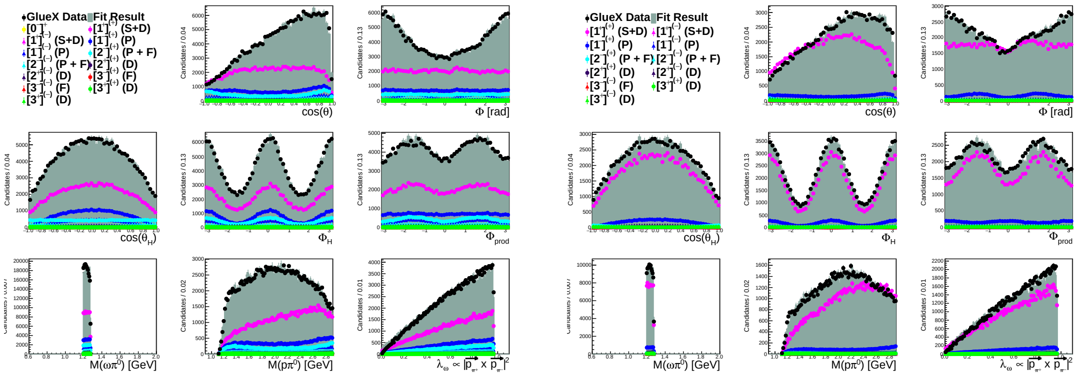

(a) $0.15 < |t| < 0.30$ GeV^2 **(b)** $0.30 < |t| < 0.50$ GeV^2

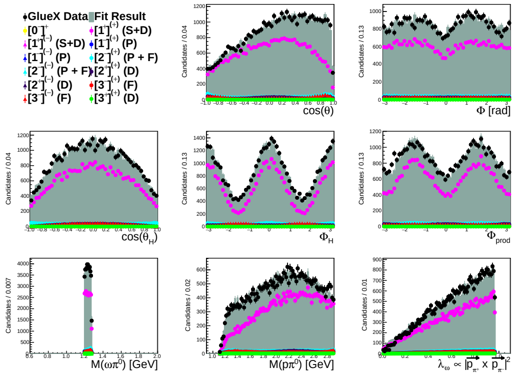

(c) $0.50 < |t| < 1.00$ GeV^2

Figure B.13: Angular distribution for the waveset `All Wave`

Appendix C

APPENDIX : Systematics in b_1 mass region

C.1 Fit fraction for various J^P for different orientations

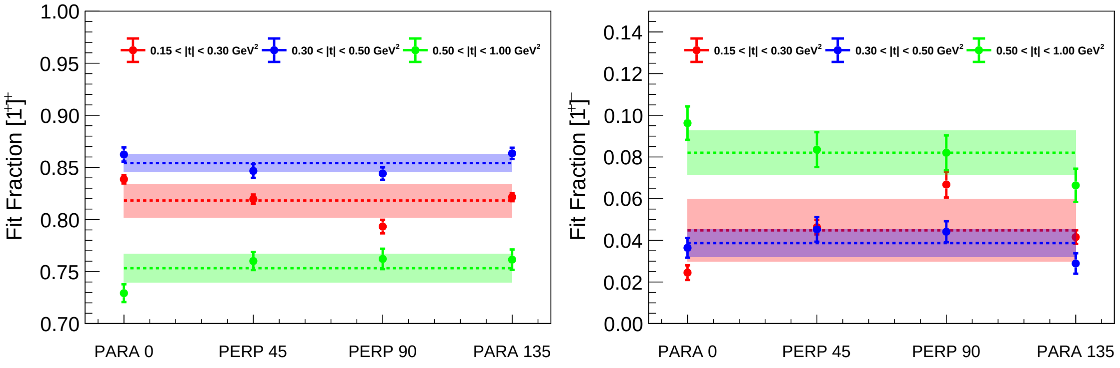

Fit fraction for $[1^+]^{(+)}$ Fit fraction for $[1^+]^{(-)}$

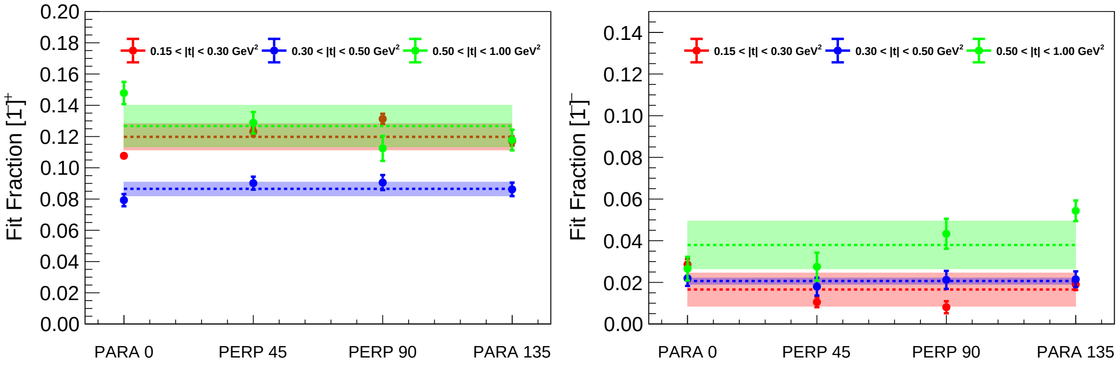

Fit fraction for $[1^-]^{(+)}$ Fit fraction for $[1^-]^{(-)}$

Figure C.1: Fit fraction for various J^P states for the four different polarization orientation. Top row plots correspond to $[1^+]^{(\pm)}$ and the bottom row plots correspond to $[1^-]^{(\pm)}$. The plots on the first column correspond to positive reflectivity ($\epsilon = +1$) while the second column on the right correspond to negative reflectivity ($\epsilon = -1$)

C.2 Fit Systematic Study

Fit Systematic study result for Signal MC

Fit Systematic study result for GlueX Phase-I data

Waveset Name	**Remarks**	**Wave sets**			**Total Events** N			**Negative Log Likelihood (N2LL)**			**NPARS**	$\frac{\Delta N2LL}{\Delta NPARS}$ **w.r.t** $[1^+]^\pm$			$AIC = \frac{N2LL+2*NPARS}{N}$			$BIC = \frac{NLL}{N} + \log{(N)} * NPARS$		
		$[J^P]^\epsilon$	m	L	t Bins			t Bins				t Bins			t Bins			t Bins		
1p	-	$[1^+]^\pm$	$-1,0,1$	S,D	$3.58M \pm 0.01M$	$2.84M \pm 0.01M$	$2.72M \pm 0.01M$	-435223	-348540	-337467	11	0	0	0	-0.122	-0.123	-0.125	-0.122	-0.123	-0.125
0m1p	-	$[0^+]^\pm$	0	P				-1758780	-1079640	-528407	15	358.0	330.0	345.0	-0.122	-0.123	-0.126	-0.122	-0.123	-0.126
		$[1^+]^\pm$	$-1,0,1$	S,D																
1p1m	-	$[1^+]^\pm$	$-1,0,1$	S,D				-2010460	-1146930	-540693	23	1908.75	1569.17	1348.25	-0.129	-0.131	-0.133	-0.129	-0.131	-0.133
		$[1^-]^\pm$	$-1,0,1$	P																
0m1p1m	-	$[0^+]^\pm$	0	P				-2018070	-1148710	-541734	27	1444.5	1194.43	1027.94	-0.129	-0.131	-0.133	-0.129	-0.131	-0.133
		$[1^+]^\pm$	$-1,0,1$	S,D																
		$[1^-]^\pm$	$-1,0,1$	P																
0m1p1miso	-	Same as above + Isotropic Bkg						-2018070	-1148710	-541734	28	1360.17	1124.18	967.53	-0.129	-0.133	-0.133	-0.129	-0.133	-0.133
0mNeg1pPos1mPosiso	-	$[0^+]^-$	0	P				-2014670	-1147350	-540664	14	7683.67	6335.33	5455.33	-0.129	-0.133	-0.133	-0.129	-0.133	-0.133
		$[1^+]^+$	$-1,0,1$	S,D																
		$[1^-]^+$	$-1,0,1$	P																
		Isotropic Bkg																		
1pPos1mPos	-	$[1^+]^+$	$-1,0,1$	S,D				-2009310	-1146250	-539666	12	22803.0	18797.0	16123.0	-0.129	-0.130	-0.133	-0.129	-0.130	-0.133
		$[1^-]^+$	$-1,0,1$	P																
0mNeg1pPos1mPosisoSepDS	Seperate dsratios for 3 m	Same as 0mNeg1pPos1mPosiso						-2014880	-1147730	-540804	16	4665.4	3839.6	3329.2	-0.130	-0.130	-0.133	-0.130	-0.130	-0.133
1pPos1mPosSepDS	Seperate dsratios for 3 m	Same as 1pPos1mPos						-2010610	-1146670	-540190	14	7749.67	6394.0	5539.33	-0.130	-0.131	-0.133	-0.130	-0.131	-0.133

Table C.1: Summary on systematic study on various fit wave combinations for Signal MC. Detailed results extracted in the three t bins are presented.

Waveset Name	Remarks	**Wave sets**			**Total Events** N			**Negative Log Likelihood (N2LL)**			**NPARS**	$\frac{\Delta N2LL}{\Delta NPARS}$ **w.r.t** $[1^+]^{\pm}$			$AIC = \frac{N2LL+2*NPARS}{N}$			$BIC = \frac{NLL}{N} + \log{(N)} * NPARS$		
		$[J^P]^\epsilon$	m	L	t Bins			t Bins				t Bins			t Bins			t Bins		
1p	-	$[1^+]^\pm$	$-1,0,1$	S,D	$22M$ $\pm$ $0.05M$	$11M$ $\pm$ $0.05M$	$5M$ $\pm$ $0.05M$	-1753110	-1079000	-528190	14	0	0	0	27.9	27.9	27.8	473.5	454.4	432.1
0m1p	-	$[0^+]^\pm$ $[1^+]^\pm$	0 $-1,0,1$	P S,D				-1758780	-1079640	-528407	18	1417.5	160.0	54.25	35.9	35.7	35.8	608.8	584.2	555.4
1p1m	-	$[1^+]^\pm$ $[1^-]^\pm$	$-1,0,1$ $-1,0,1$	S,D P				-2010460	-1146930	-540693	26	21445.8	5660.8	1041.9	51.9	51.7	51.8	878.8	843.6	802.2
0m1p1m	-	$[0^+]^\pm$ $[1^+]^\pm$ $[1^-]^\pm$	0 $-1,0,1$ $-1,0,1$	P S,D P				-2018070	-1148710	-541734	30	16560.0	4356.9	846.5	59.9	59.9	59.6	1014.0	972.3	925.6
0m1p1miso	-	Same as above + Isotropic Bkg						-2018070	-1148710	-541734	31	15585.9	4100.6	796.7	61.9	61.7	61.5	1047.8	1005.8	956.4
0mNeg1pPos1mPosiso	-	$[0^+]^-$ $[1^+]^+$ $[1^-]^+$ Isotropic Bkg	0 $-1,0,1$ $-1,0,1$	P S,D P				-2014670	-1147350	-540664	17	87186.7	22783.3	4158	33.9	33.8	34.0	574.5	551.5	524.5
1pPos1mPos	-	$[1^+]^+$ $[1^-]^+$	$-1,0,1$ $-1,0,1$	S,D P				-2009310	-1146250	-539666	15	256200	67250	11476	29.9	29.9	29.9	506.9	486.6	462.8
0mNeg1pPos1mPosisoSepDS	Seperate dsratios for 3 m	Same as 0mNeg1pPos1mPosiso						-2014880	-1147730	-540804	19	52354	13746	2522.8	37.9	37.9	37.9	642.1	616.4	586.2
1pPos1mPosSepDS	Seperate dsratios for 3 m	Same as 1pPos1mPos						-2010610	-1146670	-540190	17	85833.3	22556.7	4000.0	33.9	33.9	33.9	574.5	551.5	524.5
1p1m2mPos	Not using all m	$[1^+]^\pm$ $[1^-]^\pm$ $[2^-]^+$	$-1,0,1$ $-1,0,1$ $-2,-1,0,1,2$	S,D P D,F				-2038380	-1153960	-542681	46	8911.6	2342.5	452.8	91.9	91.9	91.9	1555.2	1492.6	1419.3
1p1m2mPos2pPosiso	Not using all m	$[1^+]^\pm$ $[1^-]^\pm$ $[2^-]^+$ $[2^+]^+$ Isotropic Bkg	$-1,0,1$ $-1,0,1$ $-1,0,1$ $-1,0,1$	S,D P P,F D				-2032900	-1153480	-543005	45	9025.5	2402.6	477.9	89.9	89.9	89.9	1521.1	1460.2	1388.7

Table C.2: Summary on systematic study on various fit wave combinations for GlueX Phase-I data. Detailed results extracted in the three t bins are presented.

C.2.1 Extracted `dsratio` for various combinations of wavesets explored

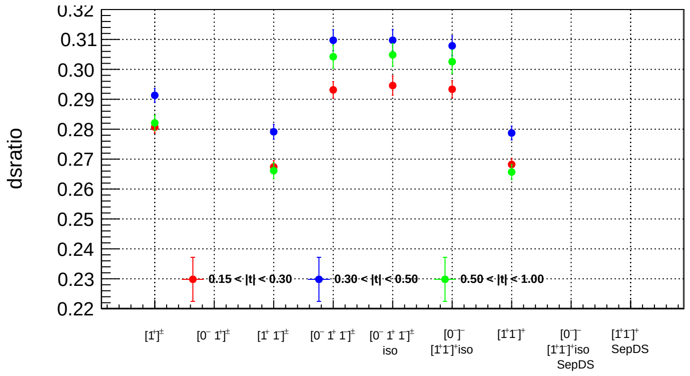

Figure C.2: Extracted `dsratio` for various combinations of wavesets used for fitting Signal MC.

Signal MC:

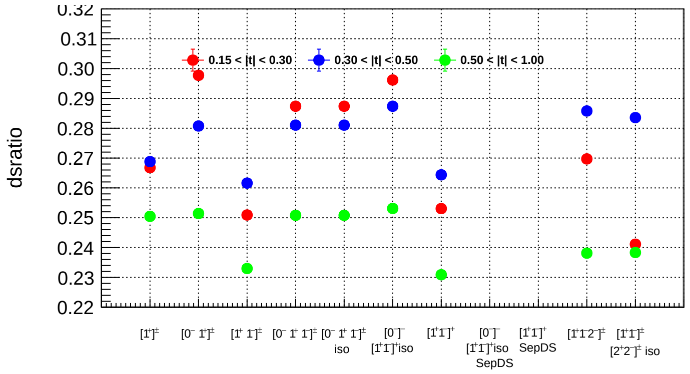

Figure C.3: Extracted `dsratio` for various combinations of wavesets used for fitting GlueX Phase-I data.

GlueX Phase-I data:

C.3 t Study systematics for Signal MC

Similar to GlueX Phase-I data, a Signal MC is split into 39 $|t|$ bins such that each bin has roughly the same statistics, and using the waveset `1p1mPosRefl`, 25 randomized fit are performed in each t bin and the result is summarized in Figure C.4.

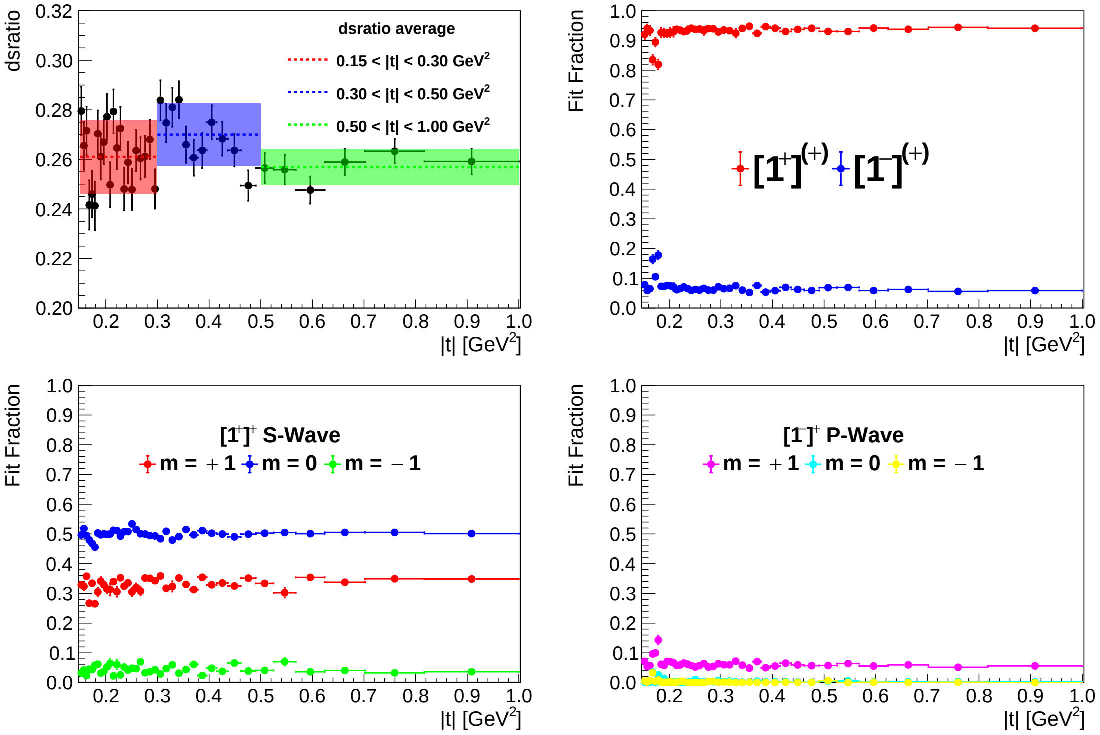

Figure C.4: Extracted `dsratio` in fine t bins for Signal MC. The `dsratio` is consistent across the whole $|t|$ range and also, the fit fractions are stable across the whole t range.

It can be seen that, there are no discrepancy in extracting `dsratio` across the t bins unlike GlueX Phase-I data.

C.4 t Study for GlueX Phase-I data in `OmNeg1pPos1mPos`

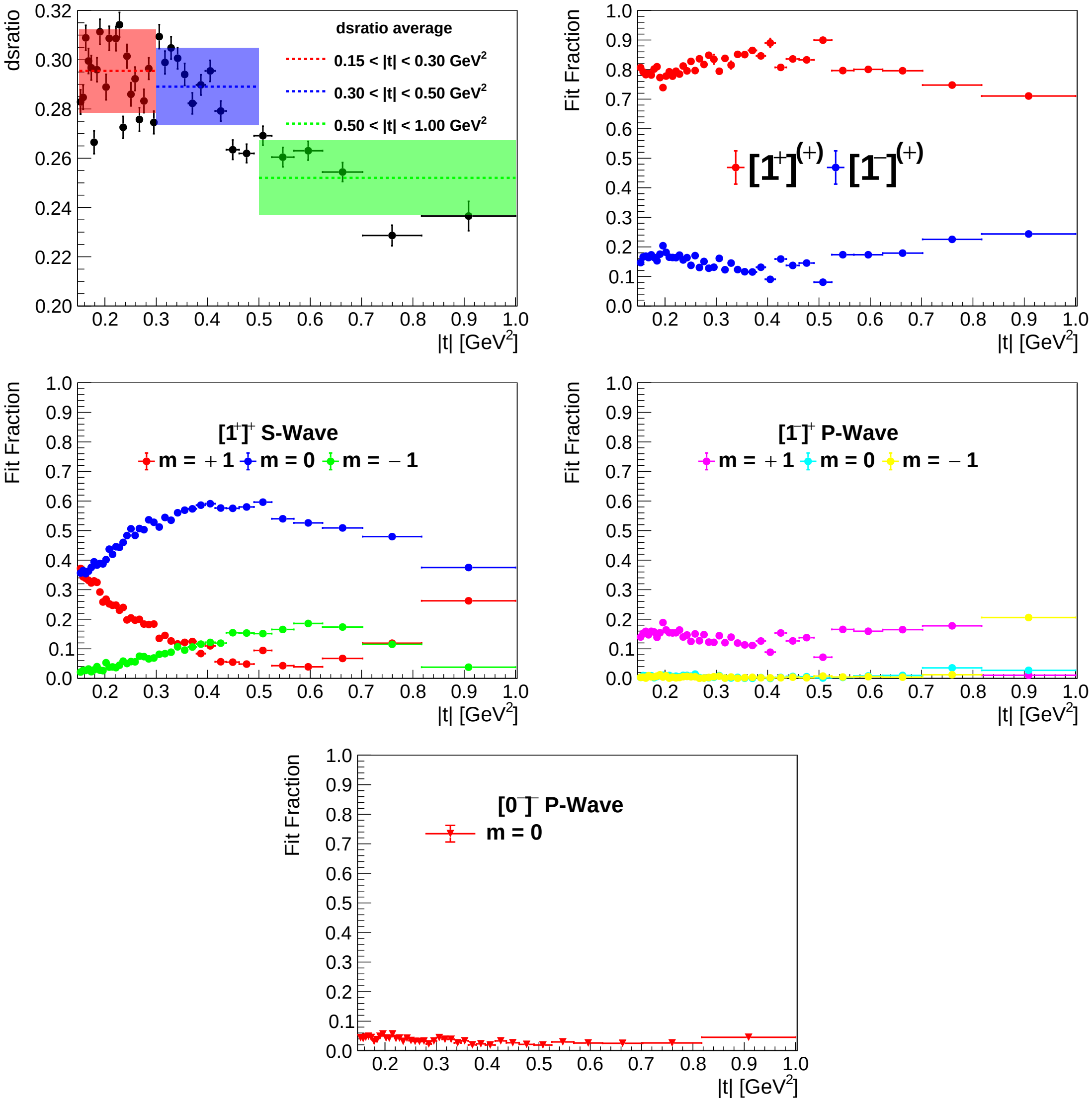

Figure C.5: Extracted `dsratio` in fine t bins for GlueX Phase-I data using `OmNeg1pPosRefl1mNegRefl`.

C.5 Φ angle distribution across various t range

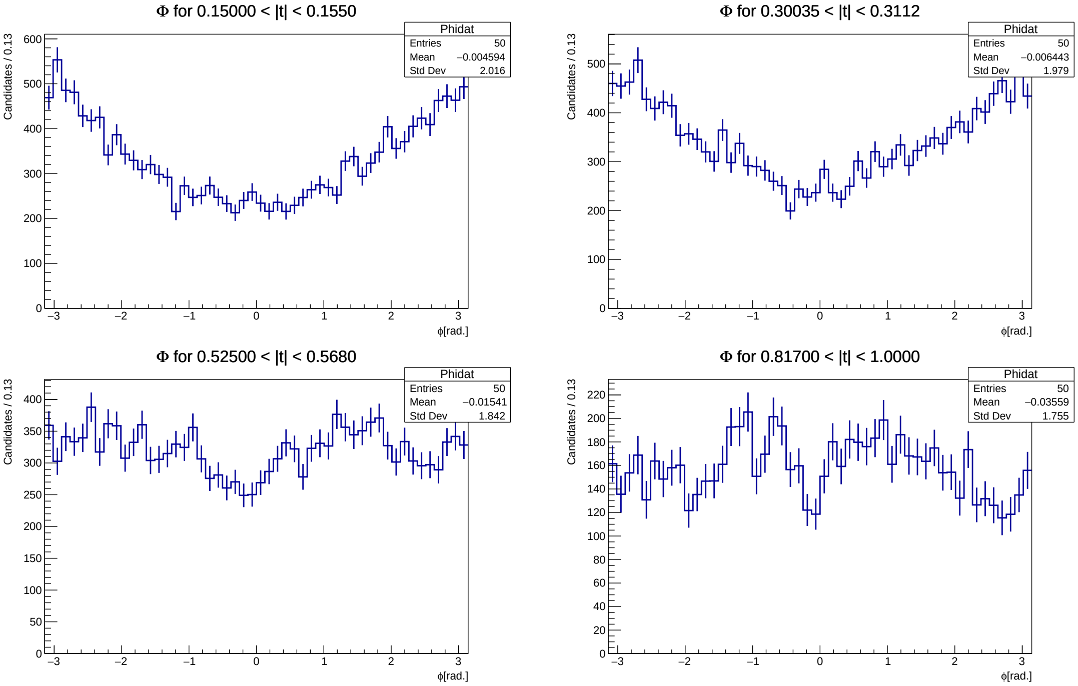

Figure C.6: Φ angular distribution across t for GlueX Phase-I data. One can see that the angular distribution changes as a function of t bin. This is why the end projection show change in dominance as discussed in Section 6.5

C.6 *t* Study for GlueX Phase-I data Sep `dsratio`

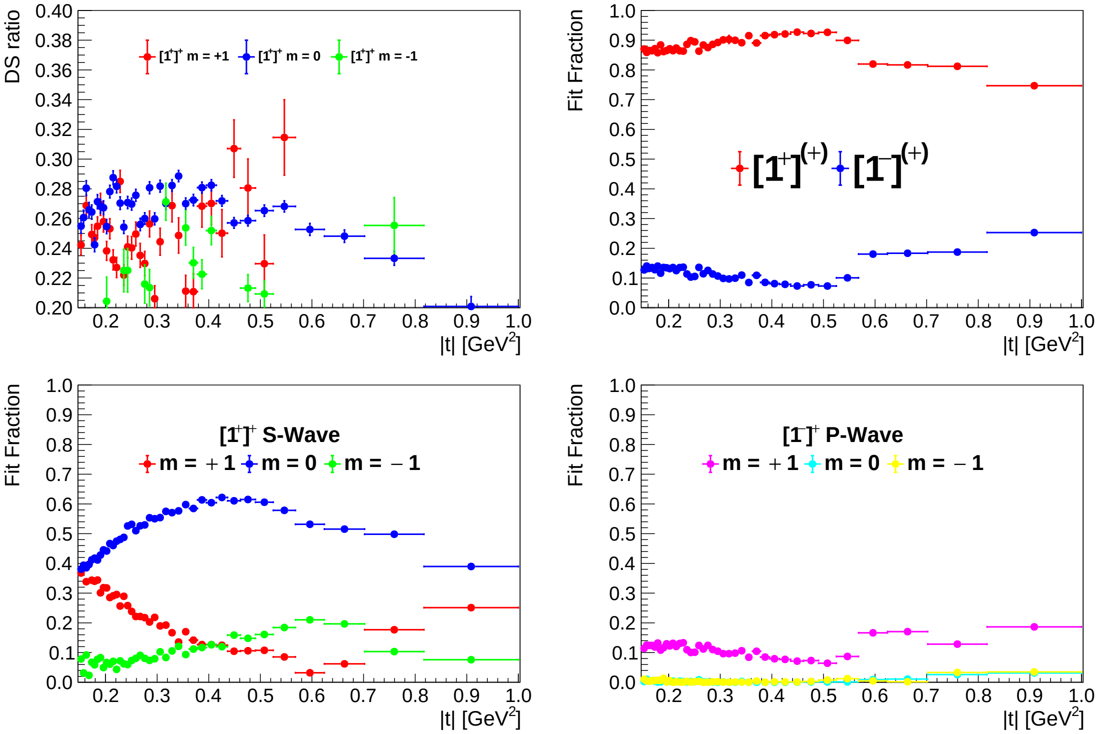

Figure C.7: Extracted `dsratio` in fine *t* bins for GlueX Phase-I data. The waveset used has three `dsratio` for each of the end projections corresponding to $[1]^+$ state.

Appendix D

APPENDIX : ECCE Tracking studies

D.0.1 Fundamental Concepts of MOO

The definitions below are with reference to Figure 7.5.

Design space: The space spanned by the design/search variables (x_i). The goal of the optimization is to find the most optimal set of design parameter solutions that performs optimally in the objective space.

For designing the ECCE tracker, the design space is spanned by geometric parameters of the detectors. For eg. the radius, length or 'z' position of detectors. Section 7.5.4 and Section 7.5.5, summarizes various detector design parameters that were optimized

Objective space: The space spanned by the number of objectives ($f_m(x)$). These functions depend on the design parameters. For optimizing the detector, the objectives used are detector performance metrics like momentum resolution, position resolutions, vertex resolutions, and track reconstruction efficiency. Further detector design can also be driven by specific physics observables which could best perform for a focused physics goal. Table 7.1 summarizes the objectives used for the optimization.

Constraints: During the process of optimization, there could exist a strictly non-feasible design region. For instance, during the construction of detectors, there could be the imposition of mechanical constraints, like the minimum distance required between two adjacent layers of detectors. Therefore, these constraints reflect in the design parameters. This is termed a Non Feasible region in the design space. Likewise, one can have Non-feasible regions in the objective space as well. However, this is not discussed in this thesis as it is beyond the scope of this study.

Optimization Algorithms: Navigating through the design space to minimize the objectives requires a back-end algorithm. One can understand the use of optimization algorithms by looking into the mapping function $\mathfrak{F}$. In most optimization problems, the mapping is a black function that can be "minimized" by heuristic or analytical methods. Two main methods of optimization algorithms were chosen for this study. Multi Objective Evolutionary Algorithm (MOEA) is an efficient semi-heuristic approach in solving MOO, The other method that is used is Multi Objective Bayesian Optimization (MOBO) which uses Gaussian Processes to construct a function that maps the design space to its objective space ($\mathfrak{F}$).

Non-dominated solutions: are solutions that are not worse than any other solutions in all objectives, and it is not possible to find another solution that is better in all objectives. Figure 7.5 (left) consider the points A and B, solution at point A performs better in objective f_1 compared to the solution at point B while the solution at point B performs better in objective f_2 compared to point A. These solutions are said to be non-dominating to one another. And one can note that all the points along the blue line are non-dominating to one another forming a "front" (F_2) of non-dominating solutions. One can observe the three fronts of non-dominated solutions marked as F_1, F_2, F_3 respectively. These fronts of solutions guide the selection of a solution that is most suitable for a given application.

Pareto-optimal set of solutions: a solution is said to be Pareto optimal if there does not exist any other solution that would be considered better by all objectives. In other words, a solution is Pareto optimal if no other solution can be found that would improve at least one objective without degrading at least one other objective. Pareto optimality is a way of finding a set of solutions that represents the trade-offs between different objectives. The set of all Pareto optimal solutions is called the Pareto front. It's important to note that Pareto optimality is a concept of relative optimality, it does not imply that the solutions are optimal in an absolute sense. In Figure 7.4 the black points on the objective space correspond to the Pareto optimal solutions for the given problem and the red line is called an approximated Pareto front.

Hyper Volume: As the optimization algorithm works on obtaining the optimal design parameters, One can evaluate the performance of the solutions at different stages. Hyper Volume (HV) is a measure of the volume of the region in the objective space that is dominated by a set of non-dominated solutions. It is often used as a performance metric for evaluating the quality of a set of solutions in multi-objective optimization problems. In Figure 7.5 the shaded red region corresponds to the Hyper Volume (HV). To calculate HV, a reference point is defined during the start of the optimization which often corresponds to the "worst" performing objectives. Then, the volume enclosed by the reference point and the approximated Pareto front is calculated [107].

Tolerance: refers to the change in parameters compared to previous iterations/calls. There are two types of tolerances, (i) Design tolerance which refers to the change in design parameters compared to previous iterations/calls and (ii) Objective tolerance which refers to the change in objectives computed compared to previous iterations/calls. To optimize ECCE tracker, objective tolerance is used.

Convergence criterion: A convergence criterion is a set of conditions or a specific test used to determine whether a numerical algorithm has reached a satisfactory level of accuracy or if it has reached a stable state. It is used to decide when to stop iterating or repeating a calculation. In other words, it's a rule used to determine whether an algorithm has "converged" to a solution. The criteria for convergence can vary depending on the algorithm, the problem being solved, and the desired level of accuracy. The following convergence criterion was used for optimizing ECCE tracker.

- Achieving an error tolerance of 10^{-4} in any one of the objectives.
- Reaching a maximum number of iterations.
- When improvement in Hyper Volume (HV) is no more than a threshold continuously for the last N iterations.

D.0.2 Bayesian Optimization

Bayesian Optimization is a method for the global optimization of expensive and noisy black-box functions. It is particularly useful for optimization problems where the number of function evaluations is limited, and the function evaluations are expensive or time-consuming.

The main idea behind Bayesian Optimization is to model the unknown function using a probabilistic surrogate model such as a Gaussian Process (GP). The GP is then used to make predictions about the function at new points, and the predictions are used to guide the search for the global optimum.

The process of Bayesian Optimization starts with an initial set of observations of the function, which are used to train the GP model. At each iteration, the GP model is used to predict the function value at the point that is expected to have the highest expected improvement. The function is then evaluated at this point, and the new observation is used to update the GP model.

In Bayesian Optimization, the acquisition function is a criterion that is used to decide which point to evaluate next. Popular examples of acquisition functions include Probability of Improvement (PI), Expected Improvement (EI), and Upper Confidence Bound (UCB). The choice of the acquisition function depends on the specific problem and the desired features. Pseudo code for Bayesian optimization is given in Algorithm 3

Algorithm 3 Pseudo code for Bayesian Optimziation

```
procedure BO
    Input: Initial set of observations, acquisition function, GP model
    Output: Optimal solution
    Initialize GP model with the initial set of observations
    for $i = 1$ to number of iterations do
        Choose the next point to evaluate based on the acquisition function
        Evaluate the function at the chosen point
        Update the GP model with the new observation
    end for
    Return the point with the highest acquisition function value as the optimal solution
end procedure
```

D.0.2.1 Gaussian Processes

Gaussian Processes (GPs) are a powerful and flexible tool for modelling non-linear and non-parametric functions. They are a type of Bayesian model that can be used for regression, classification, and other machine-learning tasks.

A GP is defined by a mean function and a covariance function (also known as a kernel function), which together determine the distribution of the function values at any point. The mean function defines the overall trend of the function, while the covariance function defines the smoothness and correlation of the function values at different points. The key property of a GP is that it is a distribution over functions, rather than just a single function. This allows for the modelling of uncertainty and the ability to make predictions at unseen points.

The process of fitting a GP model to a set of data is called training. During the training process, the GP learns the mean and covariance functions that best describe the data. A common method for training a GP is to use the maximum likelihood estimate (MLE) of the hyperparameters, which are the parameters of the mean and covariance functions. Once the GP is trained, it can be used to make predictions at new points by computing the posterior distribution of the function values at those points.

GPs have several advantages over other machine learning models. They can model complex and non-linear functions, they can handle large amounts of noise, and they can provide a measure of uncertainty in the predictions. Additionally, GPs are often used to model functions with a large number of input variables, and they are particularly useful when the number of observations is small. However, GPs have some disadvantages as well, such as they can be computationally expensive and they may not be able to handle large datasets efficiently.

Gaussian Processes provide a way to model uncertainty in the predictions. GPs have been widely used in various applications and have shown to be effective in many cases.

D.0.2.2 Acquisition functions for MOBO

An acquisition function is a key component of Bayesian optimization and MOBO methods. It is used to guide the search for the global optimum or the Pareto front by balancing the exploration and exploitation of the search space.

An acquisition function takes as input the current probabilistic model of the function (e.g. a Gaussian process) and the current set of observations and outputs a measure of the expected improvement of the function at a given point. The point with the highest expected improvement is then selected as the next point to evaluate the function.

There are several popular acquisition functions that have been proposed in the literature, each with its own trade-offs and advantages. Some popular examples of acquisition functions include:

- Probability of Improvement (PI): This acquisition function returns the probability that the function value at a given point will be better than a given threshold. This function is useful for problems where the global optimum is known to exist, but its location is uncertain.

- Expected Improvement (EI): This acquisition function returns the expected improvement of the function at a given point, relative to the current best function value. This function is useful for problems where the global optimum is unknown and the goal is to find the best possible solution.

- Upper Confidence Bound (UCB): This acquisition function returns the upper bound of the function value at a given point, based on the current probabilistic model. This function is useful for problems where the global optimum is unknown and the goal is to balance exploration and exploitation.

- Expected Hyper Volume Improvement (EHVI): These are the acquisition functions used in Multi-objective Bayesian optimization, they return the expected improvement of the hypervolume of the Pareto front. The EHVI is calculated as the expected value of the improvement in hyper volume that would be achieved if a new solution were selected at random from the set of candidates, compared to the current hyper volume defined by the reference point. The EHVI is calculated by first determining the hypervolume of the current Pareto front, defined by the set of candidate solutions, using the reference point. Next, the contribution of each solution to the improvement in hypervolume is calculated, and these contributions are weighted by the probability of selecting that solution. The expected value of these contributions is then taken as the EHVI. EHVI is a useful metric for evaluating the quality of a set of candidate solutions, as it takes into account both the diversity and convergence of the solutions. A high EHVI value indicates that there is still room for improvement in the Pareto front, while a low EHVI value indicates that the Pareto front is well-converged and that further improvement is unlikely. For optimizing ECCE tracker, MOBO with qNHEVI is used as its acquisition function.

D.1 Software framework

Figure D.1 represents a schematic of the ECCE Software. Various repositories hold relevant Fun4All analysis code. The macros combine the needed packages into one root script to run jobs. Default macros can run a wide variety of event generators, detector configurations, etc. One can pick and choose what to run depending on the analysis needs. The framework allows one to create the relevant module and register it with Fun4All. So various detector systems can be registered with Fun4All making it a modular framework and ideal for prototyping.

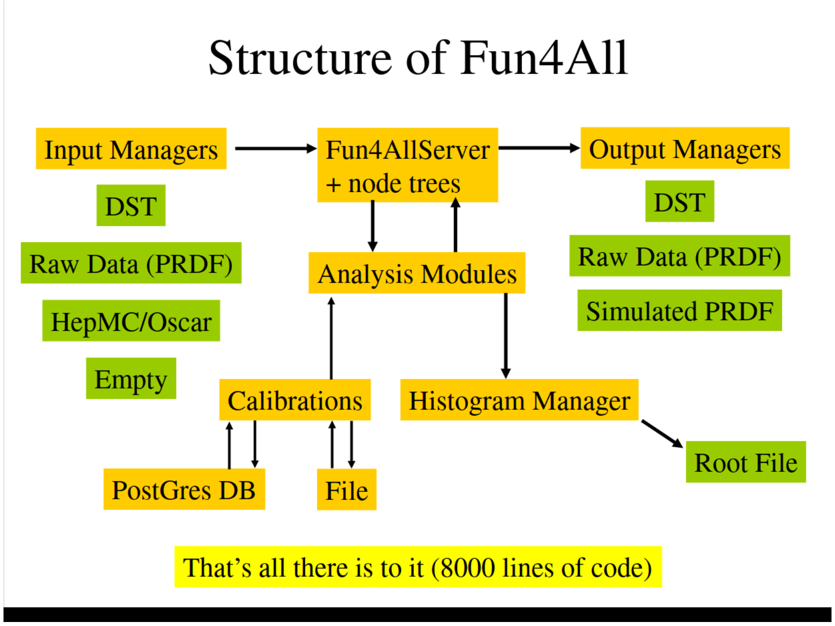

Figure D.1: Working of Fun4All framework: Input manager corresponds to all detector subsystems that are registered (DSTs) along with its physics generator (HepMC), Then the control passes on to Fun4AllServer where all the detector systems are registered. Relevant calibration files are loaded onto the server as well for simulation and reconstruction. After reconstruction, the output is produced in various formats starting from low-level reconstructions to high-level reconstructions. Figure from [108]

D.2 ECCE Tracking Studies

D.2.0.1 Tracking performance at the end of 2^{nd} Simulation Campaign

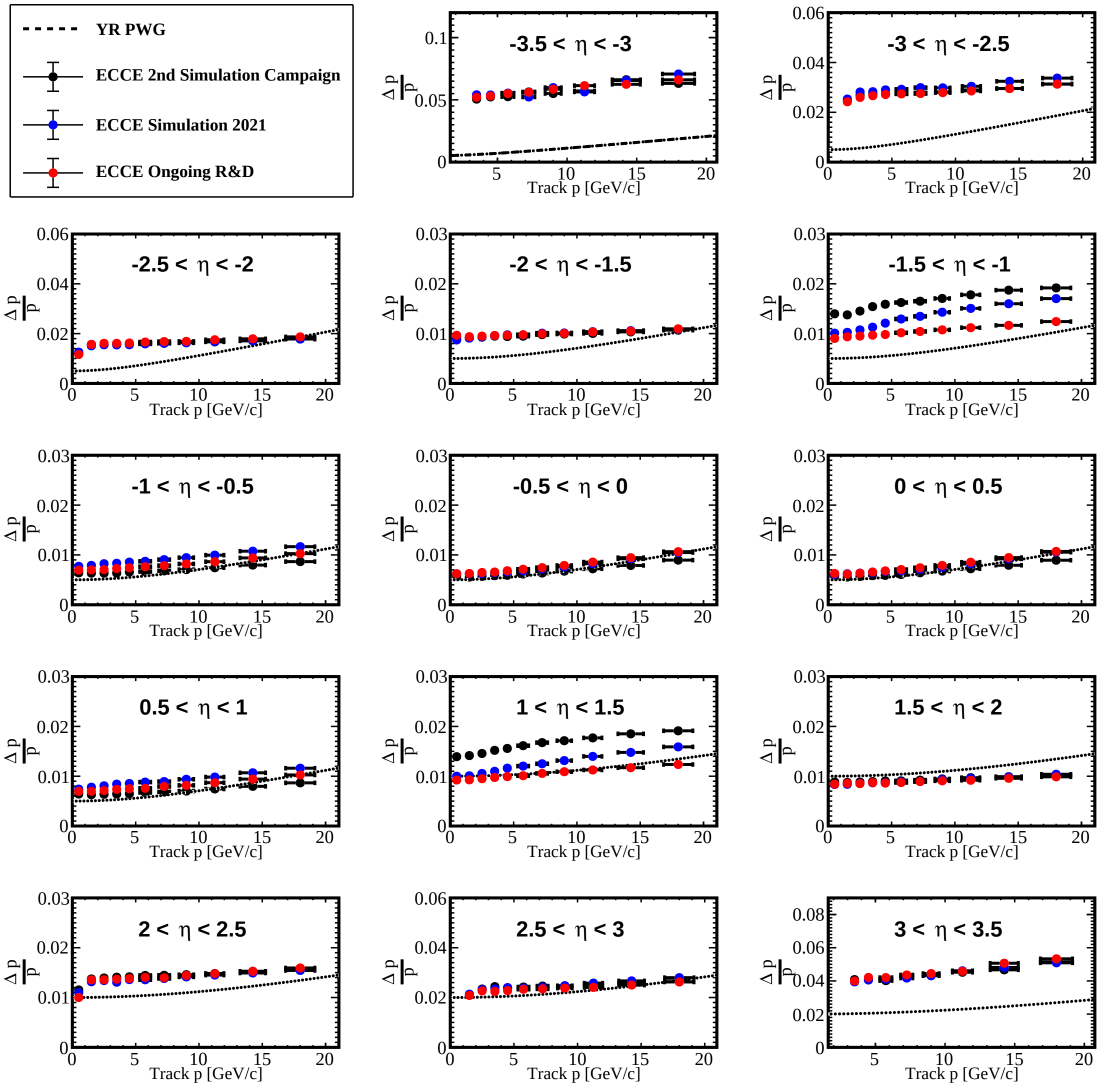

Figure D.2: Momentum resolution for ECCE 2^{nd} simulation campaign

D.2.0.2 Projected angular resolutions at DIRC PID location

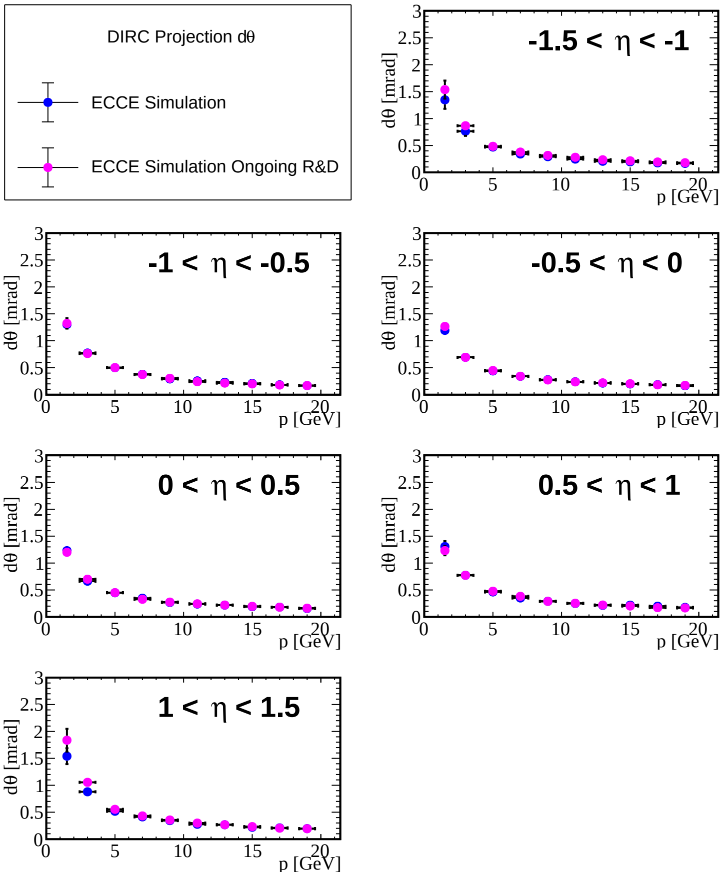

Figure D.3: Projected θ resolution at DIRC PID location

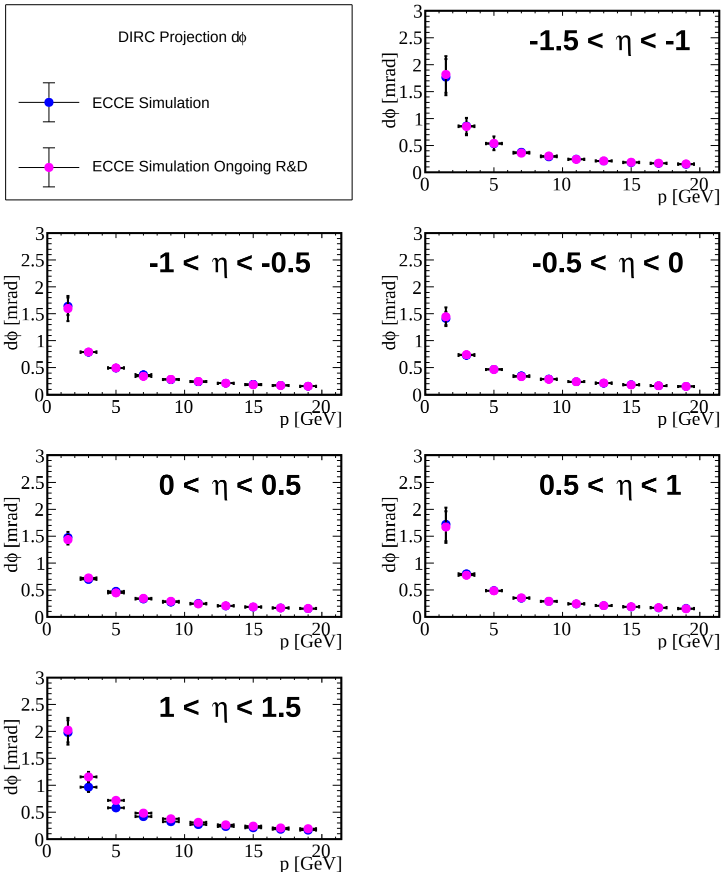

Figure D.4: Projected ϕ resolution at DIRC PID location

D.2.0.3 Projected angular resolutions at mRICH PID location

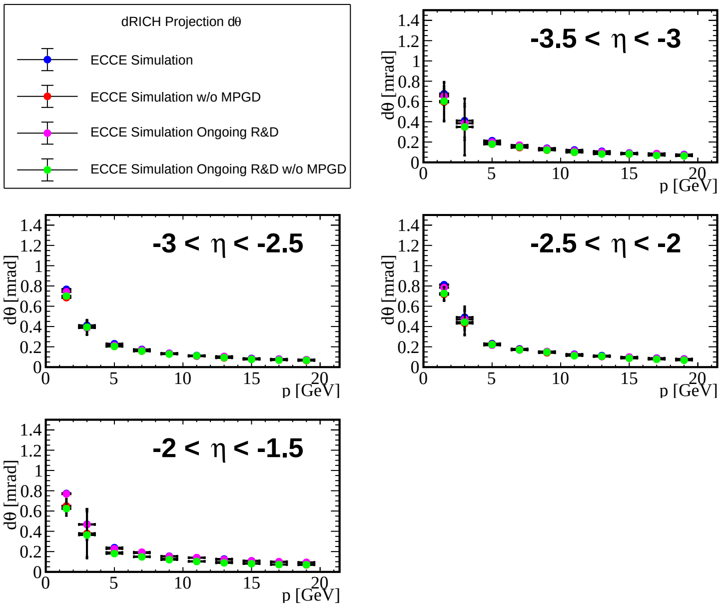

Figure D.5: Projected θ resolution at mRICH PID location

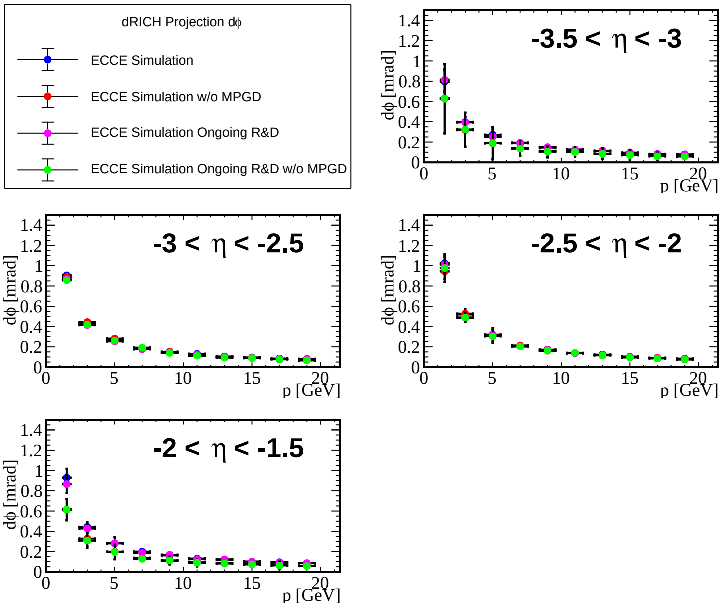

Figure D.6: Projected ϕ resolution at mRICH PID location

D.2.0.4 Projected angular resolutions at dRICH PID location

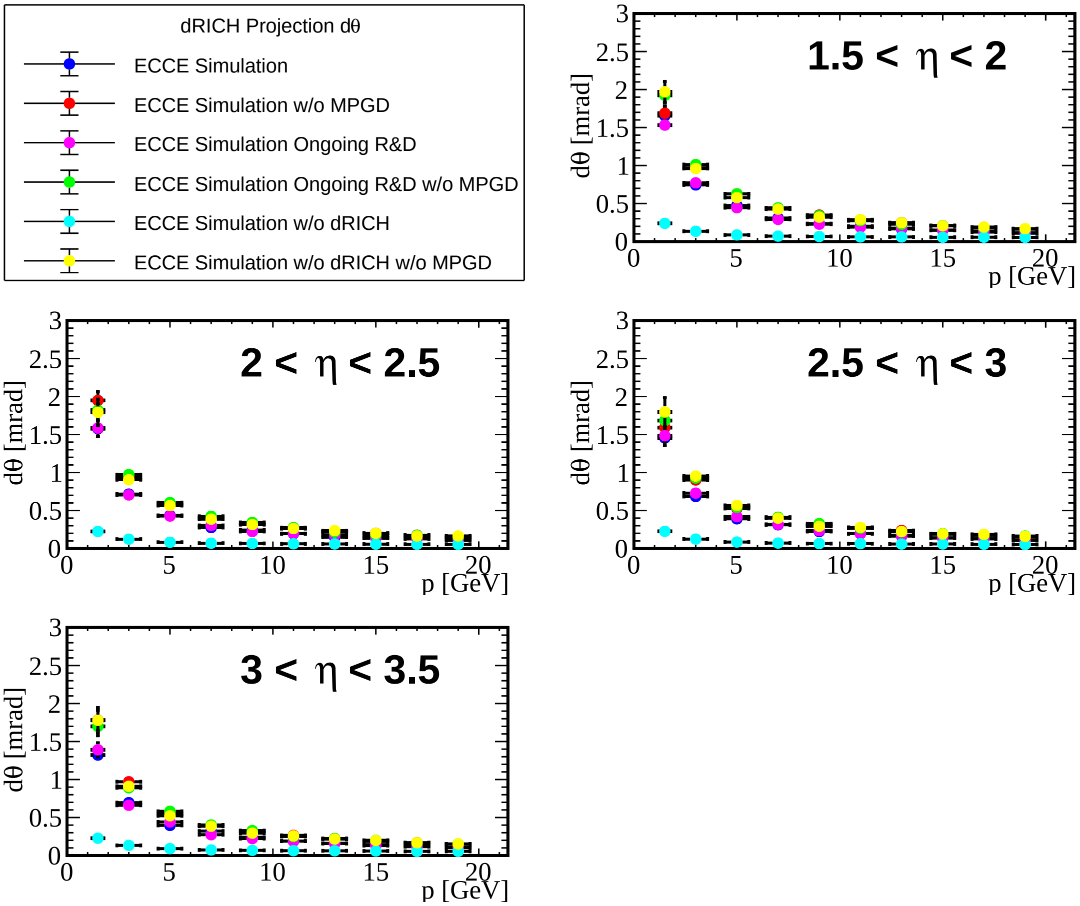

Figure D.7: Projected θ resolution at dRICH PID location

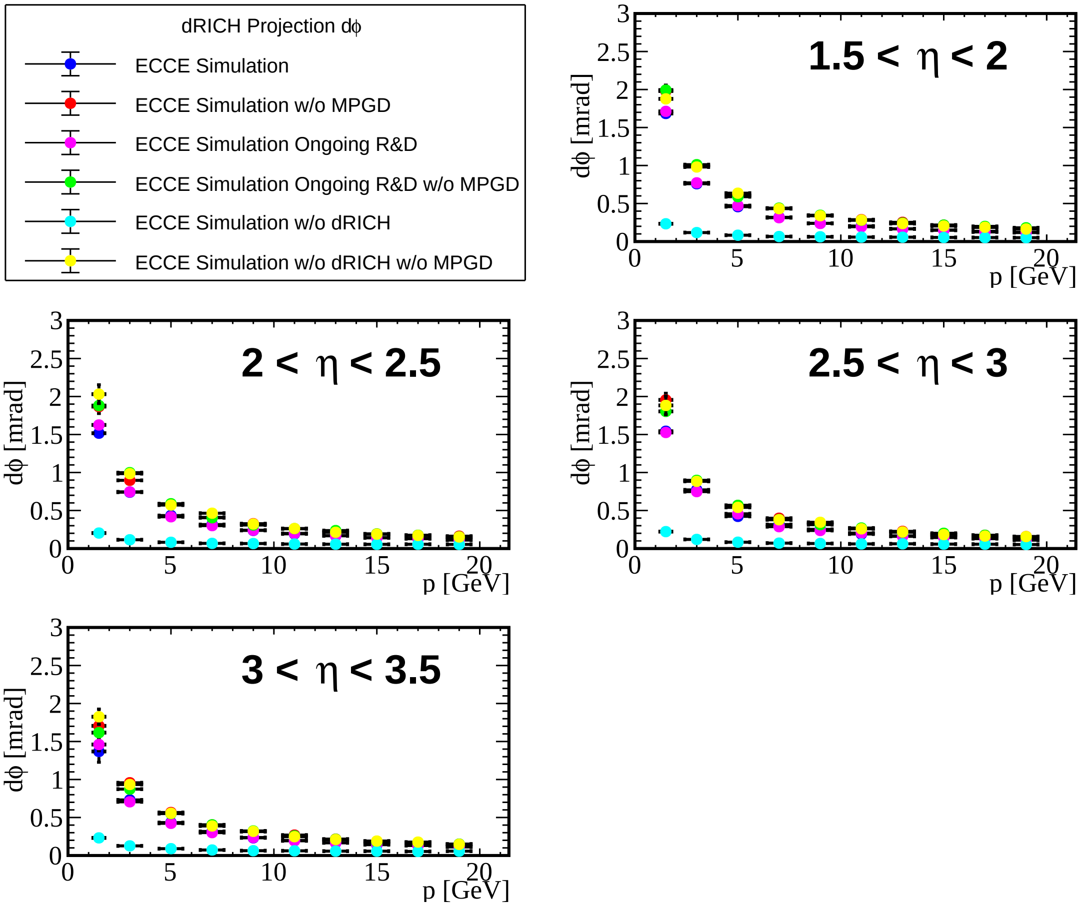

Figure D.8: Projected ϕ resolution at dRICH PID location

D.3 Calculating Errors on Objectives

D.3.1 Definitions

- Ratio of a given objective (f), $R(f)$ in one bin of η and in one bin in p is defined as

$$R(f)_{p,\eta} = \frac{\sigma_f(\text{current})}{\sigma_f(\text{reference})}\Bigg|_{p,\eta} \tag{D.59}$$

- The Error on $R(f)_{p,\eta}$ is $\Delta R(f)_{p,\eta}$

$$\Delta R(f)_{p,\eta} = \sqrt{\Big(R(f)_{p,\eta}\Big)^2 \left\{ \left(\frac{\Delta\sigma_f(\text{current})}{\sigma_f(\text{current})}\right)^2 + \left(\frac{\Delta\sigma_f(\text{reference})}{\sigma_f(\text{reference})}\right)^2 \right\}}\Bigg|_{p,\eta} \tag{D.60}$$

- Square of the Error is

$$\Big[\Delta R(f)_{p,\eta}\Big]^2 = RSq = \Big(R(f)_{p,\eta}\Big)^2 \left\{ \left(\frac{\Delta\sigma_f(\text{current})}{\sigma_f(\text{current})}\right)^2 + \left(\frac{\Delta\sigma_f(\text{reference})}{\sigma_f(\text{reference})}\right)^2 \right\}\Bigg|_{p,\eta} \tag{D.61}$$

- we have the weights defined as

$$w(f)_{p,\eta} = \frac{1}{\Big[\Delta R(f)_{p,\eta}\Big]^2} = \frac{1}{RSq} \tag{D.62}$$

$$\Delta w(f)_{p,\eta} = w(f)_{p,\eta}\left\{\frac{\Delta\big[\Delta R(f)_{p,\eta}\big]^2}{\big[\Delta R(f)_{p,\eta}\big]^2}\right\}$$

$$\Delta w(f)_{p,\eta} = \big[w(f)_{p,\eta}\big]^2\Big\{\Delta\big[\Delta R(f)_{p,\eta}\big]^2\Big\} = \big[w(f)_{p,\eta}\big]^2 \cdot \Delta RSq \tag{D.63}$$

- Now the metric f_η extracted in a given eta bin (reducing in all bins of p) is

$$f_\eta = \frac{\sum_p R(f)_{p,\eta} w(f)_{p,\eta}}{\sum_p w(f)_{p,\eta}} \tag{D.64}$$

- Then the Error associated in Equation D.64

$$\Delta f_\eta = f_\eta \sqrt{\left(\frac{\Delta[\sum_p R(f)_{p,\eta} w(f)_{p,\eta}]}{\sum_p R(f)_{p,\eta} w(f)_{p,\eta}}\right)^2 + \left(\frac{\Delta[\sum_p w(f)_{p,\eta}]}{\sum_p w(f)_{p,\eta}}\right)^2}$$

Or equivalently,

$$\Delta f_\eta = f_\eta \sqrt{\left(\frac{\sum_p \Delta[R(f)_{p,\eta} w(f)_{p,\eta}]}{\sum_p R(f)_{p,\eta} w(f)_{p,\eta}} + \frac{\sum_p \Delta[w(f)_{p,\eta}]}{\sum_p w(f)_{p,\eta}}\right)} \tag{D.65}$$

or equivalently

- Now the metric f_η and its error Δf_η extracted from all bins of η is defined as

$$f = \frac{\sum_\eta f_\eta}{N_\eta} \tag{D.66}$$

$$\Delta f = \frac{1}{N_\eta}\sum_\eta \Delta f_\eta \tag{D.67}$$

D.3.2 Calculating Δf_η

Looking into Equation D.65. we are calculating the part $\Delta\Bigg[\sum_p R(f)_{p,\eta}w(f)_{p,\eta}\Bigg]$. For simpler notation

$$R(f)_{p,\eta} \equiv R$$

$$w(f)_{p,\eta} \equiv w$$

$$\Delta R.w = w.\Delta R + R.\Delta w \qquad \text{(D.68)}$$

ΔR is defined in Equation D.60. Now we should calculate Δw.

Formula for Δw is defined in Equation D.63.

$$\Delta w = \Delta(Rsq)$$

and we know RSq is $R^2\Bigg\{\left(\frac{\Delta\sigma_f(\text{current})}{\sigma_f(\text{current})}\right)^2 + \left(\frac{\Delta\sigma_f(\text{reference})}{\sigma_f(\text{reference})}\right)^2\Bigg\}$

Therefore, calculating ΔRSq

$$\Delta RSq = RSq\Bigg\{\frac{2\Delta R}{R} + \Delta\Bigg\langle\left(\frac{\Delta\sigma_f(\text{current})}{\sigma_f(\text{current})}\right)^2 + \left(\frac{\Delta\sigma_f(\text{reference})}{\sigma_f(\text{reference})}\right)^2/...\Bigg\rangle\Bigg\}$$

I am not considering the second part because I am going to work with only first moments.

Therefore, The error ΔRSq is,

$$\Delta w = \Delta RSq = RSq\left(\frac{2\Delta R}{R}\right) = \frac{1}{w}\left(\frac{2\Delta R}{R}\right) \tag{D.69}$$

Now we put these back in Equation D.68

$$\Delta(R.w) = R.\frac{1}{w}\left(\frac{2\Delta R}{R}\right) + w.\Delta R$$

$$\Delta(R.w) = \frac{2\Delta R}{w} + w\Delta R$$

$$\Delta(R.w) = \Delta R\left(\frac{2}{w} + w\right)$$

Giving back the original η, p notation

$$\Delta\left(R(f)_{p,\eta}.w(f)_{p,\eta}\right) = \Delta R(f)_{p,\eta}\left(\frac{2}{w(f)_{p,\eta}} + w(f)_{p,\eta}\right)\Bigg|_{p,\eta} \tag{D.70}$$

and

$$\Delta w(f)_{p,\eta} = \frac{2\Delta R(f)_{p,\eta}}{w(f)_{p,\eta}R(f)_{p,\eta}} \tag{D.71}$$

Finally we have the expression for Δf_η

$$\Delta f_\eta = f_\eta\left\{\frac{\sum_p \Delta R(f)_{p,\eta}\left(\frac{2}{w(f)_{p,\eta}} + w(f)_{p,\eta}\right)}{\sum_p R(f)_{p,\eta}w(f)_{p,\eta}} + \frac{\sum_p \frac{2\Delta R(f)_{p,\eta}}{w(f)_{p,\eta}R(f)_{p,\eta}}}{\sum_p w(f)_{p,\eta}}\right\} \tag{D.72}$$

D.3.3 Can reduce further in just R and ΔR

As per definitions in Equation D.62 and Equation D.61

$$w(f)_{p,\eta} = \frac{1}{\Bigg[\Delta R(f)_{p,\eta}\Bigg]^2}$$

, Replace all w's in numerator with the above expression in Equation D.72

$$\Delta f_\eta = f_\eta \left\{ \frac{\sum_p \left(2\Delta[R(f)^p_\eta]^3 + \frac{1}{\Delta R(f)^p_\eta]} \right)}{\sum_p R(f)_{p,\eta} w(f)_{p,\eta}} + \frac{\sum_p \frac{2\Delta[R(f)_{p,\eta}]^3}{R(f)_{p,\eta}}}{\sum_p w(f)_{p,\eta}} \right\} \tag{D.73}$$